

ISSN 0911-5730

UVSOR-32

June 2005

UVSOR ACTIVITY REPORT 2004

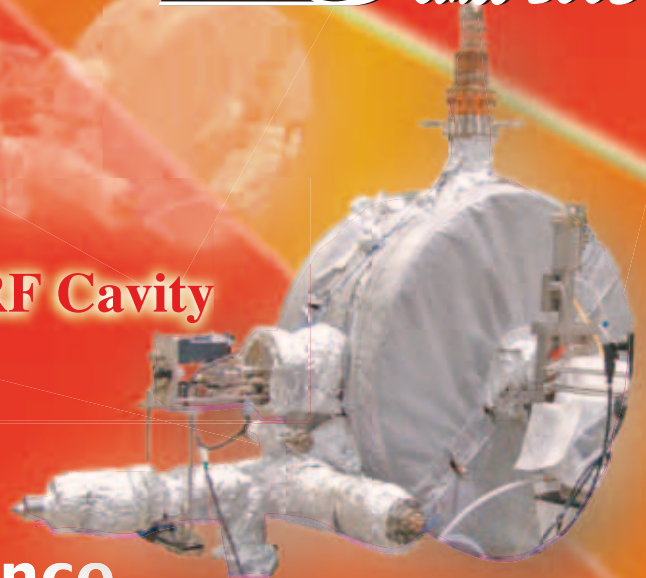


BL3U



UVSOR II
since 2003

New RF Cavity



UVSOR Facility
Institute for Molecular Science
National Institutes of Natural Sciences

UVSOR
ACTIVITY REPORT
2004

edited by

Y. Hikosaka, H. Hagiwara, T. Ito

Preface

This Activity Report covers the research activities done at the UVSOR facility in the Institute for Molecular Science (IMS) in FY2004 (April 2004-March 2005). This is the second volume in the new series for the third decade of UVSOR, corresponding to the second year of the use of the UVSOR-II storage ring. Through FY2004, the UVSOR-II ring has been stable in operation at the initial beam current of 350 mA for every injection and the beam emittance of 60 nm-rad. We have now installed a high-power main RF accelerating cavity (see the front cover of this report) to reduce the emittance to 27 nm-rad under the same or better condition of the beam current and lifetime. One of the next upgrade plans is to replace the power supply of the magnet system of the booster synchrotron for the full energy injection to the storage ring next year. A new long undulator beamline BL3U to make possible high-resolution soft X-ray photoelectron and fluorescence spectroscopy (see the front cover) has been stable in operation for FY2004. We have now started a next beamline project using another new long undulator BL7U to make possible high-resolution VUV photoelectron spectroscopy next year. The upgrade of the world-class IR/FIR(THz) beamline BL6B has been successful. We have now started a coherent THz source project by using a seed laser of 90MHz repetition rate.

IMS started an original international collaboration program last year. UVSOR could accept several foreign scientists working in the fields of accelerator science and molecular science. I have asked some of them to review the status and activities of the UVSOR facility. It is a pleasure to include here a letter from Professor Marie-Emmanuelle Couprie, who came to UVSOR three times in FY2004 to work for the storage-ring FEL.

It is another pleasure to report two awards regarding outstanding activities carried out in UVSOR. Last summer Professor Hiroyuki Hama, Tohoku University, received "The FEL Prize in 2004" for his pioneering work in the field of the storage-ring FEL. This spring Mr. Toshio Horigome, Chief of the UVSOR technical division, received "The CSJ Award for Technical Achievements" from the Chemical Society of Japan for his distinguished and long-standing achievements in high-precision and compact instrumentation (see this back page).

We look forward to more exciting activities in the coming year.

April, 2005

Nobuhiro Kosugi
Director of UVSOR

MR. TOSHIO HORIGOME
(CHIEF ENGINEER OF THE UVSOR FACILITY)
RECEIVED
THE CSJ AWARD FOR TECHNICAL
ACHIEVEMENTS!!



**“Experimental Apparatus Design&Fabrication
for Molecular Photoscience”**

*CSJ: The Chemical Society of Japan



To the attention of Professor Nobuhiro Kosugi
Director of UVSOR
Institute for Molecular Science
Myodaiji
Okazaki 444-8585

Saclay, 2005, the 15th of March

Dear Professor Kosugi,

UVSOR is a world-class research synchrotron radiation facility for VUV and soft X ray radiation. Regular up-upgrades on the machine and on the beamlines make it very competing, even now, in the new landscape of third generation synchrotron light sources such as ALS (Berkeley), ELETTRA (Trieste), BESSY-II (Berlin), MAX II (Lund), SLS (Villengen), and the newly coming Diamond (Oxford) and SOLEIL (Saclay). Besides, UVSOR hosts a storage ring Free Electron Laser (SRFEL) source. I had the chance to collaborate with FEL scientists during short time stays, and a longer three months stay this summer in Okazaki, after the shut down of the Super-ACO Free Electron Laser at the end of 2003, on which I have been working for 14 years.

Key advances for the FEL community were made on the UVSOR FEL since its first lasing in 1992. Since 1994 in UVSOR, very early systematic sophisticated experimental analysis of the FEL micropulse temporal and spectral distributions versus time with the use of a double sweep streak camera in the early days of storage ring FELs could provide a deeper insight on FEL dynamics, for different operating conditions especially versus detuning (i.e. synchronism between the electron stored in the ring and the optical pulses bouncing in the optical resonator). Detailed studies on FEL performances for different momentum compaction factors were carried out. A great progress was also made with the installation of the first helical to planar optical klystron for FEL operation, in 1996. UVSOR contributed also to the progress in short FEL wavelength operation, with FEL lasing at 238 nm in 1996. A longitudinal feedback system was developed to maintain the FEL pulse at perfect synchronism, leading to successful pump-probe two-colour experiments in gas phase using FEL light and synchrotron radiation for the first time. The production of monochromatic gamma-rays by Compton Back-Scattering with SRFELs was first demonstrated on the UVSOR FEL in 1996 and broadened the use of FELs into the field of nuclear physics. Professor Hiroyuki Hama was awarded the FEL Prize in 2004 jointly with V. Litvinenko for these pioneering works.



Recent upgrade of UVSOR II with significantly lower emittance resulting from a chromatic optics provides a unique opportunity to investigate more deeply the interaction between the FEL and the electron beam, and to compare it to the well-established saturation process in the usual achromatic mode. Indeed, in the chromatic case, the saturation process in which the electron beam is heated by the light source (enhancement of energy spread) induces not only a lengthening of the electron bunch in the longitudinal plane but also in the transverse domain, leading to a significant increase of the Touschek lifetime induced by the FEL. Besides, a very high current can be stored, allowing the appearance of various types of instabilities, with which the FEL is competing, and under given circumstances, to the level of suppressing them. Such an understanding of the interplay between the FEL and the electron beam will be fruitful for the new slicing project to be conducted by Prof. Masahiro Katoh, with a high intense Titanium:Sapphire laser interacting with the electron beam in an undulator, for the production of femtosecond synchrotron radiation.

Apart from the increasing interest for Linac based FEL for short wavelength radiation (i.e. VUV and X ray range) and from the FEL user facilities operating in the infra-red, Storage Ring Based FELs appear to be quite valuable sources for the UV and VUV range. At present, after the closing of Super-ACO in France, four installations are operating. The European ELETTRA FEL (Trieste, Italy), installed on a third generation light source, detains the record of the shortest wavelength (172-182 nm) for FEL oscillators, and a program of harmonic generation is under development. On the NIJI-IV FEL (Tsukuba, Japan), different studies on the FEL sources are in progress. Besides, the DUKE FEL (DUKE University, USA), after various successful results (gamma-rays produced by Compton Back Scattering exploited by users, short wavelength operation in the oscillator and harmonic generation configuration...) is planning the installation of an multiple optical klystron (OK5) on a long straight section.

The FEL source quality of UVSOR II should be pointed out, and it offers a high stability level, very unique nowadays. This is of crucial importance for the quality of the data of the user experiments, and especially requested for pump-probe two-colour experiments. Pump-probe two-color experiments have been performed only on the SRFELs installed on UVSOR and Super-ACO so far, because of the very limited intensity fluctuations of these particular sources. Besides, the possibility of changing the polarisation of the UVSOR FEL, will be exploited soon at 250 nm for chirality studies in biological molecules.

The high FEL stability also permits to progress further in the FEL dynamics, which is understood in this case with the point of view of the conventional laser systems. Indeed, the study of pass to pass equations of the FEL electric field exhibits some phase singularities, which signature can be given by the presence of holes in the spectral distribution and temporal drifts in the temporal domain. These correlated phenomena were clearly observed on the UVSOR FEL. The nonlinear dynamics approach also allowed the pulsed regimes at the millisecond time scale to be controlled, thanks to the existence of an unstable cw state coexisting with the limit cycles regimes. The region of the detuning curve in which the FEL is cw can then be further extended, and offers a wider zone of operation for users applications.



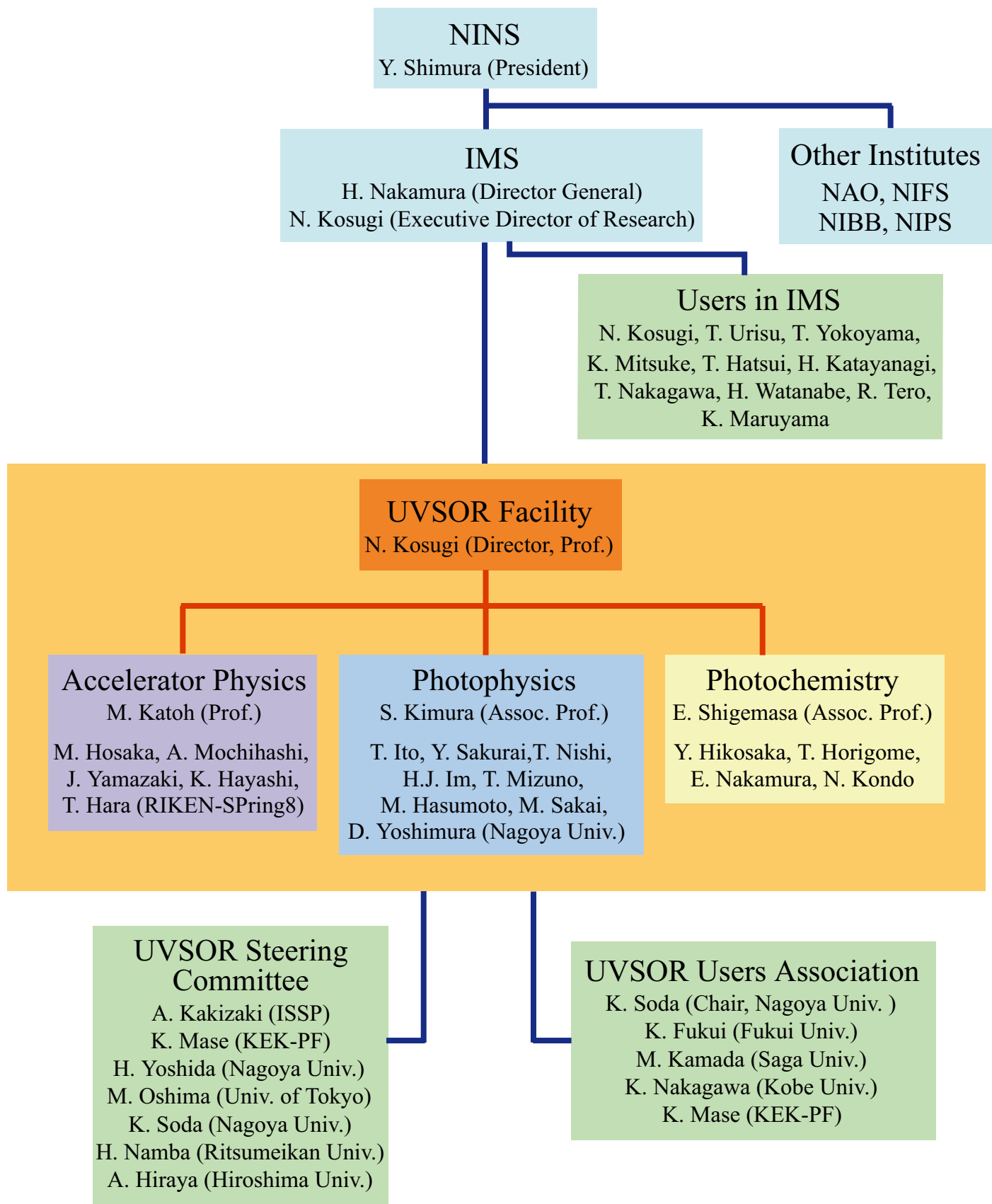
Finally, it is quite relevant to stress the advantage of developing an FEL in the environment provided by the synchrotron radiation community of UVSOR, and the laser oriented laboratories of IMS. Such a double culture is key issue for the establishment and fruitful exchanges between sources builders and user scientists, for conventional lasers, high harmonics produced in gases and accelerator based light sources such as synchrotron radiation centres and fourth generation light sources based on Free Electron Laser devices. IMS can be considered as combined facility providing short and ultra-short light sources for a multi-disciplinary community. Gathering accelerator light sources and conventional lasers facilities at the same location provides an enhancement expertise and opens the way for new opportunities of scientific challenges. Besides, the interaction between scientists takes place in a very nice atmosphere, which makes the exchanges even more fruitful.

Yours sincerely,

A handwritten signature in blue ink, which appears to read 'M. Couprie', is positioned to the right of the 'Yours sincerely,' text.

Marie-Emmanuelle Couprie
Commissariat à l'Énergie Atomique,
Service de Photons, Atomes et Molécules, ATTO group

UVSOR Organization (2005/4/1)



UVSOR Staff

Director

KOSUGI, Nobuhiro	Professor	kosugi@ims.ac.jp
------------------	-----------	------------------

Light Source Division (Accelerator Physics)

KATO, Masahiro	Professor	mkato@ims.ac.jp
HOSAKA, Masahito	Research Associate	hosaka@ims.ac.jp
MOCHIHASHI, Akira	Research Associate	mochi@ims.ac.jp
YAMAZAKI, Jun-ichiro	Unit Chief Engineer	yamazaki@ims.ac.jp
HAYASHI, Kenji	Engineer	h-kenji@ims.ac.jp
MURAKAMI, Takayuki	Supporting Engineer	tmurakami@ims.ac.jp (until Mar. 2005)
HARA, Toru	Guest Professor	(since Apr. 2005)

Beamline Division (Photophysics)

KIMURA, Shin-ichi	Associate Professor	kimura@ims.ac.jp
ITO, Takahiro	Research Associate	tito@ims.ac.jp
HASUMOTO, Masami	Unit Chief Engineer	hasumoto@ims.ac.jp
SAKAI, Masahiro	Engineer	sakai@ims.ac.jp (since Apr. 2005)
SAKURAI, Yoko	Post-Doctoral Fellow	sakurai@ims.ac.jp
YOSHIMURA, Daisuke	Guest Researcher	daisukey@ims.ac.jp (since Apr. 2005)

Beamline Division (Photochemistry)

SHIGEMASA, Eiji	Associate Professor	sigemasa@ims.ac.jp
HIKOSAKA, Yasumasa	Research Associate	hikosaka@ims.ac.jp
HORIGOME, Toshio	Facility Chief Engineer	horigome@ims.ac.jp
NAKAMURA, Eiken	Unit Chief Engineer	eiken@ims.ac.jp
KONDO, Naonori	Engineer	nkondo@ims.ac.jp
ITO, Kenji	Guest Professor	(until Mar. 2005)

Secretary

HAGIWARA, Hisayo		hagiwara@ims.ac.jp
ONITAKE, Naoko		onitake@ims.ac.jp (until Mar.2005)

Graduate Students

NISHI, Tatsuhiko	Grad. Univ. Adv. Studies	tnishi@ims.ac.jp
IM, Hojun	Grad. Univ. Adv. Studies	hojun@ims.ac.jp
MIZUNO, Takafumi	Okayama Univ. Sci.	(since Apr. 2005)

Visiting Scientists

KWON, Yong-Seung	Sungkyunkwan Univ.	(until Sep. 2004)
COUPRIE, Marie-Emmanuelle	CEA	(Jun.-Sep.&Dec. 2004)
SICHELSCHMIT, Joerg	Max Planck Institute	(May 2004, Feb. 2005)
RUBENSSON, Jan-Erik	Uppsala Univ.	(Jul. 2004)
LABLANQUIE, Pascal	LURE	(Sep. 2004-Feb. 2005)
MEYER, Michael	LURE	(Nov.-Dec. 2004)
BIELAWSKI, Serge	Lill Univ.	(Dec. 2004)
SZWAJ, Christophe	Lill Univ.	(Dec. 2004)
STANKEVICH, Vladimir	Kurchatov Institute	(since Jan. 2005)
SIMON, Marc	LCPMR	(Jan. 2005)
NOH, Tae Won	Seoul National Univ.	(Feb-Mar. 2005)
ZHANG, Shancai	Univ. Sci. Tech. China	(Mar. 2005)
FENG, Guangyao	Univ. Sci. Tech. China	(Mar. 2005)

UVSOR Steering Committee (FY2004-2005)

KOSUGI, Nobuhiro	UVSOR, IMS	Chair
KIMURA, Shin-ichi	UVSOR, IMS	
KATOH, Masahiro	UVSOR, IMS	
SHIGEMASA, Eiji	UVSOR, IMS	
ITO, Kenji	UVSOR, IMS	(Guest Professor from KEK-PF, until Mar. 2005)
HARA, Toru	UVSOR, IMS	(Guest Professor from RIKEN, since Apr. 2005)
YOKOYAMA, Toshihiko	IMS	
MATSUMOTO, Yoshiyasu	IMS	
OGAWA, Takuji	IMS	
MITSUKE, Koichiro	IMS	
KAKIZAKI, Akito	Univ. of Tokyo	
MASE, Kazuhiko	KEK-PF	
YOSHIDA, Hisao	Nagoya Univ.	
OSHIMA, Masaharu	Univ. of Tokyo	
SODA, Kazuo	Nagoya Univ.	
NAMBA, Hidetoshi	Ritsumeikan Univ.	
HIRAYA, Atsunari	Hiroshima Univ.	

Light Source in 2004

Masahiro KATOH

UVSOR Facility, Institute for Molecular Science

1. Status of UVSOR-II

In the fiscal year 2004, we have operated the UVSOR-II accelerators from May '04 to March '05. We had two shut-down periods, in April '04 and March '05. The former was to install a new vacuum chamber for the bending magnet, B6. This chamber was specially designed and constructed for the infrared beam-line BL6B(IR) [1]. The latter was to install the new RF accelerating cavity. The new cavity has capability of producing three times stronger accelerating field. We also stopped the operation for one week in September for some maintenance works and for two weeks around the New Years day.

We had only a few troubles on the accelerators during FY2004. The most serious one happened on the power supply of the booster-synchrotron magnets, which has been working for more than 20 years. Fortunately, the power supply was soon recovered by replacing the broken electronic device. The users operation was canceled only for one day. This power supply will be replaced in FY2006. The new one will have capability of increasing the maximum beam energy of the booster synchrotron from 600 MeV to 750 MeV. Then, we will be able to inject a full energy electron beam into the storage ring.

We had 36 weeks for the users operation in multi-bunch mode and had two weeks in single bunch mode. We had two weeks dedicated for machine studies. The monthly statistics of the operation time and the integrated beam current are shown in Figures 1. The normal operation pattern in a week is as follows. From Tuesday to Friday, the machine is operated for users. The beam injection is twice a day, at 9:00 and 15:00. The initial beam current of each run is 350 mA in multi-bunch mode and 100 mA in single bunch mode. On Monday, the machine is operated for machine studies.

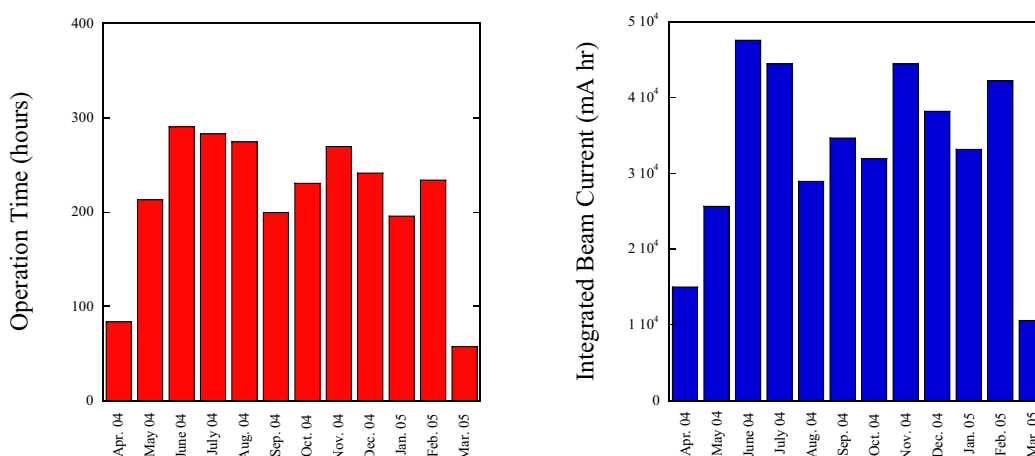


Fig. 1 Monthly statistics of the operation time (left) and Monthly statistics of the integrated beam current (right).

2. Improvements

New Vacuum Chamber for the Bending Magnet B6

The vacuum chamber of the bending magnet B6 was replaced in spring, 2004. The BL6A1 was an infrared beam-line, which had been in operational for many years [2]. This beam-line was converted to a new infrared beam-line BL6B, which would be the world most powerful beam-line in the far infrared regime. To construct this beam-line, we replaced the vacuum chamber of the bending magnet B6. The new chamber has a mirror room directly connected to the bending beam pipe, as shown in Figure 2. In this chamber, a distributed sputtering ion pump (DIP), a normal sputtering ion pump (SIP) and a titanium sublimation pump (TGP) are installed. Two sets of the button type beam position monitor were installed at the both ends. The chamber was made of stainless steel. The chamber was installed in the ring and baked. The vacuum was almost recovered after the high current operation for a few weeks.



Fig. 2 New Bending Chamber for B6 just after the installation.

New RF Accelerating Cavity

In the fiscal year 2004, the new RF cavity will be constructed [3]. With the present RF power source whose maximum output power is 20 kW, the new cavity will produce 150 kV accelerating voltage for the beam current of 500 mA. This will greatly improve the Touschek lifetime.

The new cavity was delivered in March 2005. The old cavity was removed from a straight section between the bending magnet B6 and B7. In this section, a short in-vacuum undulator is in operation. This undulator will move to another short straight section. Then, this section will be available for a new long undulator. The new cavity was installed in the short straight section between B1 and B2.



Fig. 3 Old (left) and new (right) RF cavities.

3. Researches and Developments

Free Electron Laser

The smaller emittance of UVSOR-II has increased the gain of the free electron laser [4]. We have succeeded in oscillating in deep UV region around 250 nm with an average power of a few hundred mW, as shown in Fig. 4. The reinforcement in the RF accelerating system is expected to increase the FEL gain more. We will try an oscillation in VUV region in near future.

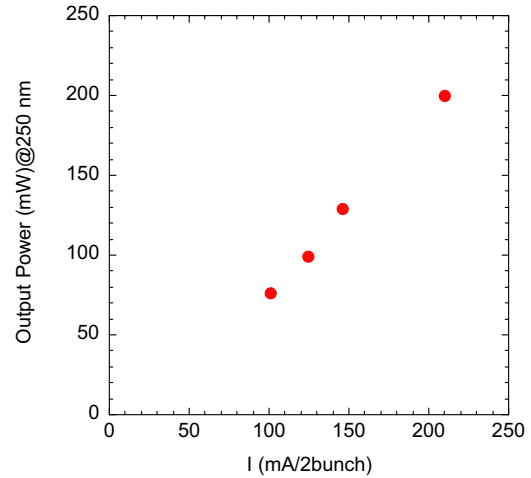


Fig. 4 Average Output Power of the Free Electron Laser oscillating at 250 nm.

Observation of Terahertz Bursts

At the UVSOR-II storage ring, possible coherent synchrotron radiation was observed in the wavelength region between 0.2 and 3.0 mm [5]. Bursts of terahertz emission were detected, as shown in Fig. 5 when the ring was operated in single bunch mode and the beam current exceeded a certain threshold current, typically around 100 mA. Typical duration and interval of the bursts are about 200 micro-seconds and 10 - 15 milliseconds, respectively. Each burst contains many peaks and shows quasi-periodicity of about 30 micro-seconds. The peak intensities of the bursts are 10000 times higher than that of normal synchrotron radiation in the same wavelength region. The threshold current depends on the operation condition of the storage ring, especially that of the RF system.

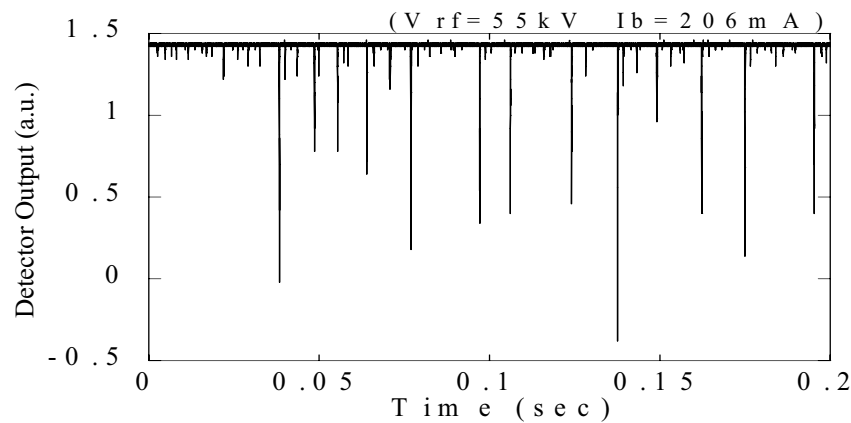
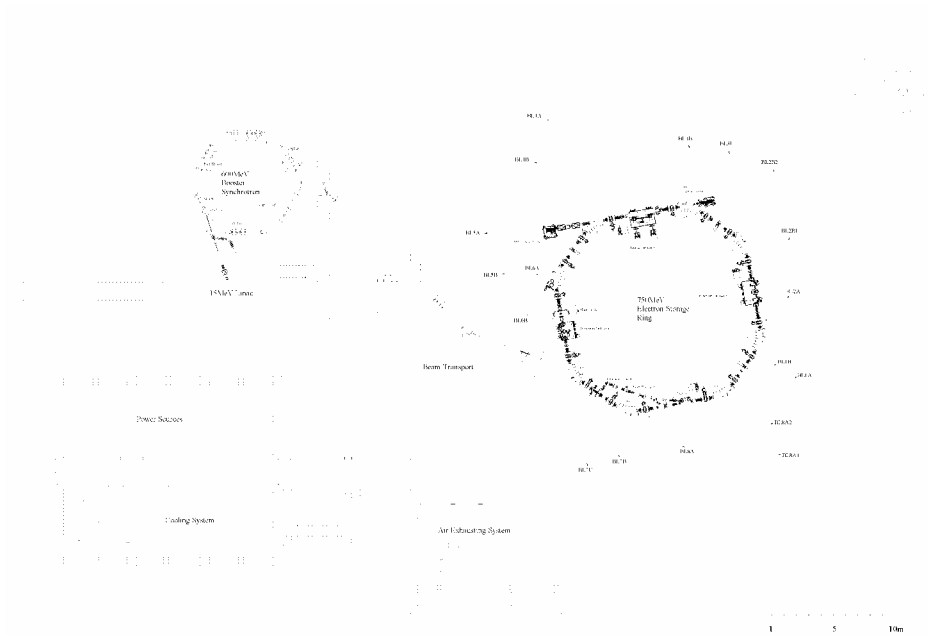


Fig. 5 Terahertz Bursts observed at BL6B(IR) in a single bunch operation.

- [1] S. Kimura, E. Nakamura, J. Yamazaki, M. Katoh, T. Nishi, H. Okamura, M. Matsunami, L. Chen, T. Nanba, Proceedings of 8th International Conference on Synchrotron Radiation Instrumentation (2004) 416.
- [2] T. Nanba *et al.*, Int. J. Infrared and Millimeter Waves **7** (1986) 1769.
- [3] A. Mochihashi *et al.*, in this report.
- [4] M. Hosaka, M. Katoh, A. Mochihashi, J. Yamazaki, K. Hayashi, Y. Takashima, Nucl. Inst. Methods Phys. Res. A **528** (2004) 291.
- [5] Y. Takashima *et al.*, in this report

Parameters of UVSOR Accelerator Complex



Accelerator complex in the UVSOR facility

Parameters of UVSOR-II Storage Ring

Energy	750 MeV
Injection Energy	600 MeV
Maximum Stored Current	500 mA (multi bunch) 100 mA (single bunch)
Natural Emittance	27.4 nm-rad
Circumference	53.2 m
RF Frequency	90.1 MHz
Harmonic Number	16
Bending Radius	2.2 m
Lattice	Extended DBA \times 4
Straight Section	(4 m \times 4) + (1.5 m \times 4)
RF Voltage	55 kV
Betatron Tune	
Horizontal	3.75
Vertical	3.20
Momentum Compaction	0.028
Natural Chromaticity	
Horizontal	-8.1
Vertical	-7.3
Energy Spread	4.2×10^{-4}
Natural Bunch Length	160 ps

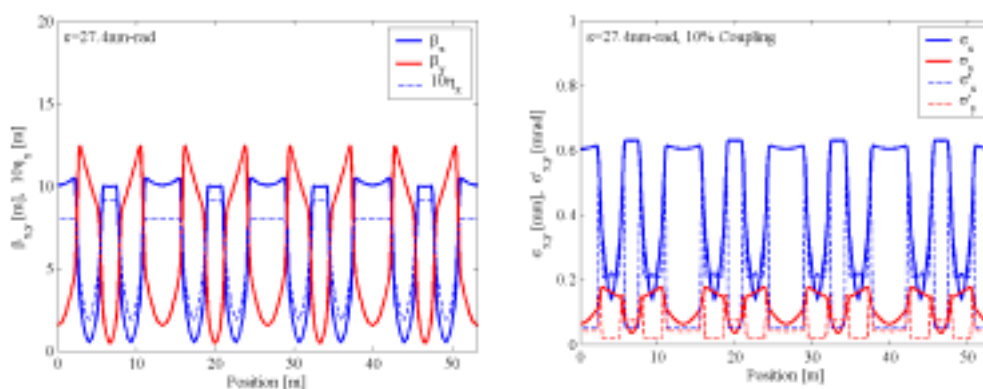
Parameters of Injection Linear Accelerator

Energy	15 MeV
Length	2.5 m
Frequency	2856 MHz
Accelerating RF Field	$2\pi/3$ Traveling Wave
Klystron Power	1.8 MW
Energy Spread	~ 1.6 MeV
Repetition Rate	2.6 Hz

Parameters of Booster Synchrotron

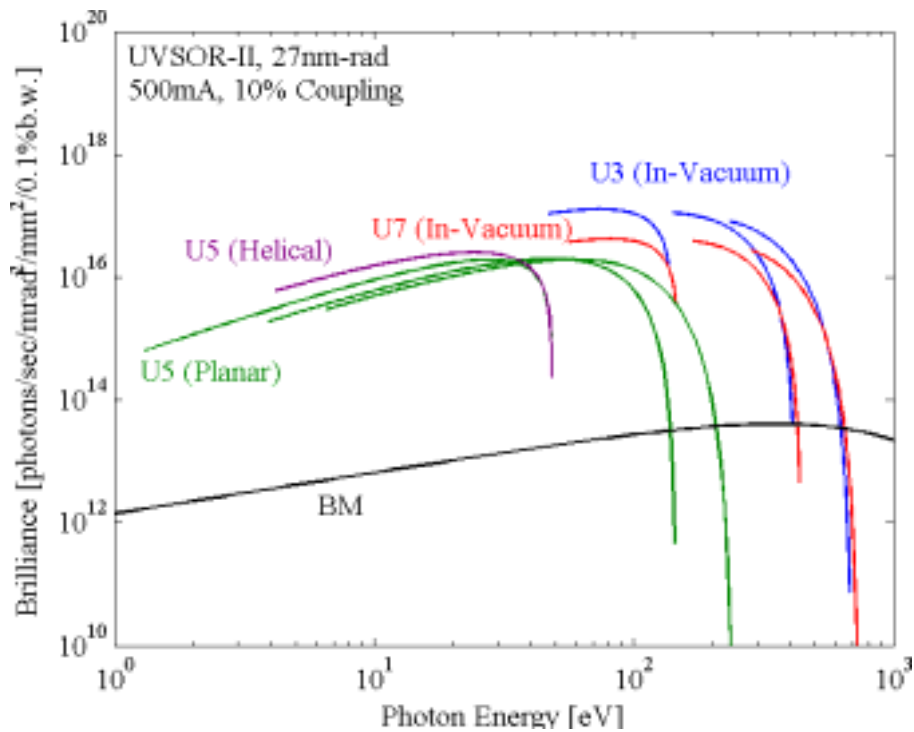
Energy	600 MeV
Injection Energy	15 MeV
Beam Current	32 mA (uniform filling)
Circumference	26.6 m
RF Frequency	90.1 MHz
Harmonic Number	8
Bending Radius	1.8 m
Lattice	FODO $\times 8$
Betatron Tune	
Horizontal	2.25
Vertical	1.25
Momentum Compaction	0.138
Repetition Rate	2.6 Hz

Electron Beam Optics of UVSOR-II Storage Ring



Horizontal/vertical betatron functions and dispersion function (left), and horizontal/vertical electron beam sizes and beam divergences (right) of UVSOR-II

Parameters of the insertion devices



Brilliance of radiation from the insertion devices (U3, U5 and U7) and a bending magnet of UVSOR-II

BL3U In-vacuum Undulator

Number of Periods	50
Period Length	38mm
Pole Length	1.9 m
Pole Gap	15~40mm
Deflection Parameter	2.0~0.24

BL7U In-vacuum Undulator

Number of Periods	26
Period Length	36mm
Pole Length	0.94m
Pole Gap	15~40mm
Deflection Parameter	2.0~0.19

BL5U Helical Undulator / Optical Klystron

Number of Periods	21 / 9+9(Opt. Kly.)
Period Length	110mm
Pole Length	23.5mm
Pole Gap	30~150mm
Deflection Parameter	4.6~0.07(Helical) 8.5~0.15(Linear)

Bending Magnets

Bending Radius	2.2 m
Critical Energy	425 eV

Beamlines in 2004

Eiji SHIGEMASA

UVSOR Facility, Institute for Molecular Science

Eight bending magnets and three insertion devices are available for utilizing synchrotron radiation at UVSOR. There is a total of sixteen operational beamlines, which are classified into two categories. Eight of them are so-called "Open beamlines", which are open to scientists of universities and research institutes belonging to the government, public organizations, private enterprises and those of foreign countries. The rest of the eight beamlines are so-called "In-house beamlines", and are dedicated to the use of research groups within IMS. We have one soft X-rays station equipped with a double-crystal monochromator, seven extreme ultraviolet and soft X-rays stations with a grazing incidence monochromator, three vacuum ultraviolet stations with a normal incidence monochromator, one infrared (IR) station equipped with Fourier-Transform interferometers, one station with a multi-layer monochromator, and three non-monochromatized stations for irradiation of white-light, as shown in the appended table for all available beamlines at UVSOR.

Discussion with users, concerning the improvements and upgrades of the beamlines at UVSOR, has been continuously held as series of UVSOR workshops. The upgrade project of the UVSOR storage ring, in which the creation of four new straight sections and the achievement of much smaller emittance (27 nm-rad) were planned, has been approved in the fiscal year of 2002 and has been accomplished on schedule. Keeping pace with this project, a new in-vacuum undulator and high performance monochromator for BL3, and a new high-resolution photoelectron energy analyzer for the end station at BL5U, have been successfully installed. The renewal of the vacuum duct at BL6 has been made during the regular shutdown in the spring of 2004. In coincidence with this, a so-called magic mirror has been installed as the first mirror for a new IR beamline, BL6B. It has been confirmed that the highest intensity in the world, has been achieved in the wavelength range from sub-milli to near IR region. Two vacant lots are left at BL2A and BL6A to construct novel beamlines. A new RF cavity has been installed to the short straight section between B01 and B02 before the end of March 2005; BL2A will be a bending-magnet beamline while BL6A is to be an undulator one, which will be called BL6U. Regarding the utilization for the long straight section between B06 and B07, a UVSOR workshop has been held in March 2005. On the basis of the review and evaluation report on the present status of UVSOR in 2004, a high resolution and high flux variable polarization beamline for spectroscopy in the VUV range has been proposed and possible scientific cases performed on this beamline have been discussed. Further serious discussion toward utilizing the available straight sections most effectively and formulating a basic plan on the beamline construction, will be continued.

All users are required to refer to the beamline manuals and the UVSOR guidebook (latest revision in 1999), on the occasion of conducting the actual experimental procedures. Those wishing to use the open and in-house beamlines are recommended to contact the stationmaster/supervisor and the representative, respectively. For updated information of UVSOR, <http://www.uvsor.ims.ac.jp/>.

Station Masters and Supervisors of Open Beamlines in FY2004

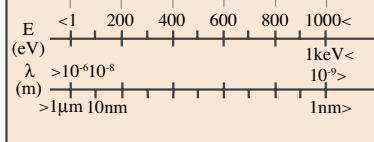
Beamline	Station Master	Sub Master	Supervisor
1A	N. Kondo	E. Shigemasa	E. Shigemasa
1B	M. Hasumoto	S. Kimura	S. Kimura
5U	T. Ito	S. Kimura	S. Kimura
5B	M. Hasumoto	E. Nakamura	E. Shigemasa
6B	S. Kimura	E. Nakamura	S. Kimura
7B	M. Hasumoto	S. Kimura	S. Kimura
8A	E. Nakamura	Y. Hikosaka	E. Shigemasa
8B1	Y. Hikosaka	E. Nakamura	E. Shigemasa

Representatives of In-House Beamlines in FY2004

Beamline	Representative	Affiliation
2B	K. Mitsuke	Dep. VUV Photoscience
3U	N. Kosugi	Dep. VUV Photoscience
3B	K. Mitsuke	Dep. VUV Photoscience
4A1	T. Urisu	Dep. VUV Photoscience
4A2	T. Urisu	Dep. VUV Photoscience
4B	E. Shigemasa	UVSOR
7U	T. Urisu	Dep. VUV Photoscience
8B2	T. Urisu	Dep. VUV Photoscience

Beamlines at UVSOR-II

Beam-line	Monochromator, Spectrometer	Energy Region (eV)	Experiments	Beamline master
1A	Double-Crystal	600 eV  4 keV	Solid (Absorption)	N. Kondo nkondo@ims.ac.jp
1B	1m Seya-Namioka	1.9 eV  40 eV	Solid (Reflection, Absorption)	M. Hasumoto hasumoto@ims.ac.jp
2B	18m Spherical Grating	20 eV  200 eV	Gas (Photoionization, Photodissociation)	K. Mitsuke mitsuke@ims.ac.jp
3U	Varied-Line-Spacing Plane Grating (Monk-Gillieson)	40 eV  600 eV	Gas (Photoionization, Photodissociation), Solid (Photoemission)	T. Hatsui hatsui@ims.ac.jp
3B	3m Normal Incidence (Dragon)	3 eV  40 eV	Gas (Photoemission)	K. Mitsuke mitsuke@ims.ac.jp
4A1	Multi-Layered-Mirror	50 eV  95 eV	Irradiation	T. Urisu urisu@ims.ac.jp
4A2	None		Irradiation	T. Urisu urisu@ims.ac.jp
4B	Varied-Line-Spacing Plane Grating (Monk-Gillieson)	80 eV  800 eV	Gas (Photoionization, Photodissociation), Solid (Photoemission)	E. Shigemasa sigemasa@ims.ac.jp
5U (FEL)	None (Optical Klystron)		Free Electron Laser	J. Yamazaki yamazaki@ims.ac.jp
5U	Spherical Grating (SGM-TRAIN*)	5 eV  250 eV	Solid (Photoemission)	T. Ito tito@ims.ac.jp
5B	Plane Grating	5 eV  600 eV	Calibration, Solid (Absorption)	M. Hasumoto hasumoto@ims.ac.jp
6B (IR)	Martin-Puplett FT-FIR, Michelson FT-IR	0.25 meV  2.5 eV	Solid (Reflection, Absorption)	S. Kimura kimura@ims.ac.jp
7U	None		Irradiation	Y. Nonogaki nonogaki@ims.ac.jp
7B	3m Normal Incidence	1.2 eV  30 eV	Solid (Reflection, Absorption)	M. Hasumoto hasumoto@ims.ac.jp
8A	None or Filters		Irradiation, Users' Instruments	E. Nakamura eiken@ims.ac.jp
8B1	15m Constant Deviation Grazing Incidence	30 eV  600 eV	Solid (Absorption)	Y. Hikosaka hikosaka@ims.ac.jp
8B2	Plane Grating	1.9 eV  150 eV	Solid (Photoemission)	D. Yoshimura daisukey@ims.ac.jp



* Spherical Grating Monochromator with Translating and Rotating Assembly Including Normal incidence mount

BL1A

Soft X-Ray Beamline for Photoabsorption Spectroscopy

BL1A is a soft X-ray beamline for photoabsorption spectroscopy. The beamline is equipped with a focusing premirror and a double crystal monochromator [1]. The monochromator serves soft X-rays in the energy region from 585 to 4000 eV by using several kinds of single crystals such as β -Al₂O₃, beryl, KTP (KTiOPO₄), quartz, InSb, and Ge. The throughput spectra measured by a Si photodiode (AXUV-100, IRD Inc.) are shown in Fig. 1. Typical energy resolution ($E/\Delta E$) of the monochromator is about 1500 for beryl and InSb. There are no experimental setups specific of this beamline, except for a small vacuum chamber equipped with an electron multiplier (EM) detector. Photoabsorption spectra for powdery samples are usually measured in a total electron yield mode, with the use of the EM detector.

[1] Hiraya *et al*, Rev. Sci. Instrum., **63**, 1264 (1992).

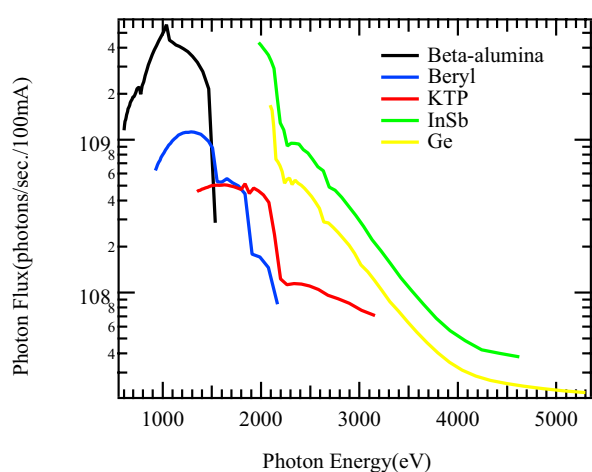


Fig. 1 Throughput spectra of the double crystal monochromator at BL1A.



Fig. 2 A side view of BL1A.

Beamline Specifications

Monochromator	Double crystal monochromator
Monochromator crystals: (2d value, energy range)	β -Al ₂ O ₃ (22.53 Å, 585-1609 eV), beryl (15.965 Å, 826-2271 eV), KTP (10.95 Å, 1205-3310 eV), quartz (8.512 Å, 1550-4000 eV), InSb (7.481 Å, 1764-4000 eV), Ge (6.532 Å, 2094-4000 eV)
Resolution	$E/\Delta E = 1500$ for beryl and InSb
Experiments	Photoabsorption spectroscopy

BL1B

Seya-Namioka Monochromator for General Purposes

BL1B has been constructed to perform various spectroscopic investigations such as absorption, reflectivity, and luminescence in condensed matters. This beamline consists of a pre-focusing mirror, a 1-m Seya-Namioka type monochromator, and post-focusing mirrors with different focal lengths. Three gratings of 600, 1200, and 2400 l/mm can cover the wavelength region ranging from 40 to 650 nm ($h\nu = 2 - 30$ eV). The post mirror with a longer focal length is usually used with an LiF window to separate the vacuum condition of the monochromator from a main experimental station, which make experiments for liquids and bio-specimens possible, while the other is mainly utilized for solid-state spectroscopy. The output flux from this monochromator is about 10^{10} photons/sec. around 200 nm with 0.1 mm slit openings. The spectral distributions for two gratings measured by a conventional photomultiplier are shown in Fig. 1. A second monochromator (Spex 270M) and a LN-cooled CCD detector (Princeton Inc.) are available for luminescence measurements, together with a liquid helium-flow type cryostat. To perform time-resolved experiments, a TAC system is also available.

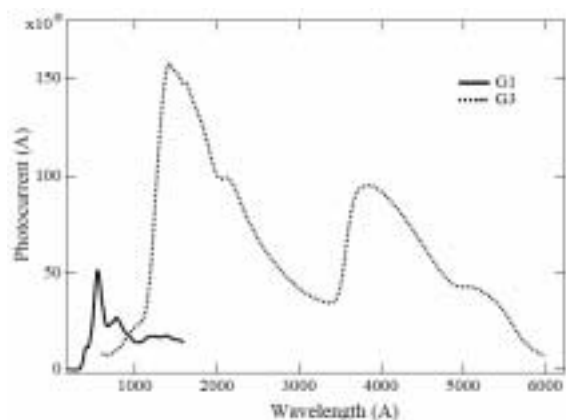


Fig. 1 Photocurrent at the sample position at BL1B.

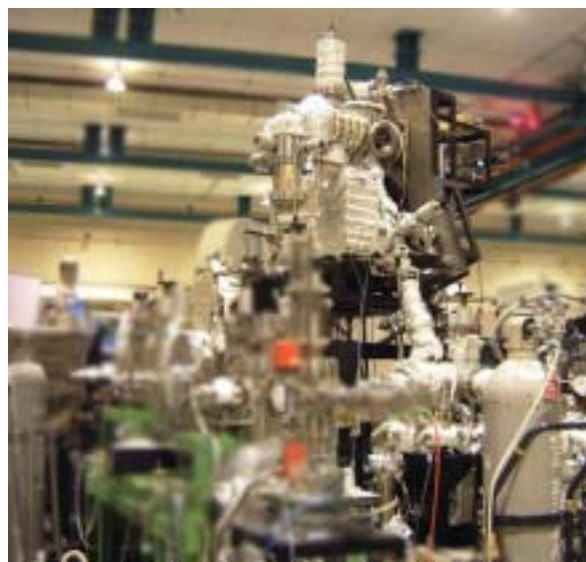


Fig. 2 Photo of BL1B.

Beamline Specifications

Monochromator	1-m Seya-Namioka type
Wavelength Range	40 to 600 nm (2-30 eV)
Resolution	$E/\Delta E \sim 1000$ at 100 nm (10 eV)
Experiment	Absorption, reflection, luminescence spectroscopy for solids

BL2B

Beamline for Gas Phase Photoionization and Reaction Dynamics

This beamline has been developed for the purpose of studying ionization, excitation and decay dynamics involving inner-valence electrons, $2p$ electrons of the third row atoms, and $4d$ electrons of the lanthanides. The monochromator is a spherical grating Dragon-type with 18-m focal length. High throughput (1×10^{10} photons s^{-1}) and high resolution ($E/\Delta E = 2000 - 8000$) are achieved simultaneously under the condition of the ring current of 100 mA [1]. A second-order light of 7 % is contained at a photon energy of 45.6 eV (G3). The optical system consists of two prefocusing mirrors, an entrance slit, three spherical gratings (G1 - G3), two folding mirrors, a movable exit slit and a refocusing mirror [2]. The monochromator is designed to cover the energy range of 23 - 205 eV with the three gratings: G1 (2400 lines mm^{-1} , $R = 18$ m) at 80 - 205 eV; G2 (1200 lines mm^{-1} , $R = 18$ m) at 40 - 100 eV; G3 (2400 lines mm^{-1} , $R = 9.25$ m) at 23 - 50 eV.

We have been taking photoion yield curves of various fullerenes. Geometrical structures and electronic properties of fullerenes have attracted widespread attention because of their novel structures, novel reactivity, and novel catalytic behaviors as typical nanometer-size materials. However, spectroscopic information is very limited in the extreme UV region, which has been probably due to difficulties in acquiring enough amount of sample. This situation has been rapidly changed in these few years, since the techniques of syntheses, isolation, and purification have been advanced so rapidly that appreciable amount of fullerenes can be readily obtained.

[1] M. Ono *et al.*, Nucl. Instrum. Meth. Phys. Res. A **467-468**, 577 (2001).

[2] H. Yoshida and K. Mitsuke, J. Synchrotron Radiat. **5**, 774 (1998).

Beamline Specifications

Monochromator	18-m spherical grating Dragon-type
Wavelength Range	6 – 55 nm
Resolution	2000-8000
Experiment	Mass spectrometry; Photoelectron spectroscopy



Fig. 1 18-m spherical grating monochromator installed at the Beamline 2B.

BL3U

Varied-Line-Spacing Plane Grating Monochromator for Molecular Soft X-Ray Spectroscopy

The beamline BL3U is equipped with an in-vacuum undulator composed of 50 periods of 3.8 cm period length. The emitted photons are monochromatized by the varied-line-spacing plane grating monochromator (VLS-PGM) designed for various spectroscopic investigations in the soft x-ray range including soft x-ray emission studies. Three holographically ruled laminar profile plane gratings are designed to cover the photon energy range from 60 eV to 800 eV. The beamline has two endstations, namely XES setup and Multi-purpose setup. The XES setup is used for soft x-ray emission spectroscopy. The beam is horizontally focused onto the sample position by plane-elliptical mirror, M2X. In the Multi-purpose setup, the beam is focused by the toroidal mirror M2. Between the sample position and M2, the differential pumping is placed.

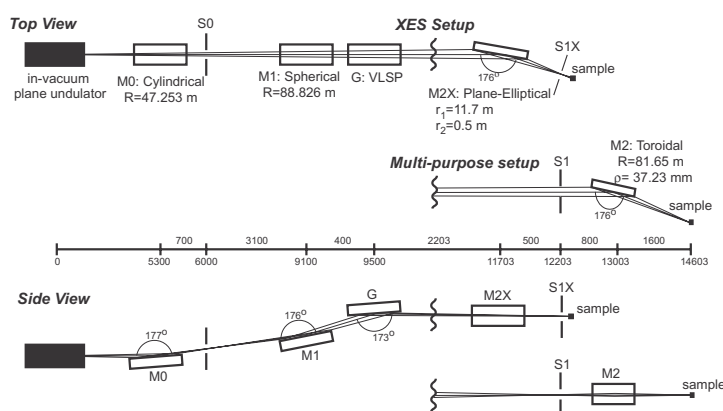


Fig. 1 Schematic layout (left) and the photography (right) of the BL3U. The distances along the beam from the center of the in-vacuum plane undulator are shown in mm. S1X and M2X can be replaced with the other exit slit S1 so that experiments can be carried out at either the XES or multi-purpose endstation. In the XES setup, the sample is placed at 5-10 mm downstream of S1X.

Beamline Specifications

Monochromator	Varied-line-spacing plane grating monochromator
Energy Range	60-800 eV
Resolution	$E/\Delta E > 7000$
Experiment	Soft X-ray spectroscopy (XPS, XES, XAS)
Beam Size (XES Endstation)	Gaussian shape Vertical 5-20 μm ; Horizontal 68 μm (FWHM)

BL3B

Beamline for Gas Phase Photoelectron Spectroscopy

This beam line is devoted to studies of elementary atomic and molecular processes induced by excitation of valence electrons. A monochromator is a vertically dispersed normal incidence type with 3m focal length and 10° angle between the incident and diffracted photon beams. The maximum wavelength resolution of 0.007nm is narrow enough to separate vibrational levels of excited states for various molecules. A main component in an experimental chamber is a spherical sector electrostatic energy analyzer which has been designed and setup for photoelectron spectroscopy. One can perform two-dimensional photoelectron spectroscopy with good resolution ($\leq 30\text{meV}$) in which the photoelectron yield is measured as a function of both photon energy and electron kinetic energy (binding energy). A two-dimensional spectrum, usually represented as a contour plot, contains rich information on photoionization dynamics and properties of superexcited states. A great variety of interesting high-lying states involved in autoionization have been studied [1-5].

- [1] K. Mitsuke *et al.*, J. Electron Spectrosc. Rel. Phenom. **79**, 395 (1996).
- [2] H. Hattori and K. Mitsuke, *ibid.* **80**, 1 (1996); H. Hattori *et al.*, J. Chem. Phys. **106**, 4902 (1997).
- [3] Y. Hikosaka *et al.*, J. Chem. Phys. **105**, 6367 (1996); *ibid.* **107**, 2950 (1997); *ibid.* **110**, 335 (1999).
- [4] K. Mitsuke *et al.*, J. Electron Spectrosc. Rel. Phenom. **112**, 137 (2000).
- [5] Y. Hikosaka and K. Mitsuke, J. Phys. Chem. **105**, 8130 (2001); J. Chem. Phys. **121**, 792 (2004).

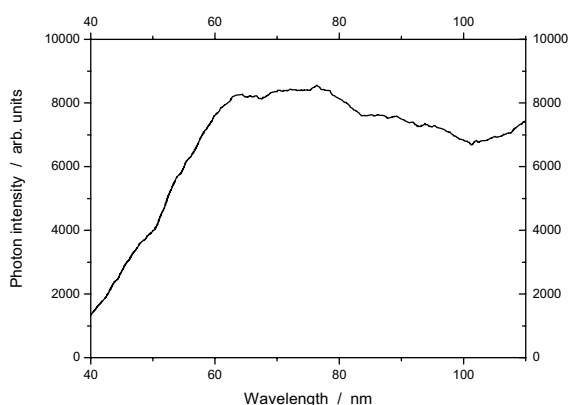


Fig. 1 Relative photon intensity at the sample point of BL3B.

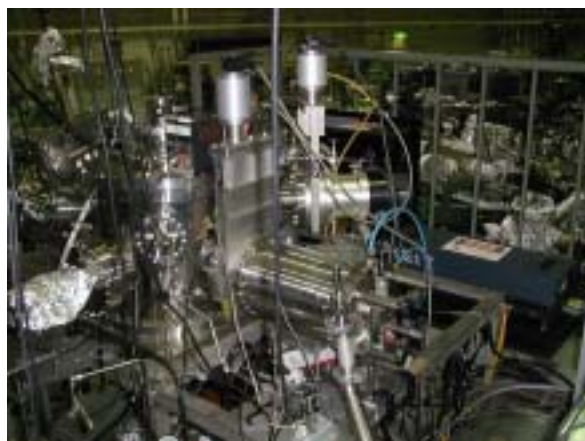


Fig. 2 Apparatus for gas-phase photoelectron spectroscopy at the Beamline 3B.

Beamline Specifications

Monochromator	3-m normal incidence
Wavelength Range	30 – 200 nm
Resolution	14000 at 100 nm
Experiment	Photoelectron Spectroscopy

BL4A1

SR-Induced Sputtering Deposition and Annealing Beamline

This beam line is used for synchrotron radiation (SR)-induced sputtering deposition and annealing onto substrates. The beam line has multilayered-mirror (MLM) monochromator. The beam line optics is optimized to obtain a high photon flux. Optimization concerning the reduction of the low energy background due to the total reflection has been made for the combination of the Mo/Si MLMs and the C filter. Mo/Si MLMs have a (normal incident) reflectivity of over 60% can be made for the energy region around 100 eV, which contains the core electron binding energies of Al and Si [1].

The SR-induced sputtering deposition and annealing chamber is connected to the beam line as shown in Fig. 1. The sample and deposition source can be easily introduced into the chamber, and the angle of them can be changed from outside.

[1] H. Mekarū *et al.*, Rev. Sci. Instrum. **70** (1999) 2601.

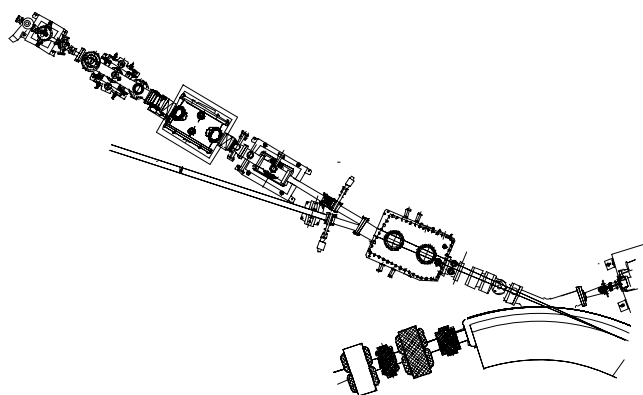


Fig. 1 Top view of BL4A1.

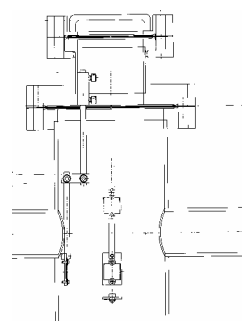


Fig. 2 Annealing chamber.

Beamline Specifications

Monochromator	Multilayered-mirror monochromator
Energy Range	50-95 eV
Resolution	5-9 eV (FWHM)
Experiments	Synchrotron radiation (SR)-induced sputtering deposition and annealing onto substrates

BL4A2

Beamline for Synchrotron Radiation Chemical Vapor Deposition

This beam line is used for synchrotron radiation chemical vapor deposition (SR-CVD) and photo-etching experiments. The beam line has no monochromator for high photon flux to irradiate and consists of only two mirrors. One is for focusing and the other is for branching. At the beam line, the gas supply and extinction system is equipped for using legally controlled high pressure gasses such as SiH_4 , Si_2H_6 and GeH_4 . They are commonly used to CVD of semiconductor crystals.

The SR-CVD and photo-etching chambers are connected to the beam line as shown in Fig. 1. In those chambers, infrared reflection absorption spectroscopy (IRRAS) system is installed to study the surface photochemistry on Si surfaces modified with various kinds of molecules.

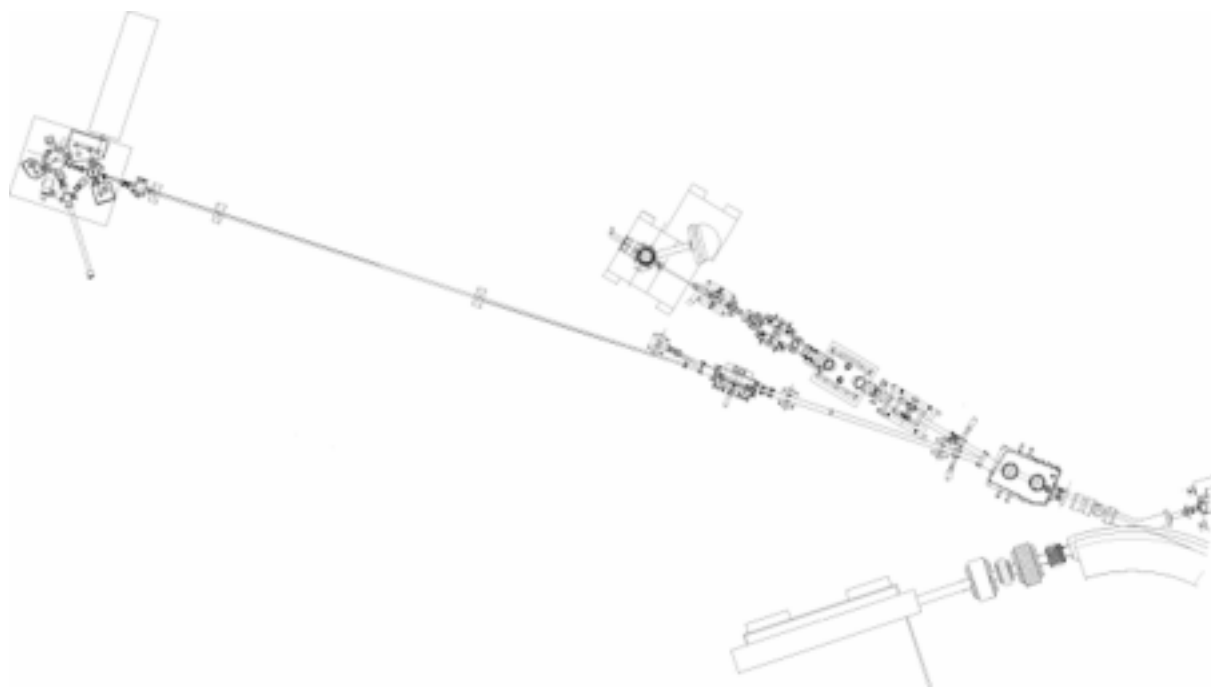


Fig. 1 Top view of BL4A2.

Beamline Specifications

Monochromator	None
Energy Range	The whole energy range of the synchrotron radiation
Resolution	—
Experiments	Synchrotron radiation chemical vapor deposition, and photo-etching experiments

BL4B

Varied-Line-Spacing Plane Grating Monochromator for Molecular Soft X-Ray Spectroscopy

The beamline BL4B equipped with a varied-line-spacing plane grating monochromator (VLS-PGM) was constructed for various spectroscopic investigations in a gas phase and/or on solids in the soft X-ray range. Two holographically ruled laminar profile plane gratings with SiO₂ substrates are designed to cover the photon energy range from 80 eV to 800 eV. The gratings with the groove densities of 267 and 800 l/mm cover the spectral ranges of 60-300 and 200-1000 eV, respectively, and are interchangeable without breaking the vacuum. Fig. 1 shows the absolute photon flux for each grating measured by a Si photodiode (IRD Inc.), with the entrance- and exit-slit openings set at 25 and 10 μm , respectively. Under this condition, the corresponding resolving power ($E/\Delta E$) for the 800 l/mm grating is expected to be more than 8000 at 400 eV.

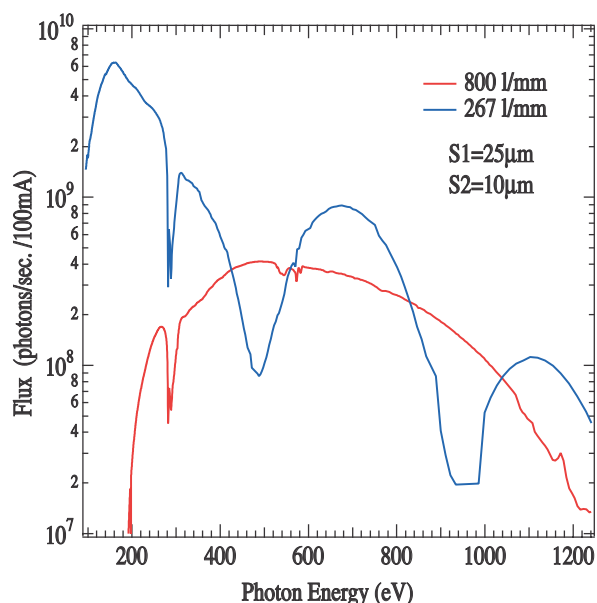


Fig. 1 Throughput from the VLS-PGM monochromator on BL4B.



Fig. 2 A photo of BL4B taken from the upper platform of BL3B.

Beamline Specifications

Monochromator	Varied-line-spacing Plane Grating Monochromator
Energy range	60-1000 eV
Resolution	$E/\Delta E > 5000$ (at maximum)
Experiments	Soft X-ray spectroscopy (mainly, angle-resolved photoion spectroscopy for gaseous targets and photoelectron spectroscopy for gaseous and solid targets)

BL5U

Photoelectron Spectrometer for Solids and Surfaces

This beamline is designed for high-resolution angle-resolved photoemission study for solids and surfaces with the linearly and circularly polarized synchrotron radiation from a helical undulator. The beamline consists of a Spherical Grating Monochromator with Translational and Rotational Assembly Including a Normal incidence mount (SGM-TRAIN), and a high-resolution angle-resolved photoemission spectrometer.

The SGM-TRAIN is an improved version of a constant-length SGM to aim the following points; (1) wide energy range of 5-250 eV, (2) high resolving power, (3) use of linearly and circularly polarized light, (4) reduction of second-order light, and (5) two driving modes by a computer control. The second-order light is well suppressed by using laminar profile gratings and combinations of mirrors and gratings.

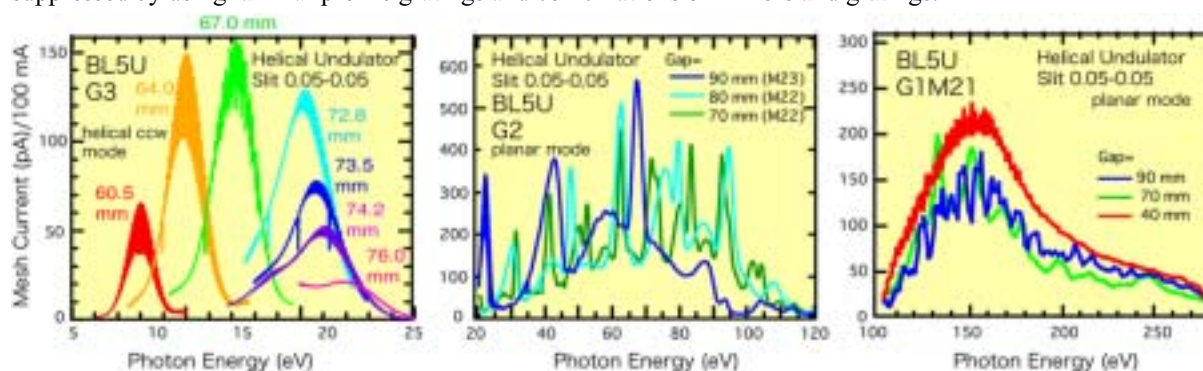


Fig. 1 Throughput spectra from the SGM-TRAIN monochromator on BL5U.

Beamline Specifications

Monochromator	SGM-TRAIN
Energy Range	5-250 eV
Resolution	0.5-80 meV (with slits width of 0.01 mm)
Experiment	ARPES, AIPES, XAS
Flux	1×10^{12} photons/s for undulator radiation in MPW mode
Main Instruments	Hemispherical photoelectron analyzer (MBS-Toyama, A-1), LEED of reverse type (OMICRON), Liq-He flow cryostat (5 – 400 K)

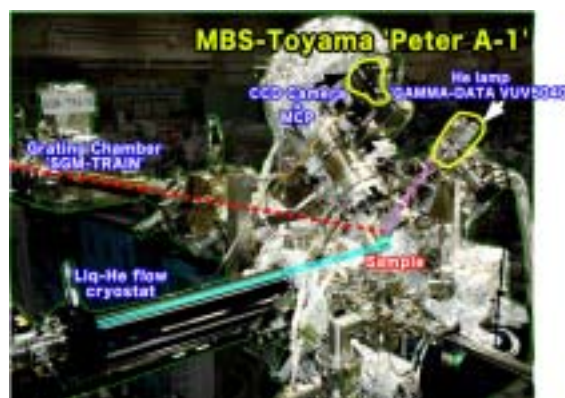


Fig. 2 High-resolution angle-resolved photoemission apparatus for BL5U.

BL5B

Calibration Apparatus for Optical Elements and Detectors

BL5B has been constructed to perform calibration measurements for optical elements and detectors. This beamline is composed of a plane grating monochromator (PGM) and three end stations in tandem. The most upstream station is used for calibration measurements of optical elements, the middle one for optical measurements for solids and the last for photo-stimulated desorption experiments. The experimental chamber at the most downstream station is sometimes changed to a chamber for photoemission spectroscopy.

The calibration chamber shown in Fig. 2 is equipped with a goniometer for the characterization of optical elements, which has six-degree-of-freedom; X-Y translation of a sample, and interchange of samples and filters. These are driven by pulse motors in vacuum. Since the polarization of synchrotron radiation is essential for such measurements, the rotation axis can be made in either horizontal or vertical direction (s- or p-polarization).

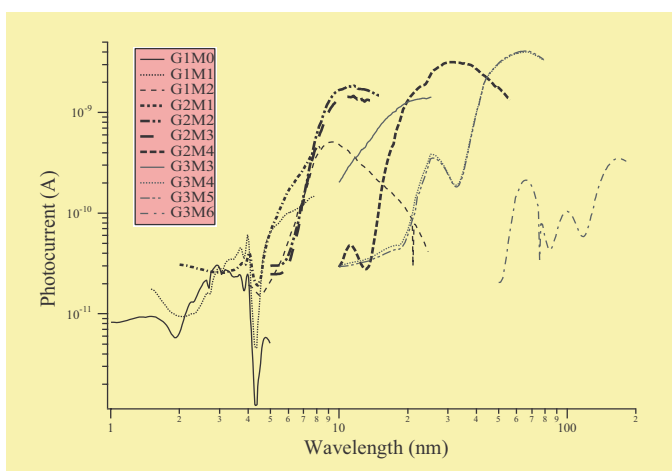


Fig. 1 Throughput spectra for possible combinations of gratings and mirrors at BL5B measured by a gold mesh.

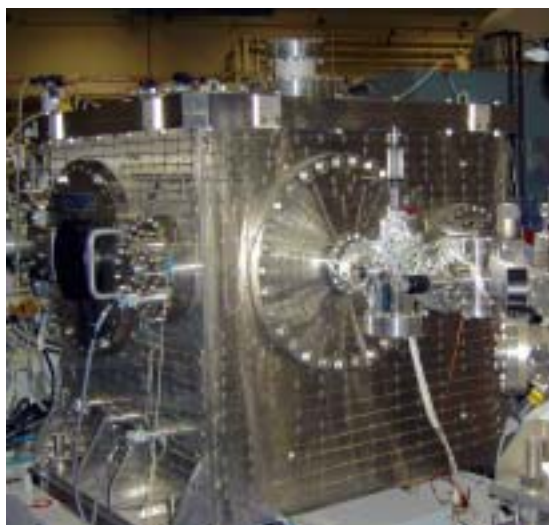


Fig. 2 A side view of the experimental chamber for calibration measurements.

Beamline Specifications

Monochromator	Plane Grating Monochromator
Energy range	6-600 eV (2-200 nm)
Resolution	$E/\Delta E \sim 500$
Experiments	Calibration of optical elements, absorption of solids, photo-stimulated desorption from rare gas solids

BL6B (IR)

Infrared and Terahertz Spectroscopy of Solids

SR has a good performance (high brilliance and high flux) not only in VUV and SX regions but also in IR and terahertz regions. This beamline covers in the IR and terahertz regions. The previous beamline BL6A1 that has been constructed in 1985 is the pioneer of the infrared SR research. The beamline was upgraded in the spring of 2004 and the name was changed to be BL6B (IR). The front-end part including the bending duct #6 was replaced to a new one with higher acceptance angle using a magic mirror as shown in Fig. 1.

The beamline is equipped with two interferometers, one is Michelson-type (Bruker IFS-66v) and the other Martin-Puplett-type (JASCO FARIS-1), for the wide spectral region from several to 20,000 cm^{-1} ($h\nu =$ several 100 $\mu\text{eV} - 2.5 \text{ eV}$) as shown in Fig. 2. The experimental chamber in which users bring can be equipped at the free port. In the near future, an IR microscope covering down to terahertz region will be set up.

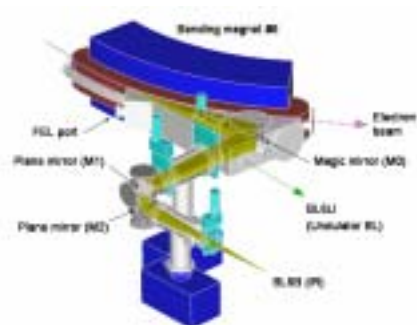


Fig. 1 The design of optics and front end of BL6B.

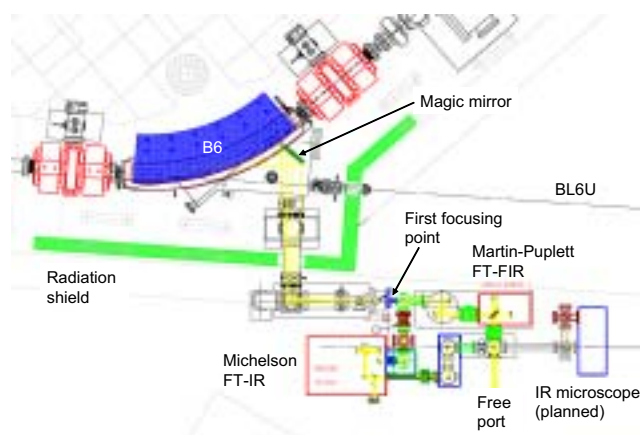


Fig. 2 Schematic figure of top view of BL6B.

Beamline Specifications

Interferometer	Michelson (Bruker IFS66v), Martin-Puplett (JASCO FARIS-1)
Wavenumber Range (Energy range)	several – 20,000 cm^{-1} , (several 100 $\mu\text{eV} - 2.5 \text{ eV}$)
Resolution in cm^{-1}	0.1 cm^{-1} for IFS66v, 0.25 cm^{-1} for FARIS-1
Experiments	Reflectivity and transmission, Magneto-optics (Microspectroscopy)
Miscellaneous	Users can bring their experimental system in this beamline.

BL7U

Undulator Irradiation Beamline for STM Observation

This beamline has been constructed for STM observation of surface photochemical reactions stimulated by undulator irradiation. The schematic drawing of the BL7U is shown in Fig. 1. The undulator is in-vacuum type, of which the period is 36 mm and the number of the period is 26. The 1st harmonic is tuned from 70 eV to 140 eV [4]. Two Pt-coated cylindrical mirrors are used for the vertical and horizontal focusing. These two mirrors also suppress the higher harmonics of the undulator radiation into $\sim 10\%$ with respect to the first harmonic. The focus point is set at the point of 9100 mm downstream from the middle of the undulator. The spot size on the sample surface was 1.0 mm (H) x 0.4 mm (V) and the estimated photon flux density was 10^{18} photons (cm² sec 100 mA)⁻¹.

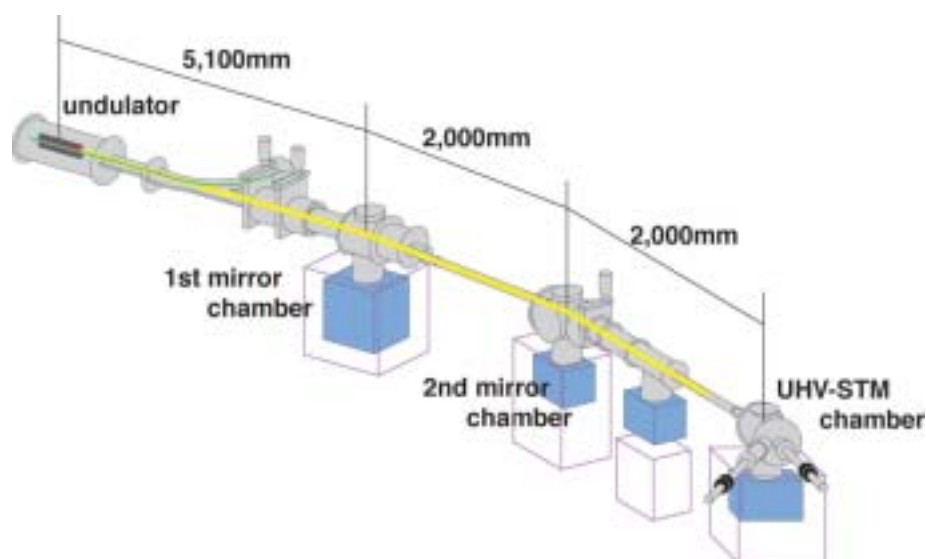


Fig. 1 Schematic drawing of BL7U.

Beamline Specifications

Monochromator	None
Wavelength Range	70 – 140 eV (1st harmonic)
Resolution	~ 10 -
Experiment	Undulator Irradiation and STM Observation
Miscellaneous	

BL7B

3-m Normal Incidence Monochromator for Solid-State Spectroscopy

BL7B has been constructed to provide sufficiently high resolution for conventional solid-state spectroscopy, enough intensity for luminescence measurements, a wide wavelength coverage for Kramers-Kronig analyses, and the minimum deformation to the polarization characteristic of the incident synchrotron radiation. This beamline consists of a 3-m normal incidence monochromator which covers the vacuum ultraviolet, ultraviolet, visible and infrared, *i.e.* the wavelength region of 40 -1000 nm, with three gratings (1200, 600, and 300 l/mm). Two interchangeable refocusing mirrors provide two different focusing positions. For the mirror with the longer focal length, an LiF or a MgF2 window valve can be installed in between the end valve of the beamline and the focusing position. Figure 1 shows absolute photon intensity for each grating with the entrance and exit slit openings of 0.5 mm. A silicon photodiode (AXUV-100, IRD Inc.) was utilized for measuring the photon intensity and the absolute photon flux was estimated, taking the quantum efficiency of the photodiode into account.

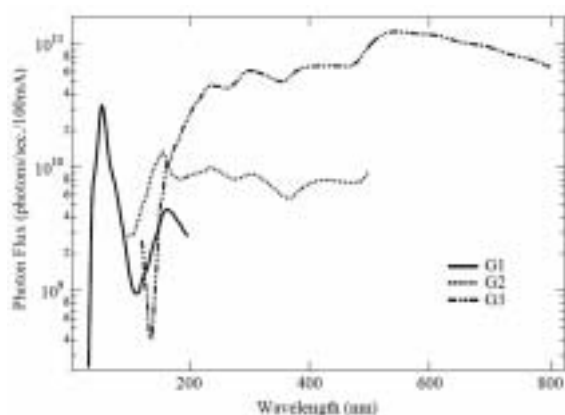


Fig. 1 Throughput spectra of BL7B measured by a silicon photodiode.



Fig. 2 Photo of BL7B.

Beamline Specifications

Monochromator	3-m Normal Incidence Monochromator
Wavelength Range	50 to 1000 nm (1.2 - 25 eV)
Resolution	$E/\Delta E = 4000 - 8000$ for 0.01 mm slits
Experiment	absorption, reflection, fluorescence spectroscopy, mainly for solids

BL8A

Irradiation Beamline for Studies of Photochemical Reaction on Solids

The beamline BL8A was constructed for providing synchrotron radiation without monochromatization. The white synchrotron radiation is focused into a 3.5 mm × 2.5 mm size by use of a toroidal mirror. The focusing mirror can be removed for obtaining a bigger irradiation area. A differential pumping system with three stages is introduced, which enables users to perform experiments under a very low vacuum condition (<0.5 Torr). The intense white light available at this beamline is suitable for studies on photochemical reaction, chemical vapor deposition, photo-etching and irradiation damage effects. No standing experimental stations are placed at the beamline; users may install their own experimental chambers, while some standard chambers are arranged by UVSOR.



Fig. 1 A top-view photo of the beamline.

Beamline Specifications

Monochromator	None
Energy Range	The whole energy range of the synchrotron radiation
Resolution	—
Experiments	Photochemical reaction, chemical vapor deposition and photo-etching experiments
Miscellaneous	Beam spot size: (H)3.5 mm × (V)2.5 mm

BL8B1

Spherical Grating Monochromator for Soft X-Ray Spectroscopic Studies on Solids and Surfaces

The beamline BL8B1 equipped with a constant-deviation constant-length spherical grating monochromator [1] provides soft X-ray photons in the energy range 30-800 eV with medium energy resolution. The photon energy range is covered by using three gratings (R=15 m; 1080 l/mm, R=15 m; 540l/m, and R=7.5m; 360 l/mm) which are interchangeable in vacuum. Figure 1 shows a throughput spectrum measured with the entrance- and exit-slit openings of 10 μm . Under this condition, the achievable resolving power is about 4000 at 400 eV and 3000 at 245 eV, respectively.

An experimental chamber is equipped for conventional measurements of electron yield spectra, or pseudo-photoabsorption spectra, under a $\sim 1 \times 10^{-6}$ Torr vacuum condition.

[1] Hiraya *et al*, Rev. Sci. Instrum. **66**, 2104 (1995).



Fig. 1 Photo of the monochromator at BL8B1.

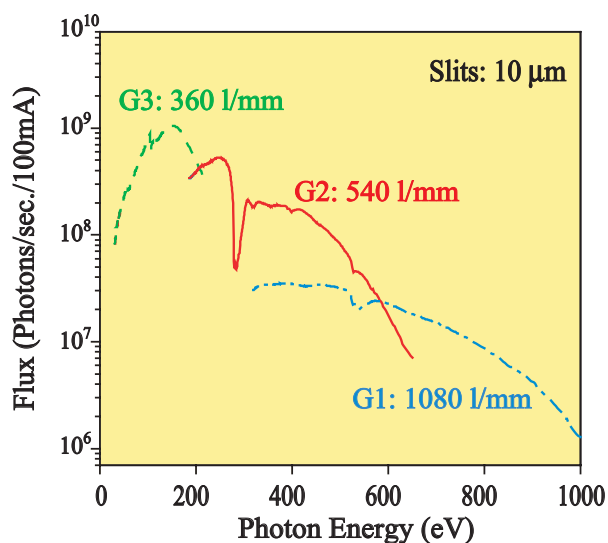


Fig. 2 Throughput of the monochromator at BL8B1.

Beamline Specifications

Monochromator	Constant-deviation constant-length spherical grating type
Energy range	30-800 eV
Resolution	$E/\Delta E = 4000$ at 400 eV and 3000 at 245 eV
Experiments	Photoabsorption spectroscopy, electron spectroscopy and electron-ion coincidence spectroscopy for solids and surfaces

BL8B2

Angle-Resolved Ultraviolet Photoelectron Spectrometer for Solids

BL8B2 is a beamline for angle-resolved ultraviolet photoemission spectroscopy (ARUPS) system which is designed for measuring various organic solids such as molecular crystals, organic semiconductors, and conducting polymers. This beamline consists of a plane-grating monochromator (PGM), a sample preparation chamber with a fast entry Load-Lock chamber, a measurement chamber with an accurate for temperature dependence (base pressure 1×10^{-10} Torr), a cleaning chamber (base pressure 1×10^{-10} Torr), and a sample evaporation chamber (base pressure 3×10^{-10} Torr). The cleaning chamber is equipped with a back-view LEED/AUGER, an ion gun for Ar^+ sputtering, and an infrared heating unit. The PGM consists of premirrors, a plane grating, focusing mirror, and a post-mirror, with an exit slit. It covers the wide range from 2 to 150eV with exchanging two gratings (G1: 1200l/mm, G2: 450l/mm) and five cylindrical mirrors. The toroidal mirror focuses the divergent radiation onto the sample in the measurement chamber. The spot size of the zeroth-order visible light at the sample surface is about $1 \times 1 \text{mm}^2$. Figure 1 shows the throughput spectra of PGM (slit=100 μm). The energy resolution at a slit width of 100 μm was found to be 0.004-0.3eV in the wavelength range from 2 to 130eV. A hemi-spherical electron energy analyzer of 75mm mean radius with an angular resolution less than 2° can be rotated around vertical and horizontal axes. The sample mounted on a manipulator can be also rotated around two axes.

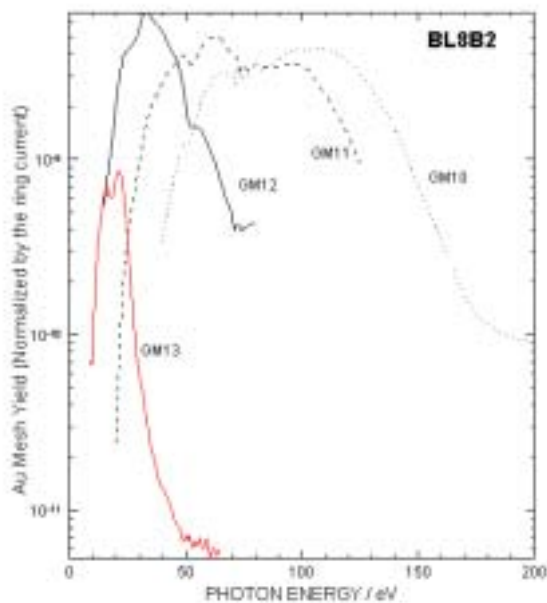


Fig. 1 Throughput spectra of plane-grating monochromator at BL8B2 (slit=100 μm).



Fig. 2 A photo of BL8B2.

Beamline Specifications

Monochromator	Plane-grating monochromator
Wavelength Range	9- 600nm
Resolution	$E/\Delta E = 1000$
Experiment	Angle-resolved ultraviolet photoemission spectroscopy

Ion Trapping Phenomenon in UVSOR Electron Storage Ring

A. Mochihashi¹, M. Katoh¹, M. Hosaka¹, K. Hayashi¹, J. Yamazaki¹, Y. Takashima², Y. Hori³
¹*UVSOR Facility, Institute for Molecular Science, Okazaki 444-8585 Japan*
²*Graduate School of Engineering, Nagoya University, Furo, Chikusa, 464-8603 Japan*
³*Photon Factory, Institute of Materials Structure Science, KEK, Tsukuba, 305-0801, Japan*

We observed the dependence of vertical tune on the vacuum condition in the UVSOR ring. We changed the vacuum conditions by turning off distributed ion pumps (DIPs) and sputtering ion pumps (IPs), and measured the vertical tune with the RF-KO method. In a series of experiments, we performed the measurement under a multibunch condition in which a series of 12 bunches followed by 4 empty buckets are stored in the ring. Figures 1(a) and 1(b) show that the tunes changed when the averaged vacuum pressure was changed. We also observed the dependence of the vertical tune on beam current under the multibunch condition without changing the vacuum conditions but different two vacuum conditions: at a low vacuum pressure (Exp. 1) and at a high vacuum pressure (Exp. 2). Figure 2(a) shows the change in average pressure in the ring during each experiment. As seen in Fig. 2(b), under the multibunch conditions the dependence of vertical tune on beam current tends to become larger with increasing the vacuum pressure. Weak dependence in single-bunch condition and that of horizontal tune in the multibunch condition implies the change in the vertical tune is caused by ion-trapping phenomenon.

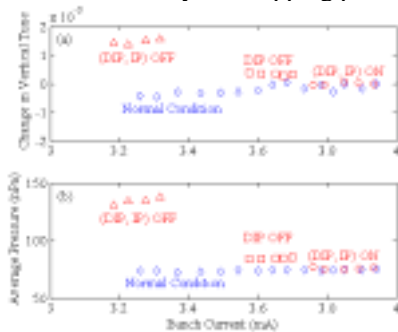


Fig. 1 (a) Change in the vertical tune when vacuum pumps were intentionally turned off. (b) Change in average pressure when the pumps were turned off.

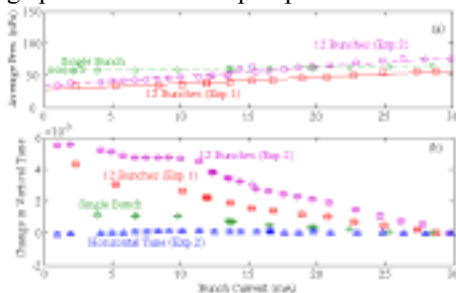


Fig. 2 (a) Averaged vacuum pressure for Exp. 1, Exp. 2 and single-bunch condition. (b) Dependence of tune on beam current in vacuum condition in Fig. 2(a).

According to the ion-trapping theory [1], vertical tune decreases as beam current decreases, however, experiments say that the vertical tune increases with the beam current decreases. This contradiction suggests that the neutralization factor of trapped ions increases as beam current decreases; namely, the number of trapped ions increases as beam current decreases. We have estimated theoretically the dependence of neutralization factor on beam current by evaluating capture rate [2] of ions by both an analytic method based on the classical theory of ion trapping [1,3] and tracking method. In the calculation we assume CO⁺ as a main ion species because CO is a main residual gas component in the UVSOR ring. To reconstruct the experimental results, we considered not only the change in partial pressure of CO during the experiments but also effects from C⁺ and O⁺ which come from multiple ionization of CO⁺. Figures 3(a) and 3(b) show the tracking and analytic calculations for Exp. 1 and 2 with experimental results. The tracking calculations considering all ions agree with the experiments qualitatively, however, they overestimate the change in vertical tune at a bunch current of less than ~15 mA. One of the causes of the overestimation is estimation of multiple ionization cross section of CO, that is difficult to estimate properly. The analytic calculations also tend to overestimate the change in vertical tune; this is because stability condition can be only considered in the analytic calculation.

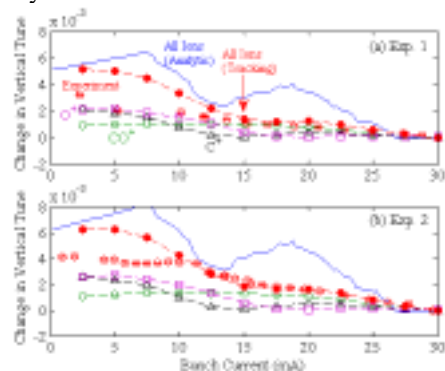


Fig. 3 (a) Experimental results, tracking and analytic calculations of change in vertical tune for Exp. 1 and (b) Exp. 2.

[1] R.D. Kohaupt, DESY Interner Bericht No. H1-71/2 (1971) (unpublished).

[2] A. Mochihashi *et al.*, Jpn. J. Appl. Phys. **44** (2005) 430.

[3] Y. Baconnier and G. Brianti, CERN Internal Rep. No. CERN /SPS/80-2(DI) (1980) (unpublished).

Upgrade of RF Cavity in UVSOR-II Electron Storage Ring

A. Mochihashi¹, M. Katoh¹, M. Hosaka¹, K. Hayashi¹, J. Yamazaki¹, Y. Takashima²

¹UVSOR, Institute for Molecular Science, Okazaki 444-8585 Japan

²Graduate School of Engineering, Nagoya University, Chikusa-ku Nagoya 464-8603 Japan

As we have referred in previous activity report [1] we have built new main RF cavity of the UVSOR-II electron storage ring. The new cavity can generate RF voltage of 150 kV [1] without exchanging high-power RF transmitter that has maximum output of 20 kW. The cavity has been installed in a short straight section in the UVSOR-II at shutdown period in the spring 2005, and soon has been achieved designed RF voltage of 150kV in high-power commissioning.

Figure 1 shows a layout of the UVSOR-II before/after the improvement of the main RF cavity. Due to the upgrade, the RF section has been moved from a long straight section (S7 section) to a short straight section (S2 section). Previous RF cavity has been already dismantled from the ring; the site will be able to be made good use of other devices such as undulators in the future.



Fig. 1 Layout of the UVSOR-II before and after the upgrade of the main RF cavity.

Figure 2 and Table 1 show a drawing and basic specification of the new main RF cavity. For comparison, the same parameters for the previous cavity are shown in the table. Basic design of the new cavity is unchanged compared to the previous one, however, the shunt impedance and unloaded quality factor become about 4 and 2.5 times larger. The previous cavity was made from clad steel plates (SUS+Cu), whereas the new cavity is made from OFHC; that makes temperature control to be easier. To keep tuning condition stable, SUS materials are partly used as mechanical supports in out-of-vacuum surfaces. The new cavity has 2 movable plunger-type tuners; one is used for auto-tuning and the other is usually fixed and can be used for detuning higher-order-mode. These tuners have enough tuning width for operation of the cavity (full width of 400 kHz for each tuner). Input coupler for previous cavity was air-cooled, but new coupler has water-cooling channel to cool especially ceramic window part.

Figure 3 shows a photograph of new RF cavity just after installation to the UVSOR-II. After installation

and evacuation, high-power commissioning was started. The commissioning went smoothly, and designed RF voltage of 150 kV was achieved easily.

Now not only high-power aging but also beam test has been proceeding to improve stability of RF field and vacuum condition in the cavity. After the commissioning the cavity will be operated in users run from May 2005.

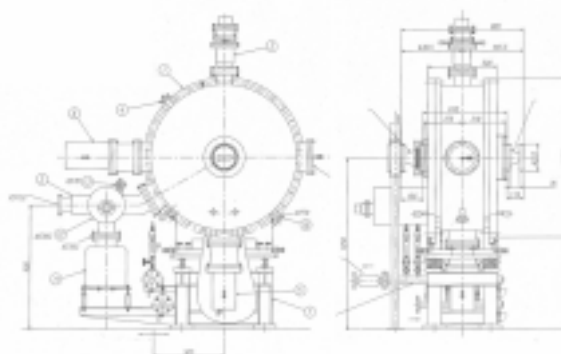


Fig. 2 Drawing of the new main RF cavity.

Table 1 Parameters for the previous and present cavities.

	Previous	Present
Frequency	90.1 MHz	90.1 MHz
Cavity voltage	55 kV	150 kV
Shunt impedance	0.5 MΩ	2.45 MΩ
Unloaded Q	8000	20300
Coupling	1.75	1.34
Material	SUS + Cu	Cu (OFHC)
Cells	Re-entrant×1	Re-entrant×1
Coupler	Air-cooled	Water-cooled
Tuner	Plunger×1	Plunger×2
Inner diameter	1000mm	1175mm
Bore radius	50mm	55mm



Fig. 3 Photograph of new cavity covered with jacket heaters. A view from outside the storage ring.

[1] A. Mochihashi *et al.*, UVSOR Activity Report 2003 (2004) 35.

High Power FEL Lasing in the Deep UV Region

M. Hosaka¹, M. Katoh¹, A. Mochihashi¹, J. Yamazaki¹, K. Hayashi¹,
Y. Takashima², H. Nishino³, M. E. Couprie⁴

¹UVSOR Facility, Institute for Molecular Science, Okazaki 444-8585 Japan

²Department of Material Processing Engineering, Graduate School of Engineering, Nagoya University, Chikusa-ku, Nagoya 464-8603 Japan

³Entropy Control, Japan Science and Technology Agency, Toyonaka 560-0085 Japan

⁴CEA/SPAM, Gif-sur-Yvette, France

An out-coupled power of a storage ring free electron laser (FEL) is a critical issue for its application experiments. Recently we planned to apply the UVSOR-FEL to an irradiation experiment on biosphere [1]. In the experiment, a switchable circular polarized laser in the deep UV region (200 ~ 300 nm) is necessary. We already succeeded in lasing in the wavelength region in 1997; however the out-coupled power was too small for further application experiment. At that time, we had to employ high reflectivity mirrors for an optical cavity and the transmission which is proportional to the out-coupled power was small. While since the upgrade of the storage ring (UVSOR-II), the FEL gain has been increased by more than factor 2 because of smaller beam size and we can employ high transmission mirrors that allow high out-coupled power.

The lasing experiment was made in the wavelength region around 255 nm. Multi-layers of HfO₂/SiO₂ were chosen as cavity mirrors because they have the highest efficiency (= transmission/cavity loss) at the wavelength. Numbers of layers of the mirrors were chosen to be 19 and 15 for front and backward cavity mirrors, respectively. We employed small number of layers for the backward mirror because higher transmission was needed for the mirror from which the laser power was extracted. The calculated round trip reflectivity is 99.3% and the transmission of the backward mirror is 0.4%.

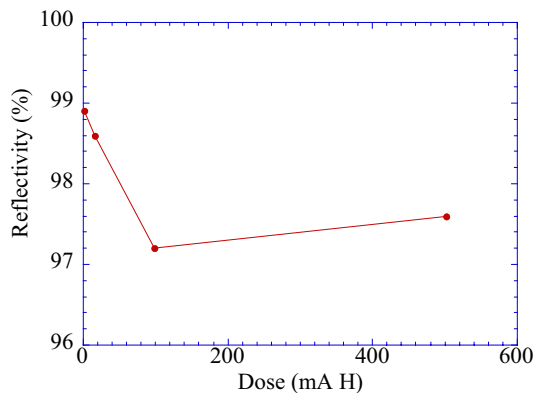


Fig. 1 Roundtrip reflectivity of the cavity mirrors as a function of irradiation dose.

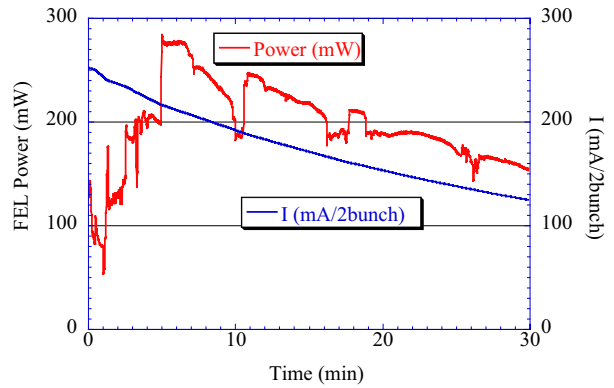


Fig. 2 Out-coupled FEL power and the beam current.

During the lasing experiment, we measured round trip reflectivity as the front mirror was irradiated by synchrotron radiation from the helical optical klystron type undulator. Fig. 1 shows measured round trip reflectivity as a function of irradiation dose. As the dose increases, the reflectivity decreases quickly but the degradation seems to be saturated at a dose more than 100 mA hours. The averaged value of the reflectivity after the irradiation was 97.4%. With the reflectivity, the calculated threshold beam current was 25 mA/bunch and was almost consistent with the measured threshold current of 34 mA/bunch. With such a high threshold current, it is important to store high beam current in the storage ring. By optimization of the injector system, we have been able to store a beam current of more than 100 mA/bunch. Then we could succeed in the lasing with the mirrors and we proceeded to the application experiment. In the application experiment, we irradiated a biosphere with a circularly polarized FEL and analyze a chirality of the product. During the experiment, power irradiated on the sample was recorded and an example is shown in Fig. 2. As seen in the figure, the maximum extracted power was 0.28 W but it decreased as the beam current decreased. The average power was about 0.2 W and was found to be enough to dissociate the sample.

[1] H. Nishino *et. al.*, in this issue.

Observation of Intense Far-Infrared Synchrotron Radiation at UVSOR-II

Y. Takashima¹, M. Katoh², M. Hosaka², A. Mochihashi², S. Kimura², T. Takahashi³

¹Graduate School of Engineering, Nagoya University, Chikusa-ku Nagoya 464-8603 Japan

²UVSOR Facility, Institute for Molecular Science, Okazaki 444-8585 Japan

³Research Reactor Institute, Kyoto University, Kumatori-cho, Osaka, 590-0494 Japan

We have observed intense far-infrared synchrotron radiation at the beam line BL6B [1] of UVSOR-II storage ring [2] operated in single bunch modes. The wave length region of the far-infrared radiations which are detected by using an InSb bolometer is between 0.2 mm and 3.0 mm. The duration and the period of the bursts are about 200 μ sec and 10 - 15 msec, respectively. Each burst consists of several quasi-periodic micro-bursts whose periods are about 30 μ sec. The peak intensity of the bursts is about 10000 times larger than the intensity of synchrotron radiations in the same wavelength region observed in normal multi-bunch modes. We expect that the bursts of the far-infrared radiation are “coherent synchrotron radiations”.

Experiments and Results

We measured the bursts of far-infrared synchrotron radiation at the BL6B beam line constructed for using the synchrotron radiation of infrared region [1]. The electron beam energy was 600 MeV in our measurements.

We used an InSb hot electron bolometer (Infrared Laboratories, Inc) to detect the far-infrared radiations. The detector was sensitive to the wavelength region between 0.2 mm and 3 mm. The response of the detector was several microseconds.

Fig. 1 shows the average intensities of the far-infrared radiations in the single bunch mode (dots) and the multi-bunch mode (gray line) with the average beam currents. The far-infrared radiations passing through a chopper (100 Hz) were detected by the InSb bolometer. The output signals from the bolometer were inputted in a lock-in amplifier. In the multi-bunch mode, the intensity of the far-infrared radiations is proportional to the beam current. In the single bunch mode in lower beam current, the average intensity is also proportional to the beam current and is the same as it in the multi-bunch mode. However, when the beam current is over 140 mA, the intensity of the far-infrared radiations is suddenly increased. There are also increases of the intensity at around 80 mA.

Fig. 2 shows the time structure of the far-infrared radiations at the beam current of 178 mA measured by using an oscilloscope. The radiations are generated as periodic bursts at this beam current. The period of the bursts is about 10 - 15 msec.

The time structure of a typical burst at 201 mA is shown in Fig. 3. The pulse width of the burst is about 200 msec in which there were several micro-bursts of the width of about 30 msec. The peak intensities of

the bursts are about 10000 times larger than the intensity of the ordinary synchrotron radiations of the same wave length at the same average beam current.

Summary

We observed bursts of far-infrared synchrotron radiation in the wave length region between 0.2 mm and 3.0 mm at BL6B of UVSOR-II. The bursts were generated when the beam current exceeded a certain threshold current. We expect that the bursts are coherent synchrotron radiations caused by density modulations of electrons in a beam bunch.

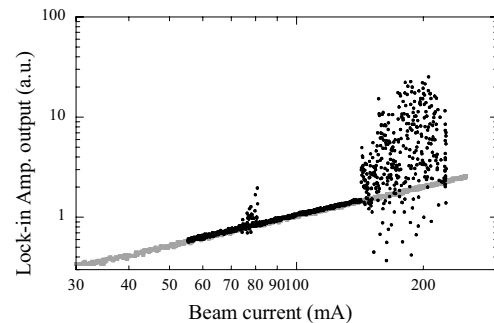


Fig. 1 Average intensity of THz-radiation.

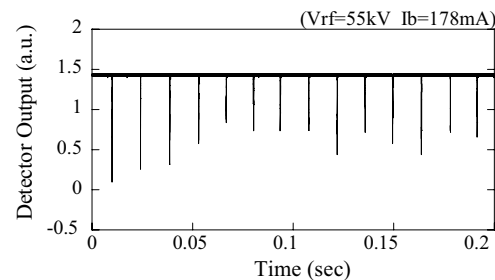


Fig. 2 Time structure of THz-bursts.

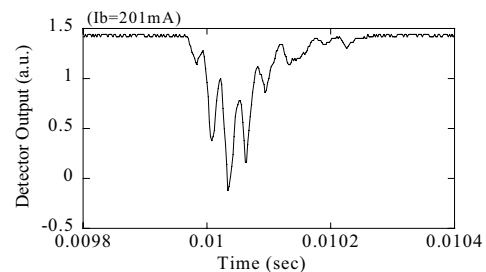


Fig. 3 Time structure of a burst.

- [1] S. Kimura *et al.*, AIP Conf. Proc. 705.
- [2] M. Katoh, Journal of Japanese Society for Synchrotron Radiation Research, **17**(1) (2004) 10.

Construction of an Endstation of BL3U for X-Ray Emission Studies

T. Hatsui¹, T. Horigome², K. Matsushita³, H. Yoshida⁴, M. Suzui⁴, N. Kosugi¹

¹Dept. of Vacuum UV photoscience, Institute for Molecular Science, Okazaki 444-8585 Japan

²UVSOR Facility, Institute for Molecular Science, Okazaki 444-8585 Japan

³Technical Center, Nagoya University, Chikusa-ku, Nagoya, 464-8602, Japan

⁴Equipment Development Center, Institute for Molecular Science, Okazaki, 444-8585 Japan

Optical Design

High-resolution soft-x-ray emission spectroscopy (XES) generally requires small beam size at the sample position, because a smaller opening of the spectrometer entrance slit is needed to achieve higher energy resolution. Such a beam is usually produced by refocusing optics downstream of the exit slit. In the case of BL3U, installation of such refocusing optics is impossible, due to a very limited space.

On the other hand, monochromators with short arm lengths, such as BL3U, are operated with small exit-slit opening for practical energy resolution. It is feasible to carry out XES studies at the exit-slit position. The constant exit-arm length of the BL3U monochromator is essential for such design. Based on the above consideration, an XES endstation has been constructed at the exit-slit position of the in-vacuum undulator beamline BL3U.

Figure 1 represents the optical layout of the XES endstation. X-rays dispersed by the varied-line-spacing plane grating are horizontally focused by the plane-elliptical mirror, M2X, with the demagnification of 20 [1]. The exit slit, S1X, monochromatizes the x-rays. The ray-trace calculations based on the upgraded lattice parameters (the lowest emittance mode), which will be operated from May 2005, indicate that the beam on the sample position has a Gaussian profile with full width at half maximum (FWHM) in horizontal direction of 62 μm .

On the other hand, the vertical beam size is determined by the slit opening of S1X, and the diffraction effect. The distance between S1X and the sample position is set to 22.5 mm. The smallest vertical beam size limited by diffraction through S1X is shown in Fig. 2. Here the smallest beam size is defined as the beam size, where the slit opening of

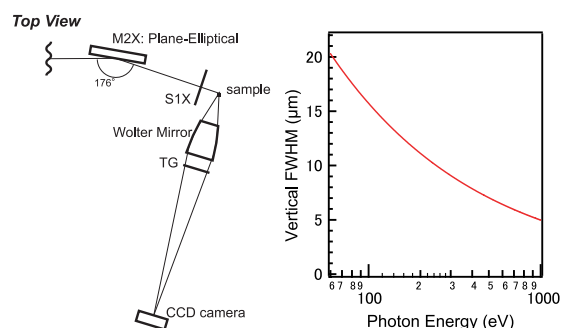


Fig. 1 Schematic layout of the XES endstation (left), and theoretical prediction of the vertical beam size (right).

S1X matches FWHM of the beam at the sample position, which is estimated within Fraunhofer diffraction.

Results and Discussion

Horizontal beam size is evaluated by using a knife-edge scanning method. Obtained profile was well fitted a Gaussian function with FWHM of 68 μm (Fig. 2, left), which is slightly larger than the theoretical prediction of 62 μm . This deviation arises from the operation with the moderate emittance mode (60 nm-rad). The horizontal beam size will be improved after the user operation with the upgraded lattice (27.4 nm-rad).

Vertical size was evaluated by measuring the 0th order diffraction of the recently developed transmission-grating spectrometer for XES (Fig. 1) [1,2]. The Wolter type I mirror has a magnification of 10, which enables the measurement of the vertical beam size at the sample position. Fig. 2(right) shows the observed image of the beam at 110 eV with the S1X opening of 18.5 μm , corresponding to $E/\Delta E=7000$. In the vertical direction, the beam shows only a simple Gaussian profile with FWHM of 24 μm , slightly larger than the theoretical prediction. No undulated tail originated from the diffraction through S1X is observed. This may indicate slight misalignment of the Wolter type I mirror, which causes blur in the image. The obtained flux was 10^{10} - 10^{11} ph/sec.

In summary, a new XES endstation was successfully constructed at BL3U. The beam size of 68 (horiz.) x 24 (vert.) μm^2 is obtained.

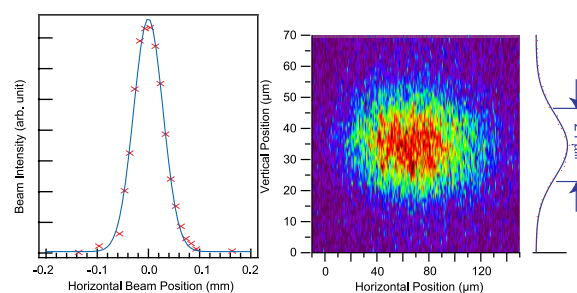


Fig. 2 Horizontal beam profile (left), and a image of the beam (right) at 110 eV.

- [1] T. Hatsui, *et al.*, AIP Conf. Proc. **705**, 921 (2004).
 [2] T. Hatsui, *et al.*, J. Electron Spectrosc. Relat. Phenom., in press.

Improvement of the SGM-TRAIN Monochromator at UVSOR-II BL5U for Low Excitation-Energy Photoemission

T. Ito^{1,2}, H.J. Im², S. Kimura^{1,2}, E. Nakamura¹, T. Horigome¹

¹UVSOR Facility, Institute for Molecular Science, Okazaki 444-8585, Japan

²School of Physical Science, The Graduate University for Advanced Studies, Okazaki 444-8585, Japan

BL5U at UVSOR-II storage ring has been reconstructed in 2004's for high-resolution photoemission (HRPES) study for solids and surfaces [1]. The energy and angular resolutions of the photoemission apparatus constructed at the end-station of BL5U have been improved to $\Delta E \sim 1.2$ meV and $\Delta\theta \sim \pm 0.1^\circ$, which is sufficient to study the anomalous physical properties such as the metal-insulator transition, superconductivity, magnetic phase transition, *etc.* However, it has been hard to study the above properties at BL5U because of the old-type beamline designed in 1995's, in spite of the extensive improvement of the end-station and the storage ring [1,2]. Main problems interrupting a high-resolution study were as follows. (1) Mechanism for optimizing the front mirror was too rough to operate the focus position of the undulator light. (2) Entrance slit has no cooling system. (3) The grating G3 with normal incident mount for the low energy region ($h\nu = 5 - 25$ eV) has been optimized to the bending magnet radiation [3]. The above has caused the extremely low throughput at the low-energy region and restricted the HRPES experiment.

Taking account of the problems listed above, we have reconstructed the beamline in the following way to improve the efficiency in the PES experiment with using the low-energy photons at BL5U. (1) The mechanics at the front mirror was updated to the high-precision system controlled by the pulse-motors. (2) The water-cooling system was attached at the holder of the entrance slit. (3) The monochromator (SGM-TRAIN) was re-arranged to the optimum condition to the undulator light.

Figure 2 shows the improved throughput from the SGM-TRAIN monochromator after the present reconstruction. Comparing with the previous throughput spectra (Fig. 1), we can clearly find that the mesh current increases about 30 times higher, and the energy resolution becomes better because of the sharper interference from the optical klystron-type undulator as shown in Fig. 2. Due to the high-throughput of the photocurrent at the low-energy region, the HRPES measurement at BL5U becomes available. For example, HRPES spectrum at the Fermi-level of gold (Fig. 3) has been corrected within 1 hour with the resolution of $h\nu/\Delta E \sim 1000$. We believe that the present reconstruction makes it possible to explore the origin of the anomalous physical properties by using the high-resolution bulk-sensitive angle-resolved photoemission

apparatus at UVSOR-II BL5U.

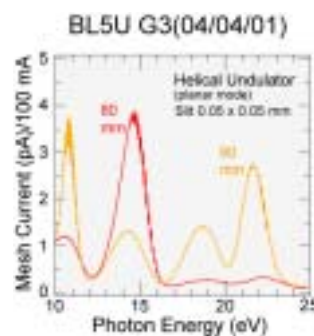


Fig. 1 Throughput spectra from the SGM-TRAIN monochromator with the normal incident grating G3 measured before the present reconstruction [1].

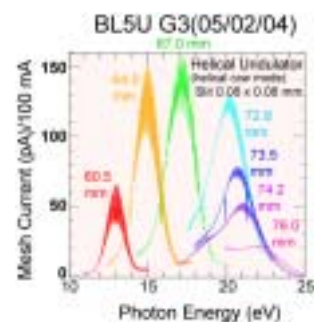


Fig. 2 Same as Fig. 1, but measured after the present reconstruction.

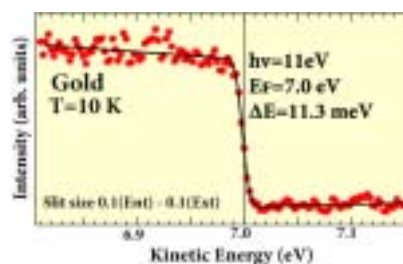


Fig. 3 HRPES spectrum at the Fermi level of gold measured after the present reconstruction.

- [1] T. Ito *et al.*, UVSOR Activity Report 2003, 40.
- [2] M. Katoh *et al.*, UVSOR Activity Report 2003, 5.
- [3] M. Kamada *et al.*, Rev. Sci. Instrum. **66** (1995) 1537.

Aging Stability of Mg-Based Reflection Multilayers in the 25–35 nm Region

T. Ejima¹, A. Yamazaki¹, T. Banse¹, K. Saito^{1,2}, Y. Kondo^{1,3}, S. Ichimaru⁴, H. Takenaka⁴

¹IMRAM, Tohoku University, Sendai, 980-8577 Japan

²Venture Business Laboratory, Saga University, Saga 840-8502, Japan

³Akita Research Institute of Advanced Technology, Akita 010-1623, Japan

⁴NTT-AT Co., Tokai 319-1193, Japan

Reflection measurements in the 25–35 nm region are made for Mg/SiC- and Mg/Y₂O₃- multilayers kept under a low humid atmosphere for 4 or 5 years. Both aged Mg/SiC and Mg/Y₂O₃ multilayers keep their reflectances.

Introduction

In the 25–35 nm wavelength region, Mg/SiC- and Mg/Y₂O₃-multilayers have been proposed and fabricated as a reflection multilayer [1, 2]. However, magnesium is known to have a high reactivity and is usually found in nature in the form of oxide, carbonate or silicate, often in combination with calcium. This aspect of high reactivity presents a demerit for the practical application of Mg-based multilayers, despite their high reflectance.

Experiments

All samples used for the aging-stability measurements were kept in a desiccator at RT and a humidity estimated at lower than 50%, except for during the time of the measurements.

Reflectances of the aged and heated multilayers were measured with the reflectometer at the beamline BL5B. In the measurements, a combination of the G3 grating and the M24 mirror was used. The resolving power of the wavelength, $\lambda/\Delta\lambda$, was about 500 at 30 nm. Reflectances of the non-aged multilayers were measured with a home-made reflectometer [3], a 166° constant-deviation type using a grating that was 600 grooves/mm concave with a 3 m radius of curvature. The resolving power of the wavelength was estimated to be 240 at 25.6 nm.

Experimental Results

One of measured reflectances of the aged Mg/SiC-multilayers is represented with the simulation result in Fig. 1(a). The ordinate of the figure is s-polarized reflectance. The measured results are represented by solid curves and the simulation results, by broken ones. As can be seen in the figure, measured reflectances were well reproduced by the simulated ones. The reflectance of the non-aged multilayer measured before storage is represented in Fig. 1(b). The ordinate of the figure is non-polarized reflectance. A comparison of reflectances between before and after storage, and a comparison of the measured reflectances with the simulated ones show that the multilayer represents high reflectance after 4 years storage. Mg/Y₂O₃-multilayers retained also their reflectance even after 5 years storage in a low

humidity atmosphere. The condition will be easily achieved in the EUV instruments.

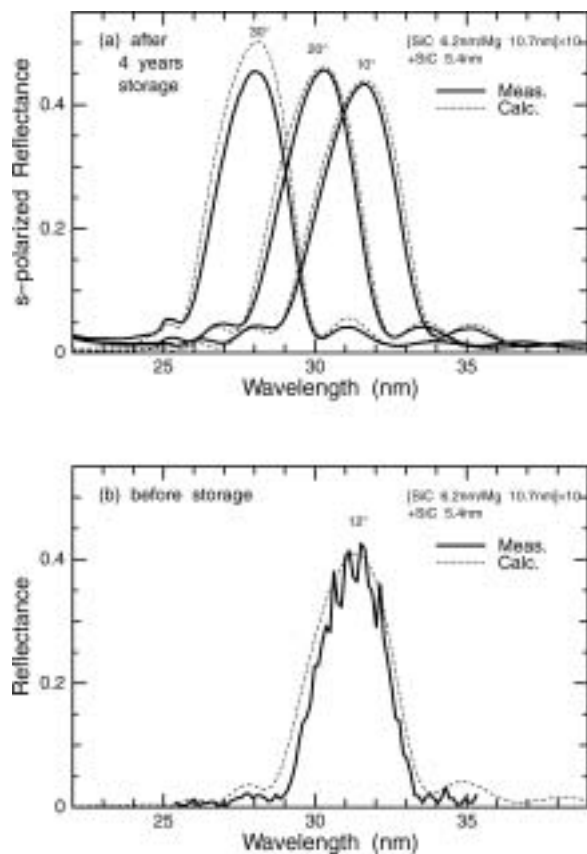


Fig. 1 Reflectance of Mg/SiC multilayer after 4 years storage (a), and before storage (b).

[1] Y. Kondo, T. Ejima, K. Saito, T. Hatano, and M. Watanabe, Nucl. Inst. Meth. Phys. Res. A **467-468** (2001) 333.

[2] T. Ejima, Y. Kondo, and M. Watanabe, Jpn. J. Appl. Phys., **40** (2001) 376.

[3] S. Nakayama, M. Yanagihara, M. Yamamoto, H. Kimura, and T. Namioka, Physica Scripta, **41** (1990) 754.

Thermal Stability of Mg-Based Reflection Multilayers

T. Ejima¹, A. Yamazaki¹, T. Banse¹, K. Saito^{1,2}, Y. Kondo^{1,3}, S. Ichimaru⁴, H. Takenaka⁴

¹IMRAM, Tohoku University, Sendai, 980-8577 Japan

²Venture Business Laboratory, Saga University, Saga 840-8502, Japan

³Akita Research Institute of Advanced Technology, Akita 010-1623, Japan

⁴NTT-AT Co., Tokai 319-1193, Japan

Reflection measurements in the 25–35 nm region are made for Mg/SiC- and Mg/Y₂O₃- multilayers annealed from room temperature to 400°C with 50°C intervals. Both Mg/SiC and Mg/Y₂O₃ multilayers keep their reflectances under 200°C annealing.

Introduction

In the 25–35 nm wavelength region, Mg-based multilayers have been proposed and fabricated as a reflection multilayer [1, 2]. Reflection multilayers used for practical optics are usually exposed to high heat-load circumstances through being baked in a vacuum chamber or enduring a high flux of incident light. Magnesium is known to have a low melting point (648.8°C), much lower than that of typical molybdenum (2622°C) and silicon (1414°C). This low melting-point presents a demerit for the practical application of Mg-based multilayers, despite their high reflectance.

Experiments

The multilayers used for the thermal-stability measurements were heated from RT to 400°C at 50°C intervals in an IR furnace with an Ar atmosphere for 1 hour. Temperature was monitored by three thermocouples in contact with the sample surface.

Reflectances of the heated multilayers were measured with the reflectometer at the beamline BL5B. In the measurements, a combination of the G3 grating and the M24 mirror was used. The resolving power of the wavelength, $\lambda/\Delta\lambda$, was about 500 at 30 nm. The resolution of the angle of incidence was about 0.1°. To suppress high ordered light from the monochromator, a reflection-type filter was placed in front of the sample.

Experimental Results

The measured reflectances of the annealed Mg/Y₂O₃ multilayers are represented in Fig. 1(a). Bragg reflection peaks are observed at around 25.5 nm, and no movement of the peak positions is observed with increases in the annealing temperature. Temperature dependence of the reflectance that are normalized by the reflectance at RT is represented in Fig. 1(b). The value obtained for the measured reflectance in the Mg/Y₂O₃ multilayer at RT was 0.43, and in Mg/SiC multilayer it was 0.42. The temperature dependence of both multilayers is that the reflectance remained constant from RT to 200°C, but decreases with increases of temperature above 200°C, becomes half at 300°C, and then vanishes

over 400°C. This temperature-durability will be high enough in the EUV instruments.

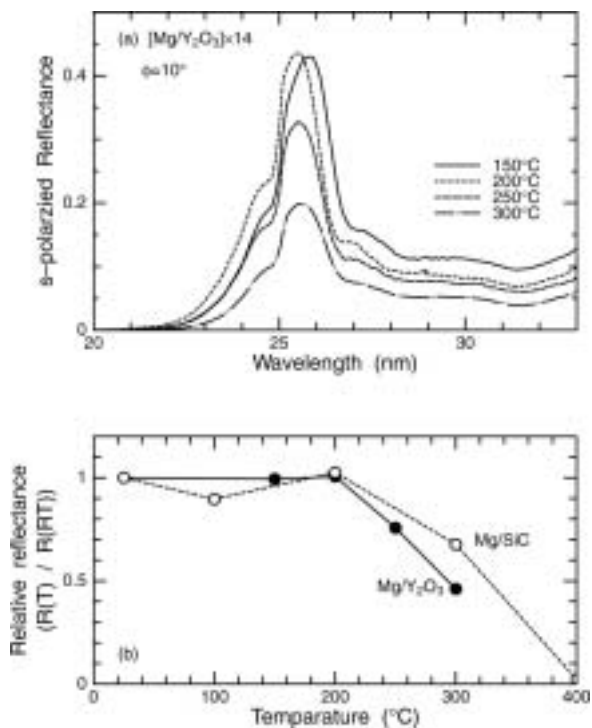


Fig. 1 Reflectances of Mg/Y₂O₃ multilayers annealed from 150°C to 300°C with 50°C intervals (a), and the relative reflectance of each annealing temperature normalized by that of RT (b).

[1] Y. Kondo, T. Ejima, K. Saito, T. Hatano, and M. Watanabe, Nucl. Inst. Meth. Phys. Res. A **467-468** (2001) 333.

[2] T. Ejima, Y. Kondo, and M. Watanabe, Jpn. J. Appl. Phys. **40** (2001) 376.

Development of Multi-Layer Mirror for Imager of O⁺ Ions Flowing from Planets

T. Murachi¹, K. Okada¹, M. Kanao¹, A. Yamazaki², I. Yoshikawa³,
W. Miyake⁴, M. Nakamura¹

¹*Institute of Space and Astronautical Science, Japan Aerospace Exploration Agency,
Sagamihara, Kanagawa 229-8510 Japan*

²*Planetary Plasma and Atmospheric Research Center, Graduate School of Science,
Tohoku University, Aoba-ku, Sendai, Miyagi 980-8578 Japan*

³*Graduate School of Science, The University of Tokyo, Bunkyo-ku, Tokyo 113-0033 Japan*

⁴*National Institute of Information and Communications Technology, Koganei,
Tokyo 184-8795 Japan*

It is known that the hydrogen atoms and ions and the oxygen ions are main components of outflow from the atmospheres of the Venus and the Earth to the interplanetary space. The oxygen ions make important roles in the interaction with the solar wind plasma. In order to investigate the 2 dimensional distribution and temporal variation of the oxygen ions, which is difficult for the in-situ observation using the satellites, we think of the remote sensing of the solar photons resonant-scattered by the oxygen ions (O II: 83.4 nm).

However, resonant-scattered light of the hydrogen atoms (the Lyman α line: 121.6 nm) has the wavelength near that of the O II (83.4 nm). The hydrogen atoms surrounding the planets resonant-scatter the solar light and shine to form a corona. The brightness of the hydrogen Lyman α line is 100 - 10000 times stronger than that of the O II. Therefore, it is necessary to produce the optics, which have little sensitivity at the hydrogen Lyman α line. Until now, we produce the optics using a molybdenum mono-coated mirror (Mo mirror) and an indium filter, and it rejects the Lyman α line. In this experiment in order to make the sensitivity of the hydrogen Lyman α line lower, we design and produce a multi-coated mirror of molybdenum and MgF₂ (1 pair of Mo: 8.0 nm over MgF₂: 8.5 nm, Mo/MgF₂ mirror) on an aluminum substrate.

Fig. 1 shows the measurements of the reflectivity of the Mo mirror and the Mo/MgF₂ mirror in the EUV facility (using the atomic spectral line, whose wavelength is discrete) of the Institute of Space and Astronautical Science (ISAS), Japan Aerospace Exploration Agency (JAXA). At the hydrogen Lyman α line the reflectivity of the Mo mirror and the Mo/MgF₂ mirror is 28 % and 5 % respectively. The reflectivity of the Mo/MgF₂ mirror is 6 times lower than that of the Mo mirror.

Like the calculated value of the reflectivity shown in Fig. 2, the reflectivity of the Mo/MgF₂ mirror should become very low in the vicinity of 121.6 nm. Then we measured the reflectivity of the Mo/MgF₂ mirror with continual radiation of the UVSOR BL-5B line. Fig. 2 represents the measurement result

(because of P polarized light of UVSOR BL-5B, the reflectivity in Fig. 2. differs from that in Fig. 1.). The calculation of the reflectivity of the Mo/MgF₂ mirror becomes very low near 121.6 nm, but the experimental result does not become so. We elucidate this cause in future.

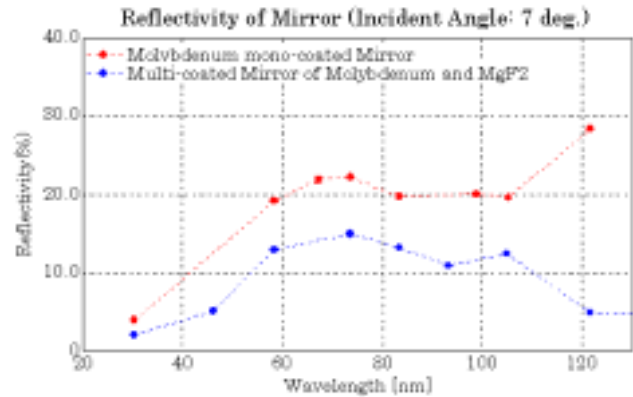


Fig. 1 The reflectivity of the Molybdenum mono-coated mirror (red) and the multi-coated mirror of Molybdenum and MgF₂ (blue) in the EUV facility of ISAS of JAXA.

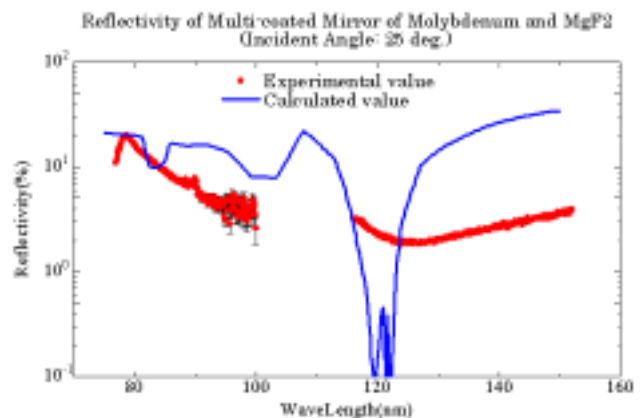


Fig. 2 The experimental value (red) and the calculated value (blue) of the reflectivity of the multi-coated mirror of Molybdenum and MgF₂ in the UVSOR BL5B.

Construction and Performance Test of BL6B(IR)

S. Kimura^{1,2}, E. Nakamura¹, T. Nishi², Y. Sakurai¹

¹UVSOR Facility, Institute for Molecular Science, Okazaki 444-8585, Japan

²Department of Molecular Structural Science, The Graduate University for Advanced Studies, Okazaki 444-8585, Japan

We have newly installed an IR-THz beam line at UVSOR-II. UVSOR had the oldest IR beamline (BL6A1) dedicated at 1986 [1]. Recently, UVSOR storage ring was upgraded to be a low emittance ring and to be able to equip six undulators at three long and three short straight sections. Since the old IR beam line locates on the extended line of one of short straight sections (S6), the emission point was moved to the downstream position in the bending magnet (B6) to make a new undulator beam line at S6. The name of the IR beam line was changed to BL6B(IR).

The beam line has a large acceptance angle of 215(H) x 80(V) mrad² to obtain the high flux in the IR and THz regions. So-called “magic mirror” with vertical angle focusing that has been installed at SPring-8 BL43IR at first [2] was employed as the first mirror. The mirror chamber was directly connected to the bending magnet chamber for collecting high photon flux [3]. To avoid heat load from SR, the orbital plane on the mirror was masked by a copper rod with water cooling. The SR is focused to the imaging source point that locates out of the ultra-high vacuum area of the bending and mirror chambers only by the magic mirror. The beam size at the first focus in the distance of 2640 mm from the magic mirror was 1.17(H) x 1.20(V) mm² that is similar to the corresponding ray-tracing result of 1.0(H) x 2.0(V) mm².

The beam line equips two rapid-scan-type interferometers, one is old Michelson-type (Bruker 66v) and the other newly installed Martin-Puplett-type (JASCO FARIS-1). The former

covers in the photon energy range of 6 meV – 3 eV (50 – 25,000 cm⁻¹) and latter of 1.2 – 25 meV (10 – 200 cm⁻¹). One of the results produced by the latter interferometer is shown in this issue [4].

The obtained and expected brilliance and photon flux are plotted in Fig. 1. In the figure, the results of SPring-8 BL43IR and an expected intensity of a black body light source (The temperature of 1400 K is assumed.) are also plotted. BL6B is higher brilliance in the THz region and higher photon flux in the whole region than BL43IR. This result indicates that BL6B is suitable for the microspectroscopy in the whole region, on the other hand, BL43IR is good for the mid-IR microscopy with diffraction limit resolution.

The present end station is only for a reflection-absorption spectroscopy for mm-size samples. In spring of 2005, a new spectromicroscopy apparatus is installed. The apparatus employs large schwartzschild mirrors with 140 mm in diameter to cover the THz region.

- [1] T. Nanba *et al.*, Int. J. Infrared and Millimeter Waves **7** (1986) 1769.
- [2] S. Kimura *et al.*, Nucl. Instrum. Meth. A **467-468** (2001) 437.
- [3] S. Kimura *et al.*, AIP Conf. Proc. **705** (2004) 416.
- [4] S. Kimura, S. Kunii, in this issue.

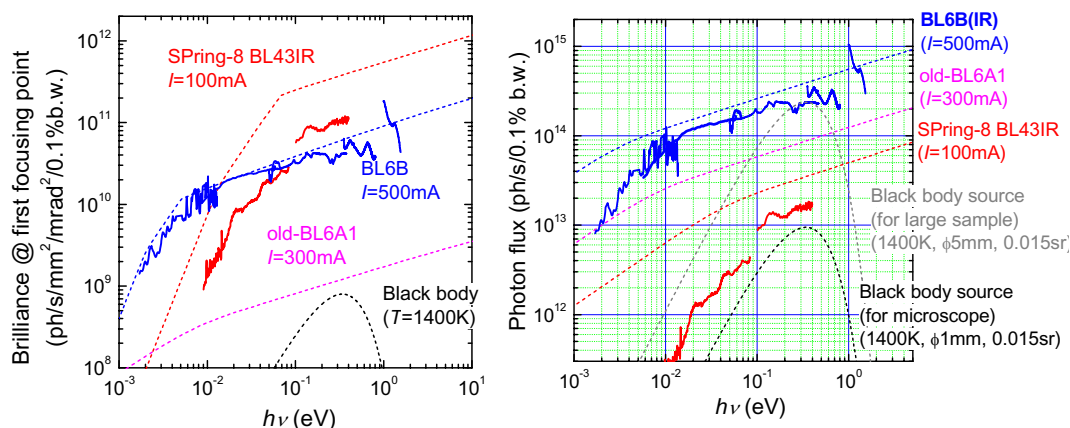


Fig. 1 Brilliance (left) and photon flux (right) spectra of UVSOR BL6B, SPring-8 BL43IR and black body light sources. The dashed and solid lines are calculated and measured spectra, respectively. UVSOR BL6B is brighter in the THz region and higher photon flux in the whole region than SPring-8 BL43IR.

Design of a High-Resolution and High-Flux Monochromator for VUV Angle-Resolved Photoemission at BL7U

S. Kimura^{1,2}

¹UVSOR Facility, Institute for Molecular Science, Okazaki 444-8585, Japan

²Department of Molecular Structural Science, The Graduate University for Advanced Studies, Okazaki 444-8585, Japan

We plan to construct a new undulator beam line for studying electronic structures of condensed matters by a high-energy-resolution angle-resolved photoemission in the VUV region. The beam line equips an undulator light source, a VUV monochromator and a photoelectron spectrometer.

The APPLE-II type undulator [1] will be installed to produce not only horizontal but also vertical linear polarization in the photon energy range of 7 – 40 eV. The undulator period length (λ_u) and the number of period are 70 mm and 40, respectively. The photoemission end station equips a 200-mm-radius hemispherical photoelectron analyzer. The target of the total energy resolution in the angle-resolved photoemission spectroscopy is below 1 meV. To attain the purpose, the monochromator must be high energy resolution below 1 meV and high photon flux above 10^{11} ph/s on samples. Here we propose the design of the new type normal-incident monochromator for such purpose.

The schematic figure of the monochromator is shown in Fig. 1. The monochromator has no entrance slit because the very small vertical beam size at the center of the undulator after upgraded UVSOR-II. The beam size (2σ) is calculated to be $0.07(V) \times 1.2(H)$ mm² in 3%-coupling operation [2]. When the light is derived to a grating without entrance slit, not only high photon flux but also high energy resolution is expected because of the long distances between the emission point and the grating and between the

grating and the exit slit. The similar monochromator has already installed at SRC, Wisconsin [3].

The distances from the emission point to the grating and from the grating to the exit slit are 22 m and 6.67 m, respectively. Then the radius of the spherical grating is 10 m. The source size is reduced by 1/3 on the exit slit. The focusing element is only the spherical grating to reduce the focusing errors. The dispersion direction of the grating is vertical and the incident angle is 0.5 deg.

Three gratings of 1,200, 2,400 and 3,600 l/mm optimized at 10, 20 and 30 eV, respectively, are installed for keeping the energy resolution below 1 meV. The highest energy resolution is expected to be $E/\Delta E \sim 6 \times 10^4$ with the grating of 3600 l/mm and 1%-coupling operation. The photon flux keeps above 10^{11} ph/s in 0.01-% band width.

The beam line equips three branches. The first is for the angle-resolved photoemission, the second for the photochemistry and the third for micro-focus photoemission.

The beam line will be constructed at BL7U in the summer of 2006.

[1] S. Sasaki *et al.*, Jpn. J. Appl. Phys. **31** (1992) L1794.

[2] M. Hosaka, private communication.

[3] J. Bisognano *et al.*, Nucl. Instr. Meth. A **467-468** (2001) 492.

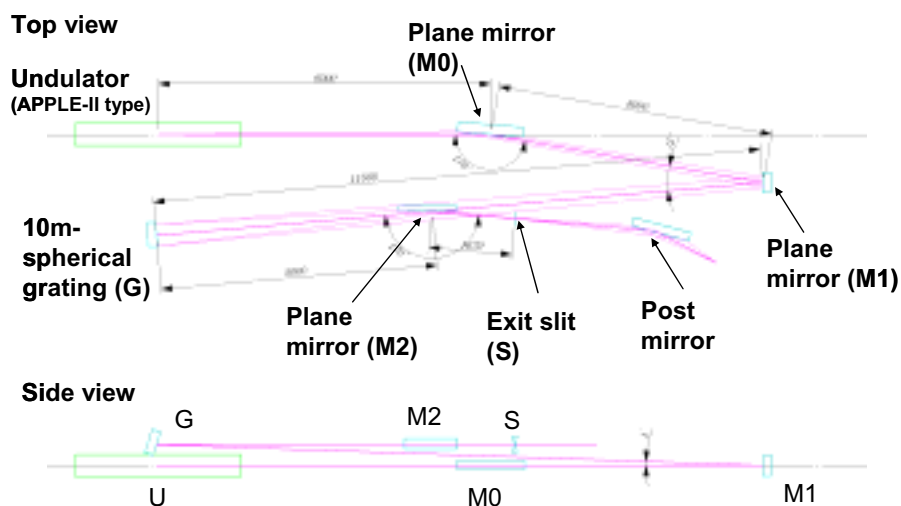


Fig. 1 Schematic figure of the new normal incident monochromator at BL7U.

Quality Evaluation of Mass-Produced Nuclear Emulsion Films for OPERA Neutrino Oscillation Experiment

S. Hiramatsu, N. Naganawa, A. Ariga, J. Kawada, S. Miyamoto, T. Ban, K. Hamada, N. Koike, K. Miyanishi, K. Narita, T. Nakamura, M. Nakamura
F-Laboratory, Faculty of Science, Nagoya University, 464-8602, Japan

Nuclear Emulsion Film can record trajectories of high-energy charged particles with sub-micron position accuracy. The trajectories are recorded as three-dimensional images in the emulsion layers of the film.

Nuclear emulsion has been used in the study of elementary particle physics from 1950s, but at the end of 60s it became a minor detector in that field, because other useful electric detectors were emerged. But, by the recent development of automated image read-out system by us, Nuclear emulsion came back to the frontier of elementary particle physics. The frontier, where the recent nuclear emulsion is working, is Neutrino physics.

In 2000, we have succeeded to detect Tau neutrinos at the first time in the world. Following this success, we are preparing a large scale neutrino oscillation experiment, named OPERA. In this experiment, we intend to confirm the existence of the neutrino masses. We intend to detect Tau-neutrinos oscillated from Mu-neutrinos during the 2.4 msec (732 km) flight from Geneva (Switzerland) to Gran Sasso (Italy). We need a large detector that the mass is around 1700 ton to detect the oscillated Tau neutrinos with high S/N ratio.

About 12 M films corresponding to the area of 150,000m² is required to realize the experiment. The emulsion film, so-called OPERA film, has been developed by us with the collaboration of Fuji Photo Film Co., Ltd. We have succeeded to implement a special function "Refreshing". By this function, we can reset or erase the images recorded in the film before its use.

For OPERA, we are applying the refreshing process after the delivery from Fuji Photo Film Co., Ltd. Then transport the film to Gran Sasso.

We must evaluate the quality of the films in each step, *i.e.*, after the delivery from Fujifilm and after the refreshing. Also we must evaluate the quality of the refreshing process. In order to do those, high energy electrons available in the UVSOR facility has been used.

The exposed electrons were produced during the electron beam transfer from the Booster Synchrotron to the Electron Storage ring. Those are the converted electrons and positrons of gamma rays produced by electron interactions with residual gas or materials surrounding the beam transport. The average energy of the produced electron (positron) is around 50 MeV.

Figure 1 shows a photograph of an electron track recorded in an OPERA film to be evaluated the sensitivity of a film is defined as a density of the



Fig. 1 A recorded trajectory of electron tracks. Horizontal scale is 120 microns.

recorded grains along electron tracks. The size of the recorded grains is around 0.6 micron. The grain density was measured by eye and machines. We specified the grain density of 32 grains/100 microns as a threshold for good quality.

By the exposure and measurement, all of the production batches and the refreshed films show enough sensitivity for our purpose. In Fig.2, the measured sensitivities of the first ten batches are shown. Though some fluctuation can be seen, the sensitivity is over 32 grains/100 microns in all samples.

The evaluation Job using the UVSOR electron will continue until the middle of 2006.

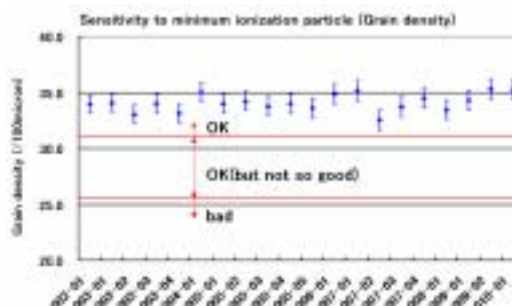


Fig. 2 Measured sensitivity of the films (grain density) of the first 10 production batches.

Fragmentation of C_{70} in Valence Ionization

H. Katayanagi^{1,2}, B. P. Kafle², T. Mori¹, J. Kou¹, K. Mitsuke^{1,2}, Y. Kubozono³

¹*Department of Vacuum UV Photo-Science, Institute for Molecular Science, Okazaki 444-8585, Japan*

²*Graduate University for Advanced Studies, Okazaki 444-8585, Japan*

³*Department of Chemistry, Okayama University, Okayama 700-8530, Japan*

In the electron impact [1] and photo [2] ionization processes of the C_{60} molecules, fragment ions such as C_{60-2n}^{z+} ($n = 1, 2 \dots; z = 1, 2 \dots$) appear when the excess energies exceed those thermochemical thresholds of dissociative ionization by 30 – 40 eV. This is because C_{60} has a large number of internal degrees of freedom and does not have specifically weak bond to rupture owing to its highly symmetrical structure. This energy storage in the fullerenes is thus referred to as the “kinetic shift”.

In our previous study [3], the fragment ion yield spectra of C_{60} in dissociative ionization by the synchrotron radiation have been recorded experimentally. From the spectra, we evaluated the appearance energies, $AE(n, z)$, which corresponds to the onset energies of ion yield spectra. The experimental values of $AE(n, z)$ were well consistent with those obtained by our RRKM calculations. The values of $AE(n, z)$ exceeded their thermochemical thresholds by 30 – 33 eV and increased by 5 – 6 eV with increasing n . From these results, we concluded that the photofragmentation of C_{60}^{z+} was governed by the mechanism of internal conversion of the electronically excited states of C_{60}^{z+} , statistical redistribution of the excess energy among a number of vibrational modes, and sequential ejection of the C_2 units.

Is this mechanism also valid in C_{70} ? The C_{70} is a stable fullerene next larger in size to C_{60} . The kinetic shift can be either smaller or larger than that of C_{60} , since the C_{70} molecules have less symmetry while they have a larger number of degrees of freedom than C_{60} . To answer the question, we measured the photofragment ion yield spectra using time-of-flight mass spectrometer coupled with a monochromator at the beamline 2B in UVSOR.

Photofragment ion yields of C_{70-2n}^{2+} divided by the yield of the parent ion, C_{70}^{2+} , are shown in Fig. 1. Corresponding triply charged ion yields are also shown in Fig. 2. Note that singly charged photofragment ions were scarcely detected in whole energy range of the measurement. At the first glance, the behavior of the photofragment yield curves for $n \geq 5$ (i. e. production of smaller fragment than C_{62}^{2+}) is different from that for $n < 5$. This fact implies the carbon number of 60 is a magic number also in the photofragmentation processes.

This difference appears more clearly in energies at onsets of the yield curves, namely $AE(n, z)$. Both in doubly and in triply charged ions, the values of $AE(n, z)$ for $n < 5$ increase by approximately 7 eV with

increasing n . The kinetic shift in C_{70}^{2+} is found to be 37 eV. In addition, the results of preliminary RRKM calculations in photofragment size of $n < 5$ are consistent with the experimental results. The mechanism to produce photofragments of $n < 5$ from C_{70} is, therefore, the same as that from C_{60} . Whereas the values of $AE(n, z)$ for $n > 5$ stay almost constant. This means that another mechanism should be invoked to explain the production of C_{60-2n}^{z+} in the photofragment size of $n \geq 5$. To elucidate the mechanism, we plan to perform a photoelectron photoion coincidence and a photofragment momentum spectroscopy to clarify energy partitionings during the dissociative photoionization of fullerenes.

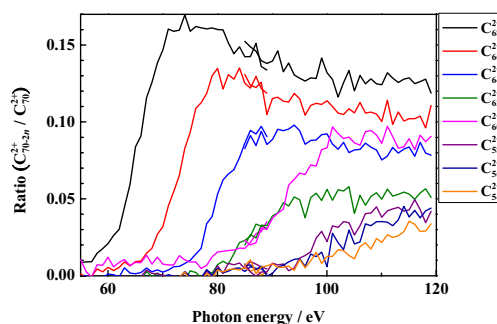


Fig. 1 Doubly charged photofragment ion yields (divided by the parent ion yield).

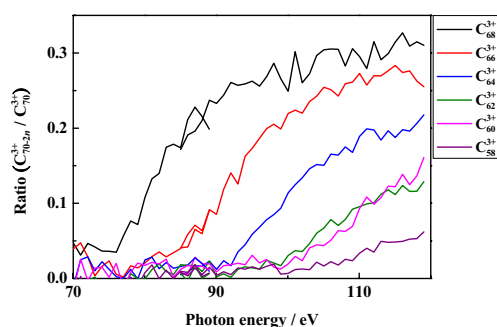


Fig. 2 Triply charged photofragment ion yields (divided by the parent ion yield).

[1] R. Wörgötter, B. Dünser, T. D. Märk, M. Foltin, C. E. Klots, J. Laskin and C. Lifshitz, *J. Chem. Phys.* **104** (1996) 1225.

[2] P. Wurz and K. R. Lykke, *J. Phys. Chem.* **96** (1992) 10129.

[3] J. Kou, T. Mori, Y. Kubozono and K. Mitsuke, *Phys. Chem. Chem. Phys.* **7** (2005) 119.

Photoion Yield Curves of Pr@C₈₂ in the Range 100 – 150 eV

H. Katayanagi^{1,2}, B. P. Kafle², T. Mori¹, J. Kou¹,
Y. Takabayashi³, E. Kuwabara³, Y. Kubozono³, K. Mitsuke^{1,2}

¹*Department of Vacuum UV Photo-Science, Institute for Molecular Science,
Okazaki 444-8585, Japan*

²*Graduate University for Advanced Studies, Okazaki 444-8585, Japan*

³*Department of Chemistry, Okayama University, Okayama 700-8530, Japan*

Endohedral metallofullerenes (M_m@C_n) have attracted attention because of their possibilities of applications toward materials of novel functionalities [1]. The metallofullerenes which have a structure of M@C₈₂ have been used in studies on their geometrical and electronic structures, because of their availability. Their, however, had been no experimental work on the optical properties of gas phase M@C₈₂ in the vacuum UV and soft X-ray regions, until our report of the photoion yield curves of Ce@C₈₂ was published in 2005 [2].

In our work on Ce@C₈₂, we found a giant resonance peak which had been predicted theoretically by Wendin and Wästburg [3]. This peak originates from 4*d* – 4*f* dipole resonance of the Ce atom. Wendin et al. found that the calculated peak consists of a broad atomic component and an oscillation induced by a fullerene cage. Observed photoion yield curves of Ce@C₈₂ had structures and thus found to be affected by the interference. In the present study, we measured the photoion yield curves of metallofullerenes containing Pr which is next to the Ce in the periodic table of the elements.

The Pr@C₈₂ beam was generated in vacuum by sublimation of the solid sample, which was synthesized by the procedure described elsewhere [4]. The typical temperature of a sample holder was 780 K. The photoion yield was measured by means of the time-of-flight (TOF) mass spectrometry in the photon energy range 100 – 150 eV.

Figure 1 shows TOF mass spectrum of Pr@C₈₂^{z+} (*z* = 1, 2) produced by the synchrotron radiation (124 eV). Peaks of the parent ions, Pr@C₈₂⁺ and Pr@C₈₂²⁺, are clearly observed. Small peaks of C₆₀⁺ and C₆₀²⁺ can also be recognized. The intensities of them are, however, insignificant.

Time-of-flight mass spectra of other photon energies were recorded in the same manner. Intensities of ion signals in the spectra were normalized by the photon flux. We thus extracted the yield curve of Pr@C₈₂²⁺ from the normalized spectra. The yield curve of Pr@C₈₂²⁺ is shown in Fig. 2. The photoabsorption spectrum of Pr atoms [5] is also shown in Fig. 2. The yield curve of Pr@C₈₂²⁺ has a similar behavior to the photoabsorption spectra of Pr atoms. This fact leads us to conclude that 4*d* – 4*f* giant resonance does not collapse in Pr@C₈₂, as well as in Ce@C₈₂.

Closer inspection reveals characteristics of Pr@C₈₂. The peak position of Pr@C₈₂²⁺ spectrum is

higher-energy shifted and its widths is slightly narrower than that of Pr atoms. This could be described that the interference effect on the spectrum for Pr@C₈₂ induced by the fullerene cage is different from that for Ce@C₈₂. We plan to make theoretical calculations necessary for more quantitative analysis of the interference effect.

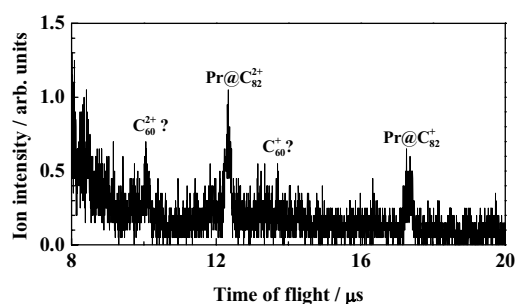


Fig. 1 TOF mass spectrum of Pr@C₈₂^{z+} at the photon energy of 124 eV.

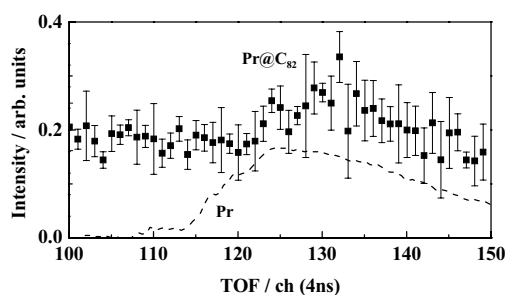


Fig. 2 Photoion yield curve of Pr@C₈₂²⁺ (Filled square). Error bars indicate 1σ of values in experimental runs repeated five times. Dashed curve shows absorption spectrum of Pr atoms [5].

- [1] H. Shinohara, Rep. Prog. Phys. **63** (2000) 843.
- [2] K. Mitsuke, T. Mori, J. Kou Y. Haruyama and Y. Kubozono, J. Chem. Phys. **122** (2005) 064304.
- [3] G. Wendin and B. Wästberg, Phys. Rev. B **48** (1993) 14764.
- [4] K. Shibata, Y. Rikiishi, T. Hosokawa et al. Phys. Rev. B **68** (2003) 094104.
- [5] M. Richter, M. Mayer, M. Pahler, T. Prescher, E. v. Raven, B. Sonntag and H.-E. Wetzels, Phys. Rev. A **40** (1989) 7007.

Photofragmentation of Fullerenes in the Extreme UV: Ion Yield Curves for the Fragment Ions

K. Mitsuke^{1,2}, J. Kou², T. Mori², Y. Kubozono³

¹The Institute for Molecular Science, Myodaiji, Okazaki 444-8585, Japan.

²Graduate University for Advanced Studies

³Okayama University, Okayama 700-8530, Japan

The C₆₀ molecule with a compact structure of a truncated icosahedron exhibits an exceptionally high stability. However, mass spectrometric studies of C₆₀ in combination with laser multiphoton ionization, heavy-ion excitation, or electron impact ionization have revealed that appreciable fragmentation occurs when the system gains energy in excitation and ionization processes. Decomposition of C₆₀^{z+} (z ≥ 1) primarily formed is known to lead to fragment ions with even numbered carbon atoms (C_{60-2n}^{z+}, n=1, 2,...) via sequential loss of C₂ units from C₆₀^{z+} ions in high-vibrational states. In contrast, experimental studies of single photon excitation are very limited [1-4]. Recent results on the relative cross section of the fullerene fragments from C₆₀ show that the appearance photon energies of C_{60-2n}^{z+} and C_{60-2n}²⁺ are higher by 30 - 40 eV than the thermochemical thresholds for dissociative photoionization of C₆₀ [2-4]. In a limited case of C₆₀ + hν → C₅₈⁺ + C₂ + e⁻ Yoo et al. [1] have discussed this large kinetic shift in terms of unimolecular decay modelled by quasiequilibrium theory. However, they could not determine the theoretical appearance energy with a good accuracy, since a reliable value for the binding energy of C₆₀⁺ was not available at that time. Since then there has been no effort to apply quasiequilibrium theory to dissociative photoionization of C₆₀ and to clarify the fragmentation mechanism of the fullerene ions to which large excess energy is initially deposited. In the present work we will discuss the detailed mechanisms of unimolecular reaction induced by equilibration of the excess energy among many density of states of the fullerene, by using the yield curves for the fragment ions obtained in a wide photon energy range.

All the measurements have been carried out at the bending magnet beamline BL2B constructed in the UVSOR synchrotron radiation facility in Okazaki, equipped with an 18 m spherical grating monochromator of Dragon type. The Experimental set-up for photoionization mass spectrometry of C₆₀ has been described in details elsewhere [5,6]. Briefly a molecular beam of C₆₀ was produced by heating the sample powder to approximately 680 K. Monochromatized synchrotron radiation was focused onto the C₆₀ beam. The produced photoions were extracted by a pulsed electric field, mass-separated by a time-of-flight (TOF) mass spectrometer, and detected with a microchannel plate electron multiplier.

In order to normalize the ion counts the fluxes of the molecular and light beams were monitored throughout the measurement by a silicon photodiode and a crystal-oscillator surface thickness monitor, respectively.

Taking TOF mass spectra with scanning the monochromator we could measure the yield curves for C_{60-2n}^{z+} from C₆₀ as a function of hν. For instance, Figure 1 illustrates the curves for C_{60-2n}⁺. The curves for C_{60-2n}^{z+} are considered to provide fractional abundances of C_{60-2n}^{z+} within ~ 25 μs after ionization, at least around the onset region for each ion. With decreasing the size of 60-2n the appearance photon energies AE(n,z) for a given z shift to higher hν positions and the curves rise more gently towards a peak. Values of AE(n,z) are found to be higher by 30 - 33 eV than the thermochemical thresholds for dissociative photoionization of C₆₀ leading to C_{60-2n}^{z+}. Reinköster et al. have found similar large kinetic shifts [2] but their appearance hν positions for z = 1 and 2 are higher by 2 - 8 eV than our values, probably due to their insufficient statistics. On the contrary, the appearance energies measured in electron impact ionization [7] show good agreement with our values.

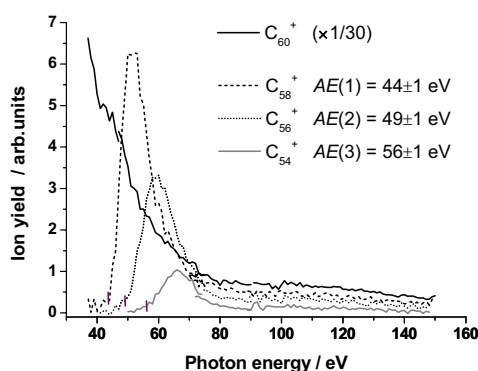


Fig. 1 Yield curves of C_{60-2n}⁺ ions (n = 1 - 3) obtained from time-of-flight mass spectra.

- [1] R.K. Yoo *et al.*, J. Chem. Phys. **96** (1992) 911.
- [2] A. Reinköster *et al.*, J. Phys. B **370** (2004) 2135.
- [3] J. Kou *et al.*, J. Electron Spectrosc. Relat. Phenom. **144-147** (2005) 247.
- [4] J. Kou *et al.*, Phys. Chem. Chem. Phys. **7** (2005) 119.
- [5] J. Kou *et al.*, Chem. Phys. Lett. **374** (2003) 1.
- [6] T. Mori *et al.*, Rev. Sci. Instrum. **74** (2003) 3769.
- [7] P. Scheier *et al.*, Int. J. Mass Spectrom. **138** (1994) 7.

Photofragmentation of Fullerenes in the Extreme UV: Remarkably Large Kinetic Shifts of the Appearance Energies of the Fragment Ions

K. Mitsuke^{1,2}, J. Kou¹, T. Mori¹, Y. Kubozono³

¹The Institute for Molecular Science, Myodaiji, Okazaki 444-8585, Japan.

²Graduate University for Advanced Studies

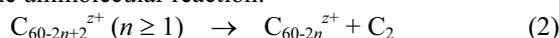
³Okayama University, Okayama 700-8530, Japan

We have measured the yield curves for C_{60-2n}^{z+} from C_{60} as a function of the photon energy $h\nu$ to study the mechanisms and kinetics of the unimolecular reaction of parent ions C_{60}^{z+} in high-vibrational states. Typical spectra for C_{60-2n}^{2+} are given in Fig. 1. These curves are considered to provide fractional abundances of C_{60-2n}^{2+} within ~ 25 μ s after ionization, at least around the onset region for each ion.

When C_{60} is photoionized at the appearance photon energies, namely at $h\nu = AE(n,z)$, we are able to write the maximum internal energy $E_{\max}(n,z)$ initially transmitted to C_{60}^{z+} as

$$E_{\max}(n,z) = AE(n,z) + E_v - IP(z) \quad (1)$$

by assuming the kinetic energy of the emitted photoelectron to be zero. Here, E_v denotes the vibrational energy of C_{60} , and $IP(z)$ is the ionization potential of C_{60} for the formation of C_{60}^{z+} (see Fig. 2). In this study, $E_v = 3.3$ eV is assumed and $IP(z)$ taken from the literature (7.6, 19.0, and 35.6 eV for $z = 1, 2,$ and 3 , respectively). We have evaluated $E_{\max}(n,z)$ from eq. (1) and listed the resultant values in Table 1 for C_{60-2n}^{z+} . It is expected that $E_{\max}(n,z)$ is nearly equal to the upper limit of the internal energies of the primary C_{60}^{z+} above which $C_{60-2n+2}^{z+}$ fragments cannot escape from further dissociating into $C_{60-2n}^{z+} + C_2$. Table 1 reveals two trends in the dependences of $E_{\max}(n,z)$ on n and z of the fragments. First, the difference $E_{\max}(n+1,z) - E_{\max}(n,z)$ depends weakly on n , varying from 5 to 9 eV. This may reflect relatively weak n -dependences [1,2] of the binding energies for the unimolecular reaction:



Second, $E_{\max}(n,z)$ for a given n is almost unchanged irrespective of z . This remarkable finding, together with the prominent kinetic shifts, implies that internal conversion of the electronically excited states of C_{60}^{z+} results in redistribution of the excess energy among the vibrational degrees of freedom followed by

successive ejection of the C_2 units, as demonstrated schematically in Fig. 2.

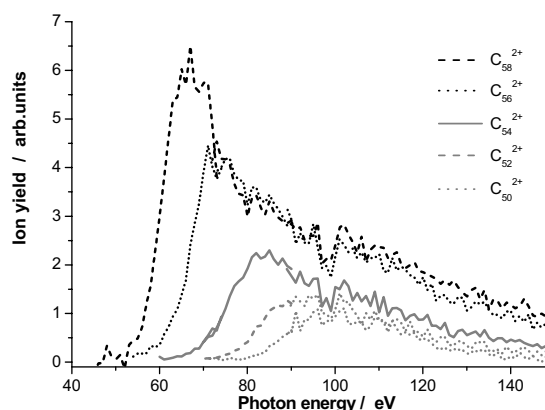


Fig. 1 Yield curves of C_{60-2n}^{2+} ions ($n = 1 - 5$) obtained from time-of-flight mass spectra.

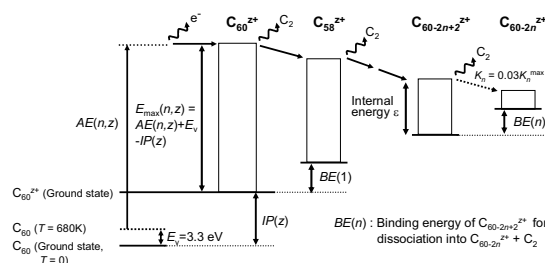


Fig. 2 Scheme of the energetics of the C_2 loss in dissociative photoionization of C_{60} .

- [1] M. Foltin *et al.*, J. Chem. Phys. **98** (1993) 9624.
 [2] R. Wörgötter *et al.*, J. Chem. Phys. **104** (1996) 1225.

Table 1 Upper limit $E_{\max}(n,z)$ of the internal energies (eV) of the primary C_{60}^{z+} ions above which $C_{60-2n+2}^{z+}$ fragments cannot escape from further dissociating into $C_{60-2n}^{z+} + C_2$ ($n \geq 1$).

	$C_{60-2n+2}^{z+}$	C_{60-2n}^{z+}	Observed, ^a $E_{\max}(n,z)$		
			$z = 1$	$z = 2$	$z = 3$
1	C_{60}^{2+}	C_{58}^{2+}	39.7 \pm 1	39.3 \pm 1	40.7 \pm 1
2	C_{58}^{2+}	C_{56}^{2+}	44.7 \pm 1	44.3 \pm 1	49.7 \pm 1
3	C_{56}^{2+}	C_{54}^{2+}	51.7 \pm 1	50.3 \pm 1	- ^e
4	C_{54}^{2+}	C_{52}^{2+}	- ^e	58.3 \pm 1	- ^e
5	C_{52}^{2+}	C_{50}^{2+}	- ^e	64.3 \pm 1	- ^e

^a Obtained by using eq. (1) from the appearance photon energies for the formation of C_{60-2n}^{z+} from C_{60} .

^e C_{60-2n}^{z+} fragment ions are not detectable.

Photofragmentation of Fullerenes in the Extreme UV: Analysis on the Critical Internal Energies

K. Mitsuke^{1,2}, J. Kou¹, T. Mori¹

¹The Institute for Molecular Science, Myodaiji, Okazaki 444-8585, Japan.

²Graduate University for Advanced Studies

We have employed the RRKM theory to derive the curves of fractional abundance (breakdown graphs) for C_{60}^{z+} and C_{60-2n}^{z+} ions ($n = 1 - 5$) as a function of the internal energy of the primary C_{60}^{z+} . The microcanonical rate constant $k_n(\varepsilon)$ for reaction



of $C_{60-2n+2}^{z+}$ having internal excitation energy ε can be given by [1-3]

$$k_n(\varepsilon) = \frac{\alpha G^*(\varepsilon - E_0^n)}{h N(\varepsilon)} \quad (2)$$

Here, α is the reaction path degeneracy, E_0^n is the critical activation energy for reaction (1), $G^*(\varepsilon - E_0^n)$ is the number of states for the transition state (activated complex), and $N(\varepsilon)$ is the density of states of $C_{60-2n+2}^{z+}$. For $n \geq 2$ the ε value of $C_{60-2n+2}^{z+}$ is computed under the assumption that the energy available after dissociation of $C_{60-2n+4}^{z+} \rightarrow C_{60-2n+2}^{z+} + C_2$ is statistically partitioned between $C_{60-2n+2}^{z+}$ and C_2 . We have used Haarhoff's approximation [3] to calculate $G^*(\varepsilon - E_0^n)$ and $N(\varepsilon)$, assuming vibrational frequencies of $C_{60-2n+2}^{z+}$ to be replaced by those of a neutral C_{60} reported by Schettino et al. [4]

The critical activation energies E_0^n in eq. (2) are taken from the binding energies of $C_{60-2n+2}^{z+}$ ($n = 1 - 5$) for reaction (1) in the literature [2,5]. We adopted the two sets of the binding energies of $C_{60-2n+2}^{z+}$, i.e. the sets for the TS-1 and TS-3 models. The TS-3 transition state is consistent with a large frequency factor in the Arrhenius relation which has been expected by a very large rotational partition function of C_2 . The binding energies of C_{60}^{z+} , for example, are 7.06 eV and 9.2 eV for TS-1 and TS-3, respectively.

Figure 1 shows the fractional abundance K_n for C_{60-2n}^{z+} ions with the TS-3 model as a function of the internal energy of the primary C_{60}^{z+} at 25 μ s after photoionization of C_{60} . We defined the appearance internal energy $E_{RRKM}(n)$ for the formation of C_{60-2n}^{z+} as the internal energy of C_{60}^{z+} corresponding to $K_n =$

$0.03K_n^{\max}$. The values of $E_{RRKM}(n)$ determined from Fig. 1 are listed in the seventh and eighth columns of Table 1. For the formation of C_{58}^{z+} , C_{56}^{z+} , and C_{54}^{z+} $E_{RRKM}(n)$ are 40.9, 47.0, and 52.8 eV, respectively, in excellent agreement with the observed maximum internal energies $E_{\max}(1,z)$, $E_{\max}(2,z)$, and $E_{\max}(3,z)$, respectively. These results are the manifestation of the validity of the present statistical treatment: large amounts of the internal energy of C_{60}^{z+} is equilibrated among the vibrational degrees of freedom, and subsequent fragmentation proceeds through reaction (1) via a transition state with the activation energy of E_0^n .

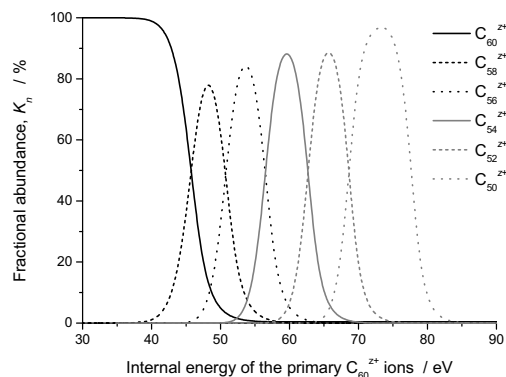


Fig. 1. Fractional abundance curves of C_{60}^{z+} and C_{60-2n}^{z+} ions obtained by using the RRKM theory (TS-3 model).

- [1] R. K. Yoo *et al.*, J. Chem. Phys. **96** (1992) 911.
- [2] R. Wörgötter *et al.*, J. Chem. Phys. **104** (1996) 1225.
- [3] W. Forst, *Theory of Unimolecular Reactions*, Chap. 6, Academic, New York, (1973).
- [4] V. Schettino *et al.*, J. Chem. Phys. **101** (1994) 11079.
- [5] M. Foltin *et al.*, J. Chem. Phys. **98** (1993) 9624.

Table 1 Upper limit $E_{\max}(n,z)$ of the internal energies (eV) of the primary C_{60}^{z+} ions above which C_{60-2n}^{z+} fragments cannot escape from further dissociating into $C_{60-2n}^{z+} + C_2$ ($n \geq 1$).

	$C_{60-2n+2}^{z+}$	C_{60-2n}^{z+}	Observed, ^a $E_{\max}(n,z)$			Calculated, ^b $E_{RRKM}(n)$	
			$z=1$	$z=2$	$z=3$	TS-1 ^c	TS-3 ^d
1	C_{60}^{z+}	C_{58}^{z+}	39.7 \pm 1	39.3 \pm 1	40.7 \pm 1	40.1	40.9
2	C_{58}^{z+}	C_{56}^{z+}	44.7 \pm 1	44.3 \pm 1	49.7 \pm 1	47.1	47.0
3	C_{56}^{z+}	C_{54}^{z+}	51.7 \pm 1	50.3 \pm 1	-	52.9	52.8
4	C_{54}^{z+}	C_{52}^{z+}	-	58.3 \pm 1	-	58.9	59.1
5	C_{52}^{z+}	C_{50}^{z+}	-	64.3 \pm 1	-	65.1	65.3

^a Obtained from the appearance photon energies for the formation of C_{60-2n}^{z+} from C_{60} .

^b Appearance internal energies of C_{60}^{z+} corresponding to $K_n = 0.03K_n^{\max}$ at 25 μ s after photoionization of C_{60} . The RRKM theory is employed to derive the rate constant for reaction (1) from which the K_n curves can be calculated.

^c $E_{RRKM}(n)$ determined from a set of the binding energies for the TS-1 model was employed.

^d $E_{RRKM}(n)$ determined from Fig. 1. A set of the binding energies for the TS-3 model was employed.

Site-Specific Photoionization of Free Krypton Clusters

T. Hatsui¹, H. Setoyama¹, N. Kosugi¹, B. Wassermann², I.L. Bradeanu³, E. Rühl^{1,3}

¹Institute for Molecular Science, Okazaki 444-8585 Japan

²Institut für Experimentalphysik, Freie Universität Berlin, 14195 Berlin, Germany

³Institut für Physikalische Chemie, Universität Würzburg, 97074 Würzburg, Germany

Cluster formation is known to give the decrease in binding energy, which is commonly interpreted in terms of final state polarization screening [1]. From earlier near-edge spectroscopy [2] it is known that the most significant changes in electronic structure are found in the regime of small clusters. In the present work, we investigate Kr 3d photoionization for variable size Kr clusters in the average size regime $\langle N \rangle \leq 30$.

The experimental setup consists of a continuous supersonic jet expansion. The correlation between the expansion conditions and $\langle N \rangle$ is taken from Karnbach et al. [3]. The jet is intersected with a beam of linearly polarized soft X-rays from the in-vacuum undulator beam line BL3U with an energy resolving power $E/\Delta E$ of $\sim 2 \times 10^3$ at 140 eV photon energy. Electrons are analyzed at 55° to the electric vector of the incident x-rays by a Scienta SES-200 electron spectrometer (path energy: 75 V).

The new features arising from cluster formation are observed at the binding energy lower than the bare atomic peaks. The cluster spectra are obtained by subtracting the atomic portion (Fig. 1). Subtraction of the atomic component from the raw spectra was only done until spectral distortions occurred because a dimer component of weak intensity exists near the atomic lines. This is consistent with the dimmer binding energy predicted by *ab initio* theoretical calculations, which is so close to the bare atomic one that the dimer components with small mixing ratio are invisible in the raw spectra. Core ionization energies calculated by using a simple model in combination with a phenomenological model, that describes perfect and defect cluster shapes, is shown at the top of Fig. 1.

We have performed a spectral de-convolution of these components by using identical Voigt profiles, which are evaluated from the atomic spectrum observed at the same instrumental condition (Lorentzian width: 93 meV [4], Gaussian width: 163 meV). The dimer- and the edge-components show no or little size effects. When the atomic profiles are used, then the two other ones (corner and face/bulk) do not give rise to a significantly different line shape, as verified by the experimental spectra. This allows us to fit the spectra with four components for each spin-orbit component (Fig. 1). The spectrum for $\langle N \rangle = 4$ consists of three surface components besides the dominant dimer. The smallest of these shifts is due to the corner sites of small clusters, followed by edge-, face-/bulk-sites. We note that face- and bulk-sites cannot be clearly distinguished from each

other since their 3d ionization energies occur in the same energy regime (Fig. 1). As $\langle N \rangle$ is increased one observes the following systematic changes in the spectra shown in Fig. 1. (i) The dimer component decreases substantially in relative intensity. Any shift is hardly observable and the different energy positions are well observable within the error limit; (ii) Corner-sites show an increasing shift reaching up to ~ -500 meV. The relative intensity of this component remains almost constant; (iii) Edge-sites gain substantially intensity, which is accompanied by a slight energy shift; (iv) Face-/bulk-sites also gain intensity and there is also a slight size dependence of this component. The model calculations show that substantially larger shifts occur for the bulk component, if large clusters are formed. This is in full agreement with recent experimental results [5]. The present work has successfully revealed size and site-specific Kr 3d ionization energies of considerably smaller clusters.

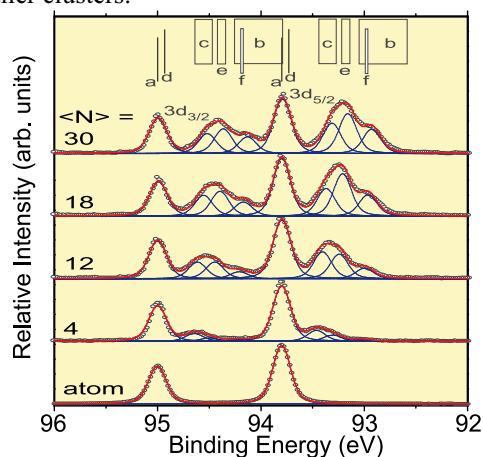


Fig. 1 Kr 3d photoelectron spectra of Kr clusters (\circ). The sum ($-$) of the spectral components ($-$) are given. The calculated energy regimes of different sites (a: atom, d: dimer, c: corner, e: edge, f: face, b: bulk) are shown at the top.

[1] O. Björneholm *et al.*, J. Chem. Phys. **104** (1996) 1846.

[2] O. Björneholm *et al.*, Phys. Rev. Lett. **74** (1995) 3017. A. Knop *et al.*, Phys. Rev. Lett. **80** (1998) 2302.

[3] R. Karnbach *et al.*, Rev. Sci. Instrum. **64** (1993) 2838.

[4] M. Jurvansuu *et al.*, Phys. Rev. A **64** (2001) 012502.

[5] M. Tchapyguine *et al.*, J. Chem. Phys. **120** (2004) 345.

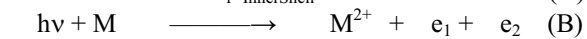
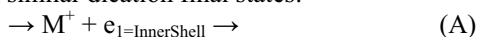
Double Photoionisation processes in SF₆

P. Lablanquie¹, Y. Hikosaka¹, E. Shigemasa¹, T. Aoto², K. Ito²

¹UVSOR Facility, Institute for Molecular Science, Okazaki 444-8585 Japan

²Photon Factory, Institute of Materials structure Science, Tsukuba 305-0801 Japan

Double photoionisation, that is removal of two valence electrons from a molecule by a single VUV photon can usually proceed by two different paths, that form similar dication final states:



(A) is the Auger effect where an inner shell electron is first extracted and subsequent relaxation leads to emission of a secondary Auger electron. Valence double ionisation, (B) is often improperly referred to as ‘direct double photoionisation’, but includes in fact large contribution of indirect, sequential paths. It was recently demonstrated [1] that these indirect paths take surprisingly long time, with similar time scales for electron emission and nuclear motion, up to the point that the intermediate states often dissociate fully prior to emission of the second electron. We present here evidence of a different process in SF₆ molecules: an intense valence singly charged intermediate state autoionizes very efficiently through ICD (Inter Atomic Coulombic Decay [2]) prior to nuclear motion.

Experiment was performed on the new BL3U undulator line with the coincidence experimental setup developed at PF by Hikosaka *et al* [3]. Investigation of double photoionisation requires detection in coincidence of both emitted electrons, in order to define the reaction paths, which often means low signal. The trick in our experiment is to impose one of the two electrons to be of zero energy, and detect it with a threshold electron analyzer. Advantages are high collection-efficiency (on 4π sr) and potentially high energy-resolution.

Fig. 1 (bottom) displays the SF₆ L_{2,3}VV Auger

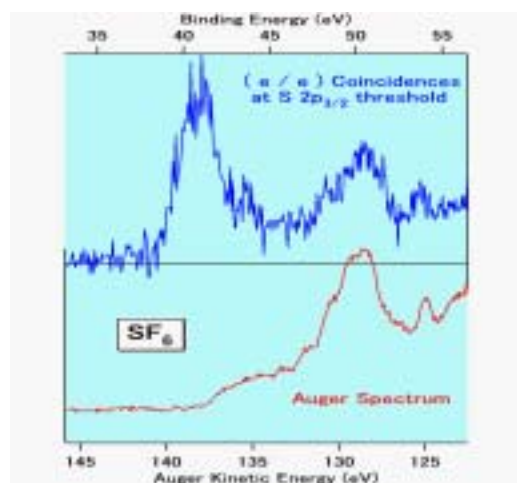


Fig. 1 Bottom: SF₆ Auger spectrum. Top: coincidence Auger spectrum measured at 2p_{3/2} threshold.

spectrum. Its measurement in coincidence with the S2p_{3/2} photoelectron (top) allows us to filter out the other S2p_{1/2} spin-orbit Auger components, and to define precisely the final M²⁺ state and its binding energy (= photon energy minus the energetic electron energy). It is observed that the M²⁺ states populated by Auger decay are excited states, with the final 2 holes probably localized on the S atom, at the vicinity of the S2p hole. But experiment also reveals that M²⁺ states of lower binding energies can be accessed, with the 2 holes lying on F atoms [4]. These states are not populated by S2p Auger decay, and they can also be formed below S2p threshold as revealed in Fig. 2. Comparison with the non coincident photoelectron spectrum (in red) shows similar intensity profiles as the valence states of 40-45 eV binding energies, which are attributed to F2s hole states. The process is thus formation of F2s holes that decay rapidly through ICD mechanism [4]. This situation is specific to the SF₆ molecule, as usually intensity profiles are markedly different in photoelectron spectra and in e/e coincidence curves, as observed for N₂ in Fig. 2 (bottom).

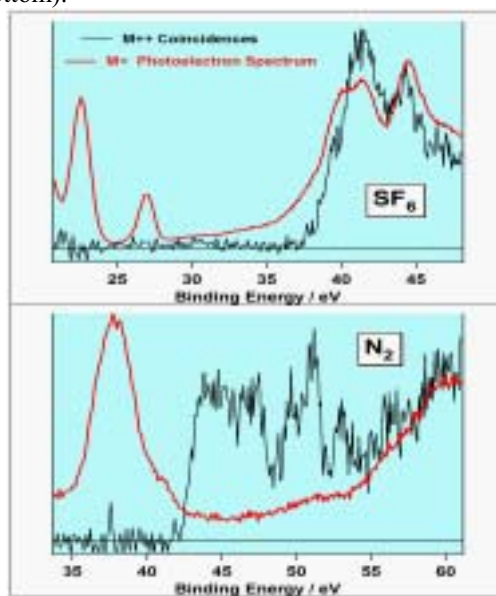


Fig. 2 Black: threshold electron / energetic electron coincidences measured with 80eV photons, and compared to the noncoincident photoelectron spectrum (red). Top: SF₆, Bottom: N₂.

[1] J. Eland *et al.*, Chem Phys **290** (2003) 27 and ref included.

[2] C. Buth *et al.*, J. Chem. Phys. **119** (2003) 10575.

[3] Y. Hikosaka *et al.*, Meas. Sci. Technol. **11** (2000) 1697.

[4] R. Feifel *et al.*, submitted to J. Chem. Phys.

Sub-Natural Linewidth Auger Electron Spectroscopy: Application to the Sulfur 2s Hole Decay in OCS

Y. Hikosaka¹, P. Lablanquie¹, E. Shigemasa¹, T. Aoto², K. Ito²

¹*UVSOR Facility, Institute for Molecular Science, Okazaki 444-8585 Japan*

²*Photon Factory, Institute of Materials structure Science, Tsukuba 305-0801 Japan*

Inner-shell photoionization and the subsequent Auger decay give dication states as the final product. Since the kinetic energy of the Auger electron corresponds to the transition energy from the core-hole state to the dication state, spectroscopic information on the dication states is obtained by the analysis of individual Auger transitions. Auger spectroscopy has been, therefore, one of the most useful tools for investigating dication states. However, the analysis of Auger spectra has been restricted mainly for the following two reasons. First, the spectral features become complicated when the spectrum consists of the superposition of Auger lines associated with various core-hole states and their satellites. Second, the spectral resolution for an Auger line is limited by the natural width of the initial core-hole state.

Auger lines associated with a core-hole state can be distinguished by coincidence detection with the corresponding photoelectrons. Thus the difficulties resulting from the first restriction above can be removed by Photoelectron-Augur electron coincidence spectroscopy. Furthermore, this coincidence spectroscopy also enables the second restriction to be overcome and achieve a spectral resolution better than the natural width of the initial core-hole state. This sub-natural linewidth regime results from the complete definition of the dication states, brought about by the coincidences.

Detection of threshold photoelectrons, i.e. electrons with near-zero kinetic energy, takes advantage of the high energy-resolution (few meV) and high (4π) collection-efficiency that can be attained. These advantages are carried over to the Auger electron spectrum measured in coincidence, when we adopt threshold photoelectrons as the coincidence counterpart. So far, we have applied the threshold electron-Augur electron coincidence technique mainly to Auger transitions of rare gases, and have gained spectroscopic information on the dication states as well as the dynamics on the multiple ionization processes ([1] and references therein).

In this work, we have studied sulfur 2s decay in OCS using the threshold photoelectron-Augur electron coincidence technique. The S 2s hole has a very short lifetime resulting from the fast $L_1L_{2,3}V$ Coster-Kronig decay, and the resultant wide natural width (1.8 eV) has hidden the spectroscopic information on the final dication states. In practice, the Auger spectrum we measured with conventional Auger spectroscopy shows in the kinetic energy range

20-50eV only broad structures which can be allocated to the $L_1L_{2,3}V$ Coster-Kronig transitions (see Fig. 1(a)), and it is difficult to deduce the spectroscopic information on the dications from this spectrum. In contrast, the threshold photoelectron-Augur electron spectrum in Fig 1b exhibits the same dication states with a much higher energy resolution. Here, the energy resolutions of the Auger electron and threshold electron analyzers are set to around 0.8 eV and 30 meV (FWHM), respectively, and the photon energy band width is to 0.25 eV; therefore the energy resolution in the coincident spectrum is expected to be around 0.85 eV and the sub-natural linewidth regime is established by the coincidence measurement. Each structure in the coincidence spectrum is attributable to an electronic state with the configuration of $(S\ 2p)^{-1}(\text{valence})^{-1}$, and their detailed interpretations are under way.

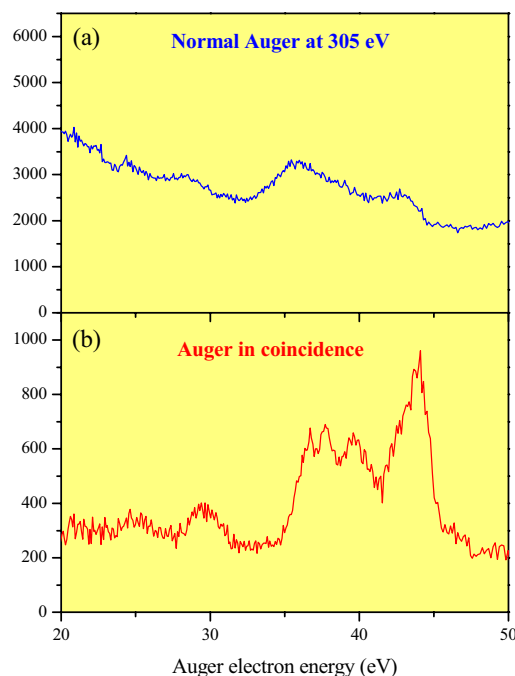


Fig. 1 (a) normal Auger electron spectrum measured at 305 eV photon energy. (b) Auger electron spectrum measured in coincidence with threshold photoelectrons at the S 2s threshold electron peak.

[1] F. Penent *et al.*, J. Electron Spectrosc. Relat. Phenom. **144-147** (2005) 7.

Velocity Imaging Spectrometer for Negative Fragment Ions

Y. Hikosaka, E. Shigemasa

UVSOR Facility, Institute for Molecular Science, Okazaki 444-8585 Japan

Negative ion mass spectrometry working with synchrotron radiation source has been extensively used in investigation of the ion-pair formation, where negative ion detection achieves a basic discrimination against abundant photoionization processes associated with the formations of photoelectrons and positive ions. The negative ion yield curves have provided spectroscopic information on the superexcited states. Onsets in the curves often match the thermochemical thresholds for different ion-pair dissociation channels, from which one could deduce the states of the positive and negative ions formed. Ordinary mass spectrometry, however, rarely has the ability to determine kinetic energies and angular distributions of the fragment ions, though such information brings about further insights into the spectroscopy of the superexcited states and the dynamical property on the ion-pair dissociation.

We have developed a negative ion imaging spectrometer [1] designed to be used in combination with an ordinary synchrotron radiation source. The powerfulness of the imaging technique has been exerted on ion and photoelectron observations in the study of laser chemical dynamics. The advantages of the imaging technique applied to the study of the ion-pair formation process are (i) high collection efficiency (4π -sr. solid angle), and (ii) observation of the velocity vector distributions of fragment ions. The first useful information derived from the velocity vector distributions is the angular distribution with respect to the electric vector of the radiation. The angular distribution may imply the molecular orientation induced by photoexcitation, where the orientation reflects the symmetries of initially-formed superexcited states. The kinetic energy distribution of the negative fragment ions is the second useful information from the velocity vector distributions on image. Internal states of negative and positive fragments are accessible from the kinetic energy distribution. The electronic and ro-vibrational populations of the final fragments closely relate to the molecular states concerning the reaction dynamics.

The present negative ion imaging spectrometer is illustrated in Fig. 1. We have installed the imaging spectrometer on the beamline BL7B. The monochromatized synchrotron radiation has been introduced into the middle point between the plates P_1 and P_2 perpendicularly to the plane of Fig. 1. The polarization axis of light was positioned perpendicularly to the axis of the flight tube. Negatively-charged particles produced after photoabsorption, *i.e.* electrons and negative ions, can be extracted by the three-element electrostatic lens into the flight tube, and projected onto the position-sensitive detector terminating the tube. For observation of

negative ion images, we have applied a strong magnetic field in the ionization region, in order to suppress electrons' arrivals to the detector.

Usefulness of the present method for observing negative ions is clearly demonstrated on the images from O_2 measured at 21.06 eV photon energy with/without a strong magnetic field. The image observed without any extra magnetic field (Fig. 2(a)) is fully occupied by the electrons due mainly to the formations of $O_2^+(b^4\Sigma_g^-$ and $B^2\Sigma_g^-)$. In contrast, only a single ring due to O^- fragments emerges in Fig. 2(b) as we applied the strong magnetic field. The single ring corresponds to the formation of $O(^2P)+O(^2D)$. The intensity distribution along the circumference of the ring shows that O^- fragments are preferably emitted along the electric vector. This fact implies that the photoexcitation to Σ_u^- symmetry state(s) is dominant at this photon energy.

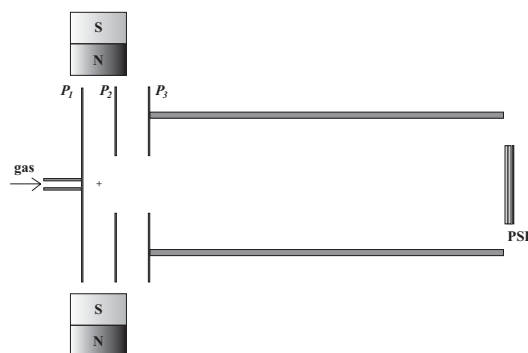


Fig. 1 A schematic view of the negative ion imaging spectrometer.

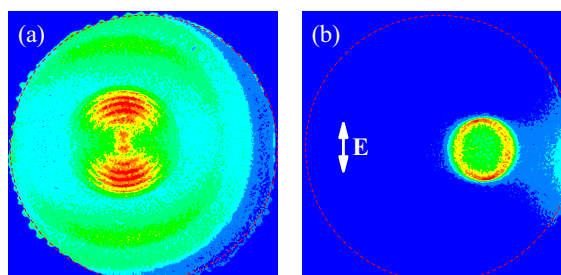


Fig. 2 Raw images from O_2 measured with 21.06 eV photons (a) without any extra magnetic field and (b) with a strong magnetic field (~ 15 mT flux around the ionization region). Each image is plotted on an individual linear scale. The electric vector of the light lies along the vertical axis.

[1] Y. Hikosaka and E. Shigemasa, *J. Electron Spectrosc. Relat. Phenom.* **148** (2005) 5.

Negative Fragment Ion Formation from N₂O Studied by Velocity Imaging Spectroscopy

Y. Hikosaka, E. Shigemasa

UVSOR Facility, Institute for Molecular Science, Okazaki 444-8585 Japan

Formation of a pair of positive and negative fragment ions following molecular photoexcitation is commonly observed in the vacuum ultraviolet region, although in general this process occupies only a small fraction in the total cross section. The cross section of the ion-pair formation is often enhanced at superexcited states which are mostly Rydberg states converging to upper-lying ion states. The enhancements result from the interactions between the superexcited states and the ion-pair states correlating directly to ion-pair dissociation limits, and the interaction strength relates to the electronic properties and the potential energy surfaces of the relevant states. Accordingly the superexcited states indiscernible in the total cross section may be exhibited on the ion-pair formation; observation of the ion-pair formation, therefore, can be utilized as a specific probe for superexcited states.

We have developed a negative ion imaging spectrometer which uses magnetic field to filter out electron signals [1]. The present method enables us to perform imaging observation of negative ions, for the first time, by the use of ordinary synchrotron radiation which offers properties of wide tunability and linear polarization. We have applied the new method to ion-pair dissociation in N₂O, which proves and demonstrates the powerfulness of the present method in study on ion-pair dissociation dynamics.

Measurements were made at beamline BL7B. Formation of O⁻ fragments from N₂O is most extensive in the 18-20 eV photon energy range [2]. Figure 1 shows a total yield curve of the imaging detection. The spectral features on the yield curve are essentially equivalent to those on the O⁻ yield curve obtained by a quadrupole mass spectrometer [2], though the background due to remaining electrons is anticipated in the present curve. Five Rydberg series converging to N₂O⁺(C²Σ⁺) have been located in this photon energy range; though the assignments of the Rydberg series have been discussed, they are still not definitely determined. Two of the Rydberg series are remarkably exhibited in Fig. 1.

Negative ion images measured at five photon energies, two of which correspond to Rydberg peaks, are displayed in the insets of Fig. 1. No clear ring can be seen on all the images, implying that the O⁻ fragments do not have some distinct kinetic energies but widely-distributed energies. Here, the kinetic energy distributions of the O⁻ fragments reflect the internal energy distributions of counterpart N₂⁺ fragments, and accordingly the counterpart N₂⁺ fragments are excited ro-vibrationally rather than only electronically. The excitation closely relates to the

shapes of the potential energy surfaces on which the ion-pair dissociation occurs. The images measured at non-resonant energies show weak preferences for the O⁻ emission in the perpendicular direction to the electric vector. In striking contrast, at the two resonant energies the O⁻ fragments are preferably emitted along the electric vector ($\beta=0.5$ at the lower resonance and $\beta=0.7$ at the higher one). This fact is a direct evidence that initial photoexcitation to the two Rydberg states results from parallel transition, *i.e.* that the two Rydberg states have Σ symmetry, inconsistent with some previous interpretations inferred mainly from the quantum defects of the Rydberg states. The assignments we propose for these two Rydberg series are given in the figure.

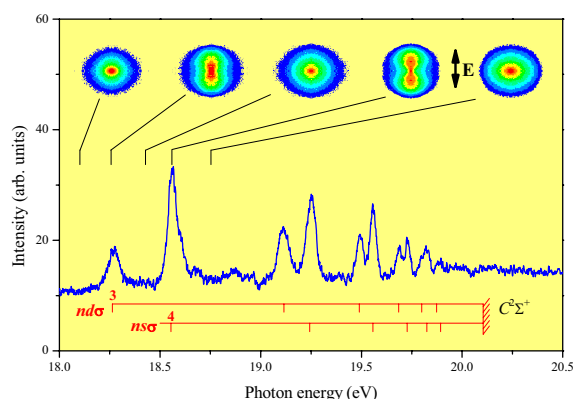


Fig. 1 A total yield curve of the imaging detection from N₂O photoionization with a strong magnetic field, which essentially corresponds to an O⁻ yield curve. Photon energy resolution is set to 20 meV. Energy levels of two Rydberg series converging to N₂O⁺(C²Σ⁺) are indicated with the assignments we propose. Raw O⁻ images measured at 18.10, 18.26, 18.43, 18.56 and 18.75 eV are attached. The electric vector of the light lies along the vertical axis.

[1] Y. Hikosaka and E. Shigemasa, *J. Electron Spectrosc. Relat. Phenom.* **148** (2005) 5.

[2] K. Mitsuke, S. Suzuki, T. Imamura and I. Koyano, *J. Chem. Phys.* **92** (1990) 6556.

Anisotropic Fragment Emission on Valence Photoionization of CF₄

Y. Hikosaka, E. Shigemasa

UVSOR Facility, Institute for Molecular Science, Okazaki 444-8585 Japan

As a prototype to understand photoionization dynamics of highly-symmetrical molecules, photoionization of CF₄ in the valence region has been studied extensively by both experiment and theoretical calculation. Photoabsorption spectra and electron energy loss spectra of CF₄ exhibit a few distinct features and are occupied mainly by broad structures. Harshbarger *et al.* assigned most of the structures to transitions into Rydberg orbitals [1], and their assignments have been accepted in several subsequent works. In contrast, Ying and Leung have ascribed the same structures to valence states associated with transitions to the unoccupied 5a₂ and 5t₂ orbitals [2].

Meanwhile, the partial photoionization cross sections and photoelectron asymmetry parameters measured for individual CF₄⁺ states have been the most important experimental data to be reproduced by theoretical calculation. Although calculation results agree, to some extent, with the experimental curves, satisfactory interpretations are still not proposed to the physical origin of the modulations on the experimental curves. The most important and critical subject on the interpretations is again the transitions from each occupied orbital to the unoccupied 5a₂ and 5t₂ orbitals: the calculation results tend to put the transitions into the photoionization continua as shape resonances, in striking contrast to the assignments by Ying and Leung.

The present work offers new experimental information to understand dynamics on the CF₄ valence photoionization. Using the photoion velocity imaging method we have measured in $h\nu=16-60$ eV angular distributions of fragment ions with respect to the electric vector of light. The photoion images measured at $h\nu=17.4, 19.9, 29.9$ and 46.5 eV are presented in Fig. 1. The photoion images correspond to projections of the initial three-dimensional photoion velocity distributions onto the detector. Here, the observed images are for all ion species, since the present imaging detection can not discriminate ion species. One would speculate that at every photon energy the isotropic fragment emissions result from the high symmetry (T_d) of the CF₄ neutral ground state; however, apparent anisotropy is practically observed on the fragment emissions at the lower three $h\nu$: the photoions at these photon energies are preferably emitted along the electric vector. The anisotropic fragment emissions directly imply that the initial molecular symmetry is broken on the dissociative photoionization.

Our interpretation to the origin of the observed anisotropies is as follows. Within the T_d symmetry, the transition from an occupied orbital to one of the unoccupied orbitals should be isotropic with respect to

the electric vector and result in a triply-degenerated excited state with T₂ symmetry. Such a degenerated state is subject to symmetry distortion, and a T₂ state originally in T_d symmetry results in an A₁ and E states after the distortion to C_{3v}. The dipole moment for the transition to the A₁ state is parallel to the C_{3v} axis, while that for the transition to the E state is perpendicular to the axis. Here, the two transition moments are not necessarily the same any more after the symmetry distortion. Autoionization from such distorted excited states produces similarly-distorted CF₄⁺ states. Since the CF₄⁺(X, A) states have potential energy surfaces being repulsive associated with the C-F bond, the axis of the ion dissociation naturally coincides with the C_{3v} axis. Photoexcitation to the A₁ and E states, therefore, promotes the positive and negative asymmetry with respect to the electric vector, respectively, for the resultant CF₃⁺ fragments. The observed anisotropy is always positive, which implies that the parallel transition forming A₁ states is preferable to the perpendicular transitions. This may be reasonable, because both the 5a₂ and 5t₂ orbitals have the σ* character and the associated transitions have large contributions to the cross sections at the measured photon energies.

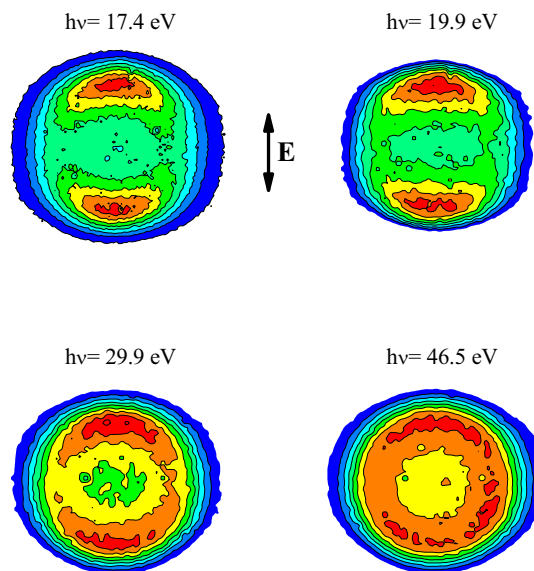


Fig. 1 Photoion images from CF₄ photoionization at $h\nu=17.4, 19.9, 29.9$ and 46.5 eV. Each image is plotted on an individual linear scale.

[1] W.R. Harshbarger *et al.*, *J. Electron Spectrosc. Relat. Phenom.* **1** (1972/1973) 319.

[2] J.F. Ying and K.T. Leung, *J. Chem. Phys.* **100** (1994) 7120.

BL1B

Two-Photon Spectroscopy of Core Excitons with the Combinational Use of Synchrotron Radiation and Laser Light

T. Tsujibayashi¹, J. Azuma², M. Watanabe³, O. Arimoto⁴, M. Itoh⁵, S. Nakanishi⁶,
H. Itoh⁶, M. Kamada²

¹Department of Physics, Osaka Dental Univ., Hirakata 573-1121, Japan

²Synchrotron Light Application Center, Saga Univ., Saga 840-8502, Japan

³Department of Interdisciplinary Environment, Kyoto Univ., Kyoto 606-8501, Japan

⁴Department of Physics, Okayama Univ., Okayama 700-8530, Japan

⁵Department of Electrical & Electronic Engineering, Shinshu Univ., Nagano 380-8553, Japan

⁶Department of Advanced Materials Science, Kagawa Univ., Takamatsu 761-0396, Japan

Synchrotron radiation facilities and lasers are the most valuable scientific inventions of the 20th century. We have constructed a system for a combinational use of both the light sources at BL1B [1, 2] and applied it to the study of valence excitons of wide bandgap materials [3]. Furthermore, we performed two-photon excitation of core excitons in BaF₂, and the results of the experiments were published recently [4, 5]. In this paper, we present the summary of those works.

The combinational use of synchrotron radiation (SR) and laser light dates back to 1980s. N₂ and Nd:YAG lasers with repetition rates lower than 100 Hz were used in the early stages of experiments [6, 7]. For the purpose of efficient measurements, it is desirable that the laser pulses are synchronized completely with SR pulses. The development of a mode-locked laser enabled such experiments.

The aim of our two-photon absorption (TPA) measurement is to investigate unoccupied states in solids. The TPA is a powerful technique as well as inverse-photoemission measurement since its final state of the transition is restricted by the selection rules. In order to specify the final states, core electron excitation are advantageous to valence electron excitation, since core states are often flat in the *k*-space and have well-defined symmetry. The TPA is suitable for the measurement of high-angular momentum states such as *d* and *f* orbitals because

these states cannot be reached by dipole transitions from many core states, which consist of *s* and *p* orbitals.

We show the experimental setup in Fig. 1. The laser pulses are synchronized with SR pulses through electronic devices. The laser light propagates through an optical fiber to the port of measurement. We detected luminescence of the sample with use of a photomultiplier of the microchannel plate-type through the time-correlated single photon counting method. The laser light was turned on and off using an optical shutter. The output of the detector is accumulated in two MCAs: one works when the laser light is on and the other when the light is off. The difference is attributed to the signal due to TPA.

Figure 2 shows the TPA spectrum of BaF₂. The spin-orbit splittings of 4*f* and 6*p* states of Ba ions in BaF₂ were found to be 0.7 and 1.4 eV, respectively [4]. These values are well explained by the relativistic quantum theory. It tells that the spin-orbit splittings of hydrogen-like orbits specified (*n*, *l*) have the following expression,

$$\Delta_{n,l} \propto (n^3 l(l+1))^{-1}. \quad (1)$$

Expression (1) gives relative values of the splittings:

$$\Delta_{5p} : \Delta_{5d} : \Delta_{4f} : \Delta_{6p} \approx 3.0 : 1.0 : 1.0 : 1.7. \quad (2)$$

Since the splitting of 5*p* levels was obtained experimentally to be 2.2 eV [8], those of the other states are calculated with use of Eq. (2).

The calculated splitting of 5*d* states raises a query about the so far proposed interpretations of the reflectivity spectrum of 5*d*-core excitons in BaF₂. The

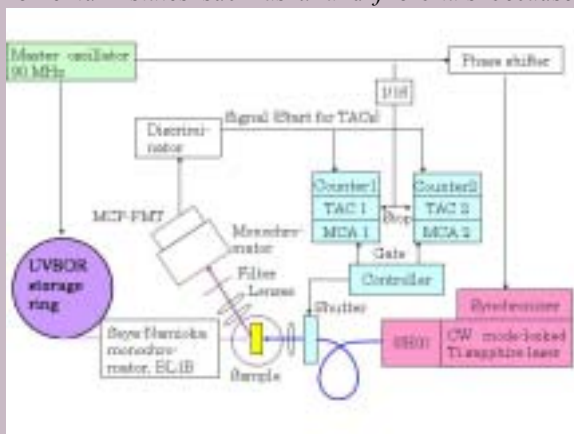


Fig. 1 The experimental setup of two-photon excitation with use of SR and laser. Luminescence from the sample is detected as the signal.

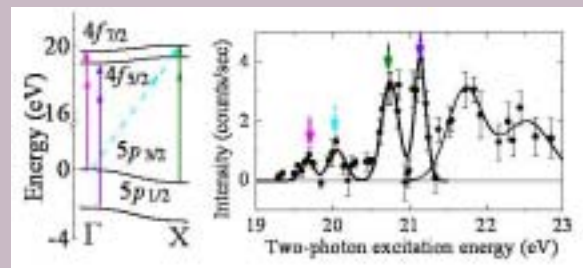


Fig. 2 The TPA spectrum of 4*f*- and 6*p*-core excitons in BaF₂. The energy diagram of 4*f* levels is depicted on the left. See Ref. 4 for the details.

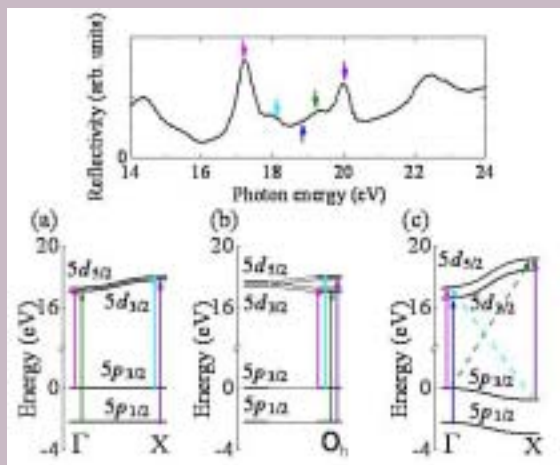


Fig. 3 Which is the true diagram? Schematic energy diagrams of $5d$ core excitons in BaF_2 based on different models are shown. The upper panel shows the reflectivity spectrum of the excitons. The $5p$ and $5d$ levels split due to spin-orbit interaction. The $p_{1/2}-d_{3/2}$ and $p_{3/2}-d_{5/2}$ transitions are allowed in electric dipole transitions. The origin of the multi peaks is attributed to the dispersion of the levels in (a) and (c), whereas to the crystal field effect in (b). The exciton binding energy is assumed to be constant and included in the diagrams above.

first precise measurement of the spectrum of BaF_2 in the core excitation region was reported in 1972 [9], and the interpretation of the peaks is schematically depicted in Fig. 3 (a). The splitting of $5d$ levels is obtained to be 0.2 eV. An alternative interpretation of the spectrum is possible [10]. Figure 3 (b) is based on a model where the crystal field splitting is assumed to be as large as 0.8 eV and dispersion of the states are not taken into consideration. The splitting of $5d$ levels is deduced to be the same as the former case, which value is inconsistent with Eq. (2).

The diagram of Fig. 3 (c) is based on a recent band calculation of energy levels [11]. It gives an interpretation consistent with Eq. (2).

Spectroscopic study of core excitons revealed the conduction band structure as described above. Besides static properties, dynamical behavior of core excitons was measured through the system depicted in Fig. 1. An example of temporal behavior of the signal luminescence is shown in Fig. 4. The lifetime of the two-photon excited $6p$ -exciton was obtained to be 0.2 ns [5].

The time resolution of the system is mainly determined by excitation pulse widths. As depicted in the upper panel of Fig. 4, the pulse width of SR was about 0.6 ns (under the single bunch operation), and that of the laser was 0.3 ns. The laser pulse expanded during the propagation through the 50-m long fiber. The laser pulse width can be shortened by shortening the length of the fiber. However, it should be noted that the shorter the pulse width is, the smaller the overlap with the SR pulse is. Consequently, the signal

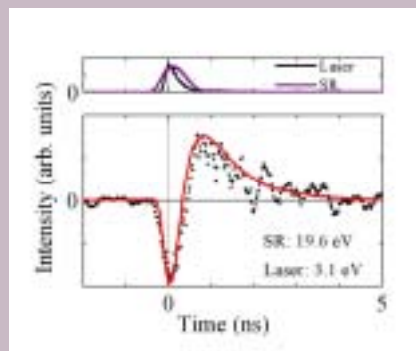


Fig. 4 Time-response of the signal of TPA. The output of the detector under excitation exclusively with SR is subtracted from that with both the SR and laser. The photon energy of SR is enough to excite a core electron to a $5d$ level. The dip can be interpreted that two-photon excited core excitons have a finite lifetime, which should be compared to the fast recombination of one-photon excited core electron. See Ref. 5 for the details.

becomes weaker. In order to secure sufficient intensity of the signal, the use of an undulator beamline may be indispensable, though sample damage should be carefully avoided.

In the present measuring system, TPA is detected by luminescence. Unfortunately, TPA is not always accompanied by characteristic luminescence, such as Auger-free luminescence of BaF_2 and other materials [12]. In order to study wide range of materials, a new technique that does not need such luminescence should be developed. Detecting reflectivity change might be a powerful technique in the future.

[1] T. Tsujibayashi *et al.*, UVSOR Activity Report 1996 (1997) 52.
 [2] S. Asaka *et al.*, Rev. Sci. Instrum. **69** (1998) 1931.
 [3] T. Tsujibayashi *et al.*, Phys. Rev. B **60** (1999) R8442
 [4] T. Tsujibayashi *et al.*, Phys. Rev. Lett. **94** (2005) 076401.
 [5] T. Tsujibayashi *et al.*, phys. stat. sol. (c) **2** (2005) 228.
 [6] V. Saile *et al.*, Phys. Lett. **79A** (1980) 221.
 [7] R. Pizzoferrato *et al.*, Europhys. Lett. **2** (1986) 571.
 [8] J. Reader and G.L. Epstein, J. Opt. Soc. Am. **65** (1975) 638.
 [9] G.W. Rubloff, Phys. Rev. B **5** (1972) 662.
 [10] M. Yuri *et al.*, J Phys. Soc. Jpn. **61** (1992) 2557.
 [11] H. Jiang *et al.*, J. Phys. Condens. Matter **15** (2003) 709.
 [12] M. Itoh, *Recent Research Developments in Physics Vol.4* (Transworld Research Network, Trivanduram, 2003) Chap. 11.

Time Resolved Decay Curves of AlGa_N and InAlGa_N Measured in the Wide Energy Range

S. Naoe¹, S. Hamada², K. Fukui², H. Hirayama³, H. Miyake⁴, K. Hiramatsu⁴

¹*Faculty of Engineering, Kanazawa University, Ishikawa 920-1192, Japan*

²*Research Center for Development of Far-Infrared Region, Fukui 910-8507, Japan*

³*The Institute of Physical and Chemical Research, Wako 351-0198, Japan*

⁴*Faculty of Engineering, Mie University, Mie 514-8507, Japan*

AlGa_N is the promising optical material having variable band gap energy by selecting a compositional rate of the elements. However, the intensity of emission in AlGa_N loses rapidly its intensity with increasing temperature, though InAlGa_N gives effective luminescence intensity at RT. The emission bands of those two alloy systems are basically similar. Both of them consist of two photoluminescence (PL) bands. One is B-band emission which is ultraviolet (UV) emission band due to exciton, and the other is visible (VIS) emission band caused by some defects or impurities (Y-band). Therefore, to investigate the precise emission process of III-V nitrides, the comparative studies of PL in between AlGa_N and InAlGa_N become important.

All samples are made by MOCVD (MOVPE) methods. The thickness of AlGa_N thin films is about 1 μm on 1 μm AlN single crystal film with sapphire substrates and that of InAlGa_N thin films is about 80 nm on SiC substrates with Al_{0.2}Ga_{0.8}N buffer layers. In our study, multi-bunch mode (15 full + 1 empty bunches, 11.1 ns period) of UVSOR is used as the usual stationary light source and single-bunch mode (177.7 ns period, ~ 0.5 ns width) as the pulse light source for time resolved measurement by using time correlated single photon counting method (TCSPC). Time resolved decay (TRD) measurements have been performed at BL7B, BL5B, BL8B1 and BL1A. Same conventional 30 cm monochromator via optical fiber is used to measure both PL spectra and TRD curves of all samples.

In our previous work, TRD results in band-to-band excitation (at BL7B) of both AlGa_N and InAlGa_N are analyzed by using the same model of three single exponential components linear combination model (decay time of the fast component is in less than sub-ns order, middle in ns, slow in 10 ns). The fast one is the main PL component at RT. Both middle and slow ones rapidly decrease with increasing temperature. Figs. 1 and 2 show B-band TRD curves at 26 K of Al_{0.54}Ga_{0.46}N and In_{0.05}Al_{0.20}Ga_{0.75}N, respectively. Excitation energies are 4.7 eV (BL7B), 95 eV (BL5B), 405 eV (BL8B1) and 1.56 keV (BL1A). The fast component of InAlGa_N TRD is much stronger than that of AlGa_N even at low temperature. This is one of the reasons that InAlGa_N is used as the active layer in UV-LED operated at RT. In the inner shell excitation, many electron-hole pairs are produced during the decay process of core hole

coming up to valence band (photon multiplication), and make recombination as both B- and Y-band PL. The behavior of three components of TRD in the inner shell excitation becomes the interesting study to analyze the emission mechanisms in AlGa_N. A rate of the fast component becomes to increase with increasing the excitation photon energy and to take the resembling curve to that of InAlGa_N gradually. This result suggests one possible model that the optical transition corresponding to the fast component in AlGa_N may be caused by direct overlap of the wave function between electron and hole states. The overlap of wave functions will occur in the situation of many electron-hole pairs gathering at the band edge. On the other hand, the fast component in InAlGa_N will be caused by the mixing of the allowed part of wave function by the effect of incorporation of In elements.

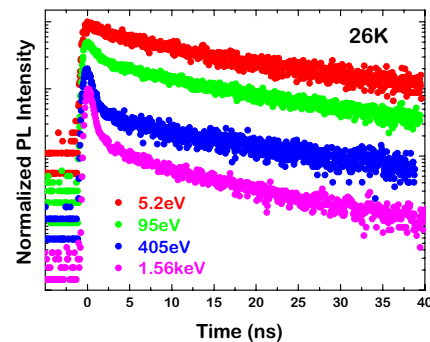


Fig. 1 Time resolved decay curves of Al_{0.54}Ga_{0.46}N at various excitation energies. Each spectrum is shifted vertically for convenience.

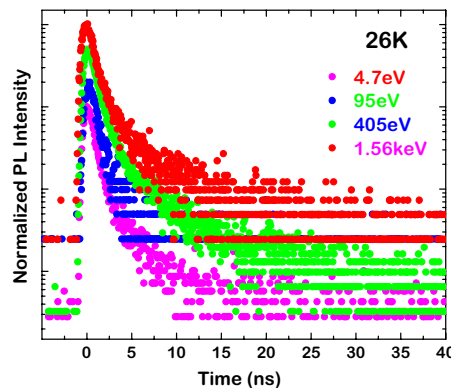


Fig. 2 Time resolved decay curves of In_{0.05}Al_{0.20}Ga_{0.75}N at various excitation energies. Each spectrum is shifted vertically for convenience.

XAFS Study on Silica Glasses Irradiated in Nuclear Reactor

T. Yoshida¹, T. Tanabe¹, H. Yoshida²

¹Department of Materials, Physics and Energy Engineering, Nagoya University, Furo-cho, Chikusa-ku, Nagoya 464-8603, Japan

²Department of Applied Chemistry, Graduate School of Engineering, Nagoya University, Nagoya 464-8603, Japan

Irradiation effects by high-energy particles such as neutron and ions on silica glasses are one of the main concerns for their application as optical windows, insulators and optical fibers in nuclear environments. The chemical states and density of defects in silica glasses should be closely related to their optical and physical properties such as the transparency and hardness. However, it is still difficult to observe the structures of the defects at an atomic scale in a SiO₂ glass, because the structural changes in its amorphous nature does not allow us to apply diffraction techniques. In the present work, we have investigated the change of the local structure of the SiO₂ glass before and after in-reactor (*i.e.*, neutron and γ -ray) irradiation by Si K-edge X-ray absorption fine structure.

Samples used in this work were a synthesized silica glass (T-4040) of 13 mm diameter and 2 mm thickness with OH content of 800 ppm. The samples were irradiated in the nuclear reactor YAYOI at the University of Tokyo. YAYOI was operated with a power of 1.5 kW, where a neutron flux was about 6×10^{11} n/m²s with an average neutron energy of 1.3 MeV and γ ray level was about 3.0 kGy/h.

Si K-edge X-ray absorption spectra were recorded under vacuum ($<10^{-6}$ Pa) at room temperature at BL7A and 1A station of UVSOR, or at BL11B station of Photon Factory, Institute of Materials Structure Science, High Energy Accelerator Research Organization (KEK-PF), using a two-crystal InSb(111) monochromator. Two different recording modes, *i.e.* a total electron yield (TEY) mode and a fluorescent X-ray yield (FY) mode were employed with detectors consisting of an electron multiplier and a gas-flow proportional counter, respectively.

Fig. 1 compares the radial structure functions (RSFs) obtained from Fourier transforms of the k-weighted Si K-edge EXAFS spectra of a synthesized silica glass before and after in-reactor irradiation together with that of a SiO₂ crystal (quartz) sample as a reference. We also performed curve-fitting analysis of the Fourier-filtered EXAFS by the least-squares method. In Fig. 1, the peaks in the region of 0.8-3.2 Å were isolated with a Hanning window, and inversely Fourier transformed. The curve-fitting analysis was carried out with Si-O and Si-Si shells. The curve-fitting results are summarized in Table 1.

The EXAFS spectra of the silica glasses irradiated with the low neutron fluence (less than ca. 1×10^{19} n/m²) were fundamentally the same as those of their unirradiated ones (not shown here). The structural

change was recognized in the EXAFS spectra of the silica glasses irradiated with more than 2×10^{19} n/m². In the RSFs, it should be noted that the peak intensity at 1.2 Å due to the Si-O bond increased to a level similar to that of the quartz crystal. Moreover, the coordination numbers of the first neighboring oxygen atoms increased from ca. 3.7 to ca. 4.3 after in-reactor irradiation (see Table 1). At the same time the coordination number of the second neighboring Si atoms decreased, *i.e.*, the Fourier-filtered EXAFS spectra of the irradiated silica glasses were not fitted well using a Si-Si shell. However, the curve-fitting using a Si-O shell instead of Si-Si shell was successful. The distance 2.92 Å thus evaluated corresponds to the path length of the multiple scattering for Si-O-O in the regular SiO₄ tetrahedron. These results suggest some decoupling of neighboring distorted SiO₄ tetrahedrons in a silica glass via the atomic displacement by neutron irradiation. Accordingly, the decoupled distorted SiO₄ tetrahedrons could be relaxed and return to regular or isolated SiO₄ tetrahedron and the O-Si-O angles would be more uniform after the irradiation, as observed in the growth of the peak assigned to Si-O in RSFs. This does not mean the recovery of long range orders (or recrystallization). The irradiation certainly gave more disorder in long range as the appearance of Si precipitates or each tetrahedron became more isolated.

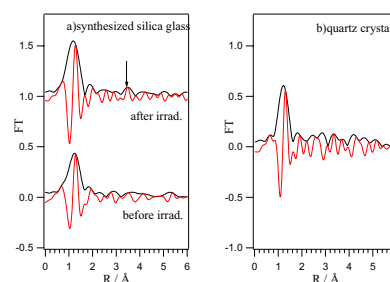


Fig. 1 Radial structural functions of k-weighted Si K-edge EXAFS spectra of (a) the synthesized silica glass before and after in-reactor irradiation, and (b) a quartz crystal. The neutron fluence of the irradiated synthesized silica glass is 2.7×10^{20} n/m².

Table 1 Results of curve-fitting analyses

Sample	Shell	coordination number	interatomic distance(Å)	$\Delta\sigma^2$ (Å ²)
Quartz	Si-O	4.0	1.61	0
	Si-Si	4.0	3.02	0.00285
Syn.silica (unirradiated)	Si-O	3.7	1.61	0.00269
	Si-Si	0.8	3.09	0.00332
Irrad. syn. silica (2.7×10^{20} n/m ²)	Si-O	4.3	1.60	0.00114
	Si-O	1.5	2.91	0.00150
	Si-Si ^{b)}	2.0	3.86	-0.00358

Two-Molecule Absorptions of Oxygen under High Pressure

Y. Akahama, T. Moriwaki, H. Kawamura

Department of Material Science, Graduate School of Material Science, 3-2-1 Kouto,
Kamigohri, Hyogo 678-1297 Japan

Introduction

The properties of condensed molecular oxygen have been of considerable interest for many years because of its simple and fundamental molecular magnetism. In order to understand the properties on the base of the electronic structure of the molecule, the study of electronic spectra is indispensable. Our recent studies on UV absorption spectra of condensed oxygen up to 13 GPa have revealed that a relatively strong absorption band was observed above 5 eV in super-critical fluid, and further the new UV band constructed the valence band of the β solid phase [1]. The results suggest that the intermolecular interaction plays a main role in the optical properties. Therefore, we concentrate our attention on the high-pressure behavior of two molecule absorptions.

Experimental

Liquid oxygen was loaded in the sample chamber of a sapphire or diamond-anvil pressure cell and the pressure was regulated at 300 K based on a ruby pressure scale. The typical thickness and diameter of the sample chamber were about 150 μm and 300 μm , respectively. UV absorption measurements were carried out over a range from 0.2 to 8 GPa using an UV source at the BL1B and 7B beam lines.

Results and Discussion

Figure 1 shows the absorption spectra of condensed oxygen at pressures up to 8 GPa and at 300 K. The absorption bands are due to two-molecule transitions of $2^3\Sigma_g^- \rightarrow 1^1\Sigma_g^+ + 1^1\Delta_g$ (0-0) and $2^1\Delta_g$ (0-0, 1-0, 2-0) and the values of wavelength of these bands are consistent with those in liquid phase at ambient pressure. The absorption intensity increases with pressure in the fluid phase. The behavior of the intensity is also consistent with the previous result in a pressure range up to 35 atoms [2]. Sudden increase in the intensity is observed above solidification pressure of 5.9 GPa. The increase in the intensity, which was correlated with the behavior of the UV absorption band at 5 eV, is suggestive of the enhancement of intermolecular interaction. The relatively weak absorption of the $2^3\Sigma_g^- \rightarrow 1^1\Sigma_g^+ + 1^1\Delta_g$ (0-0) transition could not be detected in the solid phase due to a strong absorption of diamond anvils.

Figure 2 shows the pressure dependence of the wavelengths of the two-molecule absorption bands. The wavelength of the $1^1\Sigma_g^+ + 1^1\Delta_g$ (0-0) band is independent of pressure while those of $2^1\Delta_g$ (0-0, 1-0, 2-0) bands show a blue shift. From these spectra data, we could estimate the pressure dependence of the

energy of excited states $1^1\Sigma_g^+$ and $1^1\Delta_g$ from the ground state. As the results, the energy of $1^1\Delta_g$ rose with increasing pressure. On the contrary, the energy of $1^1\Sigma_g^+$ fell down. This pressure behavior of $1^1\Sigma_g^+$ supports recent results of molecular dynamic simulations [3], in which an insulator to semi-metal transition has been suggested by overlapping between the excited state and the ground state indirectly in the momentum space.

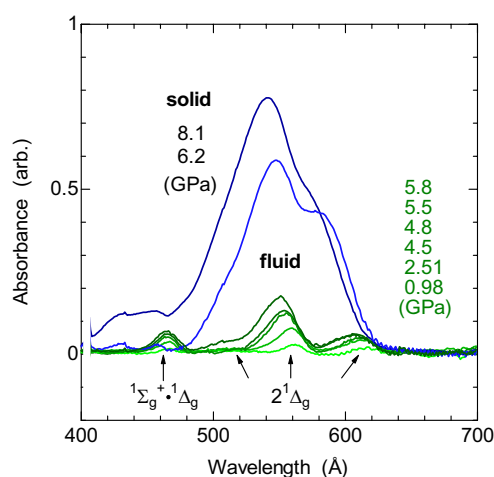


Fig. 1 Two-molecule absorption spectra at various pressure at 300 K.

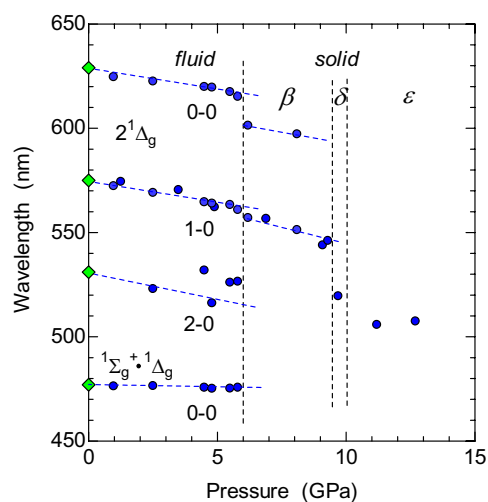


Fig. 2 Pressure dependence of the wavelengths of two-molecule absorption bands.

- [1] Y. Akahama and H. Kawamura, Chem. Phys. Lett. **392** (2004) 467.
 [2] V. I. Dianov-Klokov, Opt. Spectrosc. (USSR) **16** (1964) 224.
 [3] S. Serra *et al.*, Phys. Rev. Lett. **80** (1998) 5160.

VUV Reflectivity Spectra of CaMoO_4 and CaWO_4 Crystals

M. Fujita¹, S. Takagi², N. Fujita², T. Shimizu², M. Itoh²

¹Japan Coast Guard Academy, Wakaba, Kure 737-8512 Japan

²Department of Electrical and Electronic Engineering, Shinshu University, Nagano 380-8553 Japan

Tungstate family such as CaWO_4 and PbWO_4 is known as an intrinsic scintillation material. Recently, molybdate crystals attract much attention in the field of astro-particle physics for the detection of weakly interacting massive particles. Although extensive studies have been reported on the luminescence properties, reliable optical constants have not been established for most of tungstate and molybdate compounds. In a recent study we measured optical anisotropy of scheelite PbWO_4 crystals in detail and confirmed important contribution of Pb states to the electronic structures at the band edge [1].

The present paper reports anisotropic optical properties of CaMoO_4 and CaWO_4 as typical crystals of alkaline-earth metal molybdate and tungstate with scheelite-type structure.

Experiment

Reflectivity spectra were measured for polished surfaces of CaMoO_4 and CaWO_4 single crystals, with use of the polarized light parallel to the a-axis (E//a) and c-axis (E//c). The orientation of crystal axis was determined by means of a pair of crossed polarizer.

Results and Discussion

Figure 1 shows reflectivity spectra of CaMoO_4 and CaWO_4 at 8 K. Close similarity is observed between the spectra in Fig. 1(a) and (b). The structures in Fig. 1 are classified into three groups according to the line shape and polarization dependence. In contrast to the exciton band in PbWO_4 [1], the lowest band 1 in CaMoO_4 and CaWO_4 is broad. The width of the band 1 for E//a is larger than that for E//c for both materials. In the region 2, the dichroism is seen distinctly.

The energy positions of the main structures in Fig. 1 agree, as a whole, with those of previous studies [2-4], but there exists serious disagreement among their relative intensities. We confirmed the data reproducibility by measuring the reflectivity spectra on a cleaved surface of CaWO_4 crystal; the obtained result was almost the same as Fig. 1(b).

According to a theoretical calculation of the electronic structures of CaMoO_4 and CaWO_4 [5], the valence band is mainly built up of the O $2p$ state and the conduction band is composed of the Mo $4d$ (W $5d$) state. The molecular orbitals at the top of the valence band and the bottom of the conduction band are of t_1 and e symmetry, respectively, in MoO_4 (WO_4) oxyanion complex of T_d symmetry. Both the t_1 and e states split into two sublevels in the S_4 symmetry of scheelite crystal. The polarization dependence of the width of the band 1 would be attributed to the

splittings of the t_1 state and the e state due to the crystal-field potential of S_4 symmetry.

The structures in the region 2 are assigned to the transition from the top of the valence band to the next higher conduction band of t_2 symmetry, which is mainly made of the Mo $4d$ (W $5d$) state with some hybridization of the Ca $3d$ state.

The optical transition in the region 3 is supposed to include the excitation from the valence band to the conduction band of Ca $3d$ state.

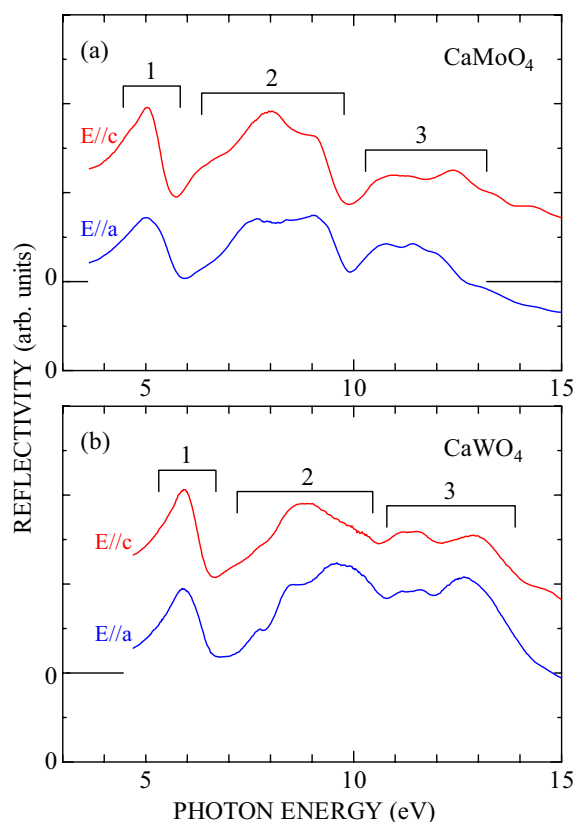


Fig. 1 Reflectivity spectra of (a) CaMoO_4 and (b) CaWO_4 at 8 K.

- [1] M. Fujita *et al.*, Phys. Rev. B **65** (2002) 195105.
- [2] R. Grasser *et al.*, Phys. Stat. Sol. (b) **69** (1975) 359.
- [3] I. A. Kamenskikh *et al.*, Nucl. Instrum. Methods Phys. Res. A **470** (2001) 270.
- [4] V. B. Mikhailik *et al.*, Phys. Stat. Sol. (b) **242** (2005) R17.
- [5] Y. Zhang *et al.*, Phys. Rev. B **57** (1998) 12738.

Characterization of Partial Discharge Degradation of Polyamide-6 Nanocomposites by a Photoluminescence Analysis

N. Fuse¹, M. Kozako^{2,3}, T. Tanaka², Y. Ohki¹

¹Department of EEBS, Waseda University, Shinjuku 169-8555, Japan

²Graduate School of IPS, Waseda University, Kita-Kyushu 808-0135, Japan

³Kagoshima National College of Technology, Aira 899-5193, Japan

Polymer nanocomposites have been attracting much attention as new materials that have high potential for wide applications. Therefore, we have been examining the dielectric properties of polyamide nanocomposites, focusing especially on their resistance against partial discharges (PDs).

Experimental

The samples investigated are polyamide-6 nanocomposite with 5 wt% mica nanofillers (NC-5) and polyamide-6 without nanofillers (PA). They are of a sheet shape 60 mm × 60 mm × 1 mm. Using the IEC (b) electrode system, which consists of a rod and a plane stainless steel electrode, ac 60-Hz high voltage was applied to the sample for 48 hours.

Using synchrotron radiation (SR) under multi-bunch operation at the BL1B line of UVSOR Facility (Institute of Molecular Science, Okazaki, Japan, beam energy: 750 MeV) as a photon source, photoluminescence (PL) spectra from the sample before and after degradation by PDs were measured. The PL decay characteristics were measured by a single photon counting method using SR under single-bunch operation (SR duration: 0.55 ns, interval: 177 ns). Furthermore, the crystalline structure was observed by X-ray diffraction spectroscopy (XRD).

Results and Discussion

In our previous work, surface observation using an atomic force microscope shows superiority in PD resistance of NC-5 to PA [1]. Fig. 1 shows PL spectra excited by SR photons at 5.2 eV, before and after degradation by PDs. Note that the PL intensities are normalized by the height of the PL peak around 4.3 eV. The spectral shape of the rather broad PL peak around 3.0 eV differs between the samples before and after the PDs, and the difference is much clearer in PA. The decay profiles of the 3.0 eV PLs observed in NC-5 and PA before and after the PD degradation agree with the profile of an apparently similar PL peak at 3.0 eV observed in polyethylene irradiated by an ArF excimer laser. Since the PL in polyethylene originates from polyenes induced in the degradation process [2], the PLs observed in NC-5 and PA should similarly originate from polyenes. The result shown in Fig. 1 indicates that the number of polyenes induced by the PD degradation is suppressed by the effect of nanofillers. Fig. 2 shows XRD spectra obtained for NC-5 before and after the degradation by PDs. Curve (a) shows a diffraction peak around 9.5°, which

indicates that Na⁺ ions are present in the inter-layer regions [3]. When NC-5 was degraded by PDs, a new peak appears around 8.5° as shown in curve (b). This result suggests that the nanofillers were rearranged and piled up in parallel with their surfaces with a mutual distance around 1.0 nm. Such layered structures seem to contribute to the high durability against PDs of NC-5.

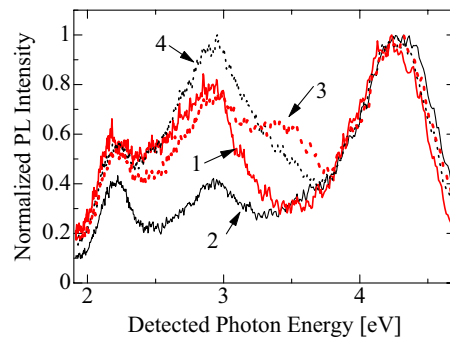


Fig. 1 PL spectra excited by SR photons at 5.2 eV. Curve 1: NC-5 before degradation, 2: PA before degradation, 3: NC-5 after degradation by PDs, 4: PA after degradation by PDs.

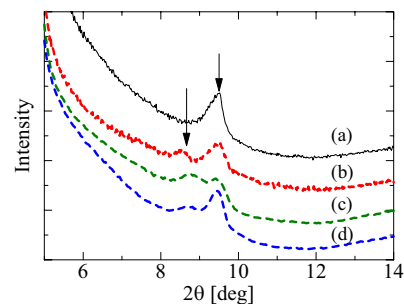


Fig. 2 XRD spectra of NC-5 before degradation (a), degraded by PDs (b), degraded by an active plasma (c), and degraded by a weak plasma (d). Since the volume of the sample differed among the samples, the intensity cannot be directly compared.

[1] M. Kozako *et al.*, IEEE Trans. Dielectr. Electr. Insul., Vol. **11**, No. 5 (2004) 833.

[2] T. Ito *et al.*, IEEEJ Trans. FM, Vol. **124**, No. 7 (2004) 624.

[3] K. Yasue *et al.*, Japan Plastics, Vol. **47**, No. 6 (1996) 100 (in Japanese).

Luminescence Properties of Tl^+ Centers Doped in KH_2PO_4

T. Fuyuki, N. Ohno

*Division of Electronics and Applied Physics, Graduate School of Engineering
Osaka Electro-Communication University, Neyagawa, Osaka 572-8530, Japan.*

Ferroelectric material potassium dihydrogen phosphate KH_2PO_4 (KDP) single crystals containing a small amount of thallium ions Tl^+ exhibit five characteristic polarized absorption bands A_z , A_{xy} , B_{xy} , and C_z in the ultraviolet region [1,2]. Symmetry of the local crystal field at Tl^+ ion which replaces the potassium ion is approximately S_4 in the ferroelectric phase. The observed experimental results have been qualitatively explained by taking into account the spin-orbit, crystal-field and electronic-vibrational interactions [3].

In the present study, photoluminescence and photo-excitation spectra of $KDP:Tl^+$ have been investigated at the BL1B station at the UVSOR facility. The optical measurements of $CDP:Tl^+$ have been also carried out. Single crystals of KDP and CDP containing ~ 0.02 mol% Tl^+ ions were grown by slowly cooling a saturated aqueous solution at about $60^\circ C$ after several times of recrystallization.

Figure 1 shows the luminescence (green solid curve) and the excitation spectra (blue and red solid curves) of $KDP:Tl^+$ measured at 12 K. The broken curve in the figure is the absorption-edge spectrum of an undoped KDP for comparison [4]. A broad luminescence band excited with 5.66 eV photons is observed at 4.50 eV, showing a Gaussian lineshape and a large Stokes shift. The excitation spectra for the 4.50 eV band for polarization $E//c$ and $E \perp c$ are depicted by blue and red solid curves, respectively. It is found that the 4.50 eV band is induced under the excitation of the A , B and C absorption bands associated with impurity Tl^+ ions [2,3]. The present excitation spectra of the 4.50 eV band indicate that the 4.50 eV is originated from the relaxed excited states of the Tl^+ ion.

Figure 2 shows the 4.50 eV luminescence spectra at temperatures between 12 and 300 K. The excitation was made with 5.66 eV photons (A band excitation). The luminescence spectra exhibit a drastic change at the ferroelectric transition temperature $T_C = 123$ K; the peak energy shows a high-energy shift with increasing temperature at $T \leq T_C$, and then an abrupt low-energy shift above T_C . The bandwidth has also been changed drastically at T_C . These results indicate clearly that the relaxed excited electronic states of the Tl^+ ions are strongly influenced by the ferroelectric local field due to surrounding ligand ions.

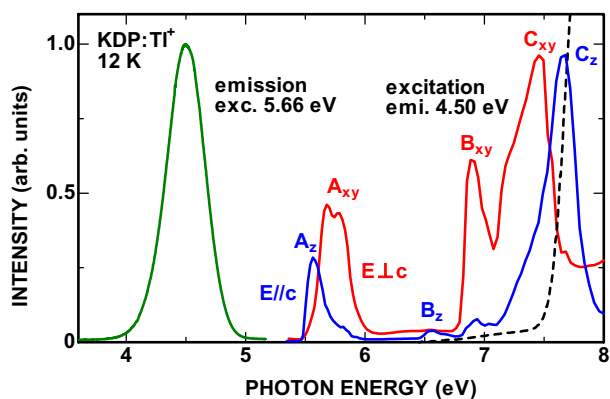


Fig. 1 Luminescence (green), excitation of the 4.50 eV band (blue and red) and absorption (broken) spectra of $KDP:Tl^+$ measured at 12 K.

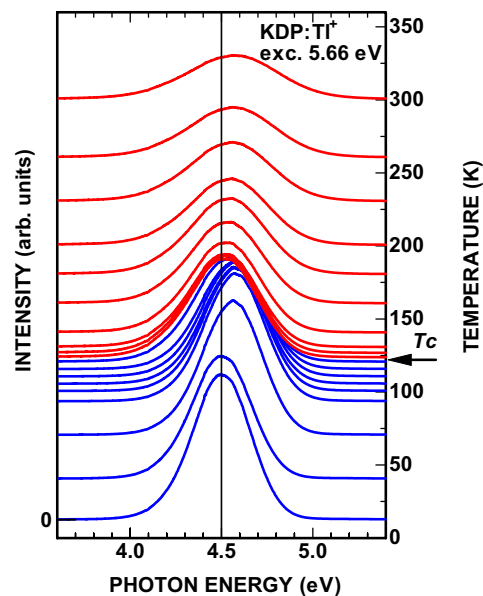


Fig. 2 Temperature dependence of the 4.50 eV luminescence spectra of $KDP:Tl^+$ at 12 to 300 K.

- [1] I. Fujita, J. Phys. Soc. Jpn. **44** (1078) 275.
- [2] I. Fujita, J. Phys. Soc. Jpn. **46** (1079) 1889.
- [3] I. Fujita, Phys. Rev. B **49** (1994) 6462.
- [4] T. Fuyuki and N. Ohno, UVSOR Activity Report 2003 (2004) 51.

Luminescence of Bi³⁺ Ions Doped in NaYF₄

T. Hirai¹, K. Chong¹, N. Ohno¹, T. Kawai², S. Hashimoto²

¹Graduate School of Engineering, Osaka Electro-Communication University, Neyagawa
572-8530 Japan

²Faculty of Science, Osaka Women's University, Sakai 590-0035 Japan

Xe dimer (Xe₂) discharge fluorescent lamps have recently attracted much attention as alternative lighting devices to conventional Hg discharge fluorescent lamps. The Xe₂ discharge generates vacuum ultraviolet (VUV) light peaking at around 172 nm. For the practical use of Xe₂ discharge fluorescent lamps, it is necessary to develop new phosphors that convert the VUV light efficiently into blue, green and red light.

Oxide phosphors have been used in the Hg discharge fluorescent lamps. In most of the oxide phosphors, the VUV light below 200 nm is little absorbed by the activators because of the absorption of the oxide hosts, so that the conversion of the VUV light is unlikely to be efficient. Most fluoride hosts, by contrast, are transparent down to ~150 nm. Thus, we expect that the fluoride phosphors are suitable for use in the Xe₂ discharge fluorescent lamps, because the VUV light generated by Xe₂ discharge (~172 nm) can directly excite the activators.

Several groups have extensively studied electronic transitions in rare earth ions doped into fluorides [1]. Some of the rare earth ions such as Eu³⁺ show absorption due to $f^n \rightarrow f^n$ ($f-f$) transitions in the VUV spectral region (150–200 nm). Since the absorption due to the parity-forbidden $f-f$ transitions is weak, the conversion of the VUV light by those rare earth ions is probably inefficient.

Metal ions with s^2 electronic configurations in insulating hosts, called TI⁺-type impurity ions, exhibit strong absorption due to parity-allowed $s^2 \rightarrow sp$ transitions at the longer wavelength side of the host absorption. The strong absorption by TI⁺-type ions may lead to efficient conversion of the VUV light. However, TI⁺-type ions in fluoride hosts have been less investigated so far.

In the present study, we have investigated luminescence and excitation spectra of Bi³⁺ ions doped in NaYF₄ by using synchrotron radiation at the BL1B of the UVSOR facility. The Bi³⁺ ions are trivalent TI⁺-type ions that easily substitute for Y³⁺ ions in NaYF₄.

The right-hand side of Fig. 1 (350–600 nm) shows the luminescence spectrum of NaYF₄:Bi³⁺ excited at 172 nm at room temperature. One can see a broad luminescence band peaking at ~430 nm. This luminescence band is attributed to the radiative transitions from the relaxed excited states (³P₁) to the ground state (¹S₀) in Bi³⁺ ions. On the left-hand side of Fig. 1 (100–350 nm), the excitation spectrum for the luminescence band at 430 nm is shown. Several excitation bands are observed at around 300, 250 and

200 nm. These excitation bands should arise from the transition from the ground state to some excited states given by the sp electronic configuration.

It is well known that TI⁺-type ions doped in alkali halide crystals with NaCl-type structure show three absorption bands originating from the intra-ionic transitions: A, B and C bands, named in sequence of decreasing wavelength. The A, B and C bands have been assigned to the transition to ³P₁, ³P₀ and ¹P₁ states, respectively. In Bi³⁺ ions doped in Cs₂NaYCl₆, A and C bands have been observed at ~320 and 220 nm [2]. In Bi³⁺ ions in fluoride hosts, those absorption bands would shift toward the shorter wavelength side, as compared to those in chloride hosts. Accordingly, we can attribute the excitation bands at 300 and 200 nm to A and C bands. However, the origin of the strongest excitation band at 250 nm is unclear at present. Further experiments are needed to clarify the origin. Finally, it should be noted that NaYF₄:Bi³⁺ absorbs the VUV light generated by Xe₂ discharge (~172 nm) due to the electric dipole allowed ¹S₀ → ¹P₁ transition (C absorption), and yields the blue luminescence (~430 nm).

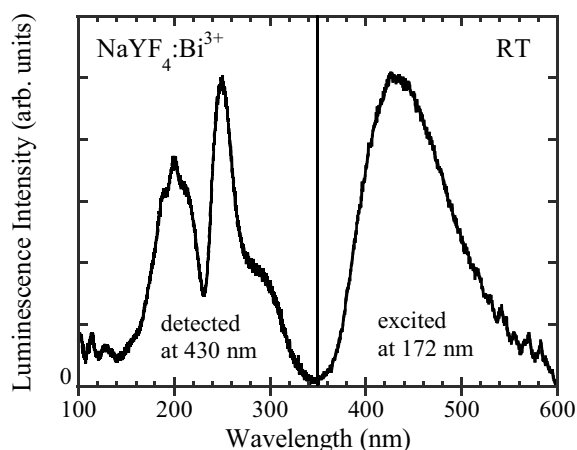


Fig. 1 Excitation (left) and luminescence (right) spectra of NaYF₄:Bi³⁺ at room temperature.

[1] R. T. Wegh, A. Meijerink, R.-J. Lamminmäki, J. Hölsä, J. Lumin. **87-89** (2000) 1002.

[2] A. C. van der Steen, phys. stat. sol. (b) **100** (1980) 603.

Detection of Host-Guest Complexation at the Water Surface by Photoionization Measurements

T. Ishioka, A. Harata

*Department of Molecular and Material Sciences, Kyushu University, Kasugakoen 6-1,
Kasuga-shi, Fukuoka 816-8680, Japan*

Photocurrent has been measured at an ionophore-modified water surface by synchrotron radiation. Lower shift of photoionization threshold was observed when guest anion (phosphoric acid) was present in the aqueous solution. It is suggested that host-guest complex is formed at the water surface by hydrogen bondings.

Introduction

Threshold energy measurements of photoionization at the water surface give useful information on electric states and structures of adsorbed species [1]. Photoionization by SR light is convenient for measuring precise threshold energy by its inherent tunability in photon energy. However, it has not been fully applied to the analysis of surface reactions such as host-guest complexation at the water surface.

Host-guest complexation by hydrogen bonding is essential for molecular recognition in biological systems and it is known that interfaces plays important roles in enhancing such interactions. Air/water interface is one of such interfaces and specific hydrophobic nature has been reported by various spectroscopic measurements such as sum-frequency generation.

In this report, neutral ionophore for dihydrogen-phosphate ion is spread on anion-containing water surface and measure threshold energies for analyzing host-guest interaction that is too weak to be measured in bulk aqueous solutions.

Experimental

The monochromated synchrotron light (4-8 eV) was obtained from BL1B at the UVSOR facility and emitted from the chamber to a He-purged cell through an MgF₂ window. The emitted light was reflected on an Al mirror and vertically irradiated on the aqueous solution surface through a Cu-mesh electrode. The electrode was set at 5 mm high above the liquid surface and high voltage (500 V) was applied. The photocurrent (~ 100 fA) was measured by a picoammeter.

An ionophore optimized for dihydrogenphosphate recognition (Fig. 1) was synthesized from 2-aminoanthraquinone and dissolved in benzene at 0.2 mM. The benzene solution was spread by 10 μ L on the surface of aqueous solutions containing 0.1 M anion species as acid solutions.

Results and Discussion

Used ionophore shows 1:1 complexation with dihydrogenphosphate in acetonitrile and its binding

constant is estimated to be 14,000 M⁻¹ by UV-VIS absorption measurements while the ionophore does not show any complexation in aqueous solutions. The difference by solvents can be explained by inhibition of host-guest complexation by hydrogen bonds with water molecules.

Photoionization threshold of the ionophore at the water surface depends which anion species is present in the bulk solution (Table 1). Compared to perchlorate and sulfate, lower shift of photoionization threshold was observed when chloride and phosphate in the solution. The trend coincides with the general affinity of anions by hydrogen bondings that is evaluated to ClO₄⁻ < NO₃⁻ < Cl⁻ < H₂PO₄⁻. These results suggest that hydrogen-bonded complex is formed at the water surface.

Photoionization threshold is known to relate with standard electrochemical potential of the molecule. If we assume that the state of molecular polarization by surrounding molecules does not largely change by complexation and the difference is regarded as constant value at the water surface, the complexation constant can be evaluated by the shift of photoionization threshold. The shift of threshold energy for the complex with dihydrogenphosphate is 0.13 eV lower than the value of perchlorate and the binding constant for the ionophore in radical cation form is estimated 160 times larger than its neutral form. The enhancement factor coincides with the value in acetonitrile and the molecular environment at the water surface resembles in acetonitrile.

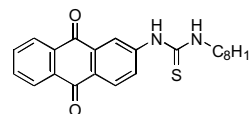


Fig. 1 Structure of synthesized ionophore for dihydrogenphosphate recognition.

Table 1 Measured threshold energy of the ionophore at the water surface with 0.1 M anion species in solution.

Solute	Threshold energy / eV
None	6.03
HClO ₄	6.12
H ₂ SO ₄	6.13
HNO ₃	6.08
HCl	6.04
H ₃ PO ₄	5.99

[1] T. Ishioka, A. Harata, UVSOR Activity Report 2003 (2004) 62.

Surface-Sensitive Variation of Reflection Spectra of ZnWO₄ in the Exciton Band Region

M. Itoh¹, N. Fujita¹, S. Takagi¹, T. Shimizu¹, M. Fujita², S. Oishi¹

¹Faculty of Engineering, Shinshu University, Wakasato, Nagano 380-8553

²Japan Coast Guard Academy, Wakaba, Kure 737-8512

As is well known, reflection spectra are very sensitive to the surface condition of samples. Zinc tungstate (ZnWO₄) is not exceptional. To our knowledge, its reflection spectrum was first measured in 1999 [1]. Since then, two research groups have reported the reflection spectra of ZnWO₄ [2-4]. However, there are some serious discrepancies among their results.

We have continued reflection measurements of ZnWO₄ at every opportunity for the past five years. The results obtained during this period are reported in the present paper.

Experiment

ZnWO₄ has the wolframite structure (*P2/c*). All the measurements were carried out for oriented crystals at 6 K. The SR light was incident on the (010) face with the electric vector parallel to the crystal *c*-axis.

Results and Discussion

Figure 1 shows three reflection spectra of ZnWO₄ in the 3-10 eV range. The spectrum (a) was measured for an as-grown surface of the crystal obtained from Dr. Alov (Russia). This spectrum resembles those of Refs. [1,2]. The spectrum (b) was measured for an as-grown surface of the crystal grown by the flux method. The curve (c) was recorded from the same surface as that of (b) two years later, in substantial agreement with the result of Ref. [3]. One may see clear discrepancy and change among the spectra (a), (b) and (c).

The crystal used for the measurement of (c) in Fig. 1 was freshly cleaved in the air. The reflection spectrum of the cleaved surface is shown by the solid curve in Fig. 2, along with the transmission spectrum (broken curve). This reflection spectrum is similar to that of Ref. [4], although fine structures are more clearly seen here. We believe that the result of Fig. 2 is the most reliable one.

In the tungstates, the valence band is mainly built of the O *2p* state and the conduction band is composed of the W *5d* state. In Fig. 2, a clear peak at 4.37 eV is reasonably attributed to the lowest exciton band originating in the cationic transition, because of the sharpness and

narrowness. This fact indicates that the Zn *3d* and Zn *4p* states contribute, to some extent, to the top of the valence band and the bottom of the conduction band, respectively. Similar hybridization of the electronic states between metal and WO₄²⁻ ions has been confirmed experimentally for PbWO₄ [5]. The broad band(s) at around 6.0 eV is commonly observed in the tungstates and is assigned to the O *2p*→W *5d* transition.

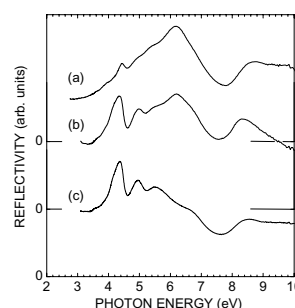


Fig. 1 Reflection spectra of ZnWO₄ crystals with different surface condition.

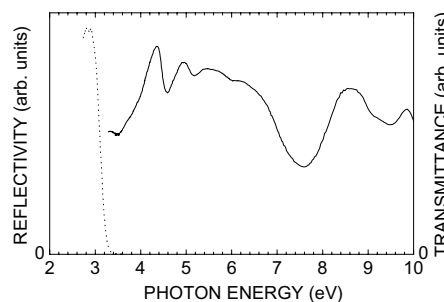


Fig. 2 Reflection (solid) and transmission (broken) spectra of a freshly cleaved surface of ZnWO₄ crystal.

[1] M. Itoh *et al.*, UVSOR Activity Report 1999 (2000) 72.

[2] V. N. Kolobanov *et al.*, SCINT99, Moscow State Univ. (2000) 648.

[3] V. N. Kolobanov *et al.*, Nucl. Instrum. Methods Phys. Res. A **486** (2002) 495.

[4] V. Nagirnyi *et al.*, Nucl. Instrum. Methods Phys. Res. A **486** (2002) 395.

[5] M. Fujita *et al.*, Phys. Rev. B **65** (2002) 195105.

Photoluminescence of Hydroxyapatite Irradiated by Ultraviolet Synchrotron Orbital Radiation Light

M. Ohta

Department of Material Science and Technology, Faculty of Engineering, Niigata University,
8050 Ikarashi 2-no-cho, Niigata 950-2181, Japan

Rare earth is used in various materials around us until now, for example phosphors, magnetic materials, catalyst, optical glass, and so on. Recently, rare earth is also useful as a contrast medium for magnetic resonance imaging, restriction enzyme, biocatalyst, and so on in fields of biochemistry, physiology, medicine, etc. However, the behavior of rare earth in the living body system remains an open question until now. It was known that rare earth ions dosed for oral administration to mouse and rat are transferred to blood vessel through the ileum and deposited its teeth and bone, which mainly consists of hydroxyapatite ($\text{Ca}_{10}(\text{PO}_4)_6(\text{OH})_2$) [1-2]. We have found that Eu ion substituted Ba ion in Eu doped $\text{Ba}_{10}(\text{PO}_4)_6\text{Cl}_2$ phosphor, which matrix is apatite structure [3]. In this study, rare earth ion-doped hydroxyapatite samples were prepared in order to make clear the segregation mechanism of rare earth ion on teeth and bone. Their characteristics were investigated by photoluminescent property of rare earth ion-doped hydroxyapatite samples excited by ultraviolet synchrotron orbital radiation light.

Gd-doped hydroxyapatite and Yb-doped hydroxyapatite samples were prepared as follows: hydroxyapatite was soaked in GdCl_3 or YbCl_3 aqueous solution. After 72 hr, Gd-doped or Yb-doped hydroxyapatite was separated from GdCl_3 or YbCl_3 aqueous solution by filtration and then dried by using with infrared ray. The photoluminescent property of each sample excited by ultraviolet synchrotron orbital radiation light (BL1B) was detected by using with a multi-channel analyzer.

Figure 1 shows photoluminescence spectra of rare earth ion-doped hydroxyapatite samples excited by BL1B. The photoluminescent spectra of rare earth ion-doped hydroxyapatite excited by 100 nm or 150 nm had many peaks which were not ascribed to rare earth ion. These facts indicate the traps of electron and/or hole due to the defects of crystal structure exists in rare earth ion-doped hydroxyapatite, since the photoluminescent property is similar to that of self doped phosphors.

The photoluminescent spectra of Yb-doped hydroxyapatite excited by 200 nm or 250 nm had a broad peak due to charge transfer state (CTS) $\rightarrow {}^2F_{2/5}$ of Yb^{3+} [4] or due to $4f^{13}5d^1 \rightarrow 4f^{14}$ of Yb^{2+} [5]. On the other hand, that of Gd-doped one are thought to have not a peak due to Gd^{3+} . These facts indicate the existence of Yb^{3+} or Yb^{2+} as a lattice ion.

When hydroxyapatite particles were soaked in GdCl_3 or YbCl_3 aqueous solution, the amount of Gd ion deposited on the surface of hydroxyapatite

particles was less than that of Yb ion. Therefore, the existence of Gd^{3+} as a lattice ion cannot be confirmed from this experiment.

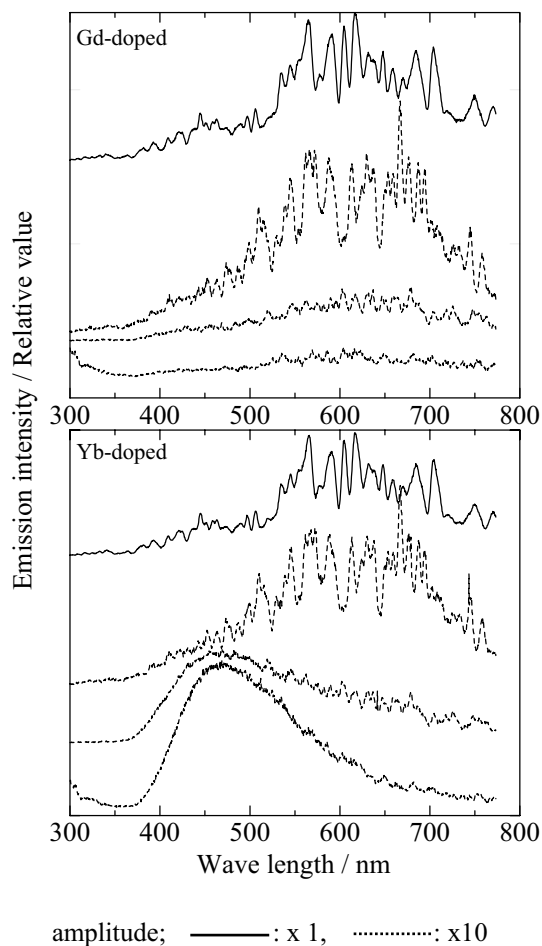


Fig. 1 Photoluminescent spectra of rare earth ion-doped hydroxyapatite samples excited by ultraviolet synchrotron orbital radiation light.

[1] S. Hirano, K. T. Suzuki, Environ. Health Perspect. **104** (Supplement 1) (1996) 85.

[2] K. Kostial, B. Kargacin, M. Lendeka, Int. J. Radiat. Biol. Relat. Stud. Phys. Chem. Med. **51** (1987) 139.

[3] M. Sato, T. Tanaka, M. Ohta, J. Electrochem. Soc. **141** (1994) 1851.

[4] F. C. Palilla, B. E. O'Reilly, V. J. Abbruscato, J. Electrochem. Soc. **117** (1970) 87.

[5] E. Nakazawa, J. Lumin. **18/19** (1979).

Band-Structure Design of Fluoride Complex Materials for Deep Ultraviolet Light Emitting Diode

R. E. Ouenzerfi¹, A. Quema¹, H. Murakami¹, S. Ono¹, N. Sarukura¹, T. Nishimatsu², N. Terakubo², H. Mizuseki², Y. Kawazoe², A. Yoshikawa², T. Fukuda²

¹ Institute for Molecular Science, Okazaki 444-8585 Japan

² Tohoku University, Aoba-ku, Sendai 980-8577, Japan

There had been continuous efforts for the development of wide-gap solid-state optical devices in the short wavelength region over these two decades. The operating wavelength is basically limited by the band gap of materials and is controlled by selecting the composition of complex materials. From this viewpoint, the most prominent candidates are fluorides. The main advantage of fluorides is their wide band gaps. Additionally, fluorides have wide-selection of complex materials, and are possible to select the band structure, band gap and lattice constant as predicted by Nishimatsu *et al.*

To determine the $\text{Li}_{(1-x)}\text{K}_x\text{Ba}_{(1-y)}\text{Mg}_y\text{F}_3$ composition suitable for the design of either a light emitting diode or a laser diode; the energy gap, band structure and the lattice constants of perovskite LiBaF_3 , LiMgF_3 , KBaF_3 and KMgF_3 are needed. Band gap energy and band structure are determined by *ab initio* calculation within the local density approximation (LDA) as reported by Nishimatsu *et al.* [1]. The variation of both band gap energy and lattice constant as a function of the composition is investigated in analogy with a previous work on semiconductor compound lasers reported by Sasaki *et al.* This study is performed as in the case of Thompson and Woolley's work for mixed semiconductors. For $\text{Li}_{(1-x)}\text{K}_x\text{Ba}_{(1-y)}\text{Mg}_y\text{F}_3$ Perovskite fluoride, the band gap energy can be written as follows :

$$E_{\text{Li}_{(1-x)}\text{K}_x\text{Ba}_{(1-y)}\text{Mg}_y\text{F}_3}^{\Gamma,\text{R},\Delta} = E_{\text{Li}_{(1-x)}\text{K}_x\text{MgF}_3}^{\Gamma,\text{R},\Delta} y + E_{\text{Li}_{(1-x)}\text{K}_x\text{BaF}_3}^{\Gamma,\text{R},\Delta} (1-y) - \frac{\alpha_{\text{Li}_{(1-x)}\text{K}_x\text{Ba}_{(1-y)}\text{Mg}_y\text{F}_3}}{\sqrt{\frac{E_{\text{Li}_{(1-x)}\text{K}_x\text{MgF}_3}^{\Gamma,\text{R},\Delta} + E_{\text{Li}_{(1-x)}\text{K}_x\text{BaF}_3}^{\Gamma,\text{R},\Delta}}{2}}} y(1-y)$$

where

$$E_{\text{Li}_{(1-x)}\text{K}_x\text{BaF}_3}^{\Gamma,\text{R},\Delta} = E_{\text{KBaF}_3}^{\Gamma,\text{R},\Delta} x + E_{\text{LiBaF}_3}^{\Gamma,\text{R},\Delta} (1-x) - \frac{\alpha_{\text{Li}_{(1-x)}\text{K}_x\text{BaF}_3}}{\sqrt{\frac{E_{\text{KBaF}_3}^{\Gamma,\text{R},\Delta} + E_{\text{LiBaF}_3}^{\Gamma,\text{R},\Delta}}{2}}} x(1-x)$$

$$E_{\text{Li}_{(1-x)}\text{K}_x\text{MgF}_3}^{\Gamma,\text{R},\Delta} = E_{\text{KMgF}_3}^{\Gamma,\text{R},\Delta} x + E_{\text{LiMgF}_3}^{\Gamma,\text{R},\Delta} (1-x) - \frac{\alpha_{\text{Li}_{(1-x)}\text{K}_x\text{MgF}_3}}{\sqrt{\frac{E_{\text{KMgF}_3}^{\Gamma,\text{R},\Delta} + E_{\text{LiMgF}_3}^{\Gamma,\text{R},\Delta}}{2}}} x(1-x)$$

and

$$\alpha_{\text{Li}_{(1-x)}\text{K}_x\text{Ba}_{(1-y)}\text{Mg}_y\text{F}_3} = \alpha_{\text{KBa}_{(1-y)}\text{Mg}_y\text{F}_3} + \alpha_{\text{LiBa}_{(1-y)}\text{Mg}_y\text{F}_3} (1-x)$$

Here, the energy gap sag α is assumed here to be 0.3 as proposed by Thompson and Woolley. For the lattice constant of $\text{Li}_{(1-x)}\text{K}_x\text{Ba}_{(1-y)}\text{Mg}_y\text{F}_3$, we considered that the variation follows the Vegard's law. Thus,

$$a_{\text{Li}_{(1-x)}\text{K}_x\text{Ba}_{(1-y)}\text{Mg}_y\text{F}_3} = a_{\text{LiBaF}_3} (1-x)(1-y) + a_{\text{KBaF}_3} x(1-y) + a_{\text{LiMgF}_3} (1-x)y + a_{\text{KMgF}_3} xy$$

The plot in Fig. 1 illustrates the quaternary chart representing the variations of R, Δ and Γ band gap valleys. The thick solid lines on the plot represent borders between either Δ and Γ domains or Γ and R

ones. Compositions with equal lattice constants are represented by straight dotted lines called equi-lattice lines. From this chart, we can propose the $n\text{-LiBaF}_3/\text{Li}_{0.875}\text{K}_{0.125}\text{Ba}_{0.876}\text{Mg}_{0.124}\text{F}_3/p\text{-LiBaF}_3$ and $n\text{-KMgF}_3/\text{Li}_{0.870}\text{K}_{0.130}\text{Ba}_{0.847}\text{Mg}_{0.153}\text{F}_3/p\text{-KMgF}_3$ double-hetero structure LD emitting in around 198 nm (6.25 eV). This structure will be sufficient for LED. With appropriate cavity design, LD will be also feasible.

The LDA generally underestimates the width of band gaps. The transmission edges of LiBaF_3 and KMgF_3 single crystals are estimated down to 126.3 nm and 121.5 nm from Fig. 2. For KMgF_3 single crystals, an absorption dip around 130 nm might be attributable to defects of crystals. The transmission edges are defined as absorption coefficient of 20 cm^{-1} . The transmission edges of LiBaF_3 and KMgF_3 correspond to energy band gaps of 9.8 eV and 10.2 eV, respectively. The measured band gaps of LiBaF_3 and KMgF_3 are 51% and 40% higher than calculated values of 6.51 eV and 7.29 eV. From these results, there is a possibility that complex fluoride optical devices operate with shorter wavelength than that predicted by *ab initio* calculation within the LDA.

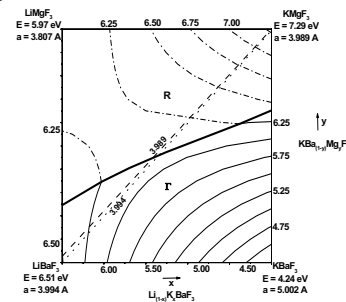


Fig. 1 Variations of band gap energy structure and lattice constants of $\text{Li}_{(1-x)}\text{K}_x\text{Ba}_{(1-y)}\text{Mg}_y\text{F}_3$ with respect to composition.

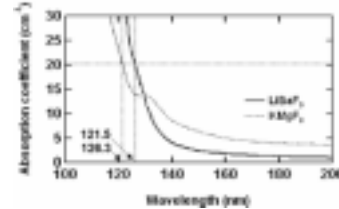


Fig. 2 Absorption coefficient of LiBaF_3 and KMgF_3 compounds in ultraviolet region

[1] T. Nishimatsu *et al.*, Jpn. J. Appl. Phys. **41** (2002) L365.

[2] R. El Ouenzerfi *et al.*, J. Appl. Phys. **96** (2004) 7655.

Vacuum-Ultraviolet Reflectance Spectroscopy of Strongly Correlated Electron System

S. Miyasaka¹, J. Fujioka¹, Y. Tokura^{1,2,3}

¹*Department of Applied Physics, University of Tokyo, Tokyo 113-8656 Japan*

²*Correlated Electron Research Center (CERC), National Institute of Advanced Industrial Science and Technology (AIST), Tsukuba 305-8562 Japan*

³*Spin Superstructure Project (SSS), ERATO, Japan Science and Technology Agency (JST), Tsukuba 305-8562 Japan*

One of the most important characteristics for the correlated electron systems is the drastic re-construction of electronic structure over an energy scale of eV with changes of temperature, doping concentration, and/or external field. Therefore, optical reflectivity measurement over a wide energy range and the optical conductivity spectra derived from the reflectivity spectra provide us with very useful information about the strongly correlated electron systems.

In this beam time, we measured the reflectivity spectra of several transition-metal oxides, including V, Cr, Mn, Fe and Mo, for an energy range of $4 \text{ eV} < E < 35 \text{ eV}$ at room temperature using the beam line BL1B. The measured reflectivity data, together with the lower-energy data below 4 eV, were used to derive the optical conductivity spectra or dielectric function via the Kramers-Kronig analysis. As an example, the imaginary part of the dielectric function of single crystals of $\text{La}_{1-x}\text{Sr}_x\text{VO}_3$ with the several Sr concentration x , which are grown by a floating zone method, is shown in Fig. 1.

$\text{La}_{1-x}\text{Sr}_x\text{VO}_3$ is one of the classic Mott transition systems, although the single-crystal specimens necessary for detailed optics measurements have been lacking so far. The parent compound LaVO_3 is a Mott-Hubbard-type insulator with the V electron configuration of $3d^2$, and undergoes a magnetic transition from a paramagnetic to an antiferromagnetic state, and also a structural phase transition from orthorhombic to monoclinic follows right below the magnetic transition temperature. Sawada and co-workers have theoretically demonstrated that this compound in the monoclinic structural phase and related compound, YVO_3 , have different types of orbital ordering, the alternate G-type $d_{xy}^1 d_{yz}^1 / d_{xy}^1 d_{zx}^1$ electron configuration for LaVO_3 and C-type for YVO_3 . The carrier doping by substitution of La with Sr causes a transition from a correlated insulator to a metal around $x = 0.176$. The metal-insulator transition accompanies the structural phase transition related to the orbital order-disorder transition. To clarify the change of the electronic structure caused by the orbital-ordered Mott insulator-metal transition, we have revisited $\text{La}_{1-x}\text{Sr}_x\text{VO}_3$.

We present the spectra of the imaginary part of the dielectric function (ϵ_2) for $\text{La}_{1-x}\text{Sr}_x\text{VO}_3$ samples with

several Sr concentrations in Fig. 1. In the spectrum of LaVO_3 ($x = 0$), the lowest optical transition A around 2 eV can be assigned to the optical transition across the Mott-type gap. Above the Mott gap, a much more intense optical transition B is clearly discerned. The position and intensity suggest that the transition be assigned to the charge transfer excitation from O $2p$ to V $3d$ upper Hubbard state. The transition is accompanied by another spectral structure C, which is 1 eV above the transition B. Above 7 eV, three peak structures, D, E, and F are observed. These absorption bands are assigned to the transition from O $2p$ to La $5d$ or V $4s/4p$ state, that from O $2s$ to V $3d$, and that from La $5p$ to La $5d$, respectively.

With the increase of Sr concentration x , the Mott-Hubbard gap disappears. In addition, the substitution of La with Sr changes the peak shape around 6 eV. The spectra for the insulating samples with $x = 0$ and 0.10 show double structure around 5-6 eV. This feature is caused by the ligand field splitting of $3d$ orbitals, which tends to stabilize the orbital ordering at low temperatures. In contrast, the double peak-structure is not observed in the spectra for the metallic sample with Sr concentration $x = 0.18$ and 0.26. The present results indicate that even in the high-energy region above 5 eV, the Sr doping causes the change of the spectral feature, which is related to the metal-insulator transition and perhaps to the orbital ordering.

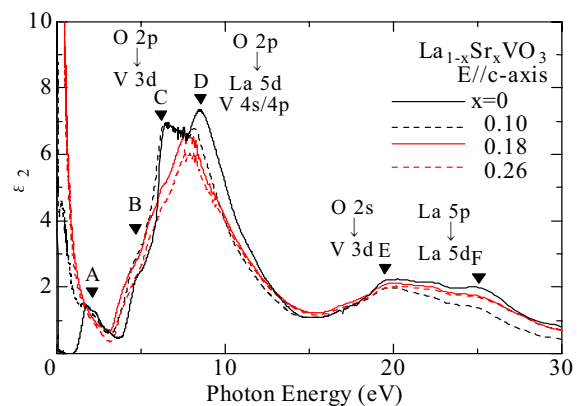


Fig. 1 The spectra of the imaginary part of the dielectric function (ϵ_2) for insulating samples (black curves, $x = 0$ and 0.10) and those for metallic ones (red curves, $x = 0.18$ and 0.26) in $\text{La}_{1-x}\text{Sr}_x\text{VO}_3$.

Vacuum Ultraviolet Spectroscopy of BaMgF₄:Ce³⁺ Crystals

E. Hayashi¹, K. Itoh¹, M. Yamaga¹, S. Ono², N. Sarukura²

¹Department of Electric and Electronic Engineering, Gifu University, Gifu 501-1193, Japan

²Institute for Molecular Science, Okazaki 444-8585, Japan

Successful laser operation based on the $5d \rightarrow 4f$ transitions of Ce³⁺ has been reported for LiYF₄, LiLuF₄, and LiCaAlF₆ [1]. Recently, laser materials operating below 200 nm is required. In order to satisfy this requirement, a frequency doubling method using a nonlinear effect is useful. Ce³⁺-doped BaMgF₄ (BMF) crystals attract attention as laser materials with a nonlinear effect. Recently, the BMF crystal growth and optical properties in the ultraviolet and visible range were reported [2]. In this report, we discuss the energy level of Ce³⁺ in BMF estimated from the optical spectra extended to the vacuum ultraviolet (VUV) range [3].

Figure 1 shows a unit cell of the crystal structure of BaMgF₄. Each octahedron consists of a central Mg²⁺ ion and six nearest-neighbour F⁻ ligand ions. Ba²⁺ ions are located at centers of trigonal prisms, each composed of six nearest-neighbour F⁻ ligand ions. Ce³⁺ ions substitute for Ba²⁺ ions. In such a configuration, the excited state of Ce³⁺ is split into E_g and T_{2g} states as shown in a lower part of Fig. 1.

Figure 2 shows absorption, excitation, and emission spectra of Ce³⁺ in BMF crystals measured at 17K in the VUV, UV and visible ranges. There are three different luminescence bands denoted by A, B, and C. Each of these luminescence bands has double peaks. The energy difference of the peak to peak is equal to the ground-state slipping between ²F_{5/2} and ²F_{7/2} of Ce³⁺.

The excitation spectrum of the A-band luminescence consists of five broadbands at 178, 197, 233, 245, 257 nm. These bands are coincident to absorption bands. The peaks at 178/197 nm and 233/245/257 nm correspond E_g and T_{2g}, respectively as shown in Fig. 1. Similarly, the excitation spectrum of the B-band luminescence has five broadbands at 159, 228, 256, 294, 300nm. In order to identify peaks of the C-band excitation spectrum, we refer to optical spectra of Ce³⁺:SrMgF₄, of which crystal structure is similar to Ce³⁺:BaMgF₄. The peak of the C-band excitation spectrum are 225, 259, 298, 325, 377 nm.

These results suggest the A-band luminescence is estimated to Ce³⁺ ions which substitute for Ba²⁺ ions. The B-band luminescence is estimated to Ce³⁺ ions perturbed by Na⁺ ions as charge compensators. The C-band luminescence is assigned to a complex center of Ce³⁺ and lattice defects which are different from Na⁺.

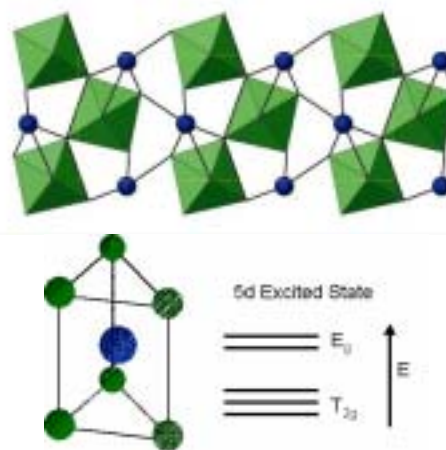


Fig. 1 A unit cell of the crystal structure of BaMgF₄.

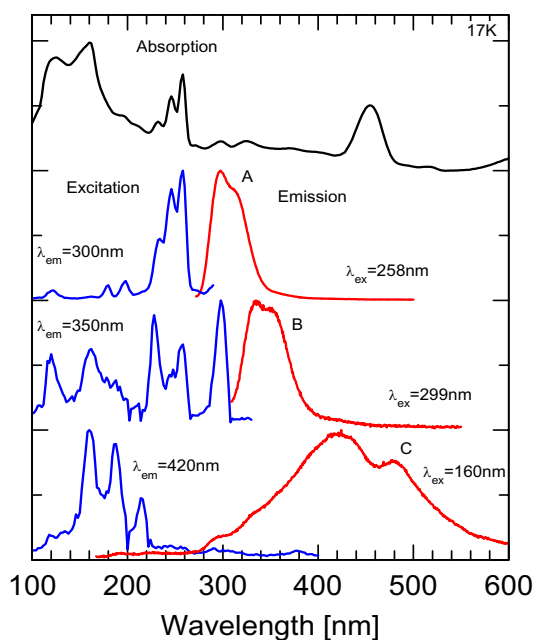


Fig. 2 Optical spectra of Ce³⁺:BaMgF₄.

[1] N. Sarukura, M. A. Dubinskii, Z. Liu, V. V. Semashko, A. N. Naumov, S.L. Korableva, R. Y. Abdulsabirov, K. Edamatsu, Y. Suzuki, T. Itoh, Y. Segawa, IEEE J. Selected Topics Quantum Electron. **1** (1995) 792.

[2] M. Yamaga, K. Hattori, N. Kodama, N. Ishizawa, M. Honda, K. Shimamura, T. Fukuda, J. Phys.: Condens. Matter **13** (2001) 10818.

[3] E. Hayashi, K. Itoh, S. Yabashi, M. Yamaga, N. Kodama, S. Ono, N. Sarukura, J. Alloys and Compounds (2005) in press.

Temperature Dependence of Reflectivity C₆₀F₁₈ Single Crystals

V. G. Stankevich^{1,2}, A. M. Lebedev², N. Yu. Svechnikov², K. A. Menshikov²,
O. V. Boltalina³, L. N. Sidorov³, S. Kimura¹, M. Hasumoto¹

¹UVSOR Facility, Institute for Molecular Science, Okazaki 444-8585 Japan.

²Russian Research Centre Kurchatov Institute, Kurchatov Sq. 1, 123182, Moscow, Russia.

³Chemistry Department, Moscow State University, 119899, Moscow, Russia.

Introduction

At present one of the most promising directions is the developing and use of new carbon nanostructures with sp² hybridization – fullerenes, nana tubes and thin films based on these compounds. Special interest represents investigations of fullerenes doped with different atoms leading to considerable changing of properties. Doping with halogens, in particular with fluorine, is leading to strong changes of chemical and physical properties. Additional interest for these compounds is connected with theoretical prediction [1] of significant decrease of penetration barrier for some ions and atoms through the walls of carbon nana tubes due to fluorination. Therefore, within the last few years we investigated fluorinated fullerenes C₆₀F_{2X} with different amount of fluorine's.

In Ref. [2], we have investigated optical properties of different thin films based on C₆₀F₄₈, C₆₀F₃₆, C₆₀F₂₄ and C₆₀F₁₈ molecules. It was established that optical absorption edge is shifting to the higher energy region (from 1.9 eV for pure C₆₀ to 4.2 eV for C₆₀F₄₈) due to destruction of initial π-electron subsystem of pure C₆₀ and creation of new σ-orbital with C-F bonds. Besides for these compounds we have observed unusual photoluminescence temperature dependence.

All fluorofullerenes molecules are very large, with atomic masses exceeding 1000 amu and with sizes about 1 nm. These nana objects manifested very interesting molecular structures, having a spherical C₆₀ skeleton, surrounded by appropriate amount of attached fluorine atoms different symmetries.

Among these, special attention should be paid to a C₆₀F₁₈ molecule due to a high asymmetry (Fig. 1) [3].



Fig. 1 Molecule C₆₀F₁₈ structure.

As seen, 18 fluorine atoms occupy only one half of a C₆₀ deformed skeleton. This is leading to a high dipole moment, and theoretical estimation [3] gives the value about 10D. In principle it is possible to arrange a ferroelectric ordering at the Curie temperature T_C for

ensemble of these polar molecules caused by dipole-dipole interaction. We have estimated the T_C value at first approximation. The interaction energy of two parallel identical dipoles is defined by [4]:

$$E = \frac{d^2}{R^3} \quad (1)$$

Where d – a dipole moment of molecule [D], R – a distance between two dipoles [Å], E – energy [eV]. If $d = 10$ D and $R = 19$ Å [3], the disorder temperature is found to be T_C = 112 K.

Results and discussion

Here we report first reflectivity spectra of the high quality C₆₀F₁₈ single crystals prepared via vacuum sublimation. Figure 2 shows the reflectivity spectra one of the rectangular plane size 100*60 microns² with room temperature and 50 K.

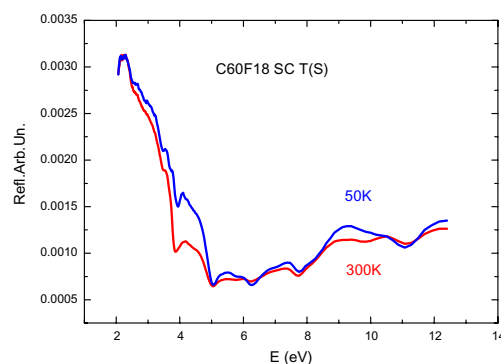


Fig. 2 Reflection spectra C₆₀F₁₈ single crystal.

The main changes in reflectivity are observed for the energy about 4 eV (typical for π-π* transitions) with shifting of reflection minimum to a low energy side, and for E > 8 eV for deeper electronic levels.

As a result, the observable changes of reflection spectra are demonstrating the existence of the ferroelectric phase transition; however the detail analysis and calculations are in progress now.

[1] P. V. Avramov, B. I. Yakobson, G. E. Scuceria, T. A. Romanova, IWFA-2003 works (St. Peterburg, Russia) (2003) 22.

[2] P. V. Dudin, S. V. Amarantov, V. G. Stankevich *et al.*, Surf. Rev. Lett. **9** (2002) 1339.

[3] I. V. Goldt, O. V. Boltalina, L. N. Sidorov *et al.*, Sol. St. Sci. **4** (2002) 1395.

[4] F. Jona, D. Shirane, *Ferroelectric crystals* (Mir, Moscow) (1965) 41.

Excitation Spectra of VIS-UV Emission in AlGaN and InAlGaN

K. Fukui¹, S. Hamada¹, S. Naoe², H. Hirayama³, H. Miyake⁴, K. Hiramatsu⁴

¹Research Center for Development of Far-Infrared Region, Fukui 910-8507, Japan

²Faculty of Engineering, Kanazawa University, Ishikawa 920-1192, Japan

³The Institute of Physical and Chemical Research, Wako 351-0198, Japan

⁴Faculty of Engineering, Mie University, Mie 514-8507, Japan

AlGaN becomes a promising semiconductor optical material because of variable band gap energy from 0.8 to 6.28 eV according to composition ratio of elements. However, the photoluminescence (PL) intensity at low temperature is not sustained in increasing temperature to RT. By contrast with this, InAlGaN gives the effective rate of PL intensity at RT. Both studies of AlGaN and InAlGaN PLs are necessary to explain the mechanism of PL process in AlGaN.

All samples are made by MOCVD (MOVPE) methods. The thickness of AlGaN thin films are about 1 μm on 1 μm AlN single crystal film with sapphire substrates and those of InAlGaN thin films are about 80 nm on SiC substrates with $\text{Al}_{0.2}\text{Ga}_{0.8}\text{N}$ buffer layers. The measurements were carried out at BL7B, BL5B and BL8B1, under multi-bunches operation in the energy range from 2 to 500 eV. Same conventional 30 cm monochromator with liquid N_2 cooled CCD detector via optical fiber is used for PL measurements of all samples.

In both AlGaN and InAlGaN, PL spectra are composed of two bands. One is UV band PL (B-emission) corresponding to exciton, the other is visible (VIS) band (Y-emission) caused by lattice defects or impurities. Figs. 1 (a) and (b) show both B- and Y-emission excitation spectra of $\text{Al}_{0.34}\text{Ga}_{0.66}\text{N}$ and $\text{In}_{0.04}\text{Al}_{0.35}\text{Ga}_{0.61}\text{N}$, respectively. Intensity (vertical axis) represents the integrated intensity per excitation photon of B- or Y-emission calculated from PL spectrum at each excitation photon energy. Each spectrum is normalized for convenience. Arrows in figures represent of the peak position of B-emission and almost correspond to the band-gap energies.

Since Y-emission is caused by the recombination luminescence of electron and hole at trapping centers of defects or impurities, the excitation spectra of Y-emission are expected to give the absorption spectra of the samples originating from band-to-band transition. In fact, the excitation spectra of both AlGaN and InAlGaN Y-emission seem to be proportional to the rate of absorption of the sample. Peak-like spectral feature is only observed near band edge of AlGaN B-emission. This result suggests that the initial state of B-emission of AlGaN constructs some bound exciton states. The tail-like structures at the lower excitation energy side of InAlGaN relative to those of AlGaN probably reflects the inhomogeneous special dispersion of In element in InAlGaN alloy.

Fig. 2 shows the both excitation spectra of AlGaN and InAlGaN in the starting area of inner shell excitation. Since vertical axis (intensity) represents

the integrated intensity per excitation photon, intensity increasing with increasing exciting photon energy suggests that more than one electron-hole pairs are produced during the relaxation process of an inner shell hole from core to valence band, which is known as photon multiplication.

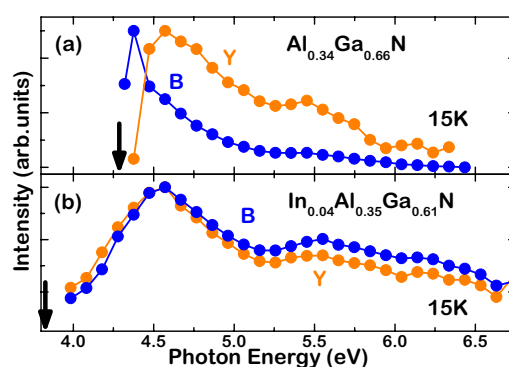


Fig. 1 Photoluminescence excitation spectra of $\text{Al}_{0.34}\text{Ga}_{0.66}\text{N}$ (a) and $\text{In}_{0.04}\text{Al}_{0.35}\text{Ga}_{0.61}\text{N}$ (b) at BL7B.

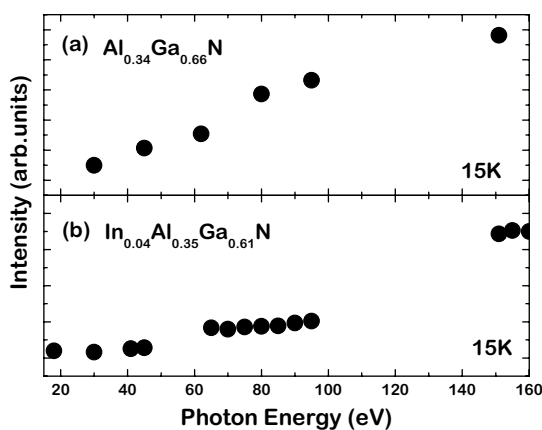


Fig. 2 Photoluminescence excitation spectra of $\text{Al}_{0.34}\text{Ga}_{0.66}\text{N}$ (a) and $\text{In}_{0.04}\text{Al}_{0.35}\text{Ga}_{0.61}\text{N}$ (b) at BL5B.

Transmission Spectra of Amorphous Semiconductor Thin Films in the Vacuum Ultra-Violet Region

K. Hayashi

Department of Electrical and Electronic Engineering, Gifu University, Gifu 501-1193, Japan

Amorphous chalcogenide semiconductor materials, such as amorphous As_2S_3 (a- As_2S_3), amorphous As_2Se_3 (a- As_2Se_3), and amorphous Se (a-Se) etc., exhibit a variety of photoinduced phenomena. The application of these amorphous semiconductor materials to the optoelectronic devices is very much expected, because these materials are very sensitive to the light. Although a large number of studies [1-3] have been done on the photoinduced phenomena of these amorphous semiconductor materials, little is known about the details of these mechanisms. These phenomena were studied by exciting outer core electrons with the irradiation of light with the energy corresponding to the optical bandgap or sub-bandgap. The interest has been attracted for the change of the optical properties in the energy region of the visible light. Little attention has been given to photoinduced effects by exciting inner core electrons with the irradiation of higher energy photon. We are interesting for the change of the optical properties in the higher energy region. To obtain a wide knowledge of the photoinduced phenomena, it is necessary to investigate to the photoinduced effects on wide energy region. In previous reports, we reported the photoinduced change at the VUV reflection spectra of the amorphous chalcogenide semiconductor films induced by bandgap light. In present report, we report the examination on the more exact measuring method of the photoinduced change at the spectrum in the VUV region. In this report, we measured the VUV transmission spectra in amorphous chalcogenide films.

Samples used for the measurement of transmission spectrum were amorphous chalcogenide (a- As_2S_3 and a- As_2Se_3) semiconductor films. Thin films of amorphous chalcogenide semiconductor were prepared onto ultrathin collodion films by conventional evaporation technique. A typical thickness of an amorphous film was around 160 nm. The ultrathin collodion films were prepared onto stainless steel metal plates with a pinhole of the 1 mm diameter. The transmission spectrum was measured through the pinhole by a silicon photodiode. The transmission spectra in the VUV region were performed at room temperature at the BL5B beam line of the UVSOR facility of the Institute of Molecular Science. In present experiment, to eliminate the higher order light from the monochromator, an aluminum thin film was inserted between the monochromator and sample. We also monitored the spectrum of the light source by measuring the photoyield of the gold mesh. The transmission spectra were obtained by normalizing

the spectra by the spectrometer system response.

Figure 1 shows the VUV transmission spectrum of a- As_2Se_3 /collodion at room temperature in the wavelength region between 15 nm and 35 nm. The transmission spectrum of an aluminum filter with 100 nm film thickness supported by the metal mesh is also shown in Fig. 1. In the figure, every transmission spectrum has not been normalized by the spectroscopic system response, and that has been normalized at the maximum value of the transmitted light intensity. Two main absorption peaks of a- As_2Se_3 were observed in this region. One absorption peak around 22 nm corresponds to the $3d$ core level of Se atom. Another absorption peak around 28 nm corresponds to the $3d$ core level of As atom. These peak positions agree well with the result of the reflection spectrum [4]. In addition, it was possible to also confirm the two peaks that correspond to the core level of Se atom of $3d_{3/2}$ and $3d_{5/2}$ in present measurement. At present, it is not possible to obtain the accurate transmission spectrum, because there is a problem on effect of higher order light and reproducibility of the wavelength. It is examined in respect of these at present. The detailed experiments and analysis will be done in the next step.

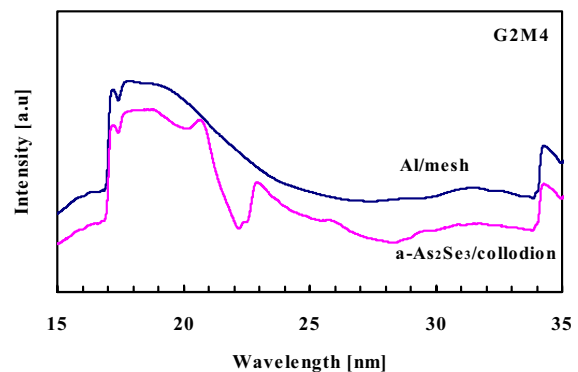


Fig. 1 Normalized transmission spectra of a- As_2Se_3 /collodion and Al/mesh.

- [1] Ke. Tanaka, *Rev. Solid State Sci.* **4** (1990) 641.
- [2] K. Shimakawa, A. Kolobov, and S. R. Elliot, *Adv. Phys.* **44** (1995) 475.
- [3] Ke. Tanaka, *Encyclopedia of Nanoscience and Nanotechnology* **7** (2004) 629.
- [4] K. Hayashi, *UVSOR Activity Report 2002* (2003) 130.

Optical Response of CuIr_2Se_4

L. Chen¹, T. Nanba¹, T. Matsumoto², S. Nagata³

¹Graduate School of Science and Technology, Kobe University, Kobe 657-8501, Japan

²National Research Institute for Metals, 1-2-1 Sengen, Tsukuba 305-0047, Japan

³Department of Materials Science and Engineering, Muroran Institute of Technology, Muroran, Hokkaido 050-8585, Japan

The spinel compound CuIr_2Se_4 at atmospheric pressure is a metal at wide temperature range, but undergoes a stabilization of the insulating phase at high pressures above 3 GPa.[1,2] To study its electronic state close to the Fermi level ambient pressure, we measured the temperature dependence of optical reflectivity spectra $R(\omega)$ of polycrystalline CuIr_2Se_4 .

Experimental

The optical reflectivity spectra $R(\omega)$ at ambient pressure was measured in the wide photon energy range from 7 meV to 30 eV in the temperature range of 8-300 K. The measurements were performed using a Fourier-transform interferometer combined with a thermal light source and synchrotron radiation source at the beam line BL6B & 7B of UVSOR. The optical conductivity $\sigma_1(\omega)$ and complex dielectric function $\varepsilon_1(\omega)$ were obtained from a standard Kramers-Kronig transformation of the measured reflectivity spectrum.

Results and discussions

Figure 1 shows the temperature dependences of the R -spectra (upper panel) and σ -spectra (lower panel) of CuIr_2Se_4 below 25 eV. The arrow in the σ -spectra shows the direction of cooling from 300 K to 8 K. In the σ -spectra, several distinct peaks corresponding to electronic interband transitions were resolved at around 0.2, 0.8, 2.0, 4.0, 6.5 and 13 eV, together with the Drude component given by conduction electrons below 0.2 eV. The Drude component still survived even at 8 K but became narrower with cooling. The peak intensity at around 0.2 eV increased instead of the suppression of the Drude component with cooling so as to compensate the spectral weight. The peaks above 0.8 eV were almost insensitive to temperature. We fitted the σ -spectra below 3 eV with a Drude-Lorentz model and estimated the carrier densities, for example, as $1.02 \times 10^{21} \text{ cm}^{-3}$ (300 K), $6.5 \times 10^{20} \text{ cm}^{-3}$ (80 K) and $4.6 \times 10^{20} \text{ cm}^{-3}$ (8 K). The carrier density decreases gradually with cooling but is still measurable even at 8 K.

CuIr_2Se_4 exhibits a broad peak structure at around 0.2 eV, which becomes distinct instead of the Drude component with cooling. The development of a low energy peak at around 0.2 eV accompanying the suppression of the Drude component suggests the precursor for the formation of the pseudo-gap state at around E_F with cooling at atmospheric pressure. Since the lattice constant of CuIr_2Se_4 is larger than that of CuIr_2S_4 , temperature cooling is not sufficient to

strengthen the hybridization between the 5d states of Ir atoms belonging to the neighboring sites, and the Ir 5d and Se 4p states in CuIr_2Se_4 so as to form a clear energy gap state at around E_F . Thus, we consider that in CuIr_2Se_4 the weak hybridization due to the larger lattice constant might be the main reason that the metal-insulator transition does not occur at atmospheric pressure. The application of the high pressure to this compound will induce the clear opening of the energy gap state because of the increase in the hybridization by the decrease in the lattice constant. Such experiment is now on progress.

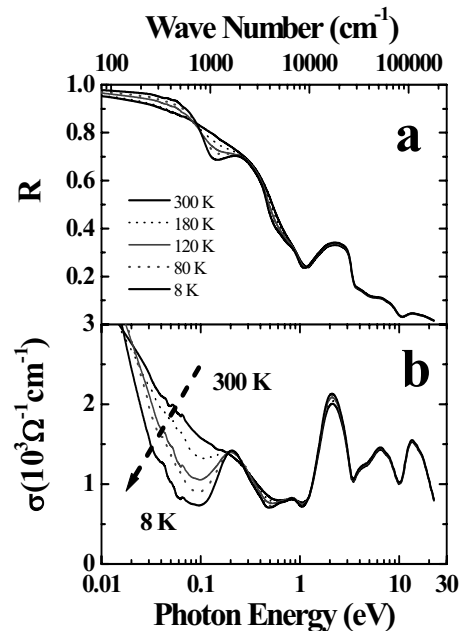


Fig. 1 Temperature dependences of (a) $R(\omega)$ and (b) $\sigma(\omega)$ -spectra from 300 K to 8 K.

[1] J. Tang, T. Furubayashhi, T. Kosaka, S. Nagata, Y. Kato and T. Matsumoto: Rev. High Pressure Sci. Technol. **6** (1997) 496.

[2] J. Tang, T. Furubayashhi, T. Kosaka, S. Nagata, Y. Kato and T. Matsumoto: Rev. High Pressure Sci. Technol. **7** (1998) 362.

Metal-Nonmetal Transition of Bismuth Clusters

H. Ikemoto, S. Yoshida, A. Asai

Faculty of Science, Toyama University, Gofuku 3190, Toyama 930-8555, Japan

Raman-scattering measurements of clusters of bismuth exhibit a phase transition from rhombohedral Bi nanocrystalline to amorphouslike clusters depending on cluster size [1]. They also suggest that amorphous clusters are semiconducting and covalent interactions increase with decreasing size.

The Raman studies are good tools but indirect evidences for the transition. So it is very important to investigate the optical property directly to reveal the mechanism of the phase transition. In the present study we report results of optical absorption coefficients for Bi clusters.

Experimental

Bismuth of 99.999% purity was slowly deposited onto the substrates from a tungsten boat. The Bi film was discontinuous with isolated island formation. Then, KBr of 99.999% purity was deposited to cover the Bi islands. By repeating these procedures, a sample of Bi clusters isolated in an alkali-halide matrix was obtained. The size of the islands was adjusted by controlling the thickness deposited on the substrates, which was monitored with a quartz oscillator. The thickness ratio of the Bi and the matrix is about 1:20. As mentioned above the Bi clusters are formed in thin films, and samples are represented by their average thickness of the Bi thin films in this paper.

Measurements of optical absorption coefficients were performed in the energy range of 0.05 ~ 0.95 eV with the rapid-scan Michelson interferometer (Bruker, IFS-66V) at the IR beam line (BL6B) by using a KBr beam splitter. A HgCdTe detector was used.

Results and Discussion

Figure 1 presents a representative set of curves for the optical absorption coefficients of various thickness films. Several of the characteristics can be seen by examining the absorption data by itself. The absorption coefficients of the 300 nm and 10 nm thick films are close to those of bulk Bi, suggesting that these films are semimetallic. There is a noticeable change in the optical behavior between the 10 nm thick film and the 5 nm thick film. The absorption coefficients of the 5, 2 and 0.5 nm thick films are rather small compared to those of bulk Bi, indicating that those films are semiconductors.

The optical absorption coefficients for Bi thin films exhibit a phase transition from semi-metallic nanocrystalline to semiconducting amorphous clusters with decreasing the size. The semimetallic nature of rhombohedral Bi is attributed to the overlap between the back lobes of orbitals in adjacent layers, and the semiconducting nature of amorphous Bi is attributed to the loss of this overlap [2]. We suppose

following mechanism of the phase transition from semi-metallic nanocrystalline to semiconducting amorphous clusters. Even if the clusters are small, the three-folded covalent bonds are similar with that of the crystalline and the layer structures are reserved. But the amorphousization of the thin films results in the disappearance of the interlayer correlation. The loss of the overlap between the orbitals in adjacent layers gives rise to the bond shrinkage and the semiconducting nature.

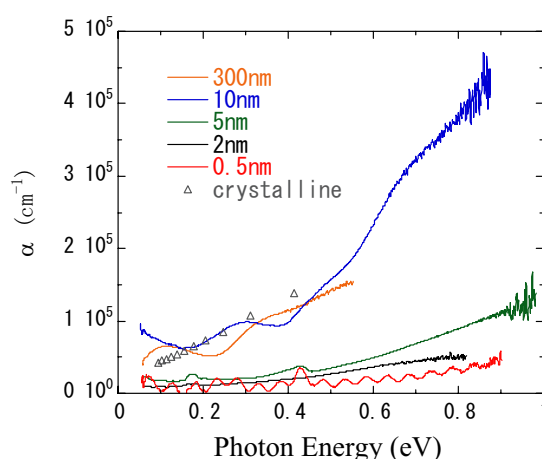


Fig. 1 Variations in optical absorption coefficients of the as-deposited Bi clusters for different thickness. Triangles denote those of polycrystalline [3].

[1] M. G. Mitch, S. J. Chase, J. Fortner, R. Q. Yu, and J. S. Lannin, *Phys. Rev. Lett.* **67** (1991) 875-878.

[2] N. F. Mott and E.A. Davis, *Electronic Progress in Non-Crystalline Materials*, Second Edition (Clarendon Press, Oxford, 1979) p. 413.

[3] E.V. Potapov, *Soviet Phys.-JETP* **20** (1965) 307.

Terahertz Spectroscopy of a Kondo Semiconductor SmB_6

S. Kimura^{1,2}, S. Kunii³

¹*UVSOR Facility, Institute for Molecular Science, Okazaki 444-8585, Japan*

²*Department of Molecular Structural Science, The Graduate University for Advanced Studies, Okazaki 444-8585, Japan*

³*Department of Physics, Tohoku University, Sendai 980-8577, Japan*

SmB_6 , which is a typical Kondo semiconductor, has been studied over two decades. In the previous studies, two different energy gap size were proposed, one is about 5 meV and the other about 15 meV [1]. However, a recent study using higher purity samples reveals that the lower energy absorption band originates from impurities because the lower energy absorption becomes small [2]. The higher energy gap is concluded to be intrinsic and to originate from the hybridization between the localized Sm 4*f* state and the Sm 5*d* conduction band, so-called *cf* hybridization [3]. In the case of the *cf* hybridization, the electronic structure including the energy gap is rigid. However, the specific heat curve cannot be explained by the rigid band model [4]. This means that there is the temperature dependent part in the electronic structure.

On the other hand, the magnetic excitation at 14 meV grows up with decreasing temperature below 20 K observed by a neutron inelastic scattering [5]. The energy of 14 meV is similar to the energy gap observed in optical spectra. Therefore if the *cf* hybridization bands exist at the energy gap edge, the character of carriers should have the same temperature dependence. Optical reflection spectroscopy is one of good probe to investigate the character of carriers. In SmB_6 case, the signal from the thermally excited carriers appears in the terahertz region. Then we measured the temperature dependence of the reflectivity spectrum in the terahertz region.

Figure 1 (a) indicates the temperature dependence of reflectivity spectrum of SmB_6 by red marked lines. At $T = 5$ K, the reflectivity at $h\nu = 1$ meV is almost constant less than unity. This indicates that the character is insulating. With increasing temperature, the spectral weight grows up from the lower energy side. The spectral weight originates from the Drude part due to thermally excited carriers. The Drude part indicates the electronic structure thermally excited area near the energy gap edge.

The fitted function using one Drude and two Lorentz functions are indicated by blue solid lines in Fig. 1 (a). The fitting functions (the parameters are not shown.) can reproduce the experimental curves well. The obtained effective electron number (N_{eff}) and relaxation time (τ) derived from the fitting parameters are shown as the function of temperature in Fig. 1 (b). N_{eff} cannot be explained by an activation type behavior [$N_{\text{eff}} \propto \exp(-2E_g / k_B T)$, where E_g is the energy gap and k_B the Boltzmann constant].

Two-state model might be assumed to explain the behavior [6]. On the other hand, τ drastically changes at 20 K. The temperature is coincident with that of the growth of the magnetic excitation at 14 meV. This means that the thermally excited carriers relates to the magnetic excitation at 14 meV.

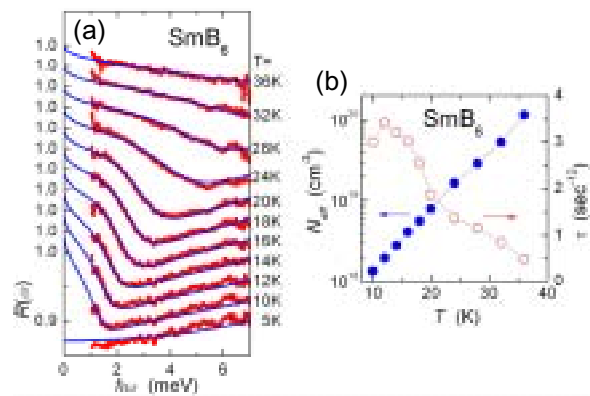


Fig. 1 (a) Temperature dependence of reflectivity spectrum of SmB_6 in the THz region (red marks) and fitting functions by the combination of a Drude and two Lorentz functions (blue lines). (b) Obtained parameters of the effective electron number (N_{eff}) and the relaxation time (τ) of the Drude function as a function of temperature.

- [1] G. Travaglini and P. Wachter, Phys. Rev. B **29** (1984) 893.
- [2] S. Kimura *et al.*, Phys. Rev. B **50** (1994) 1406.
- [3] G. Aeppli and Z. Fisk, Comments Condens. Matter Phys. **16** (1992) 155.
- [4] T. Kasuya *et al.*, *Valence Fluctuation in Solids*, (North-Holland, 1981) p. 215.
- [5] P.A. Alekseev *et al.*, J. Phys.: Condens. Matter **7** (1995) 289.
- [6] B. Gorchunov *et al.*, Phys. Rev. B **59** (1999) 1808.

Millimeter Wave Reflection Measurements of Secondary Battery Substance $\text{Li}_x\text{Mn}_2\text{O}_4$

H. Ohta¹, A. Taketani², H. Ishikawa², T. Hirano², T. Nanba², A. Hirano³, R. Kanno⁴

¹*Molecular Photoscience Research Center, Kobe University, 1-1 Rokkodai, Nada, Kobe 657-8501, Japan*

²*The Graduate School of Science and Technology, Kobe University, 1-1 Rokkodai, Nada, Kobe 657-8501, Japan*

³*Faculty of Engineering, Mie University, 1515 Kamihama-cho, Tsu 514-8507, Japan*

⁴*Interdisciplinary Graduate School of Science and Engineering, Tokyo Institute of Technology, 4259 Nagatsuda, Midori, Yokohama 226-8502, Japan*

The Li ion secondary battery substances LiCoO_2 and LiNiO_2 , are in the commercial use. LiMn_2O_4 is also a promising material for the Li ion secondary battery and it has attracted much attention recently. We have been studying the millimeter wave reflection measurements of LiCoO_2 and LiNiO_2 and related substances using UVSOR to investigate the dynamical properties of Li ions [1-9]. The increase of reflection is observed in the low energy region above 300 K for LiNiO_2 and $\text{Li}_{1-x}\text{CoO}_2$. We proposed that this increase of reflection is related to the motion of Li ion in the system but it turned out to be flat in the observed region for LiCoO_2 [8]. LiMn_2O_4 is considered as a new promising material for the positive electrode of the Li ion secondary battery from the economical point of view. Especially, a reflection measurements of $\text{Li}_x\text{Mn}_2\text{O}_4$ because it corresponds to the recharge or discharge processes in the Li ion secondary battery. Therefore, we performed the millimeter wave reflection measurements of $\text{Li}_x\text{Mn}_2\text{O}_4$.

The reflection measurements of $\text{Li}_x\text{Mn}_2\text{O}_4$ sintered sample, in which the Li ion is extracted chemically, with a diameter of 10 mm have been performed in the spectra region from 5 to 60 cm^{-1} using the beam line BL6B of UVSOR. As $\text{Li}_{1-x}\text{Mn}_2\text{O}_4$ is very fragile, the surrounding of the sample is molded by the stycast. The low pass filter was used in order to achieve the measurement below 22 cm^{-1} . The temperature was changed from 77 to 380 K. The gold plate was used as a reference and InSb detector was used as a detector.

Figure 1 shows the reflectivity results of $\text{Li}_x\text{Mn}_2\text{O}_4$. The data below 8 cm^{-1} is not reliable due to the low reflection from the reference. We can see the increase of the reflection in all temperature region from 77 to 380 K but the difference among the temperature is not clear. As $\text{Li}_{1-x}\text{Mn}_2\text{O}_4$ is very fragile, the surface condition may not be so good as other samples like LiCoO_2 and LiNiO_2 . Therefore, observed increase of the reflection is intrinsic or not remains as a future problem.

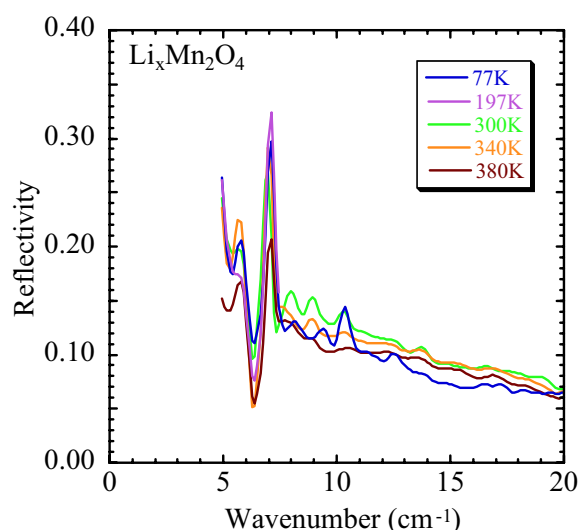


Fig. 1 Reflection spectra of $\text{Li}_x\text{Mn}_2\text{O}_4$.

- [1] H. Ohta *et al.*, UVSOR Activity Report 1996 (1997) 182.
- [2] H. Ohta *et al.*, UVSOR Activity Report 1997 (1998) 128.
- [3] H. Ohta *et al.*, UVSOR Activity Report 1998 (1999) 158.
- [4] H. Ohta *et al.*, UVSOR Activity Report 1999 (2000) 93.
- [5] H. Ohta *et al.*, UVSOR Activity Report 2000 (2001) 121.
- [6] H. Ohta *et al.*, Jpn. J. Applied Phys. **39**, Suppl. 39-1 (2000) 409-410.
- [7] H. Ohta *et al.*, UVSOR Activity Report 2001 (2002) 138.
- [8] H. Ohta *et al.*, UVSOR Activity Report 2002 (2003) 142.
- [9] Y. Nagasaka *et al.*, J. Phys. Chem. Solids **64** (2003) 1949-1951.

Far-Infrared Reflectivity Measurement of YbB₁₂

H. Okamura¹, S. Kimura², T. Nanba¹, F. Iga³, T. Takabatake³

¹Graduate School of Science and Technology, Kobe University, Kobe 657-8501, Japan.

²UVSOR Facility, Institute for Molecular Science, Okazaki 444-8585, Japan.

³ADSM, Hiroshima University, Higashi-Hiroshima 739-8530, Japan.

YbB₁₂ has been well known [1-3] as an example of the Kondo semiconductors [3-5]. It develops a small energy gap at the Fermi level below 80 K. The gap width in YbB₁₂ has been estimated to be 12.7 meV (136 K) from electrical resistivity [2], 15 meV (180 K) from Hall effect [2], and approximately 15 meV from electronic specific heat and photoemission experiments. The gap formation mechanism in the Kondo semiconductor has been discussed extensively. In the so-called band model, the gap is regarded as a band gap resulting from the hybridization between a wide conduction (*c*) band and a flat *f*-electron band [3-5]. Previously, we reported an optical study of YbB₁₂ single crystals [6]. The optical conductivity spectrum, $\sigma(\omega)$ of YbB₁₂ clearly showed an energy gap formation below 80 K. The gap development involved a progressive depletion of $\sigma(\omega)$ below a shoulder at ~ 40 meV. In addition, we observed a strong mid-infrared (mIR) absorption in $\sigma(\omega)$ peaked at ~ 0.25 eV, which was also strongly *T*-dependent. However, the minimum photon energy of the previous work was limited to about 8 meV (60 cm⁻¹), and the lowest temperature was 20 K.

In this work, we have measured $\sigma(\omega)$ of YbB₁₂ down to 1.3 meV (10 cm⁻¹) at 8 K. Owing to the recent upgrade of the BL6B front-end optics, both the total photon flux and the photon flux density at the sample position in the terahertz and far-infrared range (10 – 500 cm⁻¹) have become much higher [8]. In addition, a rapid-scan type Martin-Pupplet interferometer has been newly introduced at BL6B. Using this interferometer, the signal-to-noise ratio of the obtained spectra has become much higher.

Figure 1 shows the measured optical reflectivity spectra $R(\omega)$ and the optical conductivity spectra $\sigma(\omega)$. $\sigma(\omega)$ was obtained from $R(\omega)$ using the Kramers-Kronig relations. As the gap develops in $\sigma(\omega)$ with decreasing temperature below 80 K, a sharp minimum in $R(\omega)$ is observed to shift to lower energy. This minimum is the plasma edge due to the Drude response of residual free carriers. Since the carrier density decreases with gap development, the plasma edge shifts to lower energy. Previously, this shift was observed only to 40 K [6]. However, here we can observe it down to 20 K owing to the extended energy range of this work. In $\sigma(\omega)$, a clear onset of conductivity (indicated by the red arrow in Fig. 1) is observed at 15 meV at 20 and 8 K. This onset of $\sigma(\omega)$ is a direct result of the hump in $R(\omega)$, indicated by the blue arrow in Fig. 1. This onset energy of 15 meV is identified as the gap width of

YbB₁₂ manifested in $\sigma(\omega)$. The width of 15 meV agrees very well with those obtained by other experiments cited above. In the band model of Kondo semiconductor, there are both indirect and direct gaps in the *c-f* hybridization states near the Fermi level [4,5]. These results suggest that the gap in $\sigma(\omega)$ is due to the indirect gap. Since indirect transitions are forbidden within the first-order optical processes, it is likely that phonon-assisted transitions give rise to the appearance of indirect gap in $\sigma(\omega)$ of YbB₁₂.

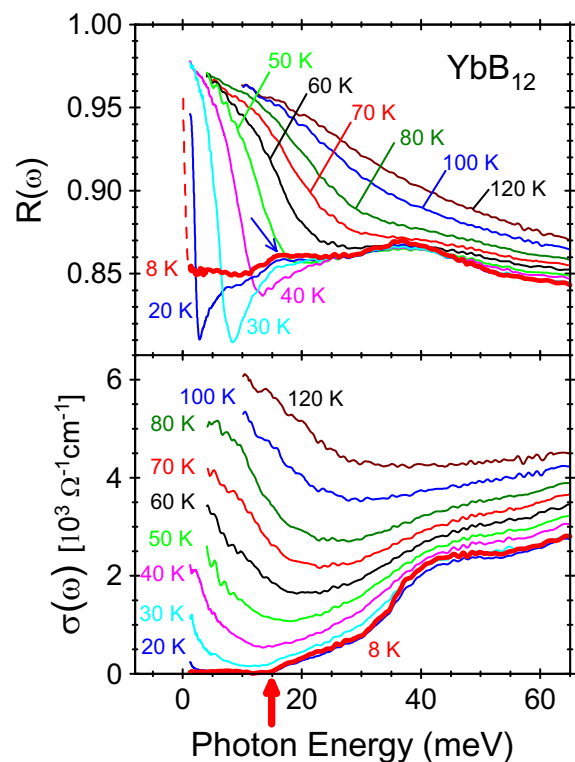


Fig. 1 (a) Reflectivity spectra $R(\omega)$ and (b) optical conductivity $\sigma(\omega)$ of YbB₁₂ at various temperatures.

- [1] M. Kasaya, F. Iga, K. Negishi, S. Nakai and T. Kasuya, *J. Magn. Magn. Mater.* **31-34** (1983) 437.
- [2] F. Iga, N. Shimizu and T. Takabatake, *J. Magn. Magn. Mater.* **177-181** (1998) 337.
- [3] T. Takabatake *et al.*, *J. Magn. Magn. Mater.* **177-181** (1998) 277.
- [4] G. Aeppli and Z. Fisk, *Comments Condens. Matter Phys.* **16** (1992) 155.
- [5] P. S. Riseborough, *Adv. Phys.* **49** (2000) 257.
- [6] H. Okamura *et al.*, *Phys. Rev. B* **58** (1998) R7496.
- [7] S. Kimura *et al.*, *AIP Conf. Proc.* **705** (2004) 416.

Infrared Reflection Absorption Spectroscopy on Li-doped Alq₃

Y. Sakurai¹, S. Kimura¹, T. Yokoyama², K. Seki³

¹*Institute for Molecular Science, Okazaki 444-8585 Japan*

²*Faculty of Engineering, Chiba University, Chiba 263-8522 Japan*

³*Research Center for Materials Science, Nagoya University 464-8602 Japan*

Tris-(8-hydroxyquinoline) aluminum (Alq₃) is most widely used as the electron transport/light emitting layer in organic light emitting diodes (OLEDs). The chemical structure of Alq₃ and its two possible geometrical isomers, meridional (C₁ symmetry) and facial (C₃ symmetry) forms are shown in Figure 1. It has been reported that the meridional isomer is the dominant species in most cases, including amorphous evaporated films.

A typical OLED consists of indium tin oxide (ITO) as the anode, on which organic thin films are sequentially deposited, with low work function metals such as Al finally deposited as the cathode. Recently, it was reported that insertion of a thin layer of an insulator such as LiF at the Al/Alq₃ interface significantly enhances electron injection. Various mechanisms for this enhancement, including the complexation between Alq₃ and Li released by the reaction between LiF and Al, have been proposed and investigated using various techniques [1,2].

Infrared Reflection Absorption Spectroscopy (IRAS) is a powerful probe for the structure and chemistry of the surface and interface. Though IR spectrum below 1000 cm⁻¹ is expected to be significantly change by interaction between metal and Alq₃, it is difficult to obtain IRAS spectrum of this region using a global source. In this paper, we report the IRAS spectra of pristine and Li-doped Alq₃ measured using synchrotron radiation (SR) source.

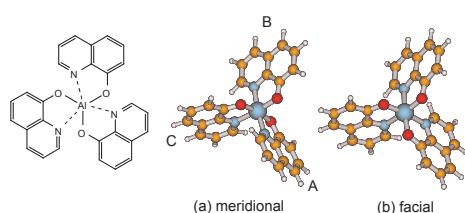


Fig. 1 The chemical structure and geometrical isomers of Alq₃.

Experiments including the sample preparation and measurement were performed in an ultrahigh vacuum chamber. Alq₃ was supplied by Nippon Steel Chemical. Ag film was deposited on Si (100) substrate from a Knudsen cell. Alq₃ film was prepared by vacuum evaporation onto this Ag film kept at room temperature. The thickness of Alq₃ film was monitored using a quartz microbalance. Lithium was deposited on the Alq₃ films from a SAES getter source. IRAS spectra were measured at BL6B of UVSOR. The spectra were obtained with SR light through a KRS-5

window and at an angle of incidence of 80° relative to surface normal. The reflected light was detected with an MCT detector.

Figure 2 shows the IRAS spectra of Alq₃ film of 20 nm thickness before and after lithium evaporation. After Li evaporation, the observed spectra show the following changes. Intensity of IR bands at 1500 and 1389 cm⁻¹ becomes weak, new band appears at 520 cm⁻¹, broad bands appear around 1535-1570 and 1250-1300 cm⁻¹, band at 1471 cm⁻¹ becomes broader. These changes in the region between 1000 and 1800cm⁻¹ are similar to those in the case of K deposition on Alq₃ [3]. The appearance of new band at 520 cm⁻¹ was newly detected by using SR source.

Figure 2 also indicates theoretically simulated spectrum of Li-Alq₃ complex in the meridional isomer by DFT calculation with B3LYP functional and 6-31G(d) basis set. The geometry optimization was carried out starting from a geometry similar to that reported by Curioni and Andreoni [4]. In the meridional isomer, the Li atom lies between ligands A and B. The simulated spectrum agrees well with the observed IRAS spectrum. The spectrum of Li-Alq₃ complex in the facial isomer is expected to be more simple and very different from that of meridional isomer because of its symmetry (Li atom is on the threefold symmetry axis) [4].

Since significant changes of IRAS spectrum are expected in the region between 300 and 500 cm⁻¹ by the DFT calculation, more information will be obtained by IRAS measurement in the far-IR region.

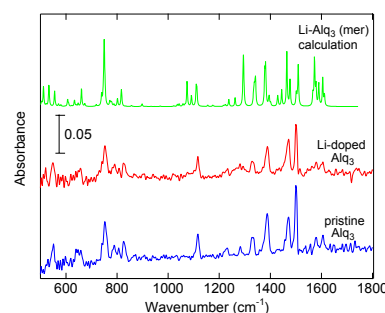


Fig. 2 IRAS spectra of pristine and Li-doped Alq₃ and theoretically simulated IR spectrum of the meridional Li-Alq₃ complex.

[1] M. G. Mason *et al.*, *J. Appl. Phys.* **89** (2001) 2756.

[2] P. He *et al.*, *Appl. Phys. Lett.* **82** (2003) 3218.

[3] Y. Sakurai *et al.*, *J. Appl. Phys.* **96** (2004) 5534.

[4] A. Curioni and W. Andreoni, *J. Am. Chem. Soc.* **121** (1999) 8216.

Optical Spectra and Electronic Structure of Calcium Fluorapatite

M. Kitaura¹, S. Oishi², M. Oda³, Y. Chikama³, H. Nakagawa³

¹*Fukui National College of Technology, Sabae 916-8507 Japan*

²*Dept. of Environmental Science and Technology, Shinshu University, Nagano 380-8553 Japan*

³*Dept. of Electrical and Electronics Engineering, Fukui University, Fukui 910-8507 Japan*

Calcium hydroxyapatite $\text{Ca}_5(\text{PO}_4)_3\text{OH}$ is of great potential for applications in medical science, because of its biocompatibility. One of the peculiar properties of this material is the ability that incorporates various cations and anions as constituents [1]. This property comes from its crystal structure, in which calcium ion and hydroxide ions are easily replaced by foreign cations and anions, respectively. Actually, it is well known that the replacement of hydroxide ions by fluorine ions causes a preventive action in the occurrence of dental cavities. The purpose of this study is to understand the fluorination effect of calcium hydroxyapatite in the viewpoint of electronic structure. In this work, the spectra of absorption and reflectivity in calcium fluorapatite $\text{Ca}_5(\text{PO}_4)_3\text{F}$ grown from KF flux [2] have been measured at 9 K using a 3-m normal incidence monochromator at BL7B.

Results and Discussion

The spectra are shown in Fig. 1. As indicated by a broken curve, the absorption edge is located around 6.01 eV. The lowest energy reflectivity peak appears at 9.51 eV. This peak accompanies a shoulder structure in the low energy side. They could not be clearly separated by varying the polarization of excitation light. Several peaks are observed in the energy range of 10-20 eV.

The electronic structure of calcium fluorapatite was calculated by the DV- $X\alpha$ method. The method has successfully applied for understanding of the electronic structure in organic and inorganic crystals. The detail of this method has been described in ref. [3]. Figure 2 shows the energy level diagram of a $\text{Ca}_{21}(\text{PO}_4)_{18}\text{F}_{30}$ cluster embedded in the crystal lattice. The valence band is primarily composed of the $2p$ orbitals of oxygen. The $2p$ orbitals of fluorine also includes in the upper valence band. The shallow core states are made of the $2s$ orbitals of oxygen. On the other hand, the conduction band is complicated as compared to the valence band. The bottom of the conduction band is dominated by the $4s$ orbitals of calcium. The band gap energy is estimated to be 9.47 eV.

From the calculated results, the electronic transition from the valence state of O $2p$ to the conduction state of Ca $4s$ is expected in the region near the fundamental gap, because this type of the transition is of allowed type. Therefore, we assign the 9.51 eV peak to the O $2p \rightarrow$ Ca $4s$ transition. A dip is located at 10.04 eV in the high-energy side of the 9.51 eV peak. The energy is in good agreement with the calculated band gap energy, so the dip is probably

regarded as an indication of the band gap position.

Our experimental results can be almost explained by the electronic structure of the model cluster mentioned here. We further continue several investigations for a detailed understanding of the electronic structure of calcium fluorapatite and calcium hydroxyapatite. On this basis, the changes in the charge density and bond overlap population by the fluorination effect will be cleared.

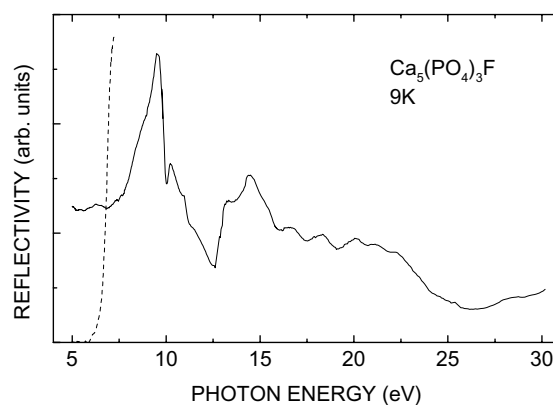


Fig. 1 Reflectivity (solid curve) and absorption (broken curve) spectra of calcium fluorapatite at 9 K.

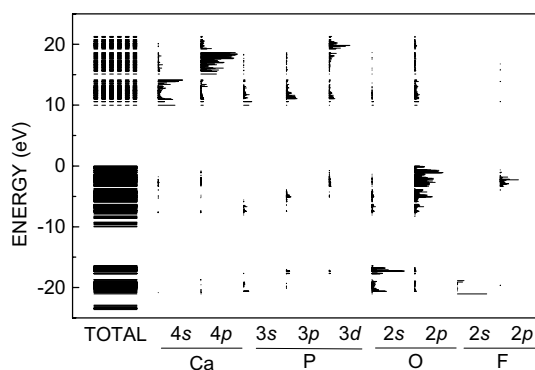


Fig. 2 Energy level diagram of a $\text{Ca}_{21}(\text{PO}_4)_{18}\text{F}_{30}$ model cluster embedded in the crystal lattice of calcium fluorapatite.

[1] For example, J. C. Rendon-Angeles, K. Yanagisawa, N. Ishizawa and S. Oishi, *J. Solid State Chem.* **151** (2000) 65.

[2] S. Oishi and T. Kamiya, *J. Chem. Soc. Jpn.* (1994) 800 (in Japanese).

[3] H. Adachi, M. Tsukada and C. Satoko, *J. Phys. Soc. Jpn.* **45** (1978) 875.

Vacuum UV Reflectivity Spectroscopy of PZT and LNO

J. Mistrik¹, T. Yamaguchi¹, N. Dai², M. Shimizu³

¹Research Institute of Electronics, Shizuoka University, Hamamatsu 432-8013 Japan

²National Laboratory of Infrared Physics, Shanghai Institute of Technical Physics, Chinese Academy of Sciences, Shanghai 200083 China

³Division of Electronic Materials and Devices, Department of Electrical Engineering and Computer Sciences, Graduate School of Engineering, University of Hyogo, Himeji 671-2201 Japan

Perovskite-type oxides $\text{Pb}(\text{ZrTi})\text{O}_3$ (PZT) and LaNiO_3 (LNO) are interesting materials for both applied and fundamental research. In spite of this, there are only a few papers devoted to its optical properties. Recently we have reported spectroscopic ellipsometry studies on LNO and PZT thin films performed in visible and near UV spectral regions [1,2]. Our further effort is focused on the development of a new dispersion model for these materials based on parameterization of the joint density of the electronic states in the vicinity of the valence and conduction bands [3,4]. Therefore, our beam time was used to record the UV and vacuum UV reflectivity spectra of PZT and LNO samples.

Polycrystalline PZT films were deposited by sol-gel and MOCVD on LNO/Pt/Ti/SiO₂/Si seed structure and platinized Si substrates Pt/SiO₂/Si respectively. Thin monocrystalline PZT film was grown by MOCVD on SRO/STO substrate. For the study of LNO reflectivity the seed structure for PZT films, LNO/Pt/Ti/SiO₂/Si, was used.

Selected spectral range (6 - 25eV) from UVSOR synchrotron radiation was scanned by the 3-m normal incidence monochromator (beam line 7B). Two monochromator gratings G2 (600 l/mm) and G1 (1200 l/mm) and LiF filter were used to cover the studied spectral range. Incident and reflected light intensity was measured in room temperature by a Si photodiode. Angle of incidence was less than 15 deg.

Fig. 1 presents selected reflectivity spectra of sol-gel deposited polycrystalline PZT and LNO films. Reflectivity in the visible and near UV spectral ranges was carried out by spectrophotometer PerkinElmer Lambda 45 and these data were used as a reference to adjust the absolute reflectivity values of UV and vacuum UV ranges. The spectral features up to about 5 eV come from the light interference in PZT and LNO films which thickness is 217 nm and 96 nm, respectively. Obtained reflectivity spectra are typical for transition metal oxide compounds with perovskite-type structure [5]. Detailed discussion of PZT and LNO electronic structure demand the knowledge of their electronic permittivity spectra and their parameterization by joint density of electronic states. This will be done in forthcoming paper.

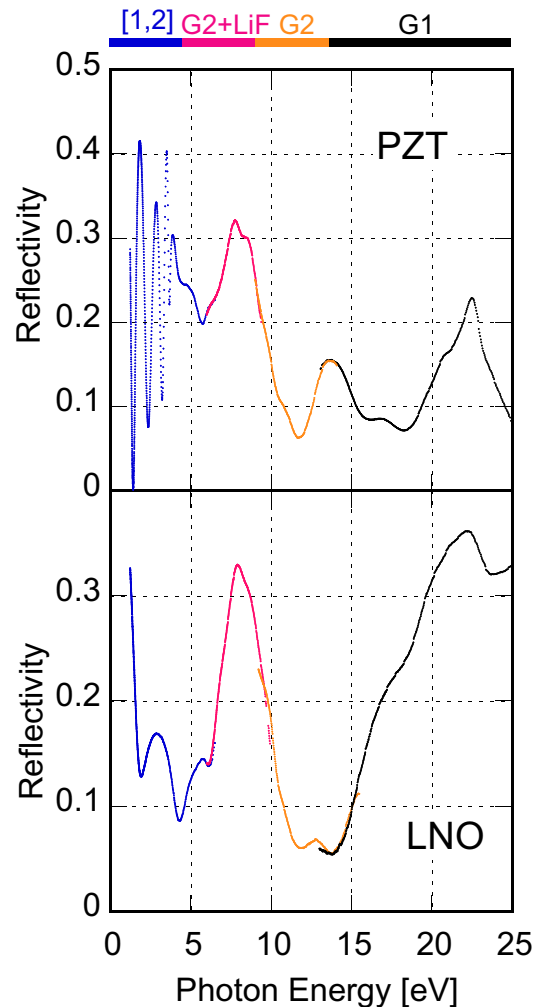


Fig. 1 Reflectivity spectra of PZT and LNO films

- [1] D. Franta, I. Ohlidal, J. Mistrik, T. Yamaguchi, G. J. Hu, and N. Dai, *App. Surf. Sci.* **244** (2005) 338-342.
- [2] J. Mistrik, T. Yamaguchi, D. Franta, I. Ohlidal, G. J. Hu, N. Dai, *App. Surf. Sci.* **244** (2005) 431-434.
- [3] D. Franta, B. Negulescu, L. Thomas, P. R. Dahoo, M. Guyot, I. Ohlidal, J. Mistrik, and T. Yamaguchi, *App. Surf. Sci.* **244** (2005) 426-430.
- [4] D. Franta, I. Ohlidal, M. Frumar, J. Jedelsky, *App. Surf. Sci.* **212-213** (2003) 116-121.
- [5] T. Arima, and Y. Tokura, *J. Phys. Soc. Jap.* **64** (1995) 2488-2501.

VUV Absorption Spectroscopy of SiO₂ Thin Film

K. Nakagawa, H. Mikami, T. Ishikawa, Y. Shiraishi,
A. Ejiri, H. Matsumoto, S. Matsumoto

School of Science & Technology, Meiji University, Kawasaki 214-8571 Japan

Absorption spectrum of silicon dioxide (SiO₂) thin film was studied in the VUV region with synchrotron radiation. Refractive index and extinction coefficient were carried out from Kramers-Kronig transformation using absolute values of absorption coefficients obtained from the experiment. It is necessary for accurate simulation to know absorption coefficients in higher photon energy region. On the basis of optical property of SiO₂, absorption spectrum in UV–VUV region is particularly important because of high band gap energy. Reflection spectrum of SiO₂ had been report by Philipp *et al.* [1], but the absorption spectrum of SiO₂ has not been studied. We report the absorption spectrum and optical constants n and κ of SiO₂ thin film up to 30 eV.

Experimental

The SiO₂ thin film was prepared by RF magnetron sputtering method. The SiO₂ plate with 99.99% purity was used as a target and the sputtering was carried out in argon gas under a total pressure of 0.8 Pa. The film was sputtered onto thin substrate of collodion at room temperature and the incident RF power of 100 W. The film thickness was about 15 nm.

The absorption spectrum of SiO₂ thin film was measured in the vacuum ultraviolet region up to 30 eV with the 3-m normal incident monochromator (grating: G1 and G2) at BL7B of UVSOR-II. And silicon photodiode sensor was used as a detector for the transmission light.

Results and Discussion

Figure 1 shows absorption coefficient of SiO₂ thin film at room temperature. The peaks are named as indicated in the figures for convenience. Five peaks named as A, B, C, D and E were observed at about 10.5 eV, 11.9 eV, 14.1 eV, 17.6 eV and 21.0 eV, respectively. One can see that peaks A, B, and C (below 15 eV) were characteristic sharp structure. Similar peaks have been found at the near position in the reflectance spectra of crystalline SiO₂ and fused SiO₂ reported by Philipp [1].

The optical constants were evaluated by the Kramers-Kronig analysis. Figure 2 shows the refractive index n and the extinction coefficient κ of SiO₂ thin film obtained by the Kramers-Kronig analysis from the absorption spectrum with experimental data. Refractive index and extinction coefficient obtained from experiment were measured with ellipsometer in the range from 1.5 eV to 5.0 eV. Comparing theoretical value and experimental value of optical constants, both values were good agreed with each other.

We calculate energy levels of SiO₂ by the DV-X α molecular orbital method. From the results of calculation, the valence band (VB) is almost composed of the O 2*p* orbital, which consists of two parts, lower part and higher part. And the lowest conduction band (CB) is composed of mixed orbital of Si 3*s*, Si 3*p* and Si 3*d*. It is found that the higher VB is very tight structure. Therefore, the sharp peaks in the region of near the fundamental absorption gap may be the transition from O 2*p* to mixed orbital of 3*s*, 3*p* and 3*d* in Si.

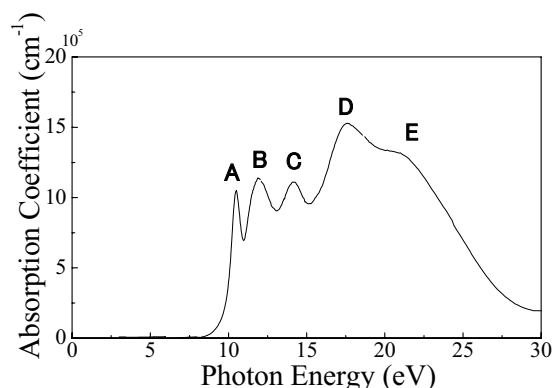


Fig. 1 Absorption spectrum of SiO₂ thin film in the region from 3 to 30 eV at room temperature.

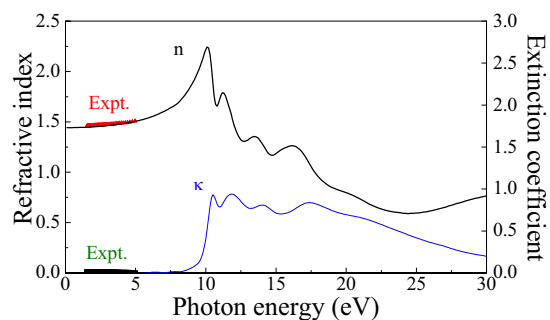


Fig. 2 Refractive index n and extinction coefficient κ spectra of SiO₂ thin film obtained by Kramers-Kronig analysis from the absorption spectrum.

[1] H. R. Philipp, *Solid. State. Commun.* **4** (1966) 73.

BL4B

Electronic Structure of DNA Characterized by Resonant Photoemission Spectroscopy

H. S. Kato¹, M. Furukawa¹, M. Kawai¹, M. Taniguchi^{1,2}, T. Kawai^{1,2},
T. Hatsui³, N. Kosugi³

¹RIKEN (The Institute of Physical and Chemical Research), Wako 351-0198 Japan

²Institute of Scientific and Industrial Research, Osaka University, Ibaraki 567-0047 Japan

³Institute for Molecular Science, Okazaki 444-8585 Japan

The characterization of electronic states near Fermi level of DNA duplexes has been desired to clarify the mechanisms of long-range charge migration in DNA, from the viewpoint of not only biochemistry but also molecular device materialization. Thorough stacking orbitals of DNA bases (Fig. 1), the dc conductivity model of DNA strands was proposed, over four decades ago, on the basis of electric conductivity measurements and a striking resemblance to conductive one-dimensional aromatic crystals. With the recent progress in nanotechnology, in addition, the electric conductivity of DNA has directly been measured in molecular scale. However, these characterizations of the electric property are still indefinite, and there is no significant observation on the electronic states near Fermi level of DNA for understanding of the charge migration mechanism. In this study, therefore, we carried out resonant photoemission spectroscopy (RPES) experiments near the Fermi level for both poly(dG)·poly(dC) (GC) and poly(dA)·poly(dT) (AT) DNA duplexes [1]. Since N atoms are included in only bases in DNA duplexes, the RPE spectra were obtained via the resonance from N 1s to unoccupied states, and thus we could purely extract the electronic orbital features of the bases in DNA.

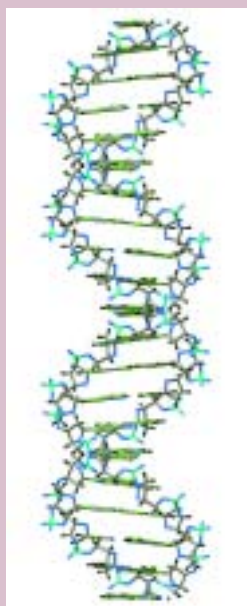


Fig. 1 Schematic structure of a DNA double helix.

Experimental

Experiments were performed at the beamline BL4B of the UVSOR facility, in which the end-station (ultrahigh vacuum systems) is equipped with an electron energy analyzer (Scienta SES200) and a retarding-field electron detector for X-ray absorption spectroscopy (XAS). The obtained RPE intensities were normalized by the excitation light intensity monitored as mesh current. We prepared thick GC- and AT-DNA films on SiO₂/p-Si(111) substrates in the atmosphere. The film thickness prepared was estimated to be 100 - 200 nm. Comparing our observed Raman spectra [2] to those previously reported, we confirmed that DNA in the prepared thick films forms a mixture of A- and B-form double helices. These samples were introduced into the ultrahigh vacuum via a sample entry system from the atmosphere, without baking procedures. Special care of freshness of DNA samples was taken throughout the experiments, to avoid any chemical changes. At the experiments, the sample was frequently replaced with new one, at least twice a day. This procedure also excluded accumulation of X-ray radiation damages on the surface. We confirmed suitable N 1s photoelectron spectra [2] for each sample.

Results and Discussion

An N *K*-edge XA spectrum of GC DNA is shown in the inset of Fig. 2. In the XA spectrum, two 1s - π* resonant peaks at 399.7 eV and 401.9 eV and a broad 1s - σ* resonant peak at 407 eV were observed. The off- and on-RPE spectra near the Fermi level of GC DNA are shown in Fig. 2 as a function of kinetic energy. The RPE spectra were measured at each resonant absorption peak marked on the XA spectrum shown in the inset. On the comparison to the off-RPE (normal Auger) spectrum, the on-RPE (resonant Auger) spectra are obviously involving additional components which is attributed to the N-*KLL* Auger electrons.

The resonant Auger signals could be extracted from the on-RPE spectra by subtracting the off-RPE spectra in binding energy plots, as the dotted lines in Fig. 2. The differential spectra commonly show a broad bump. Normally, the Auger electrons keep an identical distribution in kinetic energy, independently of excitation photon energies. The obtained resonant Auger signals were, however, strongly affected by

excitation energy; the lower photon energy light provides a higher kinetic energy distribution. This indicates that the excited electrons locate in the unoccupied states for, at least, a time scale of resonant Auger transition and affect its final state of the transition.

In addition, an appended component was observed at the first π^* resonance, as marked by a dagger in Fig. 2. We attribute the additional component to that of participant Auger transition. This finding again indicates that the excited electrons locate in the π^* states for, at least, the time scale of Auger transition.

In the case of the molecules chemisorbed on metals, such as CO/metals, their RPE spectra do not show the drastic peak shift of Auger electrons in kinetic energy. These are explained as that the molecular orbitals rehybridized with metal electronic states are delocalized, and the excited electrons in the chemisorbed molecules diffuse into the metal, immediately. In contrast, all features of the observed RPE spectra of DNA, as mentioned above, clearly show that the excited electron is localized at the excited orbitals. In other words, the unoccupied states of the bases in DNA duplexes are not delocalized.

The degree of the localization of excited electrons can be determined from the peak shift of resonant Auger signals, according to the report of Takata *et al.* [3]. For Ni metal, the *LMM* Auger peaks show a constant kinetic energy, *i.e.*, normal Auger transition behavior, under excitation above the photoabsorption maximum. For the $K_2Ni(CN)_4$ ionic crystal in which the $Ni(CN)_4$ complex exists as a quasi-isolated ion, on the other hand, the *Ni-LMM* Auger peaks show a downward shift as a function of photon energy with the slope of $\Delta KE/\Delta h\nu = -0.55 \pm 0.05$. For the vaporized Ca atom [4], the slope of a resonant Auger peak has been estimated to be -1, which would be the lower limit because of the condition ideally isolated. The upper limit must be zero as results at the Ni metal. In the case of DNA, the slope was estimated to be -0.5 ± 0.2 from the Auger peak shift shown in Fig. 1C. It is concluded that the degree of the localization of excited electrons at DNA bases is similar to that at the Ni complex in the ionic crystal.

Regarding electron migration mechanisms in DNA duplexes, several models have been proposed. Porath *et al.* carried out the conductivity measurements of a single GC DNA and described two antithetical models, namely, the charge hopping model between localized states and the charge transfer model through delocalized states [5]. They finally proposed that the charge transfer model is adequate on the basis of the observed voltage gap in I-V curves, although direct evidence could not be obtained. Our results, in contrast, clearly show the feature of the localized unoccupied orbitals of the bases in DNA. We hence conclude that the hopping model for electric conduction is pertinent when the electrons pass through the unoccupied states of bases.

Finally, we collate our results with recent

biochemical research on charge migration in DNA duplexes. In relation to the biochemical aspects of DNA damage and repair, the charge migration mechanisms in DNA duplexes have been extensively discussed. In these arguments, the carrier is regarded as a hole formed by oxidation and migrates through the bases in DNA duplexes. In spite of the detailed analysis of the LUMO structure described above, the HOMO structure cannot be directly revealed by RPES. However, it is generally expected that the energetically deeper orbitals are more compact than the shallow ones. Hence, the observation of the localized LUMO suggests the localized HOMO in DNA, which is consistent with recent findings; for the long-range charge migration, the hole hopping model between the localized DNA-base orbitals with short tunneling has been inferred.

In summary, we characterized the electronic structure near Fermi level of DNA duplexes using RPES, in order to specify the charge migration mechanism. On RPES, we observed the kinetic energy shift of N-*KLL* resonant Auger electrons and the intensity enhancement of valence electrons for both GC and AT DNAs. These directly indicate the localized unoccupied orbitals of the bases. Hence, we conclude that the charge hopping model is suitable for electric conduction in DNA duplexes rather than the charge transfer model via delocalized states, when electrons pass through the π^* states of DNA bases.

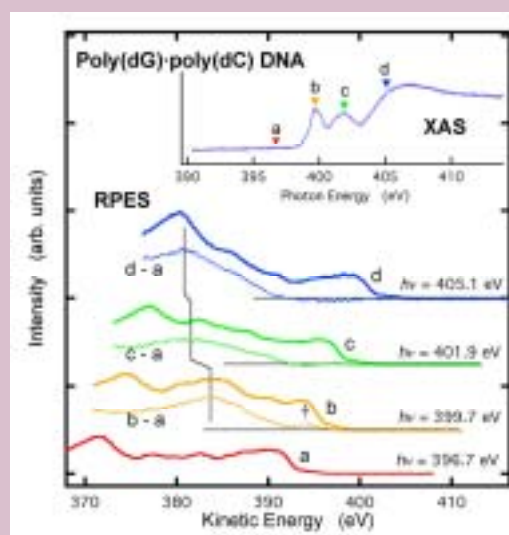


Fig. 2 Off- and on-RPE spectra of GC DNA. The inset shows an N *K*-edge X-ray absorption spectrum.

- [1] H. S. Kato, M. Furukawa, M. Kawai, M. Taniguchi, T. Kawai, T. Hatsui, and N. Kosugi, *Phys. Rev. Lett.* **93** (2004) 086403.
- [2] M. Furukawa *et al.*, (*to be published*).
- [3] Y. Takata, T. Hatsui, and N. Kosugi, *J. Electron Spectrosc. Relat. Phenom.* **101-103** (1999) 443.
- [4] K. Ueda *et al.*, *Phys. Rev. A* **54** (1996) 490.
- [5] D. Porath, A. Bezryadin, S. de Vries, and C. Dekker, *Nature* **403** (2000) 635.

Mo L_{III}-Edge XANES Study of MoO₃/H-MFI for GTL Catalysts

H. Aritani¹, S. Koyama¹, K. Otsuki¹, M. Fukushi¹, Y. Hoshino¹, S. Shinohara¹, A. Nakahira²
¹Department of Applied Chemistry, Saitama Institute of Technology, Okabe 369-0293, Japan
²Faculty of Engineering & Design, Kyoto Institute of Technology, Kyoto 606-8585, Japan

MoO₃-modified H-MFI zeolite (MoO₃/H-MFI) is a typical catalyst for so-called GTL (Gas-To-Liquid) one, which process needs to produce aromatics from natural gas. Because methane is a dominant compound in natural gas, direct conversion from methane to benzene is a catalytically desired process. For MoO₃/H-MFI catalyst system, Mo species are reduced during the reaction at high temperature (at around 973 K), and Mo-carbide species are formed mainly as an active species for methane activation. Then dehydrogenated methane is formed as carbene-like species on reduced Mo species, and followed by production of benzene onto H-MFI. For the catalytic process described above, redox behavior of Mo ions is an important role for catalytic activity for dehydroaromatization of methane. In particular, formed Mo species after the reaction needs to analyze for evaluation of catalytically active sites. Thus we characterized the active Mo species on H-MFI supports with various SiO₂/Al₂O₃ ratios by means of Mo L_{III}-edge XANES. In this report, local structure of supported Mo ions and their redox changes after dehydroaromatization of methane at 973 K for 3 h.

All the catalyst samples were prepared by impregnation of each silica-alumina support with AHM ((NH₄)₆Mo₇O₂₄•4H₂O) solution, and followed by drying and calcination at 773 K for 3 h. Amount of MoO₃-loading is 7.5wt% in all the samples. H-MFI supports were obtained by hydrothermal synthesis (at 343 K) from sodium silicate and aluminum chloride with TPABr template, and followed by filtration, H⁺-ion exchanging with NH₄OH solution, and calcination at 773 K. Mo L_{III}-edge XANES spectra were collected in BL1A beamline of UVSOR-IMS in total-electron yield (TEY) mode. XANES spectra of reference Mo compounds were shown in the previous report.

Fig. 1 shows XANES spectra of MoO₃/H-MFI with various Si/Al₂ ratios before/after methane dehydroaromatization. Before reaction, Mo species on H-MFI are due to Mo⁶⁺ in all the ratios. It is likely that components of Mo⁶⁺O₆ octahedra is larger than that of Mo⁶⁺O₄ tetrahedra in low Si/Al₂ ratio. After the reaction of methane dehydroaromatization, edge energy of XANES spectra in all samples becomes low, indicating reduction of Mo ions. In case of H-MFI with Si/Al₂ = 90, the spectrum is almost as same as that of Mo₂C, while Mo₂C can not be detected by XRD. It possesses the formation of well-dispersed Mo-carbide species on H-MFI as highly reduced ones. On the other hand, the spectrum in Si/Al₂ = 40 shows Mo₂C and another components. The spectrum in Si/Al₂ = 1880 suggests formation of slightly reduced

Mo sites partly. These results exhibit the highly reduction proceeds on H-MFI in Si/Al₂ = 90. These features can also be seen after ethene dehydroaromatization at 973 K. In fact, maximum benzene yield was obtained for MoO₃/H-MFI in Si/Al₂ = 90. It is concluded that formation of well-dispersed carbide species relates to the catalytic activity for GTL.

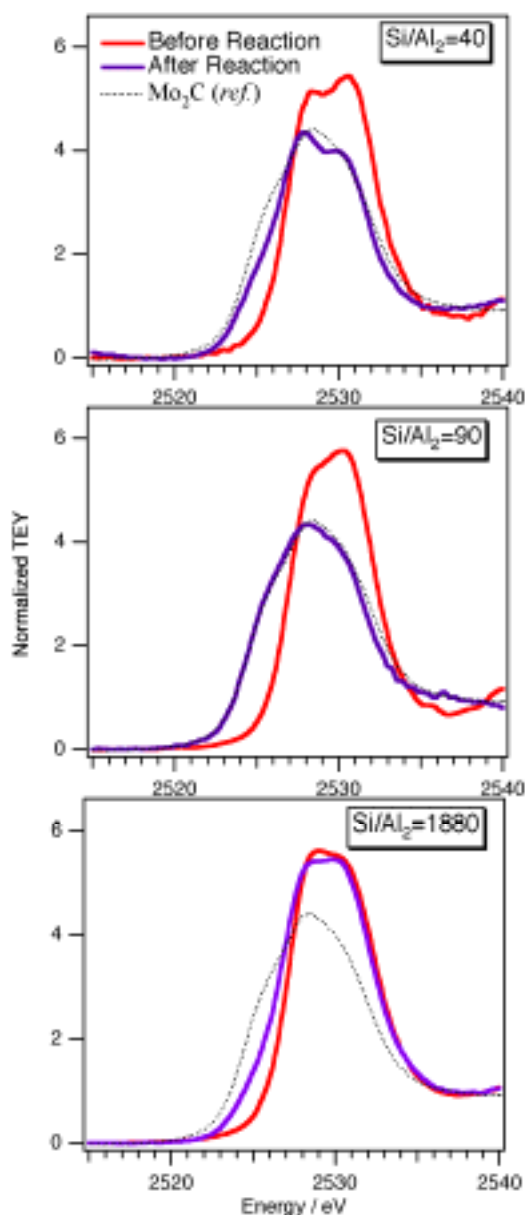


Fig. 1 Mo L_{III}-edge XANES spectra of MoO₃/H-MFI with various Si/Al₂ ratios before/after methane dehydroaromatization at 973 K.

X-Ray Absorption Near-Edge Fine Structure Study of AlInN Semiconductors

Q. X. Guo¹, J. Ding², Y. Mitsuishi¹, T. Tanaka¹, M. Nishio¹, H. Ogawa¹

¹*Department of Electrical and Electronic Engineering, Saga University, Saga 840-8502, Japan*

²*Venture Business Laboratory, Saga University, Saga 840-8502, Japan*

With a wide variable bandgap range, AlInN has great potential for applications in light-emitting diodes and laser diodes. This is particularly true, because in their natural crystal structures both AlN and InN have direct bandgaps. Moreover, Al_{0.83}In_{0.17}N can be used as a cladding layer with no strain on a GaN-based laser diode structure, leading to a reduction of defects because it is lattice-matched to GaN. In order to fulfill AlInN applications in commercially optical and electronic devices, many fundamental properties of this material should be clarified. X-ray absorption near-edge fine structure (XANES) refers to the region of the x-ray absorption spectroscopy spectrum dominated by strong photoelectron scattering that extends about 40 eV above an absorption edge, is a powerful tool to analyze electronic structures of materials, because spectral fine structure of XANES spectrum is very sensitive to a change in chemical environment. In this article, we report a characterization of AlInN using x-ray absorption measurements at the Al-*K* edges.

The AlInN thin films were prepared on (0001) sapphire substrates by reactive radio-frequency magnetron sputtering in an ambient of argon and nitrogen. The sputtering chamber was evacuated to a pressure of 10⁻⁷ Torr using a turbomolecular pump before introducing the sputtering gas. The sapphire substrates were chemically cleaned, degreased in organic solvents, etched in an acid solution, and then rinsed in deionized water. During the growth, the substrate temperature, total gas flow rate, and pressure were maintained at 100°C, 3 sccm, and 10 mTorr, respectively. The indium plate and the aluminum plate were separately mounted onto the targets and the sputtered area was varied in order to obtain AlInN films with the desired composition.

The XANES experiments were carried out at beam line BL1A of UVSOR facility in the Institute for Molecular Science, Japan. The XANES spectra were collected by recording the total yield of secondary electrons at room temperature. The photon flux was obtained simultaneously by measuring the current of an Au mesh located near the exit slit of the monochromator and used for normalization of the XANES spectra. Figure 1 shows the Al *K*-edge XANES spectra of Al_xIn_{1-x}N films at various Al compositions *x*. As shown in Fig.1, all the characteristics of XANES spectra, including the position and the slope of the absorption edge as well as the energy positions and the intensities of the resonances, depend strongly on the composition. The main peak labeled B is clearly observed in all samples

which include Al content. Its intensity increases with increasing Al content, although no linear relationship is observed because the intensity depends on both the Al content and the sample thickness and size. Therefore, we believe that the XANES spectrum can be a fingerprint of the composition of the nitride semiconductors since it is affected both by the central-absorbing atom and its neighboring atoms. Here, we note that the peak positions (A, B, and C) in Fig. 1 shift to lower energy with decreasing Al content.

Next, the XANES spectra of Al *K*-edge in wurzite AlInN was computed on the basis of the self-consistent-field real-space multiple-scattering (RSMS) theory calculations using the FEFF8 code. We find that the experimental and theoretical XANES spectra are in satisfactory agreement. Both the experimental curve shape and peak positions are reasonably reproduced in the theoretical spectra although there are some shifts in peak positions as well as differences in intensity. This discrepancy may be due to errors in the theory; for example, errors in the self-energy or the neglect of nonspherical corrections to the potential.

In conclusion, we have carried out the XANES measurements of AlInN at Al *K*-edge and the self-consistent-field real-space multiple-scattering theory calculations using FEFF8 code. It was demonstrated that the Al *K*-edge XANES spectra of AlInN are the fingerprints of their composition. The theoretical results could give a reasonable reproduction of the experimental spectral structures. This type of combined use of the experimental XANES and the RSMS calculations must be a powerful tool for systematic and qualitative analysis of the structural and electronic structures of nitride semiconductors.

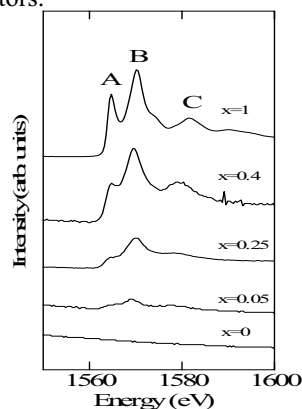


Fig. 1 Experimental Al *K*-edge XANES spectra for Al_xIn_{1-x}N.

Study on the Surface Structure of Cathode Electrode for Li-Ion Battery Cells with High Power-Type

H. Kobayashi¹, Y. Arachi², S. Emura³

¹Research Institute for Ubiquitous Energy Devices, AIST, Ikeda, Osaka, 563-8577 Japan

²Unit of Chemistry, Faculty of Engineering, Kansai University, Suita, Osaka, 564-8680 Japan

³ISIR, Osaka University, Ibaraki, Osaka, 567-0047 Japan

Lithium ion battery has attracted the interest on the application for fuel cell vehicle (FCV) because of the promising high-power sources. On the other hand, the battery for FCV requires the long period life over 15 years. Therefore, the development of the estimation method of the pulse cycle and calendar life has been strongly needed and several mechanisms have been proposed to explain the deterioration in battery performance. Although the deterioration in battery performance has instinct problem on the electrodes, the mechanism of deterioration on the electrodes is still unclear. Detailed information on the change in the both cathode and anode electrodes is very important in order to determine the origin of battery performance of electrochemical performance of battery cell. In this study, the XANES spectra about the cathode electrode after pulse cycle tests were collected by the total electron yield (TEY) method and the relationships between the changes in the surfaces and their electrochemical properties were studied.

Experimental

We used the cylindrical battery cells of c.a. 400 mAh for this study. $\text{LiNi}_{0.8}\text{Co}_{0.2}\text{O}_2$ -based material and hard carbon were used for positive and negative electrode, respectively. Each cell was characterized using standard battery test procedure given in the partnership for a new generation of vehicles (PNGV) Battery Test Manual. We checked the changes in the cell capacity and DC resistance at every several cycles. The SOC0% and SOC100% cathode electrode obtained from the battery after PNGV tests were washed with DMC and then Ni/Co *L*-edges and O *K*-edge were measured by the TEY method on BL1A or BL8B1 at UVSOR, respectively.

Results

The results after pulse cycle tests are summarized in Table 1. The decrease in capacity and increase in DC resistance were observed with increasing temperature. These results indicated that battery performance deteriorated when battery cells were used at high temperature. ICP and XRD results indicated that the valence state of Ni and Co increased to higher valence state for SOC0% samples and the valence state of Ni and Co decreased to lower valence state for SOC100% samples after the pulse cycle tests in this system, and showed that no degradation of crystallinity and appearance of impurity phases were observed for cathode material. On the other hand, both Ni and Co *L*-edges XANES results of SOC0% and 100% samples

showed the shifts of L_{III} and L_{II} peaks to higher energy above 40°C, indicating the increase in the valence state of Ni and Co on the surface. Figure 1 shows Ni *L*-edge XANES spectra for the SOC100% cathode materials. In addition, the O *K*-edges XANES spectra of SOC100% sample after test at 60°C showed the additional peak similar to NiO together with pre-edge peak originated from $\text{LiNi}_{0.8}\text{Co}_{0.2}\text{O}_2$ -based phase, indicating the existence of cubic phase on the surface. These XANES results indicated that the surface structure became to be different from bulk one after pulse cycle tests. The TEY method using soft X-ray gave us useful information to understand the origin of battery performance of battery performance.

Table 1 Results of pulse cycle test.

	$I_{\text{max}}^{\text{p}}$	DOD	Cycles	Relative Capacity	Relative DC resistance
20°C	10C	3%	50000	0.960	1.08
40°C	10C	3%	50000	0.946	1.11
40°C	20C	3%	50000	0.951	1.13
40°C	10C	30%	3000	0.932	1.25
60°C	10C	3%	50000	0.907	1.28

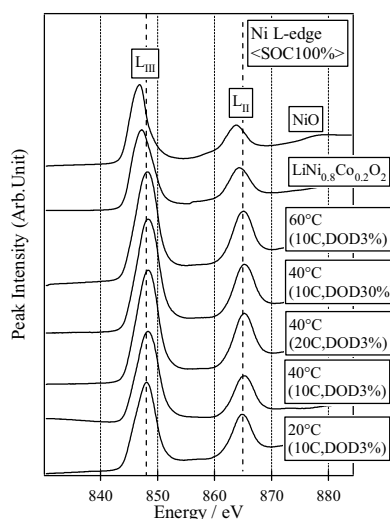


Fig. 1 Ni *L*-edge XANES spectra for the cathode materials. NiO and $\text{LiNi}_{0.8}\text{Co}_{0.2}\text{O}_2$ are given as reference.

Acknowledgement

This work was supported by Ministry of Economy, Trade and Industry (METI) and New Energy and Industrial Technology Development Organization (NEDO).

Crystal and Electronic Structures of the $\text{LiNi}_{0.45}\text{Mn}_{0.45}\text{Al}_{0.10}\text{O}_2$

H. Kobayashi¹, I. Teshima²

¹Research Institute for Ubiquitous Energy Devices, AIST, Ikeda, Osaka, 563-8577 Japan

²Department of Molecular Science and Technology, Faculty of Engineering, Doshisha University, Kyotanabe, Kyoto, 610-0321 Japan

$\text{LiNi}_{1/2}\text{Mn}_{1/2}\text{O}_2$ -based materials are one of the promising cathode materials of lithium secondary battery because of their large capacity and high thermal stability. Especially, $\text{LiNi}_{1/3}\text{Mn}_{1/3}\text{Co}_{1/3}\text{O}_2$ displays a reversible capacity of 170 mAh/g in the voltage range 2.5 to 4.5 V and keep the layered structure over 280 °C [1]. A lot of papers have reported on electrochemical performance of the $\text{Li}_{1-y}\text{Ni}_{1/2}\text{Mn}_{1/2}\text{O}_2$ -based materials until now. We have studied these materials from the perspective of structure and found the characteristic structural change during Li de-intercalation for $\text{LiNi}_{1/2}\text{Mn}_{1/2}\text{O}_2$ [2]. On the other hand, the relationship between the crystal and electronic structures are still ambiguous in these systems. Detailed information on the electronic structures is very important in order to improve the electrochemical properties of these materials and, therefore, the crystal and electronic structures of $\text{LiNi}_{0.45}\text{Mn}_{0.45}\text{Al}_{0.10}\text{O}_2$ were investigated in this study.

Experimental

$\text{LiNi}_{0.45}\text{Mn}_{0.45}\text{Al}_{0.10}\text{O}_2$ was synthesized in air at 1273 K for 24 h using appropriate molar ratios of $\text{LiOH}\cdot\text{H}_2\text{O}$, $\text{Mn}(\text{CH}_3\text{COO})_2\cdot 6\text{H}_2\text{O}$, $\text{Ni}(\text{CH}_3\text{COO})_2\cdot 6\text{H}_2\text{O}$, and AlNO_3 . The de-lithiated samples were prepared electrochemically using coin-type cells with Li/1M LiPF_6 in EC:DEC(1:1)/samples. Crystal and electronic structures were investigated by synchrotron XRD (BL02B2 at SPring-8), XAFS (BL7C at PF), and the total electron yield (BL1A/BL8B1 at UVSOR) measurements. The crystal structure was determined using the computer program RIETAN2000.

Results

$\text{LiNi}_{0.45}\text{Mn}_{0.45}\text{Al}_{0.10}\text{O}_2$ was single-phase and adopted the α - NaFeO_2 structure. The Ni and Co *K*-edge XANES spectra showed that $\text{LiNi}_{0.45}\text{Mn}_{0.45}\text{Al}_{0.10}\text{O}_2$ can be represented as $\text{Li}(\text{Ni}^{2+}_{0.45}\text{Mn}^{4+}_{0.45}\text{Al}^{3+}_{0.10})\text{O}_2$. Structural analysis using synchrotron XRD data demonstrated that the lattice parameters of $\text{LiNi}_{0.45}\text{Mn}_{0.45}\text{Al}_{0.10}\text{O}_2$ are $a = 2.881 \text{ \AA}$ and $c = 14.31 \text{ \AA}$ and that the chemical composition can be expressed referring to the Wyckoff positions 3*a* and 3*b* with the space group *R3m* as $[\text{Li}_{0.92}\text{Ni}_{0.08}]_{3a}[\text{Li}_{0.08}\text{Mn}_{0.45}\text{Ni}_{0.37}\text{Al}_{0.10}]_{3b}\text{O}_2$. The fraction of Ni on the 3*a* site is almost equal to be those observed for $\text{LiNi}_{0.5}\text{Mn}_{0.5}\text{O}_2$ and $\text{LiNi}_{0.5}\text{Mn}_{0.4}\text{Ti}_{0.1}\text{O}_2$ [3]. $\text{Li}_{1-y}\text{Ni}_{0.45}\text{Mn}_{0.45}\text{Al}_{0.10}\text{O}_2$ corresponded to the composition for showing a charge capacity of 170 mAh/g. Figure 1 shows the Ni *L*-edge and O *K*-edge XANES spectra in $\text{Li}_{1-y}\text{Ni}_{0.45}\text{Mn}_{0.45}\text{Al}_{0.10}\text{O}_2$. The Ni

L-edge XANES results showed that divalent nickel metal is oxidized to tetravalent through trivalent after charging, while the O *K*-edge showed no change over the whole composition range. These results clarified that the Li de-intercalation/ intercalation from $\text{LiNi}_{0.45}\text{Mn}_{0.45}\text{Al}_{0.10}\text{O}_2$ proceeded mainly by the valence state change of Ni without the contribution of oxygen over the whole composition range.

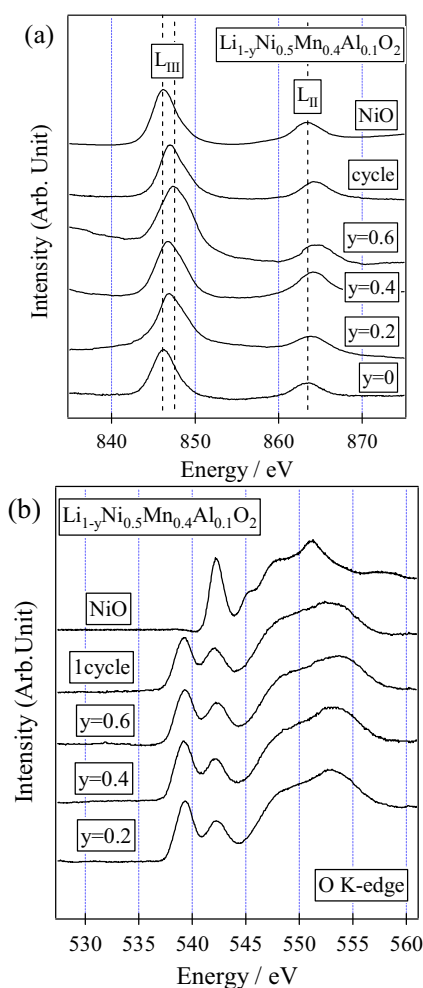


Fig. 1 Ni *L*-edge (a) and O *K*-edge (b) XANES spectra in $\text{Li}_{1-y}\text{Ni}_{0.45}\text{Mn}_{0.45}\text{Al}_{0.10}\text{O}_2$.

- [1] N. Yabuuchi and T. Ohzuku, *J. Power Sources*, **119-121** (2003) 171-174.
- [2] H. Kobayashi, Y. Arachi, K. Tatsumi, and H. Kageyama, *J. Mater. Chem.* **14** (2004) 40-42.
- [3] H. Kobayashi, Y. Arachi, H. Kageyama, H. Sakaebe, K. Tatsumi, D. Mori, R. Kanno, and T. Kamiyama, *Solid State Ionics*, **175** (2004) 221-224.

Investigation of Local Structure for Low Crystalline Calcium Phosphate Prepared by Anodic Oxidation of Ti Metal

A. Nakahira¹, H. Aritani², K. Konishi¹, S. Nishida¹, K. Kubo¹, S. Takaezoe¹, M. Ohta¹

¹*Faculty of Engineering & Design, Kyoto Institute of Technology, Matsugasaki, Sakyo, Kyoto 606-8585, Japan*

²*Faculty of Engineering, Saitama Institute of Technology, Okabe, Saitama 369-0293, Japan*

Introduction

In biomaterials, hydroxyapatite and calcium phosphates are expected to be used as an implant material. Since especially, calcium phosphate and hydroxyapatite with low crystallinity, not high crystallinity, are active for bone formation, the developments of low crystalline calcium phosphate and hydroxyapatite are desired. On the other hand, Ti metal is also one of the useful implant materials. However, Ti metal has no bioactivity for bone formation in body. Therefore, the calcium phosphate coating on Ti metal is important process for the achievement of the high bioactivity for Ti implants. In general, coatings of calcium phosphate are carried out by sol-gel coating and arc plasma methods. Recently, many studies on anodic oxidation of Ti metal are titanium oxide films prepared by are reported for novel developments of titanium oxides and other oxides coating on Ti metal. In addition, this anodic oxidation method is considered to be useful to prepare the calcium phosphate materials on Ti. In special, doping some anions into oxide is easy to perform by anodic oxidation methods.

In this study, the low crystalline calcium phosphate samples were synthesized by an anodic oxidation of Ti metal using the mixture of calcium salts and H₃PO₄ solution at room temperature. Because in medical application, this low crystalline calcium phosphates are more effective for the osteoconduction, compared to high crystalline calcium phosphate, the information of low crystalline calcium phosphates are considered to be useful for developing the high performance implant materials. The purpose is to clarify the local structure of P ion in low crystalline calcium phosphate. The investigation of local structure for this low crystalline calcium phosphate prepared by the anodic oxidation method was carried out at BL1A in UVSOR.

Experiment

Ti metal (10 mm × 10 mm × 0.4 mm) was used as an anode and carbon black (φ5 mm × 10 mm, Toyo carbon) was used as a cathode. The distance between electrodes was about 3 cm. Ti substrate was polished using abrasive paper. Finally it was washed with dionized water and dried in atmosphere before it was used as an electrode. After polishing, the Ti substrate was soaked in solution mixed with glycerophosphoric acid calcium salt (GP) and H₂O. Anodic oxidation performed under 50 V, 150 V, 250 V, and 350 V supplied direct current power.

Results and Discussion

The samples obtained by the anodic oxidation in this experiment were identified to be a calcium phosphate with low crystallinity by the results of powder X-ray diffraction analysis. P-K local structure for this low crystalline calcium phosphate prepared by the anodic oxidation method was examined at BL1A in UVSOR. The XANES spectra of low crystalline calcium phosphates obtained by anodic oxidation in solution mixed with GP and H₂O are shown in Figure 1 (shown by GP-Anodic Oxidation in figure). All spectra of low crystalline calcium phosphates synthesized by anodic oxidation were similar, although the low crystalline calcium phosphates obtained by anodic oxidation at higher voltage of 50 V and 350 V possess P⁵⁺. From these results of XANES spectra at P-K edge, P local structures for low crystalline calcium phosphates synthesized by anodic oxidation method of Ti was similar to those of Ca₂P₂O₇, not hydroxyapatite (HAP). These results will lead to the development of the high performance implant materials.

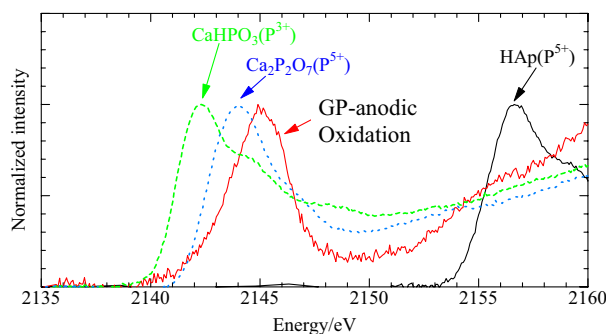


Fig. 1 XANES of P-K edge of low crystalline calcium phosphates. GP-anodic oxidation was the sample synthesized by an anodic oxidation processing. HAP shows hydroxyapatite. CaHPO₃ and Ca₂P₂O₇ are reference materials.

Investigation of Local Structure of P-K Edge for Titania Prepared by Anodic Oxidation of Ti Metal

A. Nakahira¹, H. Aritani², K. Konishi¹, S. Nishida¹, K. Kubo¹, S. Takaezoe¹, M. Ohta¹

¹*Faculty of Engineering & Design, Kyoto Institute of Technology, Matsugasaki, Sakyo, Kyoto 606-8585, Japan*

²*Faculty of Engineering, Saitama Institute of Technology, Okabe, Saitama 369-0293, Japan*

Titanium oxide (titania) is one of useful materials for photocatalyst, although titania is classified into anatase-type, rutile-type, and brookite-type. Usually, various synthesis methods, such as sol-gel, sputtering, chemical processings, and so on, have been reported by many researchers for the synthesis of titania. Although, in general, the coatings of titania on Ti substrate are carried out by sol-gel coating and arc plasma methods, these coatings have such problems that the strength between titania and Ti is weak and sometimes the delamination is generated between titania and Ti. On the other hand, anodic oxidation method of Ti metal is a unique method for preparation of strong titania coating on Ti metal. Furthermore, In addition, this anodic oxidation method is considered to be significantly useful to prepare the high performance titania coating with doping some anions. Namely, it is expected that such doping into titania is easy to perform by this anodic oxidation methods. So, this anodic oxidation will be applicable for the modification of titania by successful doping of various ions into titania on titanium metal for photocatalyst.

In this study, the various synthesis of titania doped of P ion was attempted by an anodic oxidation of Ti metal using the mixture of H₃PO₄ solution at various temperatures ranging room temperature and 343 K. The investigation of local structure, in main XANES, for this P-doped titania prepared by the anodic oxidation method in this study was carried out at BL1A in UVSOR.

Experiment

Ti metal (10 mm × 10 mm × 0.4 mm, Nilaco. Co. Ltd) was used as an anode and carbon black (φ5 mm × 10 mm, Toyo carbon) was used as a cathode. Ti substrate was polished using abrasive paper, washed with deionized water and finally dried in atmosphere before it was used as an electrode. The distance between electrodes on anodic oxidation processing was kept to be approximately 3 cm. Ti substrate was soaked in solution mixed with glycerophosphoric acid sodium salt (Na-GP) and aqueous H₃PO₄ at room temperature. Other samples were synthesized in the mixture of glycerophosphoric acid calcium salt (Ca-GP) and aqueous H₃PO₄ solution at room temperature. For comparison, Ti substrate was soaked only in aqueous H₃PO₄ solution. Anodic oxidation processing in this study was performed under a voltage of 350 V supplied with direct current power (TP0650-01, Takasago Seisakusho, Co. Ltd, Japan).

Results and Discussion

The samples obtained by anodic oxidation processing at a voltage of 350 V were identified to be anatase with low crystallinity by powder X-ray diffraction analysis. P-K local structure for these low crystalline titania samples prepared by the anodic oxidation method was examined at BL1A in UVSOR. Figure 1 shows the results of XANES of P-K of some titania samples prepared by anodic oxidation method and also some reference materials. The XANES spectra of titania obtained by anodic oxidation were similar to one of Ti₃(PO₄)₄, although the position of its peak was not agreement with ones of other references. From these results of XANES spectra at P-K edge, P local structures of titania with low crystallinity prepared by anodic oxidation method was almost similar to one of Ti₃(PO₄)₄.

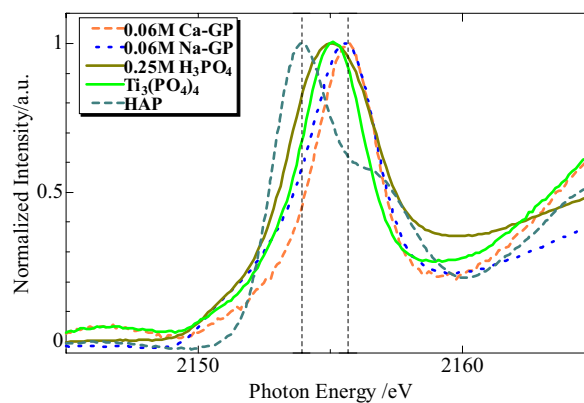


Fig. 1 XANES of P-K of some titania samples prepared by anodic oxidation method. Ca-GP samples were synthesized in the mixture of glycerophosphoric acid calcium salt (Ca-GP) and aqueous H₃PO₄ solution at room temperature. Na-GP samples were synthesized in the mixture of glycerophosphoric acid sodium salt (Na-GP) and aqueous H₃PO₄ solution at room temperature.

Characterization of Mixed Valence Complexes of Platinum by an XAFS Method

H. Yamashige¹, K. Kuroiwa², T. Kurisaki¹, H. Wakita^{1,3}

¹Department of Chemistry, Faculty of Science, Fukuoka University, Nanakuma, Jonan-ku, Fukuoka 814-0180, Japan

²Department of Chemistry and Biochemistry, Graduate School of Engineering, Kyushu University, Higashi-ku, Fukuoka 812-8581, Japan

³Advanced Materials Institute, Fukuoka University, Nanakuma, Jonan-ku, Fukuoka 814-0180, Japan

There has recently been much interest in the one-dimensional (1D) halogen-bridge metal complexes [1], because of their unique physical properties in the mixed-valence state or, equivalently, the commensurate charge density wave (CDW) state.

In this work, we applied X-ray absorption fine structure (XAFS) spectroscopy to structure analysis of the 1D chloro-bridged Pt complexes: $[\text{Pt}^{\text{II}}(\text{en})_2][\text{Pt}^{\text{IV}}(\text{en})_2\text{Cl}_2]\text{X}_4$ ($\text{X} = \text{ClO}_4, \text{Glu}, \text{Asp}$). The X-ray absorption spectra were measured at BL1A of the UVSOR in the Institute of Molecular Science, Okazaki [2]. The energy of the UVSOR storage ring was 750 MeV and the stored current was 110-230 mA. Cl *K*-edge absorption spectra were recorded in the region of 2533-3733 eV by use of two Ge(111) crystals. The absorption was monitored by the total electron yield using a photomultiplier. The Cl *K* XANES spectra for three Pt complexes are shown in Fig. 1. A pre-edge peak and a main peak are observed in these spectra.

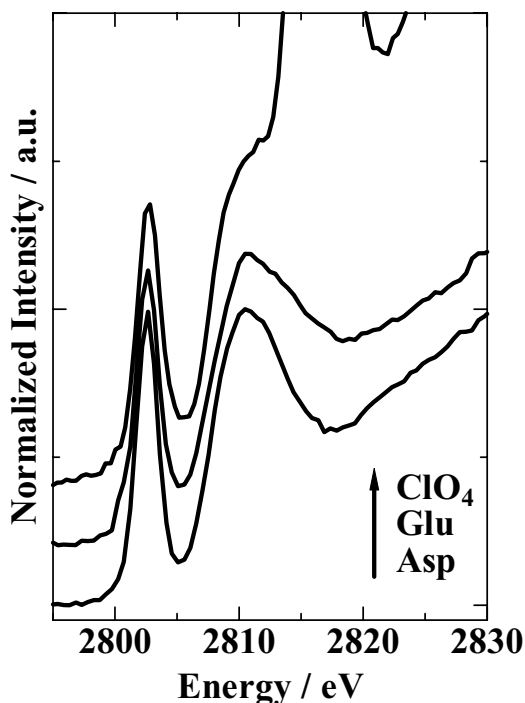


Fig. 1 Observed Cl *K*-edge XANES spectra of $[\text{Pt}^{\text{II}}(\text{en})_2][\text{Pt}^{\text{IV}}(\text{en})_2\text{Cl}_2]\text{X}_4$ ($\text{X} = \text{ClO}_4, \text{Glu}, \text{Asp}$).

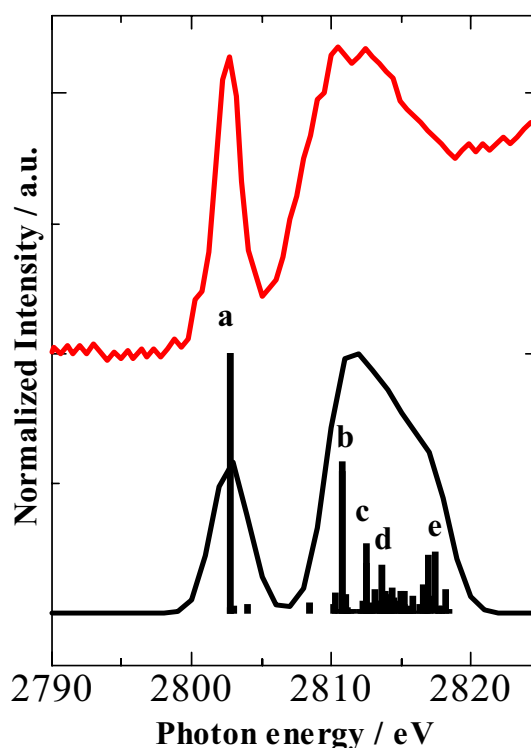


Fig. 2 Observed and calculated Cl *K*-edge XANES spectra of $[\text{Pt}^{\text{II}}(\text{en})_2][\text{Pt}^{\text{IV}}(\text{en})_2\text{Cl}_2](\text{Glu})_4$.

Observed and calculated Cl *K* XANES spectra for the $[\text{Pt}^{\text{II}}(\text{en})_2][\text{Pt}^{\text{IV}}(\text{en})_2\text{Cl}_2](\text{Glu})_4$ complex are shown in Fig. 2. The two peaks are estimated to the electron transition (pre-edge peak: Cl *1s* to Pt *5d*, main peak: Cl *1s* to mixed orbital). As a result of many other calculated data, the energy gap of two peaks is related to the distance between Pt and Cl atoms.

[1] P. Day, in H. J. Keller (eds.), *Low Dimensional Cooperative Phenomena* (Plenum, New York, 1974) 191.

[2] S. Murata, T. Matsukawa, S. Naoè, T. Horigome, O. Matsuodo, and M. Watatabe, *Rev. Sci. Instrum.* **63** (1992) 1309.

Three-Dimensional Band Dispersion of CeTe₂

T. Ito^{1,2}, H. J. Im², S. Kimura^{1,2}, Y. S. Kwon³

¹UVSOR Facility, Institute for Molecular Science, Okazaki 444-8585, Japan

²School of Physical Science, The Graduate University for Advanced Studies, Okazaki 444-8585, Japan

³BK21 Physics Research Division and Institute of Basic Science, Sungkyunkwan University, Suwon 440-746, Korea

Low-dimensional compounds have attracted much attention because of their anomalous electronic/magnetic properties, especially the coexistence of the charge density wave (CDW) formation and the antiferro-magnetism. Since their anomalous properties have been attributed to the low dimensionality, in turn, the three-dimensionality at the electronic structure is important to understand the essential nature of the anomalous properties.

Angle-resolved photoemission spectroscopy (ARPES) is one of powerful methods to directly determine the electronic band structure as well as the Fermi surface topology. However, there are few examples of the ARPES determination of the three-dimensional electronic structure by controlling the excitation energy and the detecting angle. To elucidate the three dimensionality at the electronic structure of low-dimensional compounds, we have performed the photon-energy dependent ARPES on the quasi-two dimensional CeTe₂, which crystallizes in the layered structure formed by the planar Te(1) sheet sandwiched by the corrugated CeTe(2) double layers [1].

Figure 1 shows the photon-energy dependence of the ARPES spectra of CeTe₂ at normal emission ($k_{\parallel} = 0 \text{ \AA}^{-1}$), obtained at UVSOR-II BL5U with using synchrotron radiation source. Since the control of the photon-energy at $k_{\parallel} = 0 \text{ \AA}^{-1}$ directly corresponds to the trace of the electronic structure along ΓZ axis, we have mapped out the dispersive feature of the ARPES peaks as a function of photon energy and binding energy. Here, we use the dispersion relation

$$(\hbar/2\pi)k_{\perp} = \sqrt{2mE_K \cos^2\theta + V},$$

where V is inner potential, E_K is kinetic energy at E_F and $\theta = 0^\circ$. At the left panel in Fig. 2, we show the experimental band structure along ΓZ line where $V \sim 15 \text{ eV}$ is expected from the symmetry of the dispersive features. In Figs. 1 and 2, we clearly find the two types of bands; one is almost non-dispersive bands at 0.5 and 1.0 eV binding energies, and the other is the bands with a large dispersion from 1.0 eV (1.8 eV) to 1.5 eV ($< 1.7 \text{ eV}$) along ΓZ line. From the comparison with the band calculation of the reference compound LaTe₂ (right panel in Fig. 2), the former has been attributed to the Te $5p$ orbital at the Te(1) plane (green lines), while the latter to one at the CeTe(2) plane (blue lines). The observed

highly-dispersive feature may suggest the possible three-dimensionality on the electronic structure of quasi-two dimensional CeTe₂.

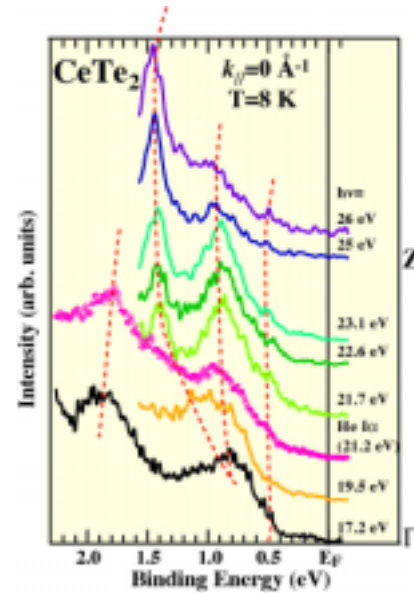


Fig. 1 Photon-energy dependence of ARPES spectra of CeTe₂. Note that the spectrum with $h\nu = 21.2 \text{ eV}$ is obtained by using the He I α resonance line.

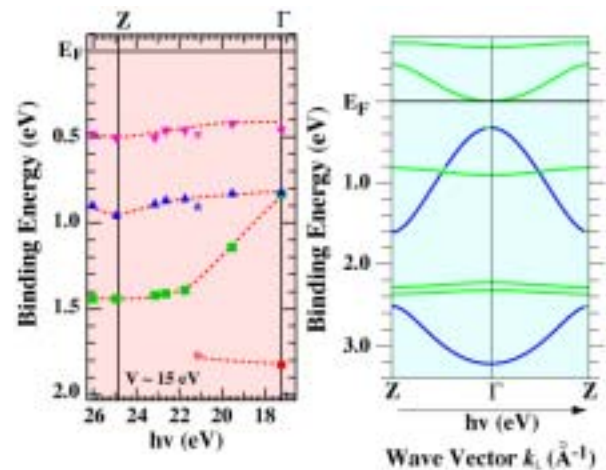


Fig. 2 (Left panel) Experimental band structure along ΓZ high-symmetry line of CeTe₂. Symbols and dashed lines are the ARPES peak positions and guide for eyes, respectively. (Right panel) LDA band calculation along ΓZ high-symmetry line of LaTe₂.

[1] M.H. Jung *et al.*, Phys. Rev. B **62** (2000) 11609.

Ce 4d - 4f Resonant Photoemission Spectroscopy on CeNi_{1-x}Co_xGe₂

H. J. Im¹, T. Ito^{1,2}, B. K. Lee³, S. Kimura^{1,2}, Y. S. Kwon³

¹*School of Physical Science, The Graduate University for Advanced Studies, Okazaki 444-8585, Japan*

²*UVSOR Facility, Institute for Molecular Science, Okazaki 444-8585, Japan*

³*BK21 Physics Research Division and Institute of Basic Science, Sungkyunkwan University, Suwon 440-746, Korea*

CeNi_{1-x}Co_xGe₂ were newly found Ce-based ternary alloys, where the ground states continuously change from a local-moment magnetism ($x = 0 - 0.2$) to an intermediate valence ($x = 0.4 - 1.0$) regimes through a quantum-critical point (QCP) ($x = 0.3$) by the hybridization between the Ce 4f and Ni/Co 3d states with the similar lattice constants in this series [1]. To elucidate the systematic change of the electronic (magnetic) structure as a function of the $d - f$ hybridization strength through QCP, we have performed Ce 4d - 4f resonant photoemission (RPE) spectroscopy on CeNi_{1-x}Co_xGe₂ with varying the Co - substitution from $x = 0$ to $x = 1.0$.

Polycrystalline CeNi_{1-x}Co_xGe₂ were grown by the arc-melting and annealed at 900°C for 3 weeks in an evacuated quartz tube. The Ce 4d - 4f RPE measurements were carried out at UVSOR-II BL5U with the energy resolution of about 150 meV at $h\nu = 122$ and 115 eV which correspond to Ce 4d - 4f on- and off- resonance energies, respectively. The clean surfaces were prepared by fracturing the polycrystalline samples *in situ* under vacuum of 2×10^{-8} Pa. The Fermi level of the sample was referred to a gold film evaporated onto the sample substrate.

Figure 1 shows the Co-substitution dependence of the Ce 4d - 4f on- (upper panel) and off- (lower panel) RPE spectra measured at $T = 5$ K. While the off- RPE spectra are formed by the Ni/Co 3d main peaks around 1.8/0.6 eV, the on- RPE spectra show additional structures around 2 and 0.3 eV where the strong Ce 4f character has been expected by the single-impurity Anderson model (SIAM) [2]. With increasing Co- substitution, $d -$ states shift from 1.8 to 0.6 eV in the off- RPES spectra and the spectral weight at E_F seems to be enhanced in consistent with the corresponding LDA band calculation. On the other hand, the spectral weight of Ce 4f structures transfers from 2.2 eV to 0.3 eV. From the comparison with the SIAM calculation on the various kind of Ce-based heavy fermion compounds [2], we have assigned that the former Ce 4f structure comes from the Ce 4f⁰ final states with a localized Ce 4f character, while the latter from the Ce 4f¹ final states with a itinerant (or strongly hybridized) Ce 4f electrons. Thus, the systematic changes of the $d -$ bands and the Ce 4f states may be attributed to the increased $d - f$ hybridization strength from the localized CeNiGe₂ to the itinerant CeCoGe₂.

Finally, we can briefly comment on the change of

the electronic structure around QCP. It has been expected by the thermodynamic experiments that the Ce 4f electronic structures show anomaly at QCP [1]. On the other hand, the Ce 4f electronic structures around 2.2 and 0.3 eV in Fig. 1 show no anomalous change between $x = 0.2$ and $x = 0.4$. We can say that the observed contradiction strongly suggests the continuous change of the Ce 4f electronic structures from localized to itinerant regime, at least, in the valence band region. To elucidate the relation between the anomalous properties at QCP and the systematic change of the Ce 4f electronic structures through QCP, further studies (detailed analysis based on SIAM, temperature dependent RPE experiments, etc) are intended.

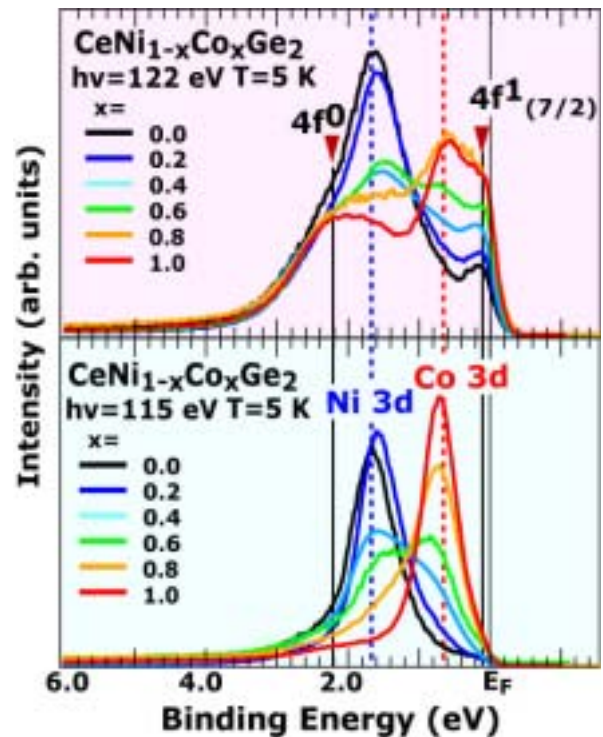


Fig. 1 Co-substitution dependence of the Ce 4d - 4f on - (Upper panel) and off - RPE spectra (lower panel), obtained with using $h\nu = 122$ eV and 115 eV photons at $T = 5$ K, respectively.

[1] B. K. Lee *et al.*, Phys. Rev. B (2005) in press.

[2] For example, D. Malterre *et al.*, Adv. Phys. **35** (1986) 275.

Electronic Structure of Zr-TM-Al (TM = Ni, Cu) Bulk Metallic Glasses

K. Soda¹, T. Suzuki¹, H. Miyazaki¹, M. Inukai¹, M. Kato¹, S. Yagi¹, T. Takeuchi², U. Mizutani¹, T. Taketomi³, M. Hasegawa³, T. Ito⁴, S. Kimura⁴

¹Graduate School of Engineering, Nagoya University, Furocho, Chikusa-ku, Nagoya 464-8603, Japan

²Ecotopia Science Institute, Nagoya University, Furocho, Chikusa-ku, Nagoya 464-8603, Japan

³Institute for Materials Research, Tohoku University, Katahira, Aoba-ku, Sendai 980-8577, Japan

⁴UVSOR, Institute for Molecular Science, Myodaijicho, Okazaki 444-8585, Japan

Introduction

Bulk metallic glasses are new materials having useful engineering properties such as high mechanical strength, good ductility, and high corrosion resistance. In order to understand the origins of their large glass formation ability and unique properties from the microscopic point of view, we have studied the electronic structure of bulk metallic glasses Zr-TM-Al (TM = Ni, Cu) by use of photoelectron spectroscopy.

Experimental

Photoelectron spectra were recorded under an ultrahigh vacuum of 2×10^{-8} Pa at low temperatures with a high-resolution energy analyzer at BL5U. Total energy resolution and the origin of the binding energy E_B , *i.e.* the Fermi level E_F , were determined by the Fermi edge of an evaporated Au film.

Specimens were bulk metallic glasses $Zr_{65}Ni_{25}Al_{10}$, $Zr_{50}Cu_{35}Al_{15}$, $Zr_{66.7}Cu_{25.8}Al_{7.5}$, and $Zr_{55}Al_{10}Cu_{30}Ni_5$ in a size of ϕ 2 mm x 3 mm and attached on a copper plate by conductive glue. Their supercooled liquid regions $\Delta T_x = T_x - T_g$ (T_x : crystallization temperature, T_g : glass transition temperature), one of the parameters representing the stability of these metallic glasses, are 52.0 K, 61.8 K, 99.8 K and 87.9 K, respectively. Clean surfaces for the measurement were prepared by *in situ* scraping the specimen with a diamond file.

Results and Discussions

Figure 1 shows typical valence-band photoelectron spectra of the metallic glasses recorded at 30 K with the excitation photon energy $h\nu$ of 40 eV. They are normalized by the intensity integrated up to the binding energy E_B of 10 eV. Three features around $E_B = 0.6$ eV, 2.0 eV and 3.7 eV are ascribed to the Zr 4*d*, Ni 3*d* and Cu 3*d* states, respectively. It seems that the peak positions of the Zr 4*d*-derived bands, indicated by arrows in the figure, are located at the higher binding energy as the metallic glass is more stable. This may imply that the hybridization of Zr 4*d* states with the states of its neighboring atoms, or the chemical bonding around Zr, becomes strong with the stability. Valence-band spectra near E_F recorded with $h\nu = 18$ eV are shown in Fig. 2 for the metallic glasses and a reference Au. The detailed analysis shows that the

intensity is reduced in comparison with Au below the binding energy indicated by arrows, which suggests that a pseudo-gap in the *sp* bands of these glasses may increase with the phase stability [1].

The present results show how the electronic states of the metallic glasses contribute to their large glass formation ability. Further systematic study is intended for Zr-Ni-Al and Zr-Cu-Al metallic glasses with different compositions.

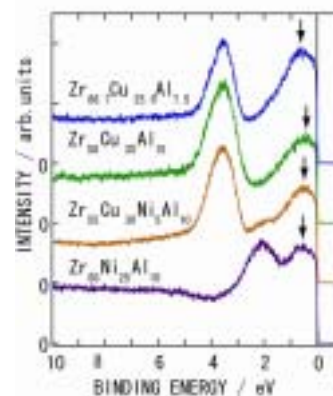


Fig. 1 Valence-band spectra of Zr-TM-Al (TM = Ni, Cu) recorded with $h\nu = 40$ eV.

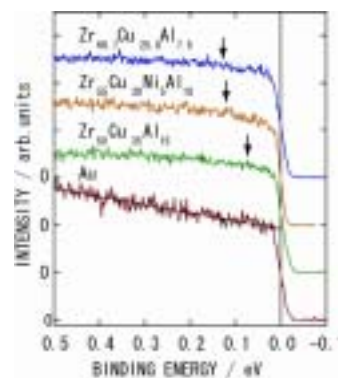


Fig. 2 Valence-band spectra near the Fermi level of Zr-TM-Al (TM = Ni, Cu) and Au recorded with $h\nu = 18$ eV.

[1] K. Soda *et al.*, J. Electron Spectrosc. & Relat. Phenom., *in press*.

Surface Photo-Voltage Effect on Cr/GaAs(100) Surface Studied by Combination of SR and Laser

K. Takahashi, Y. Nagata, S. Tokudomi, J. Azuma, M. Kamada

Synchrotron Light Application Center, Saga University, Saga 840-8502 Japan

Electronic non-equilibrium in the surface layer of photo-excited metal/semiconductor interfaces has been attracting much interest from the basic scientific point of view and also from the practical applications for photo-electronic or spin-electronic devices. In order to elucidate the electronic non-equilibrium in the surface layer of metal/semiconductor interfaces, it is indispensable to understand the transient state of photo-excited semiconductor surface. In this work, we have performed photoemission spectroscopy for Cr/GaAs(100) surface with the combinational use of synchrotron radiation and laser.

Experimental

Experiments were performed at BL5U. N-type (Si-doped, $3.0 \times 10^{16} \text{ cm}^{-3}$) and p-type (Zn-doped, $3.0 \times 10^{18} \text{ cm}^{-3}$) GaAs(100) wafers were used as the substrate. An As-capped GaAs(100) wafer was used as n-type substrate. An As capping layer was removed by heating the sample in the ultra-high vacuum. The clean surface of p-type substrate was obtained by the Ne^+ -ion sputtering and annealing cycles. We used the mode-locked Ti:Sapphire laser (COHERENT Mira 900-F) which is synchronized with the synchrotron radiation in the multi-bunch operation. The time-resolved photoemission measurements in nano-second region were performed by the so-called pump-probe technique with the synchrotron radiation and laser. The laser light was transported to the viewport of the main experimental chamber using an optical fiber. The laser light was then focused onto the sample surface with a 3 mm radius spot. The spatial overlap of the laser with the synchrotron radiation was adjusted by eyes.

Results and Discussions

Figure 1 shows the Ga 3d photoemission spectra with and without laser illumination measured at 80K. The delay time between laser and SR is 0 ns. The Cr coverage is also shown in the figure. These core-level spectra were deconvoluted into bulk, surface and eventually reacted components, using a least-square curve fitting technique. The curve fitting parameters for Ga 3d (Lorentzian width, spin-orbit splitting, and branching ratio) were identical to those reported for GaAs(100) clean surface [1]. The Ga 3d peak is composed of one bulk and two surface components and reproduced well with same fitting parameters as those reported in Ref. 1. The bulk and surface components shift to 0.23 eV higher binding energies at the Cr deposition of 0.05 nm. This energy shift corresponds to the increase of the band-bending. The further deposition of Cr produces new reacted

components at lower binding energy. At the Cr deposition of 0.5 nm, two reacted components are clearly observed at 0.76 and 1.02 eV lower binding energies than the bulk component. The spectral intensity of bulk component decrease with the Cr deposition and two surface components disappear at the Cr deposition of 0.2 nm.

As shown in Fig. 1, it is clearly seen that the peak position of the Ga 3d spectrum is shifted to lower binding energy under the laser excitation. From the conjunction with our previous studies for GaAs(100) clean surface, we have concluded that the present core-level shift is originated from the surface photo-voltage (SPV) effect. It is found that the Ga 3d peak shows larger SPV shift than that for clean surface at the Cr deposition of 0.05 and 0.10 nm. A simple SPV formula derived from the depletion approximation scheme with excess photo-carriers suggests that the surface with larger band-bending shows larger SPV value. The Cr deposition, as mentioned above, leads the increase of the band-bending. Thus, the small amount of Cr deposition leads the increase of the SPV shift. On the other hand, the further depositions of Cr decrease the SPV shift, while the band-bending value is larger than that of clean surface. The SPV value also depends on amount of the photo-excited carriers. It is considered that the small SPV values at large Cr coverage is due to the lifetime of photo-excited carriers shorter than the pulse width of the probe light.

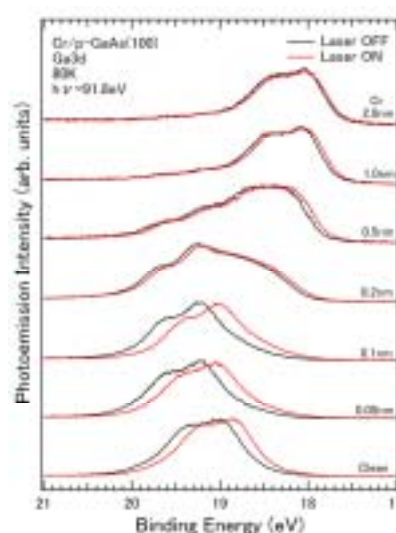


Fig. 1 Ga 3d photoemission spectra with and without laser illumination.

[1] D. Mao *et al.*, Phys. Rev. B **45** (1992) 1273.

Photoelectron Spectroscopic Study of Fe Films on NEA Surface

N. Takahashi¹, S. Nakanishi², H. Itoh², S. Koshiba², T.-H. Shen³,
T. Zhang⁴, S. Tanaka⁵, K. Takahashi⁶, M. Kamada⁶

¹Department of Physics, Kagawa University, Takamatsu 760-8522, Japan

²Department of Advanced Materials Science, Kagawa University, Takamatsu 761-0396, Japan

³Institute for Materials Research, University of Salford, Greater Manchester M5 4WT, UK

⁴Blackett Lab, Imperial College of Science, Technology and Medicine, London SW7 2BZ, UK

⁵Research Center for Materials Science, Nagoya University, Nagoya 464-8602, Japan

⁶Synchrotron Light Application Center, Saga University, Saga 840-8502, Japan

NEA (negative electron affinity) semiconductors are used as efficient photocathodes, due to their high degrees of polarization and efficiency. However, from a fundamental science point of view, the details of NEA formation are not fully understood [1]. On the other hand, the study of magnetic thin films on semiconductor substrates has been widely carried out due to the applicability to magneto-electronics devices, such as the Spin Polarised Field Effect Transistor [2]. As a typical basis for such devices, the Fe/GaAs system has been extensively studied for decades [3] because of its great promise in the possible use of hybrid ferromagnetic metal-semiconductor structures for applications. In this report, we present a study of a Fe covered NEA.

Experiment

All experiments were carried out at RT in UHV chamber with the base pressure of about 3×10^{-8} Pa. A Zn doped (1×10^{19} atoms/cm³) p-GaAs(100) wafer with (8×2) surface reconstruction was used as a substrate. The NEA intensity was measured as the absolute value of the photocurrent from the biased (-10 V) sample while the He-Ne laser was on and off. Fe was deposited on the NEA surface a total of 5 times, yielding estimated coverages of 9.7 (after the first Fe deposition, Fe#1), 29 (Fe#2), 68 (Fe#3), 97 (Fe#4) and 115 Å (Fe#5). Photoelectron spectroscopy was carried by using 100 eV.

Results and Discussion

The relative NEA intensity is shown in Figure 1 as a function of Fe coverage and is compared with the lowering of the work function. The intensity is kept at 50, 20 and 7 % of the maximum intensity obtained from the pure NEA surface after Fe depositions Fe#1, #2 and #3, respectively. The intensity decreases with increasing coverage, although the work function is almost constant even at thicker coverages. This is in good agreement with the literature [1] which suggests that the band bending is not a sufficient condition for the amplitude of the NEA effect.

Figure 2 shows normalized core peaks from (a) Cs 4d, (b) As 3d and (c) Ga 3d levels. Spectra from the bottom to the top of each panel indicate different stages of Fe growth (layers Fe#1 and Fe#2, respectively) after NEA treatment. The Cs 4d and Ga 3d peaks shift to higher kinetic energies, and a new

component is seen to grow at the lower energy side of the As 3d peak. The Ga 3d peak appears to obtain a higher energy side component whilst losing a lower side one. Moreover, the width of the Cs 4d peak was found to decrease.

It was found that the Fe covered surface still has NEA characteristics which is comparable to the standard NEA, even in the thicker Fe coverage region of about 100 Å. Furthermore, the change of NEA intensity appears to be independent of the change of the work function. The core level peak results imply that the overlayer has a complicated structure, dependent on its depth from the top of the layer.

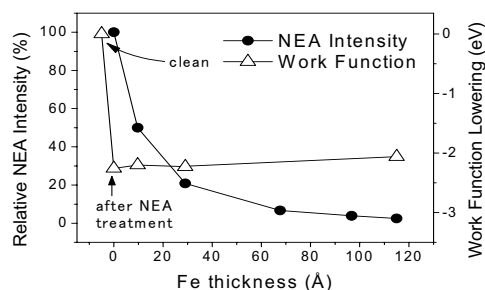


Fig. 1 The variation of the relative NEA intensity and the relative work function lowering of the sample.

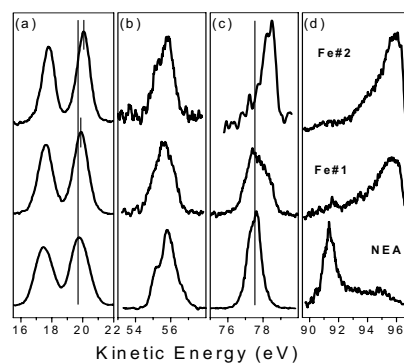


Fig. 2 Panel (a), (b) and (c) show core peaks from Cs 4d, As 3d and Ga 3d levels, respectively. Panel (d) is the VB.

- [1] ex, S. Moré *et al.*, Surface Science **527** (2002) 41.
[2] S. Datta and B. Das, Appl. Phys. Lett. **56** (1990) 665.
[3] J. Shen *et al.*, Surface Science **500** (2002) 300.

Electronic Structure of Relevant Crystals of Bulk Metallic Glasses

T. Takeuchi¹, S. Nakano², T. Kondo², T. Kitao², T. Ito³, S. Kimura³

¹*EcoTopia Science Institute, Nagoya University, Nagoya 464-8603 Japan*

²*Department of Crystalline Materials Science, Nagoya University, Nagoya 464-8603 Japan*

³*Institute for Molecular Science, Okazaki 444-8585 Japan*

Amorphous metals are generally produced by rapidly solidification techniques, such as liquid quenching and vapor deposition methods. These techniques restrict the sample shape to ribbons or thin films. Recently, however, formation of amorphous metals without rapidly quenching was reported for Zr-based, Fe-based, and Pd-based alloy systems, and amorphous metals with bulk shape of nearly ten centimeter in dimension had been produced. Since amorphous phase are characterized by high mechanical strength and extremely soft magnetic properties, amorphous phase with bulk shape encourages us to utilize it in a large number of applications. Unfortunately, however, guiding principles to produce “stable” amorphous phases and to control their physical properties have not been well understood yet. In order to utilize them in many applications, it is highly required to investigate their “stabilization” mechanism.

To gain deep insight into the origin of their stabilization mechanism, we have to evaluate the free energy of the bulk amorphous phases. Internal energy and entropy should be equally taken into account to estimate the free energy of the amorphous, whereas the crystalline phases are stabilized dominantly by the contribution of the internal energy. If the covalent bonds associated with d -orbital of the constituent transition-metal elements reduce the internal energy of the relevant crystals, local atomic arrangements (clusters) in the crystals especially around the transition metal elements should be regarded as the most important factor for the phase stabilization. This consideration lets us strongly believe that the local atomic clusters in the relevant crystals exist also in the corresponding amorphous phase, and their random arrangements leads to sufficient reduction in the free energy both by the low internal energy and the large entropy.

In order to confirm validity of this idea, we analyzed the local atomic clusters in the relevant crystals of the Zr-Ni-Al amorphous phase. As the simplest approximation, all coordination polyhedra centered at a Zr atom in the crystalline phases are picked up. Their compositions are calculated by assuming that the surrounding atoms supply $1/Z$ of single element, where Z is the coordination number of the surrounding atom. We found as a result of this analysis that the composition of the most “stable” amorphous phase is surrounded by compositions of the local atomic clusters of the relevant crystals. The entropy associated with the random arrangement of the clusters was calculated on the basis of the

well-known Bragg-Williams approximation. The resulting entropy possess its maximum value in the vicinity of the composition for the largest $\Delta T_x = T_x - T_g$, where T_x and T_g represent crystallization temperature and glass-transform temperature of the amorphous phase, respectively. This result strongly suggests the crucial role of the entropy in reducing free-energy of the bulk amorphous phases.

The internal energy associated with covalent orbital was investigated using the DXV α cluster calculation. The validity of the resulting energy levels was confirmed by the high-resolution photoemission spectroscopy, HRPES. HRPES measurements were carried out in the BL5U of the UVSOR, Okazaki. The incident photon energy was selected to be 20 ~ 40 eV, with which high-flux and high-energy resolution of $\Delta E \sim 20$ meV are simultaneously obtained.

We confirmed that the calculated cluster levels associated with d -orbital of the Zr atoms reproduce well the energy levels of the d -orbital measured by the HRPES. From the calculated cluster levels, total energy of the clusters was quantitatively evaluated. We confirmed that the difference of the internal energy among the all clusters stays within the energy scale of ST at $T_x \sim 700$ K.

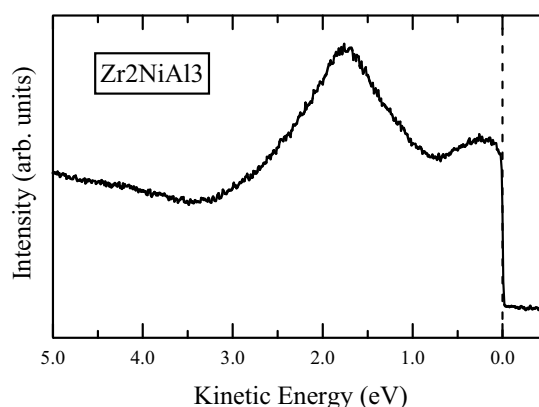


Fig. 1 HRPES spectrum of the Zr_2NiAl_3 with $h\nu = 20$ eV at 20 K. Two peaks centered at 1.8 eV and 0.3 eV correspond to the Ni 3d and Zr 4d orbitals, respectively. Widely extending d -orbitals are brought about by the hybridization of d -orbitals with s,p -orbitals of the surrounding elements.

Surface-Passivant Dependence of Photoemission Spectra of Alkanethiolate-Passivated Au Nanoparticles on the HOPG Substrates

A. Tanaka¹, M. Imamura^{1,2}, R. Saito^{1,2}

¹*Department of Mechanical Engineering, Kobe University, Kobe 657-8501, Japan*

²*Department of Physics, Tohoku University, Sendai 980-8578, Japan*

The chemically synthesized metallic nanoparticles surface-passivated by various organic molecules are attracting much interest from the viewpoints of both fundamental and device physics, since they show the distinctive physical and chemical properties found in neither bulk nor molecular/atomic systems. In order to develop the future nanostructured devices using these organic-inorganic hybrid nanoparticles, it is especially indispensable to understand the interface features as well as their electronic structures. In this work, we have carried out a systematic photoemission study of alkanethiolate- (AT-) passivated Au nanoparticles on the HOPG substrates in order to characterize their interface features.

The synthesis procedure of AT-passivated Au nanoparticles is described elsewhere [1]. We have used the octanethiol ($C_8H_{17}SH$, OT), dodecanethiol ($C_{12}H_{25}SH$, DT), and hexadecanethiol ($C_{16}H_{33}SH$, HDT) as the surface-passivants of AT molecules. Photoemission measurements were performed at BL5U of UVSOR Facility. Photoemission measurements were performed with the incident photon energy of 190 eV at room temperature. Further ultraviolet photoemission measurements with the He I resonance line ($h\nu = 21.2$ eV) as the excitation source were performed at Kobe University.

From the low-energy cutoff of the ultraviolet photoemission spectrum due to the vacuum level measured with He I resonance line (not give here), it is found that the effective work functions of the present all AT-passivated Au nanoparticles with mean diameters of 4 nm are smaller than bulk Au crystallite. Moreover, these effective work functions are smaller than the previously reported ones of self-assembled monolayers of AT molecules on the Au surfaces [2], and exhibit no surface-passivant dependence. This change in the surface potential is considered to originate from the interface dipoles formation at AT molecules-Au nanoparticle heterojunction. These interface dipoles are considered to be composed of the intrinsic dipoles of AT molecules (dipole moment of the hydrocarbon tail region) and the dipoles induced by charge transfer due to the Au-S chemical bonds formation. In order to characterize the bonding nature at the interface between AT molecules and Au nanoparticle surface, we have performed the Au $4f$ core-level photoemission measurements as shown in Fig. 1. As previously reported [2, 3], Au $4f$ core-level spectra of AT-passivated Au nanoparticles consist of two components. The components with lower binding energy (blue lines in Fig. 1) and higher binding energy (red lines in Fig. 1) originate from the inner Au atoms

of Au nanoparticles (bulk component) and the surface Au atoms of Au nanoparticles bonded to surface-passivants of AT molecules (surface component), respectively. As shown in Fig. 1, the chemical shifts of the surface components relative to the bulk components are almost same among the present AT-passivated Au nanoparticles. This indicates that the charge transfer between the surface passivants of AT molecules and Au nanoparticle surfaces and the resultant dipoles are almost same among the present AT-passivated Au nanoparticles. Therefore, the intrinsic dipoles of AT molecules dominate the dependence of effective work function on the surface-passivant molecules, and are almost same among the present AT-passivated Au nanoparticles.

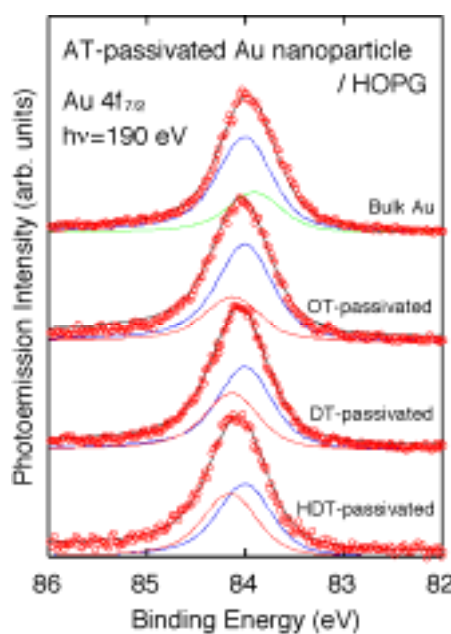


Fig. 1 Au $4f_{7/2}$ core-level photoemission spectra of various AT-passivated Au nanoparticles with mean diameter of 4 nm on the HOPG substrates bulk Au polycrystalline film for a comparison.

- [1] M. Imamura and A. Tanaka, submitted.
 [2] D. M. Alloway, M. Hofmann, D. L. Smith, N. E. Gruhn, A. L. Graham, R. Colorado, Jr., V. H. Wysocki, T. R. Lee, P. A. Lee, and N. R. Armstrong, *J. Phys. Chem. B* **107** (2003) 11690.
 [3] A. Tanaka, Y. Takeda, T. Nagasawa, and K. Takahashi, *Solid State Commun.* **126** (2003) 191.
 [4] A. Tanaka, Y. Takeda, M. Imamura, and S. Sato, *Phys. Rev. B* **68** (2003) 195415.

Desorption of Ionized Clusters from Water Physisorbed on Solid Neon

T. Tachibana¹, Y. Yamauchi¹, T. Miura¹, T. Hirayama², M. Sakurai³, I. Arakawa¹

¹*Dept. Phys., Gakushuin Univ., Mejiro, Toshima, Tokyo 171-8588, Japan*

²*Dept. Phys., Rikkyo Univ., Nishiikebukuro, Tokyo 171-8501, Japan*

³*Dept. Phys., Kobe Univ., Rokkodai, Nada, Kobe 657-8501, Japan*

There has been a growing interest in the properties of ice surface and ice particle for both fundamental and practical points of view in the field of surface, environmental and planetary sciences. Understanding electronic excitations and relaxation processes of water molecule is one of the most important subjects in these fields. A variety of studies have been made on electron- and photon-stimulated desorption (ESD/PSD) at ice surface [1, 2].

We have investigated the PSD of $(\text{H}_2\text{O})_n\text{H}^+$ from water physisorbed on solid Ne. From the measurements of the desorption yield as a function of the incident photon energy, the desorption of $(\text{H}_2\text{O})_n\text{H}^+$ is effectively and indirectly induced by the multiple-excitation and -ionization of rare gas substrates. The direct excitation of the water molecule does not induce noticeable desorption of $(\text{H}_2\text{O})_n\text{H}^+$.

The PSD-experiments have been carried out in an ultra high vacuum system at the beam line 5B at UVSOR in Institute for Molecular Science, Okazaki. The mass spectrum of PSD ions was measured by a time-of-flight (TOF) technique. The desorption yield was normalized by the light intensity, which was continuously monitored by the photoemission current from a gold-plated mesh inserted in the beam lines. The sample film was prepared on a Pt(111) substrate, which was fixed to a liquid He cryostat and cooled down to 6 K. The sample was irradiated by the photon in the energy range between 6 and 1000 eV. The incident angle of the photon beam was 20 deg from the normal.

Photodesorption yield of $(\text{H}_2\text{O})_n\text{H}^+$ [$n = 2 - 5$] from water adsorbed on Ne substrate in the 38 - 100 eV photon energy is shown in Fig. 1. The desorption yield increases gradually from 60 eV to 90 eV of the excitation energy. The threshold of ESD $(\text{H}_2\text{O})_n\text{H}^+$ from ice surface was reported at 70 eV [1], however we have not observed the threshold-like increase of the yield near 70 eV excitation energy. The increase of $(\text{H}_2\text{O})_n\text{H}^+$ desorption yield above 60 eV is probably related to direct double photoionization of Ne because the threshold energy is reported at 62.5 eV in the gas phase [3]. This result leads us to the conclusion that the desorption of $(\text{H}_2\text{O})_n\text{H}^+$ is caused by the multiple-hole states of the rare gas substrates.

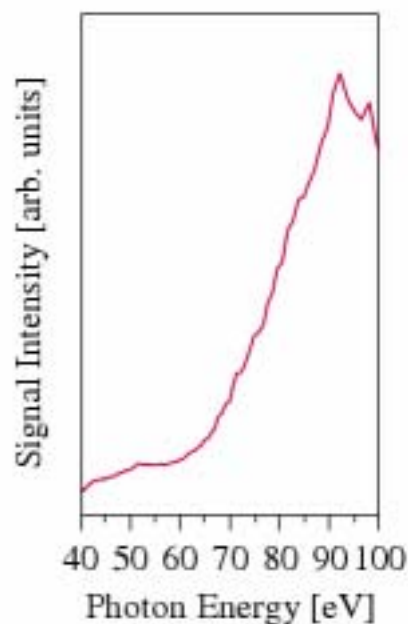


Fig. 1 $(\text{H}_2\text{O})_n\text{H}^+$ desorption yield [$n = 2 - 5$] as a function of the incident photon energy from water (0.2 ML) on solid Ne (100 ML) in the 40 - 90 eV energy range at 6 K of the sample temperature.

[1] J. Herring, A. Aleksandrov, and T. M. Orlando, *Phys. Rev. Lett.* **92** (2004) 187602.

[2] R. Rosenberg, V. Rehn, V. Jones, and A. Green, *Chem. Phys. Lett.* **15** (1981) 488

[3] R. Bartlett and P. J. Walsh, *Phys. Rev. A* **46** (1992) 5547.

Characterization of Carbon-Based Material Formed by Focused-Ion-Beam Chemical-Vapor-Deposition

K. Kanda, J. Igaki, Y. Kato, R. Kometani, S. Matsui

University of Hyogo, Laboratory of Advanced Science and Technology for Industry, Kamigori, Hyogo, 678-1205 Japan

Nano-structure fabrication using focused ion beam-chemical vapor deposition (FIB-CVD) has been achieved in view of the production of the numerous three-dimensional nano-tools [1]. The nano-structural material formed by FIB-CVD was considered to be composed of the carbon-based material, however the structural properties has not been sufficiently understood. In the present study, we will show that the combination of Raman spectroscopy, near-edge x-ray absorption fine structure (NEXAFS) spectroscopy and other analyses can provide useful information on the structure of carbon-based material formed by FIB-CVD method.

The NEXAFS measurement was performed at the BL8B1 stage of UVSOR in the Institute for Molecular Science. The synchrotron radiation provided by the 0.75 GeV electron storage ring was dispersed by a constant-deviation constant-length spherical grating monochromator and was perpendicularly irradiated to the sample film surface. The NEXAFS C *K*-edge spectra were measured in the energy range 275-320 eV with 0.5 eV FWHM resolution. The detection of electrons coming from sample was performed in the total electron yield (TEY) mode. The intensity of the incident photon beams I_0 was measured by monitoring the photocurrent from a gold film. The absorption signal was given by the ratio between the out-coming electron intensity from the sample I_s and the intensity from the gold film, I_0 .

Figure 1 depicts the NEXAFS carbon *K*-edge spectrum of carbon material formed by 30 kV Ga⁺ FIB-CVD using *Phenanthrene* as a source gas. For comparison, the spectra of commercial diamond-like-carbon (DLC) produced by ion-plating (IP) method and graphite are also depicted in the figure. NEXAFS was useable for the characterization of amorphous carbon materials [2]. Resonance peaks of 291.9 and 292.8 eV, which are characteristic of graphite, are not observed in the NEXAFS spectrum of FIB-CVD DLC. The peaks at 295.1 eV and 297.8 eV are assignable to resonance peaks to the σ^* states from 1s level of carbon atom neighboring Ga atoms, which are residue from ion beam. A resonance at about 285.4 eV is due to transitions from C 1s level to unoccupied π^* states of sp^2 (C=C) sites. The sp^2 content of the DLC films formed by FIB-CVD method is smaller than that of the IP DLC film. This result is consistent with that the hardness measurement of the FIB-CVD DLC (67 GPa) and IP DLC (26 GPa). As the result, FIB-CVD method can construct ultra-hard structure, because the deposited material by this method is DLC with a high content of sp^3 hybridized carbon.

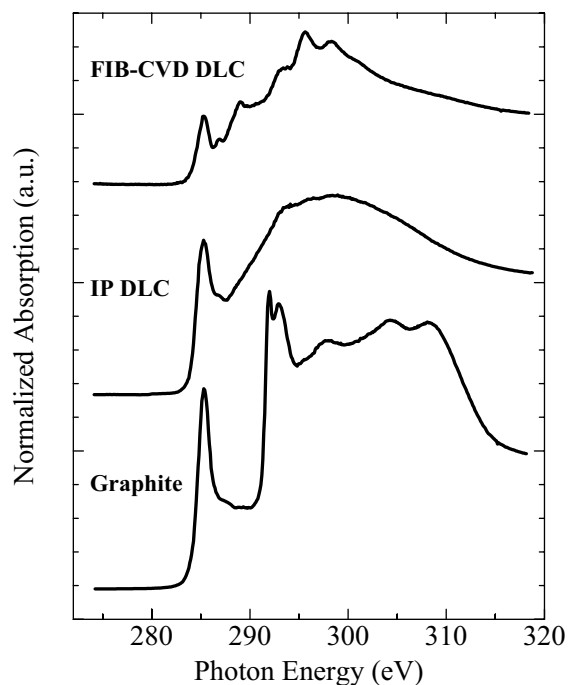


Fig. 1 NEXAFS spectra in the C *K*-edge of FIB-FVD DLC, IP DLC and graphite: The pre-edge resonance at 285.4 eV is due to the C 1s $\rightarrow \pi^*$ transitions. The broad band between 290 and 310 eV is the result of overlapping C 1s level to σ^* unoccupied states of sp , sp^2 and sp^3 sites. The sharp peak at 295.1 and 297.8 eV at the spectrum of FIB-CVD DLC are assignable to 1s $\rightarrow \pi^*$ transitions of carbon atom neighboring Ga atom.

- [1] R. Kometani *et al.*, Jpn. J. Appl. Phys. **42** (2003) 4107.
 [2] K. Kanda *et al.*, Nucl. Inst. Meth. B **206** (2003) 880.

N K XAFS Analysis of Some Porphyrin Compounds and Their Complexes

H. Yamashige¹, T. Kurisaki¹, H. Wakita^{1,2}

¹*Department of Chemistry, Faculty of Science, Fukuoka University, Nanakuma, Jonan-ku, Fukuoka 814-0180, Japan*

²*Advanced Materials Institute, Fukuoka University, Nanakuma, Jonan-ku, Fukuoka 814-0180, Japan*

Metalloporphyrins, used as biomimetic catalysts, are important prosthetic groups in enzymes, and offer the potential for substrate oxidation¹. Iron-porphyrins, in particular, have been used as cytochrome P-450 models for oxidative catalysis using a large variety of oxygen donors, such as iodobenzene and hydrogen peroxide. The introduction of electron-withdrawing substitutes at the *meso*-positions of Fe-porphyrin complexes affects the catalytic activity of the oxidation reaction for cytotoxin and pollution hazards. The chemical state of Fe ions in Fe-porphyrin complexes with *meso*-substitutes has been examined using IR, XRD, NMR, EPR, Mössbauer, electron spectroscopy, MD, and DFT calculations. Notwithstanding, it remains unclear how the influence of electron-withdrawal is transmitted to the electron state of the center Fe ion in each Fe-porphyrin complex. Elucidation of the electron structure throughout a Fe-porphyrin complex with *meso*-substitutes is an important task toward the development of stable and highly active Fe-porphyrin complexes as oxidation catalysts.

X-ray absorption spectra of near C and N *K* absorption edges were (XAFS) measured at BL8B1 of the UVSOR in the Institute of Molecular Science, Okazaki [2]. The energy of the UVSOR storage ring was 750 MeV and the stored current was 110-230 mA. The absorption was monitored by the total electron yield using a photomultiplier. The C and N *K* XANES spectra for tetraphenylporphyrin (TPP) are shown in Fig. 1 and Fig. 2. The peaks which appeared at approximately 282, 285, 395, 398, 400, and 405 eV in each experimental spectrum are labeled A, B, C, D, E, and F in the order of increasing energy. This work is to examine electron structures of TPP, TCPP, and TSPP using crosschecks of XANES data for C and N *K* absorption edges in combination with DV-X α MO calculations. These results indicated that a *p*-electron-withdrawing group on the phenyl group in porphyrin compounds engenders a unique electron state because of the electron-withdrawal strength itself.

Crosschecks of XANES data for multi-element absorption edges are important not only for porphyrin compounds and complexes, but also for other numerous metal complexes, especially those with a layer structure or chain structure, because they are closely related to intermolecular interaction of electrons. This method is applicable to the design and development of new metal complexes with a useful function by obtaining detailed information about the

electronic structure along with an electron state calculation method, such as the DV-X α MO method. An experimental setup of simultaneous measurements of XANES, which we are currently constructing for the laboratory users, will facilitate such studies.

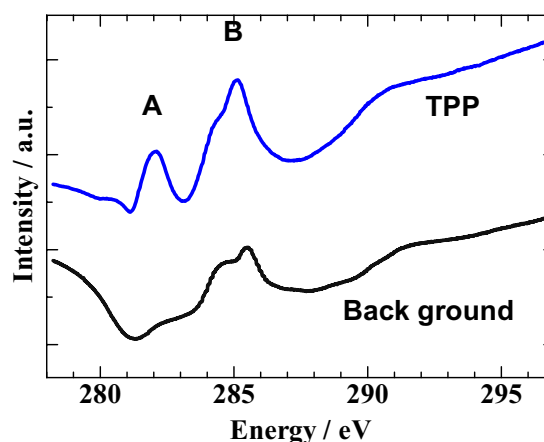


Fig. 1 C *K* XANES spectra of TPP.

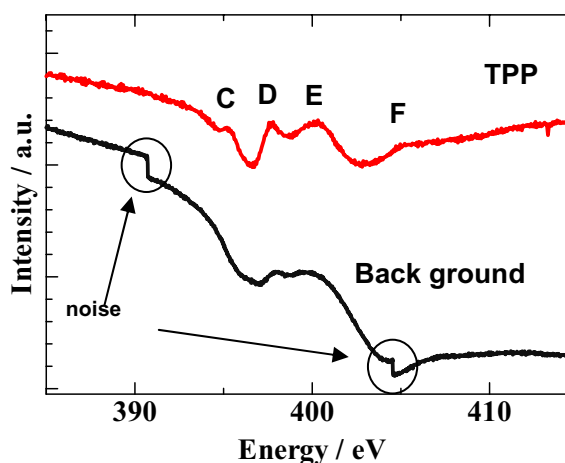


Fig. 2 N *K* XANES spectra of TPP.

[1] J. H. Chou, H. S. Nalwa, and M. E. Kosal, *The Porphyrin Handbook* vol. 7, ed. K. M. Kadish, K. M. Smith, R. Guilard (Academic Press, San Diego, CA, 2000) 41.

[2] S. Murata, T. Matsukawa, S. Naoè, T. Horigome, O. Matsuodo, and M. Watanabe, *Rev. Sci. Instrum.* **63** (1992) 1309.

Ultraviolet Photoelectron Spectra of Three Tm@C₈₂ Isomers

S. Hino^{1,2}, N. Wanita², K. Iwasaki¹, D. Yoshimura^{3,4}, N. Ozawa⁵,
T. Kodama⁵, K. Sakaguchi⁵, H. Nishikawa⁵, I. Ikemoto⁵, K. Kikuchi⁵

¹Faculty of Engineering, Chiba University, Chiba 263-8522, Japan

²Graduate School of Science & Technology, Chiba University, Chiba 263-8522, Japan

³UVSOR, Institute for Molecular Science, Okazaki 444-8585, Japan

⁴Research Center of Material Science, Nagoya University, Nagoya 464-8602, Japan

⁵Department of Chemistry, Tokyo Metropolitan University, Tokyo 192-0397, Japan

Abstract

Ultraviolet photoelectron spectra (UPS) of three Tm@C₈₂ isomers were measured with a synchrotron radiation light source. The upper valence band spectra (0 – 5 eV) of three isomers are different each other and they also differ from those of other trivalent metal atoms encapsulated metallofullerenes such as La@C₈₂, Sc@C₈₂ and Gd@C₈₂. Resemblance of the spectra of Tm@C₈₂ (II) and Ca@C₈₂ (III) suggests identical cage structures of these two metallofullerenes. The UPS are well reproduced by simulated spectra obtained with *ab initio* calculation, which indicates that isomers I – III have C_s (No. 4), C₂ (No. 5) and C_{2v} (No. 9) cage structures.

Results and Discussion

The spectral onsets of the UPS of three Tm@C₈₂ isomers (I) – (III) are 0.85, 0.75 and 0.9 eV, respectively, which is relatively large compared with those of La@C₈₂ [1] and Gd@C₈₂ [2] but almost the same as those of Ca@C₈₂ isomers [3]. This finding is closely related to the amounts of transferred electrons from encapsulated metal atom to the fullerene cage.

The spectra obtained with 40 eV photon energy show upper valence band very distinctly. As explicit difference among the spectra lies mainly in the upper valence band region (pseudo π -electron region) so that 40 eV UPS of three Tm@C₈₂ isomers are shown in Fig. 1 for comparison. As for the deeper valence band (mainly due to pseudo σ -electrons) region there is hardly any difference among the three Tm@C₈₂ spectra. This implies that electronic structures of skeletal cage structures of three isomers are not so different. As for the upper valence band region the situation is quite different. Although onset positions of these spectra do not change so much, the first structure of each spectrum differs so much. Intensity ratio of second and third structures of these spectra also differs. The UPS of two Ca@C₈₂ isomers are also shown in Fig. 1. The UPS of Tm@C₈₂ (II) and Ca@C₈₂ (III) are essentially the same which indicates that these two metallofullerenes have the same electronic structure derived from the same cage structure.

The NMR analysis suggests symmetry of three Tm@C₈₂ isomers are C_s, C₂ and C_{2v}, respectively. There are nine isolated pentagon rule (IPR) satisfying cages for C₈₂. There is only one C_{2v} cage among them so that cage structure of isomer III can be determined

exactly to be C_{2v} (No. 9). There are three C_s and C₂ cages for IPR satisfying C₈₂ cage. The NMR could not elucidate the exact cage structure for isomers I and II. The UPS of three isomers can be well reproduced by simulated spectra obtained with *ab initio* calculation assuming C_s (No. 4), C₂ (No. 5) and C_{2v} (No. 9) cage structures. Thus, cage structures of three isomers can be determined [4].

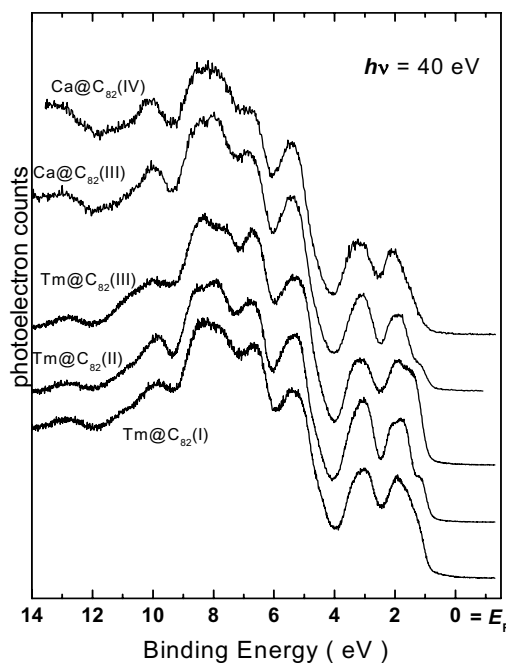


Fig. 1 The UPS of three Tm@C₈₂ isomers and two Ca@C₈₂ isomers.

- [1] S. Hino *et al.*, Phys. Rev. Lett. **71** (1993) 4261.
- [2] S. Hino *et al.*, Chem. Phys. Letts. **281** (1997) 115.
- [3] S. Hino *et al.*, Chem. Phys. Lett. **337** (2001) 165.
- [4] S. Hino *et al.*, Chem. Phys. Lett. **402** (2004) 217.

Epitaxial Growth of Copper Tetrakis(Thiadiazole)Porphyrazine Film

K. Kanai¹, E. Kawabe¹, D. Yoshimura², Y. Suzuki¹, M. Fujimori¹, H. Yoshikawa¹,
K. Awaga¹, K. Seki^{1,2,3}

¹Graduate School of Chemistry, Nagoya University, Nagoya, 464-8602 Japan

²Research Center for Material Science, Nagoya University, Nagoya, 464-8602 Japan

³Institute for Advanced Research, Nagoya University, Nagoya, 464-8602 Japan

Introduction

Thin films of organic semiconductors have been attracting much interest over the past decade for their potential technological applications. In organic devices, such as organic field effect transistor and organic light emitting diode, charge transport and luminescence properties are strongly affected by the structural properties of the films. Thus, it is important to understand the mechanism of molecular aggregation, packing, and orientation to control the structure of the film for improvement of the properties of such devices.

In this research, we focus on the epitaxial growth of phthalocyanine-based molecules, copper tetrakis-(thiadiazole)porphyrazine (CuTTDPz) film on GeS(100) surface. CuTTDPz is expected to have stronger inter-molecule interaction than that of phthalocyanine because of the close contact between the sulfur and nitrogen atoms of the thiadiazole group [1]. Comparison between CuTTDPz film and other phthalocyanine film will provide insight into the role of inter-molecule interaction on epitaxial growth of organic thin films.

Experimental

Low energy electron diffraction (LEED) was performed to study the arrangement of CuTTDPz molecules on GeS(100) surface. Angle-resolved ultraviolet photoemission spectroscopy (ARUPS) was performed to determine the molecular orientation of CuTTDPz molecule on GeS(100) surface. ARUPS experiment was done in UVSOR-II BL8B2 with VG-CLAM4 analyzer. Clean GeS(100) surface was obtained by cleaving the surface of GeS single crystal under ultrahigh vacuum condition. The film of CuTTDPz was in situ evaporated onto clean GeS(100) surface.

Results and Discussion

Clear diffraction spots from CuTTDPz molecules shown in Fig. 1 indicate epitaxial growth of CuTTDPz molecules deposited on GeS(001) surface. From this result, the unit cell of CuTTDPz film on GeS(100) surface is estimated to be twice as large as that of ZnPc.[2]

Figure 2 shows the take-off angle θ dependence of ARUPS spectra of CuTTDPz film deposited on GeS(001) surface. The inset gives the measurement geometry. ARUPS spectra show strong dependence on θ , especially in HOMO, indicating that CuTTDPz

molecules have preferred orientation on the GeS(100) surface. From comparison between the observed θ dependence of ARUPS spectra and theoretical calculation by independent atomic center approximation, CuTTDPz molecule is found to be almost flatly lying. The role of intermolecular interaction for both molecular arrangement and orientation will be discussed near future.



Fig. 1 LEED pattern of CuTTDPz film deposited on GeS(001) surface. Primary energy is 40 eV and the thickness of the film is 0.4 nm. The black circles in the figure represent diffraction spots from GeS(100).

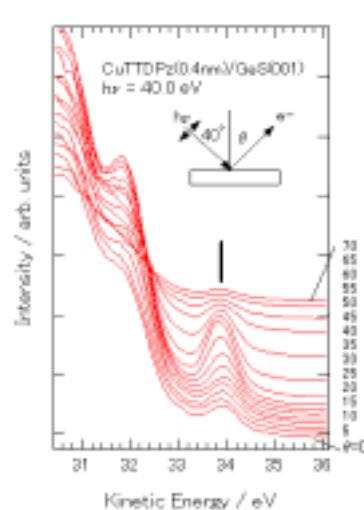


Fig. 2 ARUPS spectra of CuTTDPz film deposited on GeS(100) surface. Vertical bar points at the highest occupied molecular orbital (HOMO) CuTTDPz.

[1] Y. Suzuki, *et al*, Chem. Eur. J. **10** (2004) 5158.

[2] E. Kawabe, unpublished.

Angle-Resolved UV Photoelectron Spectra of OTi-Phthalocyanine Monolayer on Graphite

S. Kera^{1,2}, H. Yamane¹, H. Fukagawa¹, T. Hanatani¹, M. Ono¹,
S. Nagamatsu¹, T. Yokoyama¹, D. Yoshimura³, K. K. Okudaira¹, K. Seki², N. Ueno¹

¹Faculty of Engineering, Chiba University, Chiba 263-8522 Japan

²Institute for Molecular Science, Okazaki 444-8585 Japan

³Research Center for Materials Science, Nagoya University, Nagoya 464-8602 Japan

A few years ago, we succeeded to observe a very sharp HOMO band with clear vibration satellites on a well-ordered Cu-phthalocyanine (Pc) on graphite [1]. After detecting the highly-resolved HOMO band, we could discuss the complex nature of band width, shape and position in organic solid systems [1-3].

Very recently, we observed peculiar angular distribution for OTiPc doublelayer/graphite system. It may be related to a photoelectron scattering process passing through a different local potential within the film. Photoelectron angular distribution involves information on the initial wavefunction, and thus the quantitative analysis of the angular distribution provides a detailed origin of the UPS bands, as well as a geometrical structure of organic thin films [4]. In this work, we measured take-off angle dependencies of angle-resolved UPS (ARUPS) for well-defined OTiPc monolayer precisely.

Experiments

ARUPS spectra were measured at photon incidence angle $\alpha = 70^\circ$, $h\nu = 20$ eV, and $T = 295$ K. θ dependence of ARUPS spectra was analyzed using the single-scattering approximation combined with molecular orbital calculation (SS/MO) [4,5]. The purified OTiPc was carefully evaporated onto the HOPG. Characterization of the film growth of the OTiPc/graphite has been carried out [6]. Coverage of the film can be estimated from the total shift of the vacuum level as discussed in the previous paper [3]. To obtain the well-ordered monolayer film, subsequent annealing is performed at 420 K/2 h.

Results and Discussion

Figure 1(a) shows θ dependence of ARUPS of OTiPc monolayer (annealed-0.8-MLE) on HOPG surface. The intensity is normalized to the incidence photon flux and the background is subtracted. The HOMO band is assigned to a single π MO as in other Pcs (inset of Fig. 1) [1-3]. Very sharp asymmetric HOMO bands are detected for all photoelectron-take-off-angles ($\theta = 0 \sim 60^\circ$).

Figure 1(b) shows the comparison between observed and calculated θ dependences of the HOMO-band intensities with the SS/MO (HF/STO-6G) for the molecular tilt angle $\beta = 0^\circ$, which gave the best agreement with the observed θ pattern. It indicates that the OTiPc molecules orient flat to the HOPG surface with O-atom protruding the

vacuum as illustrated in Fig. 1(b). Moreover, we found that effects of a multiple scattering are negligibly small for organic molecule, since our SS/MO approximation is applicable well even for the low-energy photoelectron (~ 15 eV).

Now to compare impacts on a different local potential, further experiments on the photoelectron angular distribution both for the monolayer and the doublelayer are in progress with theoretical calculations.

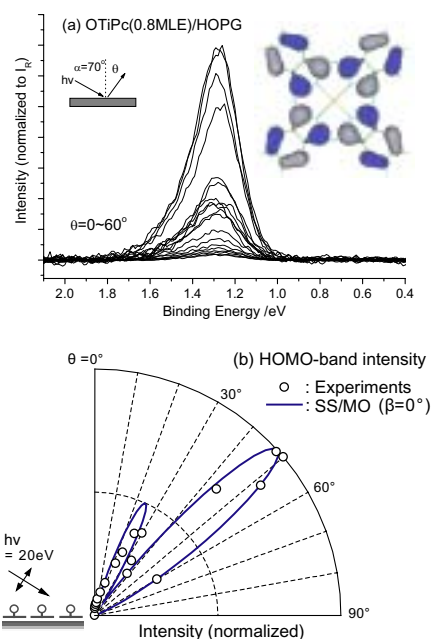


Fig. 1 (a) Take-off angle (θ) dependence of the ARUPS of the 0.8-MLE-OTiPc on HOPG(0001). The HOMO distribution of OTiPc is also shown. (b) Comparison between observed and calculated θ dependences of the HOMO-band intensities with SS/MO approximation for $h\nu = 20$ eV and $\theta = 0^\circ$.

- [1] S. Kera *et al.*, Chem. Phys. Lett. **364** (2002) 93.
- [2] H. Yamane *et al.*, J. Electron Spectrosc. Relat. Phenom. **137-140** (2004) 223.
- [3] There are some articles by us in IPAP conference proceedings, in press.
- [4] N. Ueno *et al.*, J. Chem. Phys. **107** (1997) 2079.
- [5] K. K. Okudaira *et al.*, J. Appl. Phys. **85** (1999) 6453.
- [6] S. Kera *et al.*, Jpn. J. Appl. Phys. **40** (2001) 783.

Electronic Structure of $\text{LiNi}_{1-x}\text{M}_x\text{O}_2$ Mixed Oxides (I)

T. Miyazaki¹, H. Takeno¹, D. Yoshimura², T. Yamaguchi¹

¹*Department of Applied Chemistry, Faculty of Engineering, Ehime University,
Matsuyama 790-8577 Japan*

²*Research Center for Materials Science, Nagoya University, Nagoya 464-8602, Japan*

An application of LiNiO_2 has been studied as a positive electrode of lithium secondary battery on the basis of the lamellar structure. And, the structure was maintained to over 1073 K under the oxidative atmosphere. It was reported that the surface lattice oxygen of LiNiO_2 had the catalytic property at around 1000 K for the oxidative coupling of methane [1]. Ultraviolet photoelectron spectroscopy was applied in order to discern the correlation of catalytic property and electronic states near the top of the valence band region. The valence band usually determines the electronic properties and the catalytic activities of the materials, therefore, it should be carefully investigated. At this approach, ultraviolet photoelectron spectra were measured as samples of LiNiO_2 , LiCoO_2 and $\text{LiNi}_{1-x}\text{M}_x\text{O}_2$ ($M = \text{Mn}, \text{Ti}, \text{Al}$) were replaced with other metallic element a part of Ni site in LiNiO_2 . Then, the electronic structure was examined from the incident photon energy dependence of ultraviolet photoelectron spectra in order to clarify the origin of selective catalysis and electronic properties.

LiNiO_2 , LiCoO_2 and $\text{LiNi}_{1-x}\text{M}_x\text{O}_2$ ($M = \text{Ti}, \text{Al}, \text{Mn}$; $x = 0.1$) were prepared from LiNO_3 , $\text{Ni}(\text{OH})_2$ and $\text{M}(\text{NO}_3)_2$ by the solid-state reaction. The UPS spectra were measured using the angle resolved photoelectron spectroscopy equipment at BL8B2. The UPS spectra were measured for electrons emitted normal to the sample surface with an incident angle 45° of the light beam. The Fermi energy of the UPS system was determined by using the Fermi edge of gold films. A pure processing by Ar^+ sputtering or the heating of infrared radiation was carried out as a surface pretreatment of these samples.

Figure 1 shows the UPS spectra of LiNiO_2 , LiCoO_2 , $\text{LiNi}_{0.9}\text{Mn}_{0.1}\text{O}_2$, $\text{LiNi}_{0.9}\text{Ti}_{0.1}\text{O}_2$ and $\text{LiNi}_{0.9}\text{Al}_{0.1}\text{O}_2$ at 60 eV of the incident photon energy. These spectra were measured with reference to E_F as the zero of the energy scale. Several structures, denoted by the characters A–E, are observed at $E_b = 1.6, 3.0, 4.9, 6.1$ and 9.8 eV in the spectrum of LiNiO_2 . The structure located at $E_b = 3.0$ eV of LiNiO_2 , observed clearly in this study. In case of LiCoO_2 , there were four structures on the top of the valence band. However, the B band was not clearly observed in those of LiCoO_2 . Also, each band may be shifting to the high energy side of $0.5 \sim 1.0$ eV. The UPS spectra of $\text{LiNi}_{0.9}\text{Mn}_{0.1}\text{O}_2$, $\text{LiNi}_{0.9}\text{Ti}_{0.1}\text{O}_2$, and $\text{LiNi}_{0.9}\text{Al}_{0.1}\text{O}_2$, a part of Ni site were replaced with Mn, Ti, and Al, have been composed of five bands as well as LiNiO_2 . In the case of $\text{LiNi}_{0.9}\text{Mn}_{0.1}\text{O}_2$, it may be difference with electronic structure of LiNiO_2 that the relative intensity of band B is to be conspicuous. The spectrum

of $\text{LiNi}_{0.9}\text{Al}_{0.1}\text{O}_2$ was almost equal electronic structure for LiNiO_2 , though the features in which all of the spectra were shifting to the high energy side were recognized. It has been reported that the selectivity for OCM reaction over $\text{LiNi}_{0.9}\text{Ti}_{0.1}\text{O}_2$ and $\text{LiNi}_{0.9}\text{Mn}_{0.1}\text{O}_2$ improved but $\text{LiNi}_{0.9}\text{Al}_{0.1}\text{O}_2$ was remarkably being decreased, when it tries to compare the OCM activity of these samples with those of LiNiO_2 . Comparing the electronic structures of LiNiO_2 , LiCoO_2 and $\text{LiNi}_{1-x}\text{M}_x\text{O}_2$ ($M = \text{Ti}, \text{Al}, \text{Mn}$), several differences were found. These points should be examined in more detail by the CIS spectra over a wide excitation photon energy region.

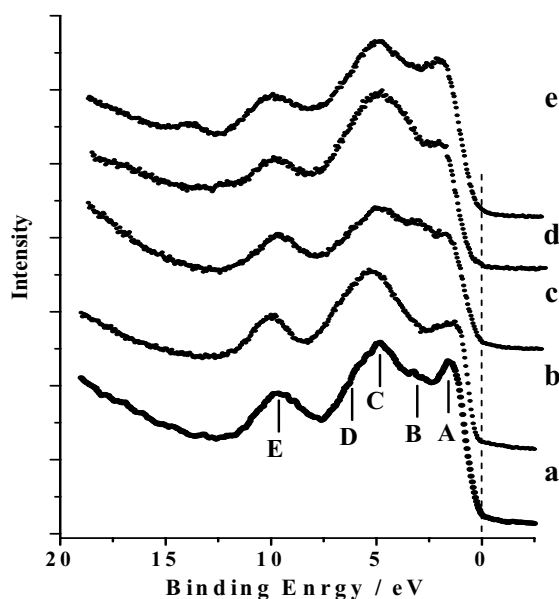


Fig. 1 The UPS spectra of a) LiNiO_2 , b) LiCoO_2 , c) $\text{LiNi}_{0.9}\text{Mn}_{0.1}\text{O}_2$, d) $\text{LiNi}_{0.9}\text{Ti}_{0.1}\text{O}_2$, e) $\text{LiNi}_{0.9}\text{Al}_{0.1}\text{O}_2$.

[1] T. Miyazaki *et al.*, Res. Chem. Inter. **28** (2002) 479.

[2] T. Miyazaki *et al.*, UVSOR Activity Report 2002 (2003) 197.

Photoemission Study of a Cu-Ga-Mg-Sc Icosahedral Phase

M. Mori¹, R. Hashimoto¹, S. Motomura¹, D. Yoshimura², S. Kashimoto³, T. Ishimasa³

¹Graduate School of Information Science, Nagoya University, Chikusa, Nagoya 464-8601 Japan

²Research Center for Materials Science, Nagoya University, Chikusa, Nagoya 464-8603 Japan

³Graduate School of Engineering, Hokkaido University, Sapporo 060-8628 Japan

Introduction

Since the discovery of an icosahedral phase (i-phase) in Al-Mn alloys by Shechtman *et al.* [1], there have been reported a large number of studies about the electronic properties of icosahedral materials in spite of remaining the arrangement of the atoms in an i-phase unclear. By intuition the pseudogap structure can be interpreted in terms of the nearly-free-electron-like energy gap inferred from the strong diffraction spots, which may be related to the stability of the i-phase.

A pseudogap-like anomaly in the DOS near E_F was directly confirmed with the photoemission study of an Al-Cu-Fe i-phase by Mori *et al.* [2]. The CIS spectra at the binding energy region between 0-2 eV show a resonant characteristic near the 3d-electron excitation of Fe atom in the i-phase.

Experimental and Results

The purpose is to observe the photoemission study of a new Cu-Ga-Mg-Sc (CGMS) i-phase and the Cu-Ga-Sc approximant crystal (CGS). The sample, an Cu-Ga-Mg-Sc i-phase quasicrystal, was an ingot prepared. It is well known that this is quite high quality of the quasicrystal. It was confirmed that the specimen used with this study consists of only a new *I-type i-phase* but does not contain the other phases.

Photoemission studies were performed with an angle-resolved spectrometer on beam-line BL8B2. All measurements were carried out at room temperature. The clean surface of the specimen was obtained by scraping with a diamond file in a vacuum of $2 \cdot 10^{-8}$ Pa. Immediately after this process, the sample was transferred to the UPS experimental chamber and measured in a vacuum of $2 \cdot 10^{-8}$ Pa.

The line shape near E_F is like a plateau cut off at E_F shown in Fig. 1. We have tried the fitting of the photoemission curve of the Al-Pd-Mn i-phase, using the (flat DOS) * (Gauss distribution function type resolution function). Using the fitting parameters of the Au spectrum, we could get the solid curves of lower two spectra. The middle one is well fitted with the CGS approximant crystal data. But the lower is not fitted with the CGMS quasicrystal data. This means that the CGMS quasicrystal has a pseudogap near E_F , and the CGS approximant crystal has not a pseudogap. It shows that this experimental result is well fitted as the quasicrystal has the pseudogap of width 0.4 eV and depth 0.6. This experimental result is the secondary example that the quasicrystal has the

pseudogap.

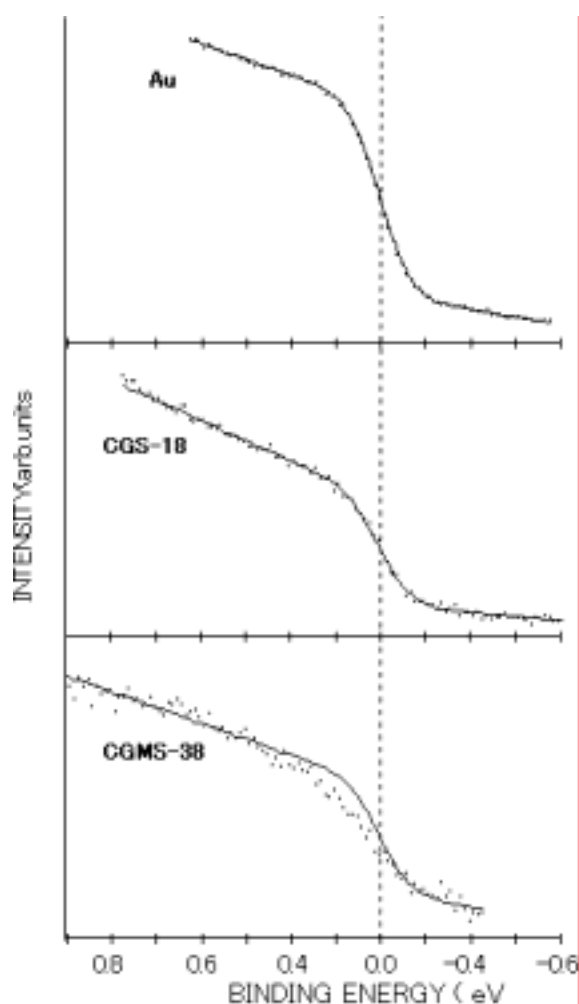


Fig. 1 Photoemission spectra near E_F measured at room temperature. Each solid curve shows the fitted curve of the DOS near E_F without pseudogap. The upper one is the spectrum of Au, and the middle is that of CGS approximant crystal and the lower is that of CGMS i-phase quasicrystal.

[1] D. Shechtman, I. Blech, D. Gratias, J. W. Cahn, *Phys. Rev. Lett.* **53** (1984) 1951.

[2] M. Mori, S. Matsuo, T. Ishimasa, T. Matsuura, K. Kamiya, H. Inokuchi, T. Matsukawa, *J. Phys.: Condens. Matter* **3** (1991) 767; *ibid.* **4** (1992) L157.

Possibility of Fermi Level Control Induced by VUV-Induced Doping: UPS Study of Photodegraded PTFE Film

M. Ono¹, H. Yamane¹, H. Fukagawa¹, S. Kera², D. Yoshimura³,
E. Morikawa⁴, K. Seki³, N. Ueno¹

¹Graduate School of Science and Technology, Chiba University, Chiba 263-8522, Japan.

²Institute for Molecular Science, Okazaki 444-8585, Japan.

³Research Center for Material Science, Nagoya University, Nagoya, 464-8602 JAPAN.

⁴CAMD, Louisiana State University, Baton Rouge, LA 70806, U.S.A.

Control of Fermi level is a fundamental and extremely important technique for the development of semiconductor devices. Control of the Fermi level in the organic molecular film has been attempted by embedding metals or organic molecules. However, the method of Fermi level control is not well established. One of the most crucial problems is the difficulty to prepare a homogeneously doped film, particularly in the case of molecular doping.

The doping induced by high-energy photon irradiation is an attractive method. If photoproducts generated in the film can act as dopants, the homogeneous doping can be achieved. In addition concentration of dopants can be also controlled by the irradiation dose. As our attempt at the Fermi level control by “high-energy radiation-induced doping”, the photodegradation of polytetrafluoroethylene (PTFE, $-(CF_2-CF_2)_n-$) film was studied [1]. As PTFE has a wide band gap, energy shift of the Fermi level can be easily detected.

PTFE film prepared by vacuum deposition in the UHV chamber was directly transferred to UPS measurement chamber under UHV condition. The 75-eV photon beam was utilized for both UPS measurement and photodegradation of the PTFE film. The photon dose was estimated by measuring the number of electrons emitted from the gold mesh by incidence photon.

Figure 1 shows the photodegradation effect on the UPS spectra of the PTFE film. During the VUV irradiation the UPS spectra are shifting toward low binding energy side. This shift is not due to the

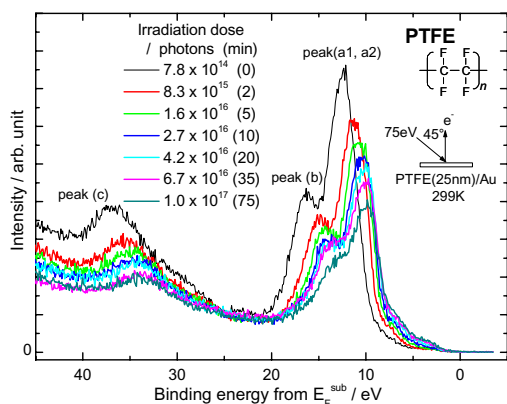


Fig. 1 VUV photodegradation effect on UPS spectra of the PTFE film.

charge-up effect, because the shift caused by charge-up moves toward high binding energy side. In Figure 2 the binding energy positions of the four peaks are plotted against the irradiation dose. The binding energy shifts of all peaks are proportional to logarithm of the irradiation dose with identical slope. In the case of simple model which assumes only one acceptor level the energy position of the Fermi level, E_F , can be expressed by following formulae under the low-temperature approximation [2]:

$$E_F = \frac{E_a}{2} - \frac{kT}{2} \ln\left(\frac{N_a}{n_0}\right) \quad \dots (1),$$

$$n_0 = 2\left(\frac{2\pi m_h kT}{h^2}\right)^{3/2},$$

where N_a is the concentration of acceptors, E_a is the energy of acceptor level from top of the valance band and m_h is the effective mass of a hole in the valance band. It should be noted that the Fermi level position is proportional to logarithm of the concentration of the acceptor. Therefore it can be considered that the shift of UPS spectra is caused by Fermi level shift. It is expected that the radical generated by VUV light has unoccupied electronic states in the PTFE band gap. In addition the lifetime of radical is much longer (~ 1000 h) than the measurement time (5 h). Hence it is considered that the radical acts as acceptor upon the degradation of the PTFE film.

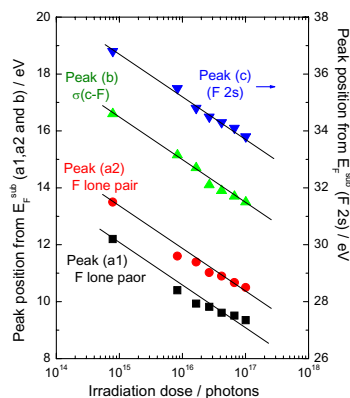


Fig. 2 The binding energy positions of the UPS peaks plotted against the irradiation dose.

[1] M. Ono *et al.*, Submitted to IPAP Conference Proceedings.

[2] C. Kittel, *Introduction to Solid State Physics*, 2nd ed. (John Wiley & Sons, New York, 1957).

Fabrication of Electrode Holes on the Supported Membrane Biosensor Substrates by Femto-Second Laser Patterning Followed by SR Etching

M.M. Rahman¹, R. Sasaki², H. Nagai², M. Yoshida², M. Aoyama³, T. Yano³, H. Uno³, R. Tero³, Y. Nonogaki^{1,3}, T. Urisu^{1,3}

¹ Graduate University for Advanced Studies, Myodaiji, Okazaki 444-8585, Japan

² AISHIN SEIKI Co., Ltd. 17-1 Kojiritsuki, Hitotsugi-cho, Kariya 448-0003, Japan

³ Institute for Molecular Science, NINS, Myodaiji, Okazaki 444-8585, Japan

Introduction

The supported membrane is a single lipid bilayer supported on a solid surface, and is useful as artificial cell membranes for the study of biological reactions of membrane proteins. We are developing supported membrane biosensors from the interest in developing the new research tool of the cell membrane surface reactions, and these devices are interesting also from the view point of application to the large scale screening method for the new medicine development.

In the present work, we have fabricated very flat Si substrates with buried-electrodes having the structure of SiO₂/CoSi₂/Si(100)/CoSi₂/Au by the thin film deposition using of sputtering and the electrode hole fabrication using the femto-second laser patterning followed by synchrotron radiation (SR) etching.

used because of its unique features of high spatial resolution, extremely high material selectivity between CoSi₂ and SiO₂, low damage, and clean etching atmosphere. There are lot of advantages such as process simplicity compared with the electron beam (EB) lithography and no contamination by beam elements compared with focused ion beam patterning. Then SR etching using SF₆ (0.05 torr) + O₂ (0.002 torr) reaction was used for the etching of SiO₂ using the Co contact mask. Etching stopped at the thin electrode (CoSi₂) surface. After the removal of Co mask with 0.1 M HNO₃ aq, AFM images showed that the surface was very flat (Rz=1.5 nm) as shown in Fig. 1.

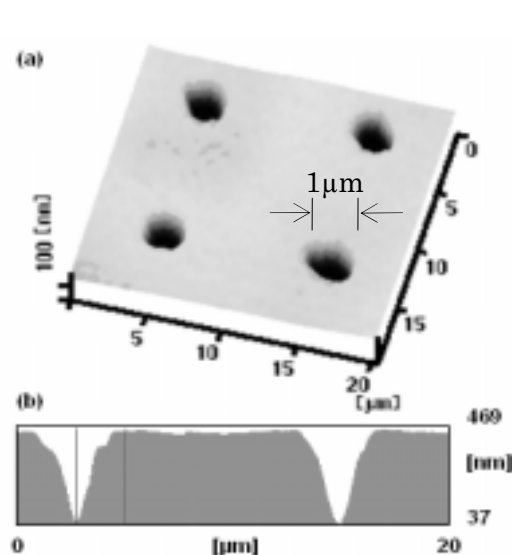


Fig. 1 AFM image (20x20 μm^2) and the cross section of the SiO₂ surface electrode hole fabricated by femto-second laser and SR etching.

Results and Discussion

Co thin film (200nm) was deposited on the SiO₂/CoSi₂/Si(100)/CoSi₂/Au substrates and small hole patterns were fabricated by the femto second laser pulses. These hole patterns were used as the contact mask of the SR-stimulated etching. SR was

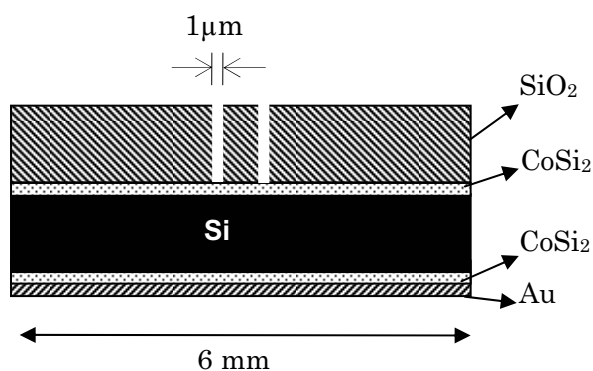


Fig. 2 A schematic illustration for the biosensor substrate.

X-Ray Magnetic Circular Dichroism Study on Cu Capping on Ultrathin Ni Films Grown on Clean and O-Adsorbed Cu(001) Surfaces

T. Nakagawa, H. Watanabe, T. Yokoyama

Department of Molecular Structure, Institute for Molecular Science, Okazaki 444-8585 Japan

Ultrathin Ni/Cu(001) films are well known to show unique magnetic properties. The spin reorientation transition (SRT) occurs twice by varying the Ni thickness; at <9 ML (monolayer) the easy axis is in plane, at 9-40 ML it is perpendicular, and at >40 ML it is again in plane. In this work, we have studied the Cu capping effect on the Ni films grown on clean and O-preadsorbed Cu(001) by means of in-laboratory magneto-optical Kerr effect (MOKE) and UVSOR x-ray magnetic circular dichroism (XMCD) methods.

Experiments

Ni was deposited on clean (1×1) and O-preadsorbed (2√2×√2)R45° Cu(001) at room temperature in ultrahigh vacuum chambers. The thickness was monitored with the RHEED oscillations. Cu was subsequently deposited on Ni/Cu(001). Ni L-edge XMCD was taken at BL4B [1] at ~100 K by applying the external magnetic of ±1000 G.

Results

In the polar and longitudinal MOKE measurements of Ni/Cu(001), we found that the SRT occurs at the critical Ni thickness of 9.0 ML before Cu capping and 7.0 ML after 2 ML Cu capping, implying the stabilization of perpendicular magnetic anisotropy (PMA). On the contrary, for the Ni/O/Cu(001), the SRT occurs at the critical Ni thickness of 5.5 ML before Cu capping and 7.0 ML after 2 ML Cu capping, indicating the instabilization of PMA.

In order to obtain structural information on these two kinds of films, the Auger electron spectra and the LEED pattern were observed. The oxygen atoms are found to act as a surfactant and locate always at the surface even after Ni and Cu deposition. Combining the MOKE and Auger results, we can conclude that the surface oxygen atom stabilizes PMA more effectively than the surface Cu atom.

For the understanding of such magnetic anisotropy, we have performed Ni L-edge XMCD. Figure 1 shows the XMCD spectra. In the 5.5 ML Ni film on clean Cu(001), the L_{III}-edge XMCD signals are gradually suppressed with the Cu capping, while in the 11 ML Ni film, the XMCD intensity is almost constant. This results indicate that with the Cu capping the orbital magnetic moments are reduced along the in-plane direction and not along the surface normal direction. On the contrary, in the 4.8 ML Ni film on O/Cu(001), the L_{III}-edge XMCD signals are gradually increased, implying the enhancement of the orbital magnetic moment.

Figure 2 shows the orbital magnetic moment (m_l) and the hysteresis loss (BH) obtained the present

XMCD and MOKE measurements, respectively. It is clearly found that these quantities behave very similar.

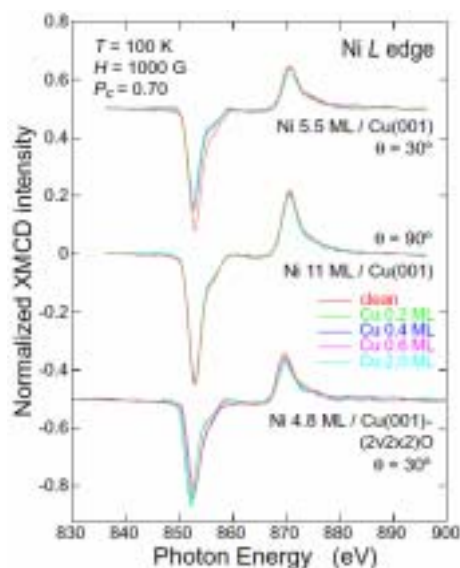


Fig. 1 Ni L-edge XMCD of 5.5 ML Ni on clean Cu(001) (always in-plane magnetized; measured at grazing x-ray incidence of 30°), 11 ML Ni on clean Cu(001) (always perpendicularly magnetized; measured at normal x-ray incidence), and 4.8 ML Ni on O/Cu(001) (always in-plane magnetization; measured at grazing x-ray incidence of 30°).

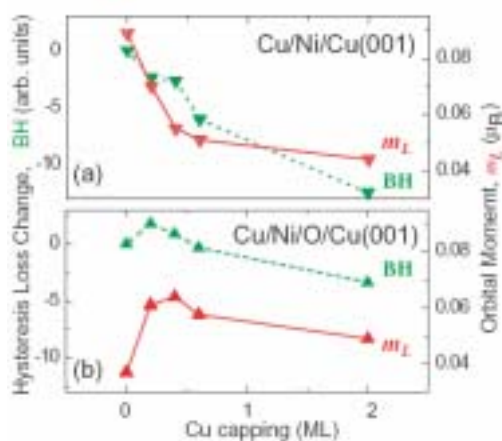


Fig. 2 Hysteresis loss and orbital magnetic moments of the Cu-capped Ni films on clean and O-preadsorbed Cu(001) as a function of Cu coverage.

[1] T. Nakagawa *et al.*, UVSOR Activity Report 2003 (2004) 39.

Spin Reorientation Transition in Ag-Covered Co Films Grown on Vicinal Cu(001) Surface

T. Nakagawa, H. Watanabe, T. Yokoyama

Department of Molecular Structure, Institute for Molecular Science, Okazaki 444-8585 Japan

Magnetic thin films grown on vicinal surfaces exhibit strong uniaxial magnetic anisotropy; the magnetic property should be essentially different between the step-parallel and perpendicular directions. In this work, in order to obtain microscopic information on the spin reorientation transition in Ag-deposited Co films on Cu(1 1 1), we performed the longitudinal magneto-optical Kerr effect (L-MOKE) and the x-ray magnetic circular dichroism (XMCD) experiments.

Experiments

6 monolayer (ML) Co was deposited on clean Cu(1 1 1) at room temperature in ultrahigh vacuum chambers. The Co thickness was monitored with the RHEED oscillations. Ag was subsequently deposited on Co/Cu(1 1 1). Co L-edge XMCD was taken at BL4B at a temperature of ~ 100 K and at grazing x-ray incidence of 30° by applying the external magnetic of ± 1000 G.

Results

Figure 1 shows the magnetic hysteresis loops of L-MOKE. In the clean Co film, the magnetization curve along the //step direction exhibits normal rectangular shape, while that along the \perp step direction shows a double loop with zero remanence, this implying the easy axis of the //step direction. On the contrary, the reverse is true for the 0.2 ML Ag-deposited Co film; the magnetic easy axis changes from //step to \perp step, exhibiting clear spin reorientation transition. This results is identical with the previous report by Weber *et al.* [1].

Figure 2 shows the Co L-edge XMCD. The intensities of the L_{III} - and L_{II} -edge peaks exhibits clear difference between the clean and Ag-deposited Co films. The sum-rule results are given in Table 1. Although the difference is rather small, one can find that a larger orbital magnetic moments give the magnetic easy axis.

Moreover, we have determined the inclination angle of the easy axis. Figure 3 shows the results of

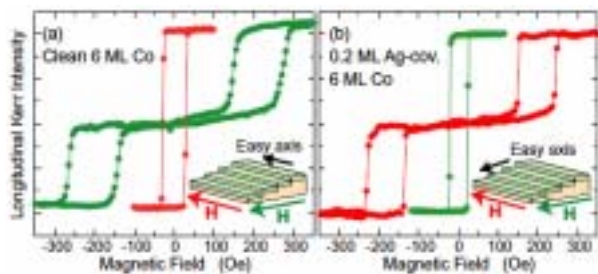


Fig. 1 L-MOKE hysteresis loops of (a) clean and (b) Ag-deposited 6 ML Co/Cu(1 1 1) at 100 K.

the XMCD variation. The x -intercept corresponds to the easy axis, where 0° and -4.8° respectively mean parallel to the physical plane and to the terrance plane. The present finding in Fig. 3 concludes that the Ag deposition induces also the out-of-plane rotation of the easy axis from the physical surface plane (0°) to the terrance plane (-4.8°).

Table 1 The results of the sum-rule analysis for 6 ML Co on Cu(1 1 1). The spin (m_s) and orbital (m_l) magnetic moments of Co are given.

	direction	m_l (μ_B)	m_s (μ_B)
Clean	// step	0.246	1.526
	\perp step	0.225	1.474
0.2 ML Ag dep.	// step	0.200	1.468
	\perp step	0.218	1.485

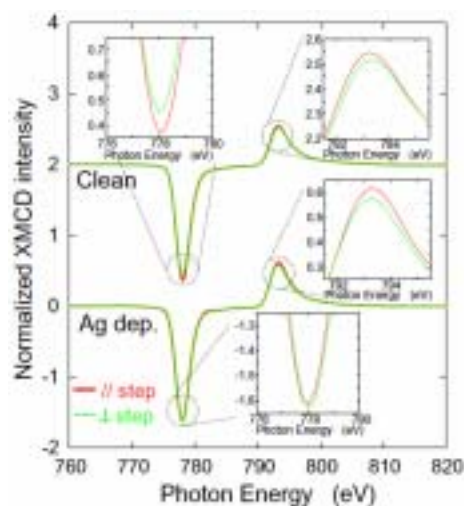


Fig. 2 Co L-edge XMCD of 6 ML Co/Cu(1 1 1) at 100 K before and after 0.2 ML Ag deposition.

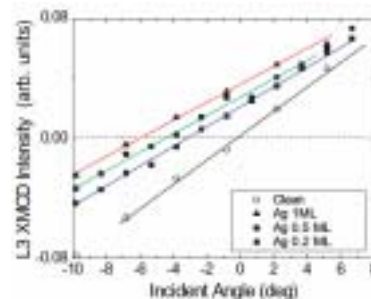


Fig. 3 Angle dependence of Co L_{III} -edge XMCD intensity of 6 ML Co/Cu(1 1 1).

[1] Weber *et al.*, Phys. Rev. **B52** (1995) R14400.

Drastic Magnetization Change Observed in NO Adsorption on Co/Cu(1 1 17)

T. Nakagawa, H. Watanabe, T. Yokoyama

Department of Molecular Structure, Institute for Molecular Science, Okazaki 444-8585 Japan

Magnetic thin films grown on vicinal surfaces exhibit strong uniaxial magnetic anisotropy and the anisotropy could be modified by surface chemical treatments. In this work, we have investigated the effect of NO adsorption on uniaxial Co films grown on Cu(1 1 17) by means of the longitudinal magneto-optical Kerr effect (L-MOKE) and the x-ray magnetic circular dichroism (XMCD) experiments.

Experiments

6 monolayer (ML) Co was deposited on clean Cu(1 1 17) at room temperature in ultrahigh vacuum chambers. The Co thickness was monitored with the RHEED oscillations. The Co film was exposed to 1 L NO to give a saturated ~ 0.5 ML adsorption state of NO/Co/Cu(1 1 17). Co L-edge XMCD was taken at BL4B at a temperature of ~ 100 K and at grazing x-ray incidence of 30° by applying the external magnetic of 1000 G.

Results

Figure 1 shows the magnetic hysteresis loops of L-MOKE. In the clean Co film, the magnetization curve along the //step direction exhibits normal rectangular shape, while that along the \perp step direction shows a double loop with zero remanence, this implying the presence of strong uniaxial magnetic anisotropy and the easy axis of the //step direction. However, drastic changes can be seen after NO adsorption. The coercivity is reduced noticeably, and the //step and \perp step loops are completely identical, this indicating the disappearance of the inherent uniaxial anisotropy and the appearance of almost fourfold symmetric magnetic anisotropy. Such a change is much more drastic than the film on flat Cu(001), as shown in Fig. 2.

Figure 2 shows the Co L-edge XMCD. The intensities of the L_{III} - and L_{II} -edge peaks exhibits clear difference between the clean and NO-adsorbed

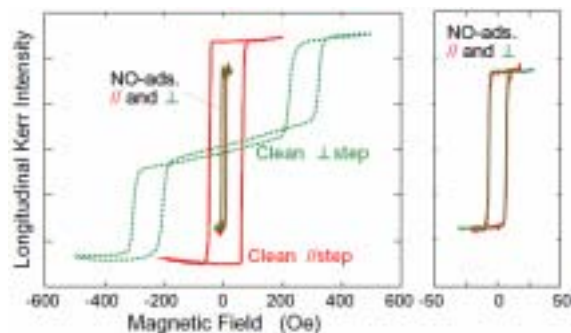


Fig. 1 L-MOKE hysteresis loops of clean and NO-adsorbed 6 ML Co films on Cu(1 1 17) at 100 K. The right figure is just the magnification along the x axis.

Co films. The sum-rule results are given in Table 1. Although the difference is rather small, one can find that in a clean Co film a larger orbital magnetic moments give the magnetic easy axis, while the orbital magnetic moments are essentially the same between the //step and \perp step directions after NO adsorption. This is consistent with the L-MOKE results.

Table 1 The results of the sum-rule analysis for 6 ML Co on Cu(1 1 17). The spin (m_s) and orbital (m_l) magnetic moments of Co are given.

d	irection	m_l (μ_B)	m_s (μ_B)
Clean	// step	0.256	1.459
	\perp step	0.224	1.454
0.5 ML NO ads.	// step	0.116	0.866
	\perp step	0.123	0.879

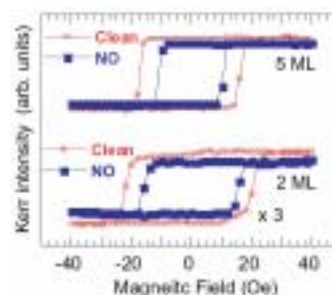


Fig. 2 L-MOKE hysteresis loops of clean (red) and NO-adsorbed (blue) 5 and 2 ML Co films on the flat Cu(001) surface.

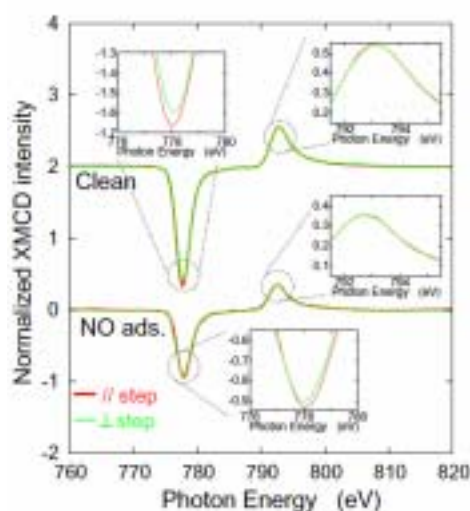


Fig. 3 Co L-edge XMCD of 6 ML Co/Cu(1 1 17) at 100 K before and after 0.5 ML NO adsorption.

Enhancement of Magnetization of Fe/Cu(001) Induced by K Deposition

T. Nakagawa, H. Watanabe, T. Yokoyama

Department of Molecular Structure, Institute for Molecular Science, Okazaki 444-8585 Japan

It is interesting to investigate whether electron donation to magnetic metal films induces the enhancement or suppression of magnetization. In the present work, we have studied the effect of K adsorption on *fcc* Fe grown on Cu(001) by means of the polar magneto-optical Kerr effect (P-MOKE) and the x-ray magnetic circular dichroism (XMCD) methods.

Experiments

3 monolayer (ML) Fe was deposited on clean Cu(001)-(1×1) at room temperature in ultrahigh vacuum chambers. Special care was taken of good vacuum because of easy oxidation of K. The thickness was monitored with the RHEED oscillations. K was subsequently deposited on Fe/Cu(001). Fe *L*-edge XMCD was taken at BL4B [1] at a temperature of ~100 K and at normal x-ray incidence (the films shows perpendicular easy axis) by applying the external magnetic of ±1000 G. For comparison, Co *L*-edge XMCD was examined for K/Co(3ML)/Cu(001) at grazing x-ray incidence.

Results

Figure 1 shows the P-MOKE intensity as a function of K coverage, which was measured during K deposition. With the increase in the K coverage, the P-MOKE intensity increases and at 0.1 ML K deposition it is maximized. More deposition leads to the suppression. The K coverage of 0.1 ML roughly corresponds to the work function minimum.

Although the MOKE intensity is usually proportional to the magnetization, it could not be the case if the electronic structure changes drastically. In order to confirm the enhanced magnetization and to obtain more direct information, we have performed XMCD measurements. Figure 2 shows the Fe *L*-edge XMCD. A small increase in the XMCD signals is actually found at the K coverage of 0.1 ML.

The results of the sum-rule analysis are summarized in Table 1, together with those of K/Co/Cu(001). In both the Fe and Co cases, the number of *3d* holes, which was estimated from the intensity of the white lines, is gradually reduced with the K coverage, this exemplifying the electron donation from K. In the Co case, the spin magnetic moment decreases monotonically with the K coverage. This finding is reasonable since the majority *3d* band of *fcc* Co is fully occupied and the donated electron is transferred to the minority *3d* bands, leading to the reduction of the spin magnetic moment of Co. On the contrary, the spin magnetic moment of Fe is maximized at 0.1 ML K. This verifies that the Fe spin magnetic moment is enhanced by a small amount of K deposition.

Table 1 The results of the sum-rule analysis for 3 ML Fe and Co on Cu(001). *3d* hole numbers and spin and orbital magnetic moments of Fe and Co are given.

	K dep. (ML)	$3d_{hole}$ number	m_s (μ_B)	m_l (μ_B)
3 ML Fe /Cu(001)	0.0	3.40	2.29	0.24
	0.1	3.27	2.40	0.24
	0.2	3.00	1.91	0.17
3 ML Co /Cu(001)	0.0	2.50	1.67	0.26
	0.1	2.37	1.58	0.26
	0.2	2.27	1.50	0.29

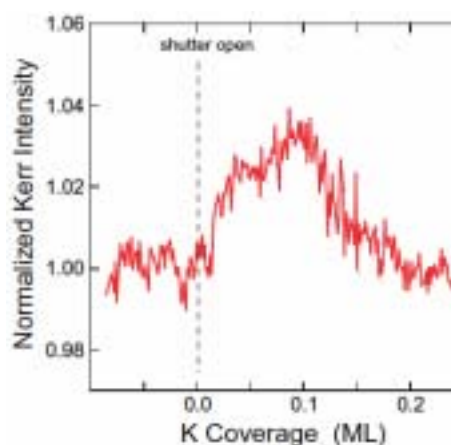


Fig. 1 P-MOKE intensity of 3 ML Fe/Cu(001) at 100 K as a function K deposition.

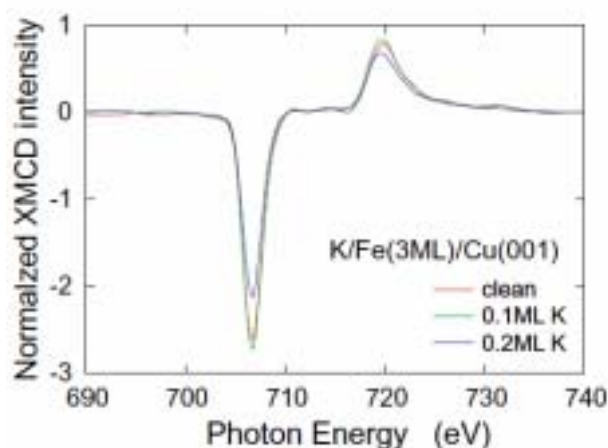


Fig. 2 Fe *L*-edge XMCD of 3 ML Fe/Cu(001) (perpendicularly magnetized) at 100 K for the K coverages of 0.0, 0.1 and 0.2 ML.

[1] T. Nakagawa *et al.*, UVSOR Activity Report 2003 (2004) 39.

Absolute Asymmetric Synthesis of *rac*-Leucine in Ice at 21 K by Circularly Polarized Synchrotron Radiation: a Terrestrial Proof of the Origin of Homochirality in Biosphere

H. Nishino¹, M. Hosaka², M. Katoh², Y. Inoue¹

¹Entropy Control, ICORP, Japan Science and Technology Agency, Toyonaka 560-0085 Japan

²UVSOR facility, Institute for Molecular Science, Okazaki 444-8585 Japan

The homochirality in biosphere is an extreme case of the entropy control in nature, while the origin of biomolecular homochirality is one of the most controversial issues in the chemical evolution on Earth [1]. It is proposed that the enantiomeric enrichment can be achieved by the circularly or elliptically polarized synchrotron radiation from a neutron star. This idea is supported by the finding of optically active amino acids in the organic mantle of the Murchison meteorite [2]. For this hypothesis, we have already reported the absolute asymmetric synthesis (AAS) of some aliphatic amino acids in aqueous solutions at varying pH (defined at 298 K), by using left- and right-handed circularly polarized light (*l*- and *r*-CPL) proceeded irrespective of the solution pH through different mechanisms [3].

In outer space, amino acids are thought to be frozen in icy carbonaceous chondrite meteorite. Recently, it was shown that a variety of racemic amino acids are photochemically produced indeed from a low-temperature matrix (12–15 K) of H₂O, CH₃OH, CO₂, CO, and NH₃ (2:1:1:1:1), which mimics the icy meteorite condition in outer space [4]. Hence, to fill the missing link of the origin of the homochirality in biomolecules, it is essential to examine whether the AAS of amino acids by CPL

proceeds in an ice matrix or not. In this study on the AAS of leucine (Leu) in ice, we irradiated the icy samples at 21 K (ice **XI**) and 81 K (ice **II**) with the 215 nm *l*- and *r*-CPL, generated by a helical undulator installed in the electron storage ring UVSOR-II.

We verified for the first time the occurrence of AAS of Leu even at 21 K by using circular dichroism (CD) spectroscopy (Figure 1). Quantitative product analyses of the irradiated samples revealed that, irrespective of the original pH (defined at 298 K), ammonia and isovaleraldehyde are the only detectable products from icy Leu irradiated at 215 nm. This is the first clear observation that the photodecomposition of Leu does occur even in a 21 K ice through photodeamination, which requires less molecular motions. In ice, HCl does not dissociate to an ion pair [H⁺ + Cl⁻], but exists as molecule at 77 K [5]. Hence, irrespective of the original pH defined at 25 °C, Leu exists as a zwitterion at 21 K. This may rationalize the very similar photochemical behavior of Leu in ice of different original pHs of 1 and 7.

These results unambiguously complete the whole scenario that, in outer space, simple starting materials, such as H₂O, CH₃OH, CO₂, CO, and NH₃, are irradiated by polarized or unpolarized VUV-UV irradiations to produce a mixture of racemic amino acids, including some of the essential amino acids [4], which in turn are enantioselectively photodecomposed on the way to Earth by the circularly polarized radiation from a neutron star or a star-forming area.

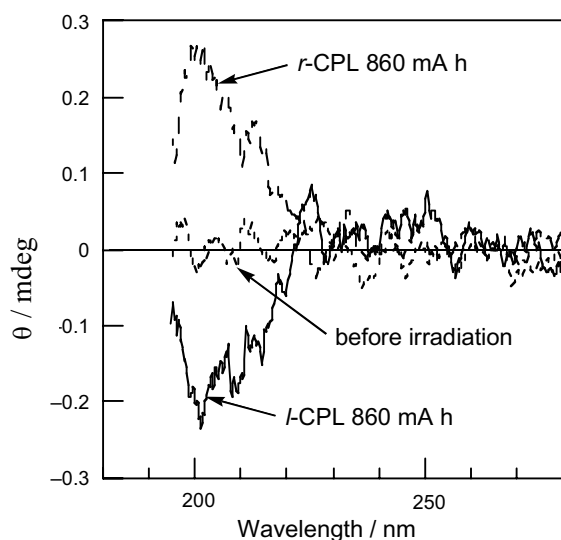


Fig. 1 The final CD of *rac*-Leu [*rac*-Leu]₀ = 6.5 mM, pH_{25°C} = 7) irradiated at 215 nm by CPL (21 K). % Decomposition: *r*-CPL 860 mA h; 20.8%, *l*-CPL 860 mA h; 17.4%. Path length of CD cell: 0.2 cm.

[1] W. A. Bonner, *Origins Life Evol. Biosphere* **21** (1991) 59.

[2] J. R. Cronin and S. Pizzarello, *Science* **275** (1997) 951.

[3] H. Nishino, A. Kosaka, G. A. Hembury, F. Aoki, K. Miyauchi, H. Shitomi, H. Onuki and Y. Inoue, *J. Am. Chem. Soc.* **124** (2002) 11618.

[4] M. P. Bernstein, J. P. Dworkin, S. A. Sandford, G. W. Cooper, L. J. Allamandola, *Nature* **416** (2002) 401. G. M. Munoz Caro, U. J. Meierhenrich, W. A. Schutte, B. Barbler, A. A. Segovia, H. Rosenbauer, W. H. P. Thiemann, A. Brack and J. M. Greenberg, *Nature* **416** (2002) 403.

[5] H. Kang, T.-H. Shin, S. -C. Park, I. K. Kim and S. -J. Han, *J. Am. Chem. Soc.* **122** (2000) 9842.

Undulator Radiation Induced Si-H Dissociation on H-Si(111) Surfaces Observed by STM

Y. Nonogaki, T. Urisu

Dept. Vacuum UV PhotoScience, Institute for Molecular Science, Okazaki 444-8585 Japan

Synchrotron-radiation-stimulated reactions, such as SR-etching and photon-stimulated desorption, have been attractive subjects from the view points of not only engineering but also surface science, due to their interesting characteristics of unique material and site selectivity, high spatial resolution and low damage.

We designed and constructed the undulator beamline equipped with an STM observation system at the UVSOR to investigate the excitation-energy dependence of SR-stimulated reactions. The undulator emits the quasi-monochromatized and tunable light of 50 - 120 eV, which is suitable for excitation of the Si 2p (~100 eV). In this study, the irradiation effects and its excitation energy dependence on the H-Si (111) surfaces were investigated by in-situ STM. Although photon-stimulated H desorptions from H-Si (111) surfaces have been studied by detecting the desorbing molecules[1,2], there is no report with the surface morphology studied by STM after the photon-stimulated desorption.

The clean Si (111) surface was exposed to atomic H at 350°C for 10 min, which gives sufficiently wide 1x1 areas. The surface was irradiated by the undulator emission with irradiation dose of 5,000 and 10,000 mA sec (ring current x exposure time) at room temperature. The undulator gap height was fixed at 17 mm, 20 mm and 25 mm.

Figure 1 (a) shows a 10 nm x 10 nm STM image of the H-Si (111) surface obtained by the 10 min atomic H exposure at 350°C. Islands and small protrusions (SPs) are visible on a flat surface with the atomic corrugation, as reported in Refs. 3 and 4. The flat surface with the atomic corrugation consists of rest-atom monohydrides. According to Ref. 4, the SPs are assigned to isolated adatom trihydrides or rest-atoms with missing H. The SP density is observed to be 1.5%ML.

Figure 1(b) shows the H-Si (111) surface after the undulator beam irradiation of 5,000 mA sec dose (1st harmonic radiation at ~84 eV). The number of the SPs significantly increased on the rest-atom monohydride surface from 1.4%ML to 4.5%ML. By increasing the exposure to 10,000 mA sec, the SP density increased to 12.8%ML, as shown in Fig. 1(c). The distribution of the SPs seems to be random and independent on the kind of the rest-atoms both on the faulted or unfaulted half of the 7x7 structure. It is most reasonable to assign the appeared SPs to the rest-atoms with missing H. This means that the rest-atom Si-H bond is easily dissociated by the irradiation of 84 eV photons.

The undulator gap height was changed to

investigate the dependence of the SP density on the incident photon energy. The irradiation dose was fixed at 5,000 mAsec. The peak energies of the 1st harmonic radiation were changed from 68 eV to 113 eV by varying the gap height from 17 mm to 25 mm.

It is found that the SP densities observed in the 38 nm x 38 nm STM images were depend not on Si 2p core electron transition threshold but on total photon flux irradiated to the surface. From these results, it is concluded that the main mechanism of the H desorption from the rest-atom monohydrides is the direct valence electron excitations by the undulator beam photons.

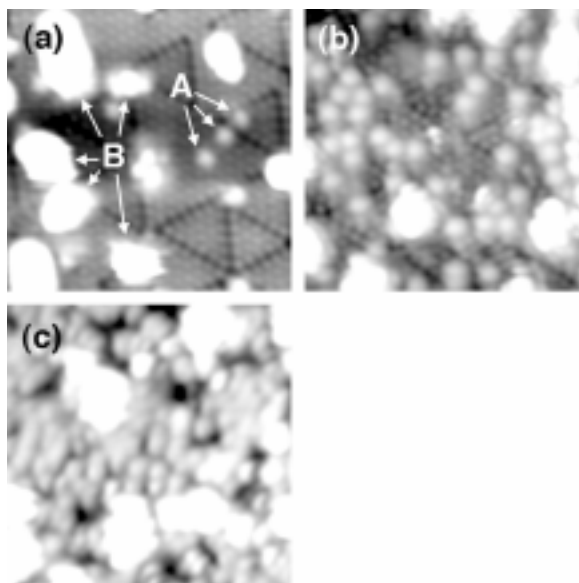


Fig. 1 10 nm x 10 nm STM images of H-Si (111) surfaces after the undulator beam irradiations with the exposure of (a) 0 mAsec, (b) 5,000 mAsec and (c) 10,000 mAsec. In (a), small protrusions (SPs) and adatom islands (AIs) are indicated by A and B, respectively. It is observed that the SP density significantly increases with increasing irradiation dose. The appeared SPs are assigned to the rest-atoms with missing H.

- [1] M.L. Knotek and G.M. Loubriel, R.H. Stulen, C.E. Parks, B.E. Koel, and Z. Hussain, *Phys. Rev. B* **26** (1982) 2292.
- [2] H. Akazawa, M. Sugiyama, S. Maeyama, M. Oshima and Y. Watanabe, *Phys. Rev. B* **57** (1998) 4883.
- [3] J.J. Boland, *Surf. Sci.* **244** (1991) 1.
- [4] F. Owman and P. Mårtensson, *Surf. Sci.* **324** (1995) 221.

Synchrotron Radiation-Excited Etching of ZnTe

T. Tanaka, Y. Kume, K. Hayashida, K. Saito, M. Nishio, Q. Guo, H. Ogawa
Saga University, 1 Honjyo, Saga 840-8502, Japan

Synchrotron radiation (SR) is an ideal light source for the photo-excited processes because of its high intensity, small divergence, and continuity of the wavelength from the x-ray to the infrared. With respect to the SR-excited etching, the materials for an integrated circuit such as Si, SiO₂, etc., have been studied actively [1]. However, few papers concerning the etching of the compound semiconductor materials such as III-V and II-VI semiconductors have been published to date in spite of their importance in the optoelectronic application. Since the single crystal films of II-VI semiconductors, e.g. ZnTe, can be grown by SR-excited growth [2], the development of the SR-excited etching is an important next step to make the electronic devices. Recently, we demonstrated the possibility of the SR-excited etching of ZnTe using Ar gas [3]. In this study, we have investigated the effect of the pressure upon the SR-excited etching process of ZnTe using Ar gas.

Experiments

The irradiation experiments were performed at a beam line, BL-8A, in UVSOR facility at IMS. The critical energy of the SR from the bending magnet field of the 750 MeV electron storage ring is 425 eV. The undispersed SR was focused on a sample in a reaction chamber using a Pt-coated toroidal mirror. The light intensities on the sample measured using an Au diode were determined as about 2×10^{16} photons/s at a stored current of 100 mA. The Ar pressure was changed between 0.02 and 0.5 Torr. The SR was irradiated perpendicularly to the surface of ZnTe (100) at room temperature through a Ni mesh mask of 100 lines/in. and 80% transmittance. The Ni mesh mask was put on the surface of the ZnTe directly. The ZnTe and the Ni mesh were negatively biased against the reaction chamber. The bias voltage was kept at -80 V in all experiments.

Results and discussion

The pattern of the Ni mask was transferred to the surface of the ZnTe exactly. However, the etched area was found to extend beyond the calculated beam size. It was also found that the etched depth depends on the photon flux density. The maximum etched depth is about 600 nm for 7×10^4 mA·min at 0.05 Torr. The dependence of the etching rate of ZnTe on the pressure is shown in Fig. 1. The etching rate is increased with increasing the pressure. In this experiment, the maximum etching rate is 16.7 nm/A·min, which is obtained at the pressure of 0.2 Torr.

In order to discuss the etching mechanism, we have also carried out the experiments using LiF window. LiF window pass through the photons with

the energy lower than about 12 eV. Although the SR was irradiated to the sample through the window for 10^5 mA·min at the pressure of 0.05 Torr under the same bias condition, the ZnTe was not etched at all. This indicates that the photons with energy less than 12 eV does not play important roles in the etching process. The photoabsorption cross section of Ar is reported to be almost zero in the energy range below the absorption edge of the LiF window, whereas it is quite large in the energy range between 12 eV and 50 eV [4]. The first ionization energy of Ar is 15.76 eV. We suspect that the ionization of Ar is necessary in this etching process. Since the mean free path of Ar is estimated to be around 1 mm at the pressure of 0.05 Torr, a part of Ar ions extends to the outside of the beam, resulting in the further expansion of the etching area. The increase of Ar gas pressure leads to the increase of Ar⁺ ion density, and consequently, the etching rate is increased according to the gas pressure.

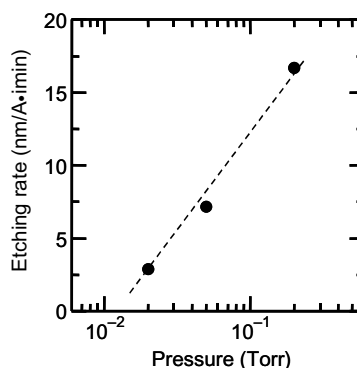


Fig. 1 Dependence of the etching rate of ZnTe on the pressure.

- [1] D. C. Mancini, S. Varma, J. K. Simons, R. A. Rosenberg, and P. A. Dowben, *J. Vac. Sci. Technol. B* **8** (1990) 1804.
- [2] T. Tanaka, K. Hayashida, S. Wang, Q. Guo, M. Nishio, and H. Ogawa, *Nucl. Instr. And Meth. B* **199** (2003) 356.
- [3] T. Tanaka, Y. Kume, S. Tokunaga, K. Hayashida, M. Nishio, Q. Guo, and H. Ogawa, *AIP series of conference proceedings* **705** (2004) 1154.
- [4] W. F. Chan, G. Cooper, X. Guo, G. R. Burton, and C. E. Brion, *Physical Review A* **46** (1992) 149.

List of Publications 2004

Published Papers

Y. Akahama, H. Kawamura

High-Pressure UV Spectroscopy on Oxygen up to 1.5 GPa

Chem. Phys. Lett. **392** (2004) 476.

T. Gejo, E. Shigemasa, E. Nakamura, M. Hosaka, S. Koda, A. Mochihashi,
M. Katoh, J. Yamazaki, K. Hayashi, Y. Takashima, H. Hama

The Investigation of Excited States of Xe Atoms and Dimers by Synchronization of FEL and SR Pulses at UVSOR

Nucl. Instr. and Meth. A **528** (2004) 627.

T. Hatsui, M. Nagasono, N. Kosugi

Ar 2p Excited States of Argon in Non-polar Media

J. Electron Spectrosc. and Relat. Phenom. **137-140** (2004) 435.

T. Hatsui, H. Setoyama, E. Shigemasa, N. Kosugi

Design of a Novel Transmission-Grating Spectrometer for Soft X-Ray Emission Studies

J. Electron Spectrosc. and Relat. Phenom. **144-147** (2005) 1059.

Y. Hikosaka, K. Mitsuke

Autoionization and Neutral Dissociation of Superexcited HI Studied by Two-Dimensional Photoelectron Spectroscopy

J. Chem. Phys. **121** (2004) 792.

Y. Hikosaka, E. Shigemasa

Velocity Imaging Spectrometer for Negative Fragment Ions: Application to Dynamics of O₂ and N₂O Ion-Pair Dissociation

J. Electron Spectrosc. and Relat. Phenom. **148** (2005) 5.

S. Hino, N. Wanita, K. Iwasaki, D. Yoshimura, N. Ozawa, T. Kodama,
K. Sakaguchi, H. Nishikawa, I. Ikemoto, K. Kikuchi

Ultraviolet Photoelectron Spectra of Three Tm@C₈₂ Isomers

Chem. Phys. Lett. **402** (2005) 217.

M. Hiyama, N. Kosugi

Ad Initio R-Matrix/MQDT Method for Near-Edge X-Ray Absorption Fine Structure

Physica Scripta. **T115** (2005) 136.

M. Hosaka, M. Katoh, A. Mochihashi, J. Yamazaki, K. Hayashi, T. Takashima

Upgrade of the UVSOR Storage Ring FEL

Nucl. Instr. and Meth. A **528** (2004) 291.

T. Ibuki, K. Okada

Mass-Selected Ion Spectroscopy of K-Shell Excited Polyatomic Molecules: Fragmentation Competing with Intramolecular Energy Relaxation

Recent Res. Devel. Chem. Physics **5** (2004) 77.

K. Iwasaki, S. Hino, D. Yoshimura, B. Cao, T. Okazaki, H. Shinohara

Ultraviolet Photoelectron Spectra of $Ti_2@C_{80}$

Chem. Phys. Lett. **397** (2004) 169.

K. Iwasaki, N. Wanita, S. Hino, D. Yoshimura, T. Okazaki, H. Shinohara

Ultraviolet Photoelectron Spectra of $Tb@C_{82}$

Chem. Phys. Lett. **398** (2004) 389.

S. Kimura, M. Okuno, H. Kitazawa, F. Ishiyama, O. Sakai

Change of Electronic Structure Induced by Magnetic Transitions in CeBi

J. Phys. Soc. Jpn. **73** (8) (2004) 2041.

S. Kimura, T. Nishi, J. Sichelschmidt, V. Voevodin, J. Ferstl, C. Geibel, F. Steglich

Optical Conductivity of a Non-Fermi-Liquid Material $YbRh_2Si_2$

J. Mag. Mag. Mater. **272-276** (2004) 36.

M. Kitaura, K. Mochizuki, Y. Inabe, M. Itoh, H. Nakagawa, S. Oishi

Fundamental Optical Properties and Electronic Structure of Langasite $La_3Ga_5SiO_{14}$ Crystals

Phys. Rev. B **69** (2004) 115120.

S. Kimura, T. Nishi, Y. Mori, Y. Sumida, T. Takahashi, Y. S. Kwon, H. J. Im,
H. Kitazawa

Infrared Study on CeSb Under High Pressures

Physica B **359-361** (2005) 190.

N. Kosugi

Spin-orbit and Exchange Interactions in Molecular Inner Shell Spectroscopy

J. Electron Spectrosc. and Relat. Phenom. **137-140** (2004) 335.

J. Kou, T. Mori, Y. Kubozono, K. Mitsuke

Photofragmentation of C₆₀ in the Extreme Ultraviolet: Statistical Analysis on the Appearance Energies of C_{60-2n}^{Z+} (n ≥ 1, z = 1-3)

Phys. Chem. Chem. Phys. **7** (2005) 119.

J. Kou, T. Mori, Y. Kubozono, K. Mitsuke

Photofragmentation of C₆₀ in Valence Ionization

J. Electron Spectrosc. and Relat. Phenom. **144-147** (2005) 247.

J. Kou, T. Mori, S. V. K. Kumar, Y. Haruyama, Y. Kubozono, K. Mitsuke

Double Photoionization of C₆₀ and C₇₀ in the Valence Region

J. Chem. Phys. **120** (2004) 6005.

K. Mitsuke

Photofragmentation Mechanisms of H₂O Studied by Ultraviolet Dispersed Spectroscopy

J. Electron Spectrosc. and Relat. Phenom. **144-147** (2005) 131.

K. Mitsuke, T. Mori, J. Kou, Y. Haruyama, Y. Kubozono

4d → 4f Dipole Resonance of the Metal Atom Encapsulated in a Fullerene Cage: Ce@C₈₂

J. Chem. Phys. **122** (2005) 064304.

A. Mochihashi, M. Katoh, M. Hosaka, K. Hayashi, J. Yamazaki, Y. Takashima,
Y. Hori

Ion Trapping Phenomenon in UVSOR Electron Storage Ring

Jpn. J. Appl. Phys. **44** (2005) 430.

T. Mori, J. Kou, M. Ono, Y. Haruyama, Y. Kubozono, K. Mitsuke
Absolute Photoabsorption Cross Section of C₆₀ in the Extreme Ultraviolet

J. Electron Spectrosc. and Relat. Phenom. **144-147** (2005) 243.

T. Naito, M. Tadano, N. Terunuma, J. Urakawa, E. Nakamura, M. Hasumoto,
H. Sakai, T. Shibuya, F. Sakai, H. Ohgaki, N. Sei

Investigation of Carbon Contamination on SR-Irradiated Devices

Nucl. Instr. and Meth. A **527** (2004) 624.

Y. Nonogaki, M. Katoh, K. Matsushita, M. Suzui, T. Urisu

Construction of the Undulator Beamline Equipped with a UHV-STM for Observations of Synchrotron-Radiation-Stimulated Surface Reaction

J. Electron Spectrosc. and Relat. Phenom. **144-147** (2005) 1113.

K. Okada, S. Tanimoto, T. Ibuki, Y. Haga, T. Gejo, K. Saito, K. Ohno

Angle-resolved, Mass-Selected Ion Spectroscopy of Carbon K-Shell Excited CF₃CCH

Chem. Phys. **304** (2004) 273.

H. Okamura, T. Koretsune, S. Kimura, T. Nanba, H. Imai, Y. Shimakawa, Y. Kubo
Carrier-Induced Magnetic Circular Dichroism in the Magnetoresistive Pyrochlore Ti₂Mn₂O₇

J. Phys. Soc. Jpn. **74** (3) (2005) 970.

M. Ono, H. Yamane, F. Katagiri, H. Fukagawa, S. Kera, D. Yoshimura,

K. K. Okudaira, E. Morikawa, K. Seki, N. Ueno

UPS Study of VUV-Photodegradation of Polyfluoroethylene (PTFE) Ultrathin Film by Using Synchrotron Radiation

Nucl. Instr. and Meth. **B**, in press.

M. Ono, H. Yamane, H. Fukagawa, S. Kera, D. Yoshimura, E. Morikawa, K. Seki
N. Ueno

Possibility of the Fermi Level Control by VUV-Induced Doping of an Organic Thin Film: Polytetrafluoroethylene

Submitted to IPAP Conference Proceedings.

I. Ouchi, I. Nakai, M. Ono, S. Kimura

Features of Fluorescence Spectra of Polyethylene Terephthalate Films

Jpn. J. Appl. Phys. **43** (12) (2004) 8407.

H. Setoyama, T. Hatsui, N. Kosugi

S 2p Excited States of OCS in Rare Gas Matrices

J. Electron Spectrosc. and Relat. Phenom. **144-147** (2005) 87.

K. Soda, K. Shimba, S. Yagi, M. Kato, T. Takeuchi, U. Mizutani, T. Zhang,
M. Hasegawa, A. Inoue, T. Ito, S. Kimura

Electronic Structure of Bul; Metallic Glass $Zr_{55}Al_{10}Cu_{30}Ni_5$

J. Electron Spectrosc. and Relat. Phenom. **144-147** (2005) 585.

T. Tanaka, Y. Kume, S. Tokunaga, K. Hayashida, M. Nishio, Q. Guo, H. Ogawa

Synchrotron Radiation-Excited Etching of ZnTe

API Conference Proceedings **705** (2004) 1154.

Published Papers (before 2004)

J. Kou, T. Mori, M. Ono, Y. Haruyama, Y. Kubozono, K. Mitsuke

Molecular- and Atomic-Like Photoionization of C_{60} in the Extreme Ultraviolet

Chem. Phys. Lett. **374** (2003) 1.

T. Mori, J. Kou, M. Ono, Y. Haruyama, Y. Kubozono, K. Mitsuke

Development of a Photoionization Spectrometer for Accurate Ion Yield Measurements from Gaseous Fullerenes

Rev. Scientific Instrum. **74** (2003) 3769.

M. Ono, K. Mitsuke

Kinetic Energy Distribution and Anisotropy of Fragment Ions from SF_6 by Photoexcitation of a Sulfur 2p-Electron

Chem. Phys. Lett. **379** (2003) 248.

The 11th UVSOR Workshop

Upgrading of VUV beamline

March 10, 2005

(Chairperson: S. Kimura)

- | | |
|---|------------------------|
| 13:30- Preface | S. Kimura (UVSOR) |
| 13:40- Present status of UVSOR light source | M. Katoh (UVSOR) |
| 14:05- Present status of UVSOR beamlines | E. Shigemasa (UVSOR) |
| 14:30- Present status of BL5U | T. Ito (UVSOR) |
| 15:00- Present status of BL7B | K. Fukui (Fukui Univ.) |
| 15:30- coffee time | |

(Chairperson: M. Katoh)

- | | |
|--|--------------------------|
| 16:00- Recent undulators | T. Hara (RIKEN/SPring-8) |
| 16:30- Present status UVSOR FEL and undulator at UVSOR | M. Hosaka (UVSOR) |
| 17:00- Creation of soft x-ray by ultra-short pulse | E. Takahashi (IMS) |
| 17:30- External appraisal report and future plan | N. Kosugi (UVSOR) |
| 18:00- Facility tour, banquet | |

March 11, 2005

(Chairperson: E. Shigemasa)

- | | |
|---|---------------------------|
| 9:00- Normal incident monochromator at SuperSOR | T. Mizokawa (Univ. Tokyo) |
| 9:30- Construction and performance check of KEK-PF BL28 | K. Ono (KEK-PF) |
| 10:00- New normal incident monochromator at UVSOR | S. Kimura (UVSOR) |
| 10:30- coffee time | |

(Chairperson: T. Ito)

- | | |
|--|------------------------|
| 11:00- Solid state photoemission spectroscopy using He-lamp and SRC | T. Sato (Tohoku Univ.) |
| 11:30- Present status and future plan of molecular spectroscopy
using high resolution normal incident monochromator | K. Mitsuke (IMS) |
| 12:00- Molecular spectroscopy in the normal incident monochromator region at PF | K. Ito (KEK-PF) |
| 12:30- Discussion | |

UVSOR Lunch Seminar

FY2004

- June 2 Dr. H. Nishino, Entropy Control Project, ICORP, Japan Science and Technology Agency
Circularly Polarized Synchrotron Radiation Photolysis of Aliphatic Amino Acids
- July 14 Prof. A. Tanaka, Department of Mechanical Engineering, Kobe University
Photoemission study of metallic nanoparticle surface-passivated by organic molecules
- Oct. 20 Dr. H. Kobayashi, Research Institute for Ubiquitous Energy Devices, AIST
Structure and charge and discharge mechanism of positive pole of lithium secondary battery
- Dec. 17 Dr. M. Takata, JASRI/SPring-8
Study on structural solid state physics by MEM and powder diffraction using SR
- Dec. 17 Dr. H. Tanaka, JASRI/SPring-8
Present status and perspective of SPring-8 light source; for the forth generation light source
- Dec. 22 Dr. T. Kawai, Osaka Women's University
New aspects of Tl^+ -impurity center
- Dec. 22 Dr. S. Bielawski, Universite des Sciences et Technologies de Lille, France
Nonlinear dynamics applied to lasers: Several problems of temporal and spatiotemporal dynamics
- Feb. 16 Dr. F. Penent, Universite Pierre et Marie Curie, France
Fluorescence from doubly excited states of Helium
- Feb. 23 Dr. J. Sichelschmidt, Max-Planck-Institute for Chemical Physics of Solids, Dresden, Germany
Kondo-ion electron spin resonance of isotope clean $^{174}YbRh_2Si_2$
- Feb. 23 Prof. M. Nakamura, Department of Physics, Nagoya University
Universe observed by microscope: OPERA experiment
- Feb. 24 Dr. I. Bradeanu, Wuerzburg University, Germany
Post collision interaction in free van der Waals clusters
- Mar. 2 Prof. T. W. Noh, Seoul National University, South Korea
Roles of orbitals in transition metal oxides probed by optical spectroscopy